

**Influence of Strontium and Nickel Co-doping on the Microstructure,  
Dielectric and Magnetic Properties of Barium-Strontium-Nickel Titanate**

by

Md. Mehedi Hasan  
Roll No.: 0417143005P  
Session: April 2017


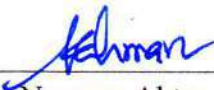



MASTER OF PHILOSOPHY IN PHYSICS



Department of Physics  
BANGLADESH UNIVERSITY OF ENGINEERING & TECHNOLOGY  
May 2023

The thesis titled “**Influence of Strontium and Nickel Co-doping on The Microstructure, Dielectric and Magnetic Properties of Barium-Strontium-Nickel Titanate**” submitted by **Md. Mehedi Hasan**, Roll No.: **0417143005P**, Session: **April-2017**, has been accepted as satisfactory in partial fulfillment of the requirement for the degree of **MASTER OF PHILOSOPHY IN PHYSICS** on 29 May, 2023.

### BOARD OF EXAMINERS

1.   
\_\_\_\_\_  
Dr. A. K. M. Akther Hossain (Supervisor)  
Professor, Department of Physics,  
BUET, Dhaka-1000. Chairman
2.   
\_\_\_\_\_  
Dr. Nasreen Akter  
Professor and Head, Department of Physics,  
BUET, Dhaka-1000. Member  
(Ex-Officio)
3.   
\_\_\_\_\_  
Dr. Md. Forhad Mina  
Professor, Department of Physics,  
BUET, Dhaka-1000. Member
4.   
\_\_\_\_\_  
Dr. Md. Azizar Rahman  
Associate Professor, Department of Physics,  
BUET, Dhaka-1000. Member
5.   
\_\_\_\_\_  
Dr. A. B. M. Obaidul Islam  
Professor, Department of Physics,  
University of Dhaka, Dhaka-1000. Member  
(External)

## CANDIDATE'S DECLARATION

It is hereby declared that this thesis or any part of it has not been submitted elsewhere for the award of any degree or diploma.



---

Md. Mehedi Hasan

*I dedicate this work to the Almighty Allah, who has been my source of strength, grace, and wisdom over the years of my academic journey*

## Acknowledgments

All praise belongs to Allah, who made us and gave us the highest place among all of his other creations. I am very appreciative to Allah SWT for bestowing upon me the stamina, bravery, and patience necessary to finish this study.

I want to convey my sincere gratitude to my supervisor, Prof. A. K. M. Akther Hossain, Department of Physics, Bangladesh University of Engineering and Technology (BUET), Dhaka for his continuous support, motivating suggestions, constructive criticism, and numerous fruitful discussion that helped me to overcome the difficult situations during the period of my research work.

I am grateful to Prof. Dr. Nasreen Akter, Head, Department of Physics, BUET. I would also like to convey my heartfelt appreciation to Prof. Jiban Podder, Prof. Md. Feroz Alam Khan, Prof. Md. Mostak Hossain, Prof. Afia Begum, Prof. Md. Forhad Mina, Prof. Md. Rafi Uddin, Prof. Md. Abdul Basith, Prof. Dr. Mohammad Abu Sayem Karal, Prof. Dr. Mohammad Jellur Rahman, Prof. Dr. Muhammad Samir Ullah, Prof. Dr. Muhammad Rakibul Islam and all other faculty members of the Department of Physics, BUET, Dhaka for their sincere cooperation.

I am thankful to all my colleagues at City University for their support in many ways throughout my research work. I want to thank Dr. Mohammed Nazrul Islam Khan, CSO, Materials Science Division, Atomic Energy Centre, Dhaka for his support in taking measurements of my specimens. I also gratefully acknowledge the IICT of BUET for the server facility. I also gratefully acknowledge the cooperation of all Ph.D., M.Phil., and M.Sc. researchers in our laboratory for their constant support in many ways.

Finally, I want to express my sincere gratitude to my parents, Md. Ramiz Uddin and Most. Mahmuda Akter as they made enormous sacrifices to ensure that their children had a more equal chance at life.

The Author  
Md. Mehedi Hasan

## ABSTRACT

The elastic, thermodynamic, and optoelectronic properties of cubic  $ABO_3$  [ $A = Ba, Ca, Sr; B = Ce, Ti, Zr$ ] perovskites have been studied theoretically. It was found that  $BaTiO_3$  has the lowest bandgap among these nine compounds. A theoretical study has also been performed to investigate the effect of the co-doping of  $Sr$  and  $Ni$  on the optoelectronic properties of  $BaTiO_3$ . An influence of co-doping was observed in optical properties of doped- $BaTiO_3$ . Based on the theoretical results, various  $Ba_{1-x}(Sr_{0.5}Ni_{0.5})_xTiO_3$  compositions were synthesized using the conventional solid-state technique. Samples prepared from each composition were sintered at different temperatures. Samples with the optimum sintering temperature of  $1250^\circ C$  have been characterized by XRD, complex impedance spectroscopy, FESEM, EDS, and VSM analysis. Different fitting approaches like Scherer and W-H methods, non-linear modified Debye equation, Jonscher's power law, and Law of Approach to Saturation have been followed to investigate experimental and calculated properties. Rietveld analysis shows a phase change for different values of  $x$ . The samples having composition with  $x = 0.15$  is less porous and has better dielectric properties, while  $x = 0.25$  has a larger grain size with better magnetic properties. Different experimental and their calculated properties show good consistencies. Co-doping of  $Sr$  and  $Ni$  in  $BaTiO_3$  shows promising electrical properties with weak magnetism, which fall in the category of iron-free multiferroics. These synthesized materials can be a promising candidate to design a wide range of novel multifunctional devices, including capacitor technology, electromagnetics sensor, spintronics etc.

# CONTENTS

	Page No.	
Abstract	vii	
Contents	viii	
List of Figures	xi	
List of Tables	xv	
Abbreviations of Symbols and Terms	xvi	
<b>CHAPTER 1: INTRODUCTION</b>		
1.1	Background	01
1.2	The Motivation for the Present Investigation	02
1.3	Objectives of the Present Work	04
1.4	Outline of the Thesis	04
<b>CHAPTER 2: LITERATURE REVIEW</b>		
2.1.	Review of Earlier Works	05
<b>CHAPTER 3: THEORETICAL METHODOLOGY AND EXPERIMENTAL TECHNIQUES</b>		
3.1.	Theoretical Methodology	19
3.1.1	The Schrödinger equation	19
3.1.2	Born-Oppenheimer approximation	20
3.1.3	Hartree-Fock approximation	20
3.1.4	Density Functional Theory	21
3.1.5	Generalized Gradient Approximation	21
3.1.6	k-point sampling	22
3.1.7	Cut-off energy	23
3.1.8	Pseudopotential	23
3.1.9	Ground state energy	24
3.1.10	CASTEP	25
3.1.11	Computation of different properties	25
3.2	Sample Preparation and Experimental Techniques	26
3.2.1	Standard solid-state reaction technique	26
3.2.2	Details of sample preparation: calcining, shaping and pressing, sintering, and etching	28
3.2.2.1	Calcining	28
3.2.2.2	Shaping and pressing	28

3.2.2.3	Sintering	29
3.2.2.4	Etching	31
3.2.3	Preparation of the samples	31
3.2.4	Structural and morphological characterization	32
3.2.4.1	X-ray diffraction	32
3.2.4.2	Lattice constant, density, and porosity	33
3.2.4.3	Microstructural and elemental analysis	34
3.2.5	Electrical Properties	34
3.2.5.1	Dielectric properties	34
3.2.5.2	Complex impedance spectroscopy	35
3.2.5.3	The ac conductivity	35
3.2.5.4	Electric modulus	36
3.2.6	Magnetic properties	36
3.2.6.1	Complex initial permeability	36
3.2.6.2	M-H plot	37

## CHAPTER 4: RESULTS AND DISCUSSION

4.1	Theoretical Investigation	38
4.1.1	Different $ABO_3$ perovskites	38
4.1.1.1	Computational parameters	38
4.1.1.2	Structural properties	39
4.1.1.3	Mechanical properties	39
4.1.1.4	Thermodynamic properties	46
4.1.1.5	Electronic properties	50
4.1.1.6	Optical properties	54
4.1.2	<i>Sr</i> - and <i>Ni</i> -doped $BaTiO_3$ : Theoretical investigation	57
4.1.2.1	Computational parameters	57
4.1.2.2	Electronic properties	58
4.1.2.3	Optical properties	60
4.2	Experimental Investigation of <i>Sr</i> and <i>Ni</i> Co-doped $BaTiO_3$	63
4.2.1	Structural properties	63
4.2.1.1	Bulk density	63
4.2.1.2	X-ray diffraction analysis	64
4.2.1.3	Crystallite size using Scherrer method, theoretical density, and porosity	67



	4.2.1.4	Crystallite size and microstrain analysis using the Williamson-Hall method	68
	4.2.1.5	Microstructural analysis	70
	4.2.1.6	Energy dispersive spectroscopy	70
4.2.2		Electric properties	73
	4.2.2.1	Dielectric properties	73
	4.2.2.2	Dielectric loss factor	77
	4.2.2.3	The ac-conductivity	78
	4.2.2.4	Complex impedance spectroscopy analysis	81
	4.2.2.5	Electric modulus study	82
4.2.3		Magnetic properties	83
	4.2.3.1	Initial permeability	83
	4.2.3.2	Magnetic loss-function	85
	4.2.3.3	Relative Quality Factor	86
	4.2.3.4	Hysteresis loop analysis	86
 <b>CHAPTER 5: CONCLUSIONS</b>			
5.1		Summary of the Present Investigation	90
5.2		Conclusions	92
5.2		Suggestions for Further Research	92
 <b>The Novelty of the Present Research</b>			94
<b>References</b>			95
<b>List of Publications</b>			112

## List of Figures

Fig. No.	Figure Caption	Page No.
Fig. 1.1	A typical unit cell of perovskite-type $BaTiO_3$ .	2
Fig. 2.1	Orthorhombic $BaTiO_3$ - (a) X-ray diffractogram and (b) Temperature-dependent variation of the $\epsilon_r$ measured at frequency values 1, 10, and 100 kHz.	6
Fig. 2.2	XRD patterns of $BST$ specimens (a) $x = 0.25$ and (b) $x = 0.90$ sintered without additives at $1230^\circ C$ for 2 h.	7
Fig. 2.3	The dependence of the dielectric constant as a function of temperature measured at 1 kHz for doped $Ba_{1-x}Sr_xTiO_3$ ( $x = 0.25, 0.50, 0.75, 0.90$ ) samples, sintered at $1260^\circ C$ for 2 h.	8
Fig. 2.4	The variation of the dielectric constant of $Ba_xSr_{1-x}TiO_3$ ( $x = 1, 0.9, 0.8, 0.7$ ) ceramics as a function of temperature for various $Sr$ concentrations at 1, 10, and 100 kHz.	8
Fig. 2.5	Graphs of $BaTiO_3 + xSr$ compositions (a) XRD spectra, and (b) Variation in dielectric constant with $Sr$ -content.	9
Fig. 2.6	Room temperature magnetic M-H hysteresis loops of $Ni_{1-x}A_xTiO_3$ ( $A = Mn, Fe, Co, Cu, Zn; x = 0, 0.05, 0.1$ ) samples with $x = 0$ , and $0.05$ .	10
Fig. 2.7	Variation of $\epsilon_m$ with mole % of the dopant.	11
Fig. 2.8	Magnetization ( $M$ ) as a function of temperature ( $T$ ) where the inset shows the magnetization ( $M$ ) versus magnetizing field ( $H_{dc}$ ) for $BaNi_{0.01}Ti_{0.99}O_3$ .	12
Fig. 2.9	Temperature dependent $\epsilon_r$ and $\tan\delta$ of $BaNi_{0.01}Ti_{0.99}O_3$ .	12
Fig. 2.10	(a) Dielectric constant as a function of frequency at room temperature of $BaTiO_3 + xNi$ thin films and (b) Dielectric constant vs $Ni$ -concentration ( $mol$ ) of the samples.	13
Fig. 2.11	Magnetic hysteresis (M-H) loops of $Ba(Ti_{1-x}Ni_x)O_3$ ( $0 \leq x \leq 0.06$ ) at room temperature.	14
Fig. 2.12	Magnetic hysteresis loops at room temperature for $Ba(Ti_{1-x}Ni_x)O_3$ ; (a) $x = 0\%$ , (b) $x = 2.5\%$ , (c) $x = 5\%$ , (d) $x = 7.5\%$ , (e) $x = 10\%$ ceramics and figure (f) shows the remnant magnetization behavior of $BTNO$	15
Fig. 2.13	SEM micrographs of $Ba(Ti_{1-x}Ni_x)O_3$ ceramics (a) $x = 0\%$ , (b) $x = 2.5\%$ , (c) $x = 5\%$ , (d) $x = 7.5\%$ , and (e) $x = 10\%$ .	16

Fig. 2.14	The $\epsilon'$ versus temperature curves at 1 kHz show the ferroelectric $T_c$ transition.	17
Fig. 2.15	Dielectric constant as a function of temperature.	17
Fig. 2.16	M–H hysteresis loops and the inset is a representation of F-center exchange interaction.	18
Fig. 3.1	Flow chart for the solid-state reaction method of sample preparation.	27
Fig. 3.2	Different stages of sintering: (a) green body (b) primary stage (c) intermediate stage, and (d) the finishing stage.	30
Fig. 3.3	Toroid- and disk-shaped samples.	31
Fig. 3.4	Bragg law of X-ray diffraction.	32
Fig. 4.1	Crystal structure of cubic $ABO_3$ [ $A = Ba, Ca, Sr$ ; $B=Ce, Ti, Zr$ ] perovskites (3D view).	37
Fig. 4.2 (a)	The 2D and 3D plots of $Y$ of $ABO_3$ perovskites at 0 GPa.	41
Fig. 4.2 (b)	The 2D and 3D plots of $K$ of $ABO_3$ perovskites at 0 GPa.	42
Fig. 4.2 (c)	The 2D and 3D plots of $G$ of $ABO_3$ perovskites at 0 GPa.	43
Fig. 4.2 (d)	The 2D and 3D plots of $\nu$ of $ABO_3$ perovskites at 0 GPa.	44
Fig. 4.3	The calculated phonon dispersion curves along the high-symmetry points (a) $BaCeO_3$ , (b) $CaCeO_3$ , (c) $SrCeO_3$ , (d) $BaTiO_3$ , (e) $CaTiO_3$ , (f) $SrTiO_3$ , (g) $BaZrO_3$ , (h) $CaZrO_3$ , (i) $SrZrO_3$ .	46
Fig. 4.4	The calculated phonon Density of states of $ABO_3$ perovskites.	47
Fig. 4.5	The calculated (a) Enthalpy, (b) $T^*$ Entropy, and (c) Free energy of $ABO_3$ perovskites.	48
Fig. 4.6	The calculated temperature-dependent (a) heat capacity and (b) Debye temperature of $ABO_3$ .	48
Fig. 4.7	The calculated band diagrams along high-symmetry points (a) $BaCeO_3$ , (b) $CaCeO_3$ , (c) $SrCeO_3$ , (d) $BaTiO_3$ , (e) $CaTiO_3$ , (f) $SrTiO_3$ , (g) $BaZrO_3$ , (h) $CaZrO_3$ , (i) $SrZrO_3$ .	50
Fig. 4.8	Comparison of band gaps of different cubic $ABO_3$ perovskites.	50
Fig. 4.9	Calculated electron density of states of various $ABO_3$ perovskites.	51
Fig. 4.10	The calculated partial density of states (PDOS) of (a) $BaCeO_3$ , (b) $CaCeO_3$ , (c) $SrCeO_3$ , (d) $BaTiO_3$ , (e) $CaTiO_3$ , (f) $SrTiO_3$ , (g) $BaZrO_3$ , (h) $CaZrO_3$ , (i) $SrZrO_3$ .	52

Fig. 4.11	The calculated (a) absorption, (b) reflectivity, (c) real part of conductivity, (d) imaginary part of conductivity, (e) real part of the dielectric function, (f) imaginary part of the dielectric function, (g) refractive index (n), (h) refractive index (k) of various $ABO_3$ perovskites.	54
Fig. 4.12	The calculated Loss function of $ABO_3$ perovskites.	55
Fig. 4.13	Geometrically optimized (a) pure $BaTiO_3$ , (b) 12.5% Sr atom doped $BTO$ , $Ba_{0.875}Sr_{0.125}TiO_3$ ( $BSTO$ ) and (c) 12.5% Ni atom doped $BTO$ , $Ba_{0.875}Ni_{0.125}TiO_3$ ( $BNTO$ ) and (d) 25% atom (Sr, Ni) co-doped $BTO$ ,	56
Fig. 4.14	Electronic band structure of (a) pristine $BTO$ (b) $BSTO$ (c) $BNTO$ and (d) $BSNTO$ .	57
Fig. 4.15	The density of states (DOS).	58
Fig. 4.16	The total and partial density of states of (a) pristine $BTO$ , (b) $BSTO$ , (c) $BNTO$ , and (d) $BSNTO$ .	59
Fig. 4.17	The calculated photon energy dependent (a) absorption, (b) reflectivity, (c) real part of conductivity, (d) imaginary part of conductivity, (e) real part of the dielectric function, (f) imaginary part of the dielectric	60
Fig. 4.18	Loss function as a function of photon energy.	61
Fig. 4.19	Density as a function of sintering temperature for various $Ba_{1-x}(Sr_{0.5}Ni_{0.5})_xTiO_3$ .	62
Fig. 4.20	XRD patterns for various $Ba_{1-x}(Sr_{0.5}Ni_{0.5})_xTiO_3$ .	63
Fig. 4.21	Calculated Rietveld refinement of several $Ba_{1-x}(Sr_{0.5}Ni_{0.5})_xTiO_3$ .	64
Fig. 4.22	Determination of crystallite size from (110) peaks using the Gaussian fitting method of various $Ba_{1-x}(Sr_{0.5}Ni_{0.5})_xTiO_3$ .	66
Fig. 4.23	Plot of $\rho_{th}$ , $\rho_B$ , and porosity (%) for various $Ba_{1-x}(Sr_{0.5}Ni_{0.5})_xTiO_3$ .	67
Fig. 4.24	Crystallite size and microstrain calculation from W-H method of various $Ba_{1-x}(Sr_{0.5}Ni_{0.5})_xTiO_3$ .	68
Fig. 4.25	FESEM images of various $Ba_{1-x}(Sr_{0.5}Ni_{0.5})_xTiO_3$ and the calculated average grain size using a histogram (in the inset of the corresponding image).	70
Fig. 4.26	The EDS spectrum of $Ba_{1-x}(Sr_{0.5}Ni_{0.5})_xTiO_3$ with $x = 0.60$ .	71
Fig. 4.27	The variation of $\epsilon'$ with frequency for $Ba_{1-x}(Sr_{0.5}Ni_{0.5})_xTiO_3$ .	73
Fig. 4.28	The $\epsilon'_{pC}$ and $\epsilon'_M$ at different frequencies for various $Ba_{1-x}(Sr_{0.5}Ni_{0.5})_xTiO_3$ .	74

Fig. 4.29	Frequency dispersion behavior of $\varepsilon'$ for various $Ba_{1-x}(Sr_{0.5}Ni_{0.5})_xTiO_3$ fit to the Nonlinear Debye's modified function.	75
Fig. 4.30	Frequency dependence of $\tan\delta_E$ for various $Ba_{1-x}(Sr_{0.5}Ni_{0.5})_xTiO_3$ .	77
Fig. 4.31	Frequency dependence of $\sigma_{ac}$ for various $Ba_{1-x}(Sr_{0.5}Ni_{0.5})_xTiO_3$ .	78
Fig. 4.32	Fitted data of frequency dependence of $\sigma_{ac}$ for various $Ba_{1-x}(Sr_{0.5}Ni_{0.5})_xTiO_3$ according to Jonscher's power law.	79
Fig. 4.33	(a) Variation of $\log\sigma_{ac}$ with $\log\omega$ (both experimental and linear fit) and (b) values of exponent $n$ calculated from JPL fit and linear fit data for different $Ba_{1-x}(Sr_{0.5}Ni_{0.5})_xTiO_3$ .	80
Fig. 4.34	Frequency dependence of (a) $Z'$ , and (b) $Z''$ for various $Ba_{1-x}(Sr_{0.5}Ni_{0.5})_xTiO_3$ .	81
Fig. 4.35	Frequency dependence of (a) $M'$ , and (b) $M''$ for different $Ba_{1-x}(Sr_{0.5}Ni_{0.5})_xTiO_3$ .	82
Fig. 4.36	The variation of $\mu'_i$ with respect to frequency for various $Ba_{1-x}(Sr_{0.5}Ni_{0.5})_xTiO_3$ .	83
Fig. 4.37	The variation of $m_i\phi$ at different frequencies with doping content for various $Ba_{1-x}(Sr_{0.5}Ni_{0.5})_xTiO_3$ .	84
Fig. 4.38	The variation of (a) $\tan\delta_M$ and (b) $RQF$ with frequency for $Ba_{1-x}(Sr_{0.5}Ni_{0.5})_xTiO_3$ .	85
Fig. 4.39	M-H hysteresis plot of various $Ba_{1-x}(Sr_{0.5}Ni_{0.5})_xTiO_3$ .	86
Fig. 4.40	Saturation magnetization as a function of doping content of various $Ba_{1-x}(Sr_{0.5}Ni_{0.5})_xTiO_3$ .	87

## List of Tables

Table No.	Table caption	Page No.
Table 2.1	Composition, crystal structure, crystalline size (d), and $T_c$ of the $Ba(Ti_{1-x}Ni_x)O_3$ samples.	11
Table 2.2	$\epsilon'_r$ , $\tan\delta$ and $\Delta\epsilon'$ of different $BaTi_{1-x}Ni_xO_3$ .	14
Table 4.1	Calculated structural parameters of cubic $ABO_3$ ( $A = Ba, Ca, Sr$ ; $B = Ce, Ti, Zr$ ) materials.	38
Table 4.2	The calculated elastic constants ( $C_{11}, C_{12}, C_{44}$ ), $Y, B, G, C'', \nu, B/G$ ratio, Compressibility ( $K$ ), Universal Anisotropic factor, $\theta_D$ and $V_m$ of various $ABO_3$ perovskites.	40
Table 4.3	The calculated Zero-point energy.	49
Table 4.4	Calculated parameters of $Sr, Ni$ -doped cubic $BaTiO_3$ perovskites.	57
Table 4.5	Calculated Rietveld refinement data from XRD data of different $Ba_{1-x}(Sr_{0.5}Ni_{0.5})_xTiO_3$ .	65
Table 4.6	Calculation of crystallite size and microstrain from (110) peaks using Scherrer's equation, crystallite size and microstrain using W-H method $\rho_{th}, \rho_B$ , porosity (%) and grain size of various $Ba_{1-x}(Sr_{0.5}Ni_{0.5})_xTiO_3$ .	69
Table 4.7	The relative density (in %) of various $Ba_{1-x}(Sr_{0.5}Ni_{0.5})_xTiO_3$ and $\epsilon'_{PC}$ and $\epsilon'_M$ at different frequencies.	73
Table 4.8	Magnetic properties of various $Ba_{1-x}(Sr_{0.5}Ni_{0.5})_xTiO_3$ compounds calculated from M-H hysteresis plots.	88

## Abbreviations of Symbols and Terms

<i>BTO</i>	<i>BaTiO<sub>3</sub></i>
<i>BSTO</i>	12.5% <i>Sr</i> atom doped <i>BTO</i> , <i>Ba<sub>0.875</sub>Sr<sub>0.125</sub>TiO<sub>3</sub></i>
<i>BNTO</i>	12.5% <i>Ni</i> atom doped <i>BTO</i> , <i>Ba<sub>0.875</sub>Ni<sub>0.125</sub>TiO<sub>3</sub></i>
<i>BSNTO</i>	25% atom ( <i>Sr</i> , <i>Ni</i> ) co-doped <i>BTO</i> , <i>Ba<sub>0.75</sub>(Sr<sub>0.5</sub>Ni<sub>0.5</sub>)<sub>0.25</sub>TiO<sub>3</sub></i> , <i>BSNTO</i>
<i>eV</i>	Electron volt
<i>DOS</i>	Density of states
<i>PDOS</i>	Partial density of states
<i>E<sub>G</sub></i>	Bandgap
<i>E<sub>F</sub></i>	Fermi level
<i>N<sub>A</sub></i>	Avogadro's number
<i>μ<sub>B</sub></i>	Bohr magneton
XRD	X-ray Diffraction
FESEM	Field Emission Scanning Electron Microscopy
<i>ε'</i>	The real part of the dielectric constant
<i>ε''</i>	The imaginary part of the dielectric constant
<i>ε<sub>0</sub></i>	Permittivity in free space/vacuum
<i>tanδ<sub>E</sub></i>	Dielectric loss factor
<i>Z*</i>	Complex impedance
<i>Z'</i>	The real part of complex impedance
<i>Z''</i>	The imaginary part of complex impedance
<i>σ<sub>ac</sub></i>	ac conductivity
<i>σ<sub>dc</sub></i>	dc conductivity
<i>α<sub>ME</sub></i>	Magnetoelectric Voltage coefficient
<i>T<sub>c</sub></i>	Curie temperature
<i>RQF</i>	Relative quality factor
<i>f<sub>r</sub></i>	Resonance frequency
<i>P</i>	Porosity
<i>C<sub>s</sub></i>	Capacitance with dielectric
<i>C<sub>o</sub></i>	Capacitance in free space
<i>d</i>	Sample thickness
<i>τ</i>	Relaxation time

$M$	Magnetization
$H$	Magnetizing field
$L_S$	Self-inductance of the sample core
$L_o$	Inductance of the winding coil without sample
$M_s$	Saturation magnetization
$\mu_i^*$	Complex initial permeability
$\mu_i'$	Real part of complex initial permeability
$\mu_i''$	Imaginary part of complex initial permeability
$\tan\delta_M$	Magnetic loss factor
$\lambda$	Wavelength
$F(\theta)$	Nelson-Riley function
$\rho_x$	X-ray density
$\rho_B$	Bulk density
EDS	Energy Dispersive X-ray Spectroscopy
$\bar{D}$	Average grain size
$T_s$	Sintering Temperature
$M'$	Real part of modulus
$M''$	Imaginary part of modulus



# CHAPTER 1

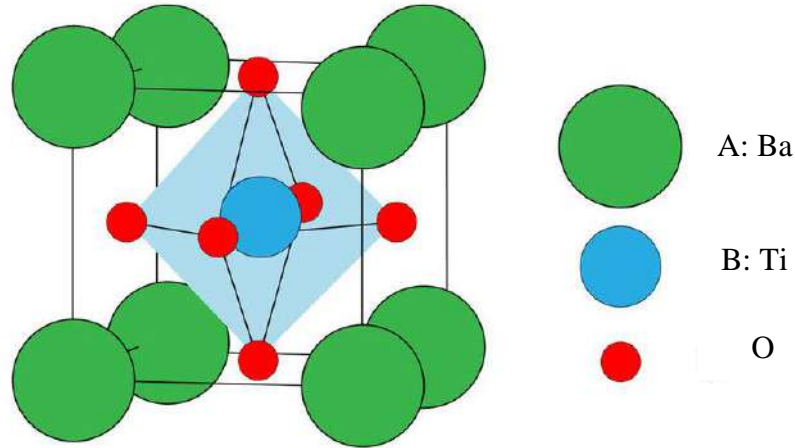
## INTRODUCTION

### 1.1 Background

The  $\text{CaTiO}_3$  is a mineral found in the Ural Mountains of Russia and was discovered in 1839 by Gustav Rose and was named “perovskite,” in honor of the Russian mineralogist, Count Lev Alekseyevich von Perovski [1]. In the later years, a broad family of crystals is found to have the same structures of  $\text{CaTiO}_3$  [2-3]. Numerous types of research have been done on the compound forming the perovskite structure [4-7]. The perovskite-type oxides have the general formula  $\text{ABO}_3$ , where “A” and “B” are cations and “O” is an anion. Usually, “A” is a metal cation and belongs to the alkaline and/or beryllium group. “A” is larger than cation “B” which has a cation with a coordination number of 6 (such as *Ti, Mg, Ta, Nb*). Cation “A” is barely any of the transition metals. The last part of these types of perovskites is an oxide anion  $\text{O}^{2-}$ . The oxide-type perovskites have always been a great consideration in the device industry and solar cell fabrication because of their decent dielectric, ferroelectric, piezoelectric, electro-optical, and thermal conductivity due to electron transport phenomena, insulator-to-metallic transitions, half-metallic behavior, the exhibition of fluorescence with laser action, etc [8-10]. Both experimental and theoretical studies are still a matter of interest for material scientists to fabricate multifunctional perovskites. They are also used as base materials for countless important ceramic components and devices in the electronics and spintronics industries [11-13].  $\text{BaTiO}_3$ ,  $\text{CaTiO}_3$ , and  $\text{SrTiO}_3$  are common perovskite-type materials used for the above purposes [14-20].  $\text{PbTiO}_3$ , different lead zirconate titanate, and lead lanthanum zirconate titanate show good ferroelectric and piezoelectric behavior, however, the lead is toxic [21-24]. As a result, lead-free perovskite structures have still been investigated to find non-toxic electronic materials.

Theoretical investigation of different cubic  $\text{ABO}_3$  [ $A = \text{Ba, Ca, Sr}$ ;  $B = \text{Ce, Ti, Zr}$ ] perovskites have been done in this research and it is found that  $\text{BaTiO}_3$  has the lowest bandgap. However,  $\text{BaTiO}_3$  is an important ferroelectric material with a perovskite structure that shows good dielectric, ferroelectric, piezoelectric, and electro-optical properties and hence it is widely used in electronic industries [25–30]. However,  $\text{BaTiO}_3$  shows a low Curie temperature,  $T_c$ , of  $120^\circ\text{C}$ . This can lead to thermal stability issues as well as redundant aging. [31-32]. Other materials were utilized as dopants to build a solid

solution with  $BaTiO_3$  to solve this challenge and this doping has a considerable technological significance for device applications [33–35]. Considerable work has been done for modifying the device parameter of these systems with a wide variety of substitutions at the  $A$ -and/or  $B$ -site of the  $BaTiO_3$  system. Doping and co-doping on  $A$ -site have been done on  $BaTiO_3$ -based ceramics to increase dielectric characteristics and achieve desired grain size for electronic device applications [36–42].



**Fig. 1.1** A typical unit cell of perovskite-type  $BaTiO_3$ .

## 1.2 The Motivation for the Present Investigation

The types of dopants, ionic radii, and valence states affect the crystal structure, defect structure, and electrical characteristics of  $BaTiO_3$  [43-48]. In doped  $BaTiO_3$ , three forms of cation site occupation are possible- the  $Ba$ -site, the  $Ti$ -site, or both. Dopants are divided into two types based on their charges- isovalent and aliovalent. In this process, isovalent doping with the same charge can replace the host ion. This relates to  $A^{2+}$  dopant amalgamation on  $Ba$ -site and  $A^{4+}$  dopant incorporation on  $Ti$ -site in the  $BaTiO_3$ . On the other hand, the substitution of a different charge ion for the host ion is known as aliovalent doping. A donor dopant is one in which the valence state of the doping content is higher than that of the host ion. Acceptor dopants have a valence state that is lower than that of the host ion. The  $A^{3+}$  and  $A^+$  ions on the  $A$ -site of the  $BaTiO_3$ , for example, are known as donors and acceptors, respectively. Excessive amounts of  $A^{2+}$  dopants prefer the  $Ba$ -site [49-50], a small amount of  $A^{4+}$  impurities occupy the  $Ti$ -site [51], and  $A^{3+}$  or  $A^{5+}$  dopants can take the place of the  $Ba$  or  $Ti$ -site depending on their size [52-57]. Researchers have also attempted co-doping in the perovskite lattice ( $A$ -site and  $B$ -site) to produce a range

of functional features [58-60]. These modifications have a significant impact on  $BaTiO_3$  attributes like Curie temperature ( $T_c$ ), permittivity ( $\epsilon_r$ ), density, lattice parameters, grain size, and electrical conductivity [61-64].

Ioachim *et al.* have found that with the addition of  $Sr$ , the temperature-dependent permittivity increases but dielectric loss and ferroelectric  $T_c$  decreases in  $Ba_{1-x}Sr_xTiO_3$  ( $0.25 \leq x \leq 0.90$ ) [65]. Shahid *et al.* have observed an improvement in crystallinity in films with the addition of  $Sr$  with  $BaTiO_3$ . Their observations of dielectric constant versus frequency demonstrated an increase in dielectric constant with increasing  $Sr$  dopant concentration [66]. Cheng *et al.* also discovered that  $Sr$  doping of  $BaTiO_3$  ceramics dramatically lowers the ferroelectric  $T_c$  [67].

The bound magnetic polaron (BMP) hypothesis, according to Coey *et al.* [68], could explain ferromagnetism in an insulating system lightly doped with transition metals. The production of a BMP is the outcome of the exchange-interaction of a bound carrier (donor or acceptor such as vacancies) with the magnetic ions under its orbit. Ferromagnetic interaction occurs when two polarons overlap.  $NiTiO_3$  is a significant perovskite of the  $ABO_3$  group. According to some previous studies, different band gaps of  $NiTiO_3$  are found, for example,  $2.16 eV$  [69],  $2.5 eV$  [70],  $3.0 eV$  [71], and  $3.4 eV$  [72]. This perovskite has huge applicability as high-temperature superconductors, metal-air barriers, gas sensors, and photocatalysis [73-77]. Tursun *et al.* [78] found  $NiTiO_3$  antiferromagnetic in nature and addition of  $Cu$  and  $Zn$  can generate ferromagnetism in  $NiTiO_3$ . Langhammer *et al.* [79] have found the enhancement of ferromagnetic properties in  $Co$ ,  $Fe$ , and  $Ni$ -doped  $BaTiO_3$  as all of them are metallic particles.

Pal *et al.* [80] have investigated the co-substitution with  $Bi^{3+}$  and  $Li^+$  on the  $A$ -site of  $BaTiO_3$  and observed that the adopted dopants balance the charge fluctuation caused by doping. The inclusion of  $(Bi_{0.5}Li_{0.5})^{2+}$  into  $BaTiO_3$  ceramics was discovered to be a viable option for improving ferroelectric properties and lowering the ferroelectric Curie temperature. This material also shows a giant photovoltaic response. Rawat *et al.* [81] have found that the amalgamation of  $(Bi_{0.5}Li_{0.5})^{2+}$  into  $BaTiO_3$  improves both ferroelectric and dielectric characteristics and also rises the  $T_c$  monotonously. This ceramic shows a low dielectric loss.

Theoretical studies have been done on nine commonly used  $ABO_3$  [ $A = Ba, Ca, Sr$ , and  $B = Ce, Ti, Zr$ ] perovskites to compare their different electronic, optical, elastic, and thermodynamic properties and then compared. Among them,  $BaTiO_3$  showed a lower bandgap with good optoelectronic properties. These will be discussed further in section 4.1.1. Considering the above results due to various substitutions, a methodical investigation will be done to observe the effect of  $Sr, Ni$  co-substitution on the structural, ferroelectric, dielectric, and magnetic properties of various  $Ba_{1-x}(Sr_{0.5}Ni_{0.5})_xTiO_3$ . The amalgamation of  $(Sr_{0.5}Ni_{0.5})^{2+}$  into the  $BTO$  ceramics is expected to enhance the dielectric and ferroelectric properties. The incorporation of  $Ni^{2+}$  may also induce magnetic properties. Therefore, the proposed ceramic may exhibit multiferroic properties and will open a new dimension in material research.

### 1.3 Objectives of the Present Work

The following are the primary goals of this research-

- Synthesis of various  $Ba_{1-x}(Sr_{0.5}Ni_{0.5})_xTiO_3$  ( $0 \leq x \leq 0.6$ ) compositions using solid-state reaction method.
- Investigation of surface morphology and compositional analysis.
- Study of different dielectric properties, impedance, and ac conductivity as a function of frequency.
- Determination of initial permeability ( $\mu'_i$ ) as a function of the frequency of different compositions has been measured with Wayne Kerr Precision impedance analyzer.
- Measurement of M-H hysteresis loop.

### 1.4 Outline of the Thesis

The layout of the thesis is as follows:

- The first chapter of this thesis discusses the significance of  $ABO_3$  perovskites as well as the reasons for and goals of the current study.
- The second chapter provides a short overview of relevant perovskites and theoretical background.
- The third chapter describes the procedures that were employed for sample preparation, computation, and measurement during this research study.

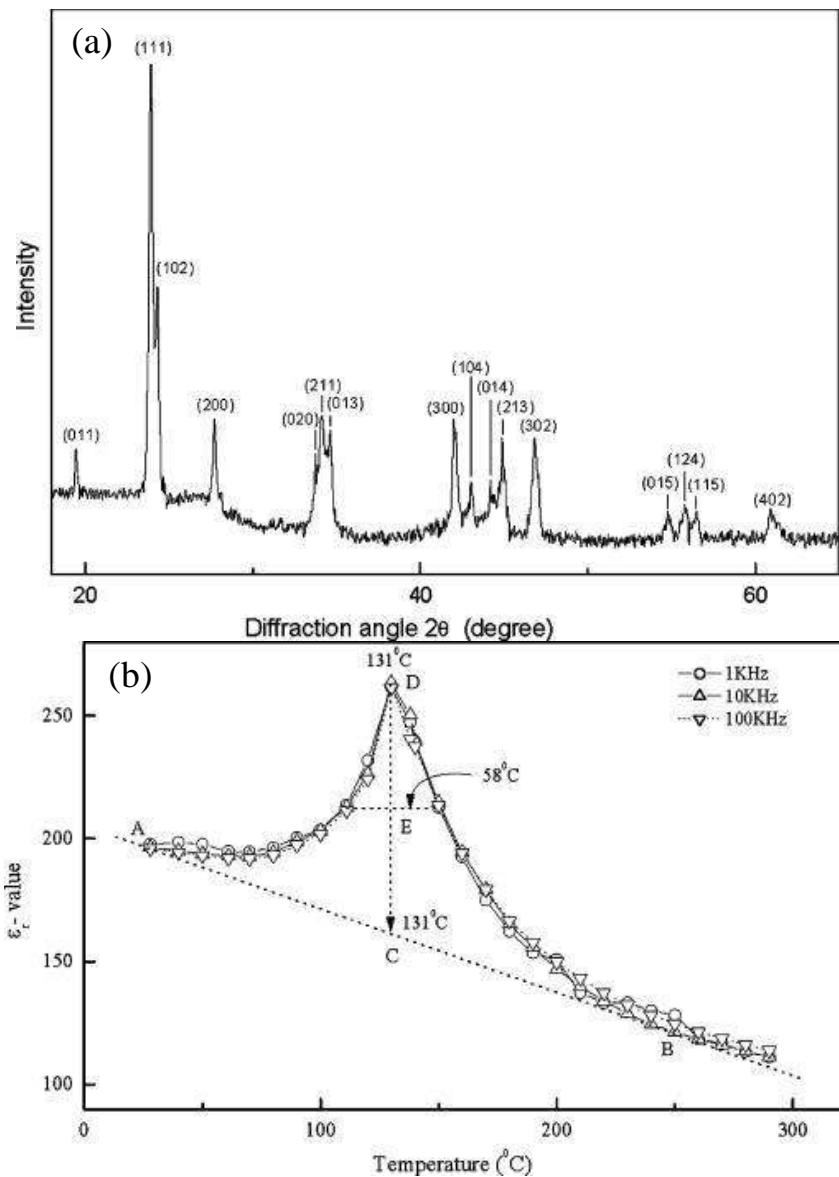
- The fourth chapter of the study is devoted to the findings of numerous investigations and how those findings are explained in the context of current theories.
- The final chapter includes a summary of key findings, conclusions, and the range of potential follow-up research.

## CHAPTER 2

### LITERATURE REVIEW

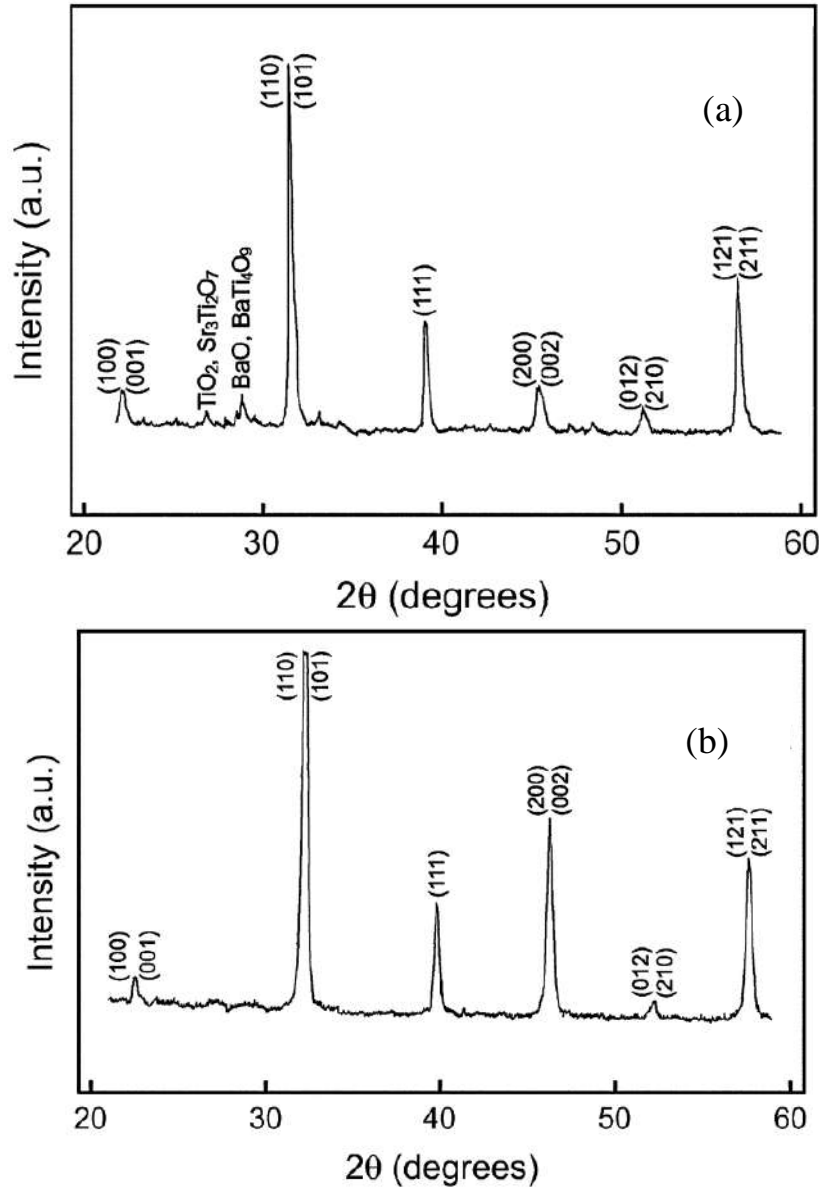
#### 2.1 Review of Earlier Works

Shirane *et al.* [82], Zeng *et al.* [83], and Ram *et al.* [84] have investigated the orthorhombic phase of  $BaTiO_3$ . Ram *et al.* studied the structural and dielectric characteristics of  $BaTiO_3$ . In Fig. 2.1 (a), sixteen unique relative peaks are depicted over a range of  $10^\circ$  to  $70^\circ$  in the diffraction angle  $2\theta$ . At ambient temperature, the  $\epsilon_r$  is as low as 200, and it barely rises further until it reaches 263 when heated to the  $T_c$  point, as shown in Fig. 2.1 (b).



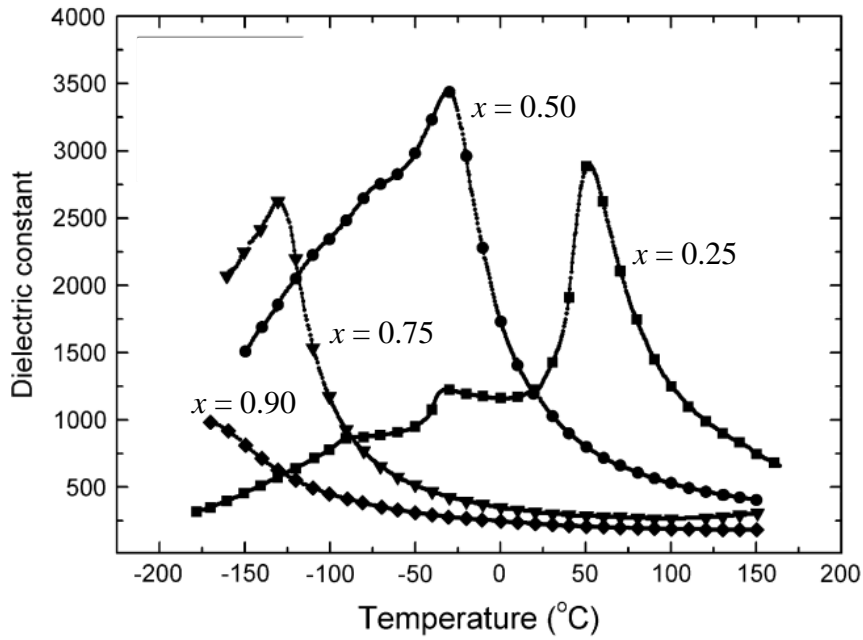
**Fig. 2.1** Orthorhombic  $BaTiO_3$ - (a) X-ray diffractogram and (b) Temperature-dependent variation of the  $\epsilon_r$  measured at frequency values 1, 10, and 100 kHz [84].

Ioachim *et al.* [65] investigated the structural and dielectric properties of *Sr*-doped  $BaTiO_3$  with compositions  $Ba_{1-x}Sr_xTiO_3$  ( $x = 0.25, 0.50, 0.75, 0.90$ ). X-ray diffraction study revealed that there is a drop in intensity with the amalgamation of *Sr* content for  $x = 0.25$  and  $0.9$ . The XRD plot also displays a single-phase solid solution which is shown in Fig. 2.2.



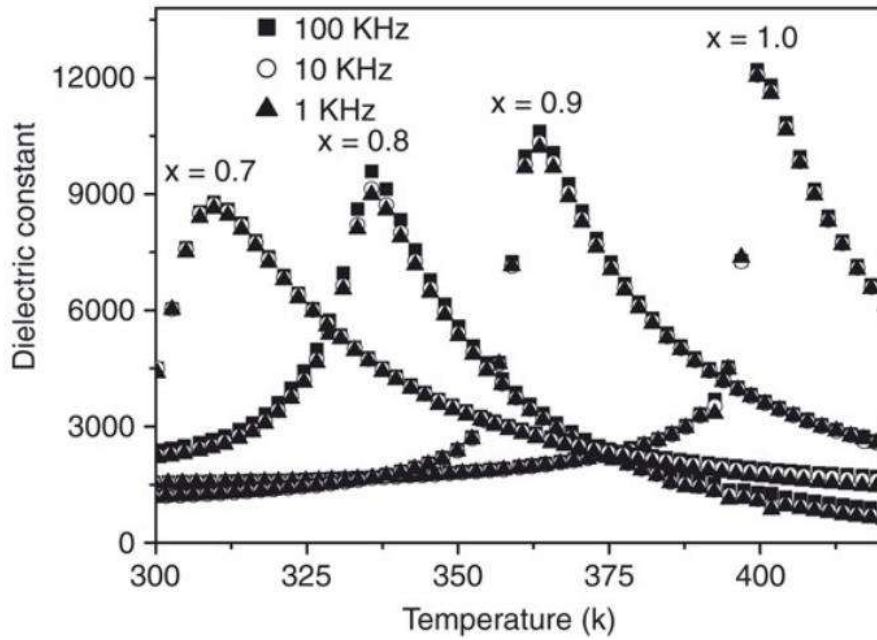
**Fig. 2.2** XRD patterns of *BST* specimens (a)  $x = 0.25$  and (b)  $x = 0.90$  sintered without additives at  $1230^\circ C$  for 2 h [65].

The addition of *Sr* content decreases ferroelectric transition temperature, dielectric constant, and dielectric losses, for both high and low-frequency ranges. The maximum value of the dielectric constant was found for  $x = 0.50$ .



**Fig. 2.3** The dependence of the dielectric constant as a function of temperature measured at 1 kHz for doped  $Ba_{1-x}Sr_xTiO_3$  ( $x = 0.25, 0.50, 0.75, 0.90$ ) samples, sintered at  $1260^\circ C$  for 2 h [65].

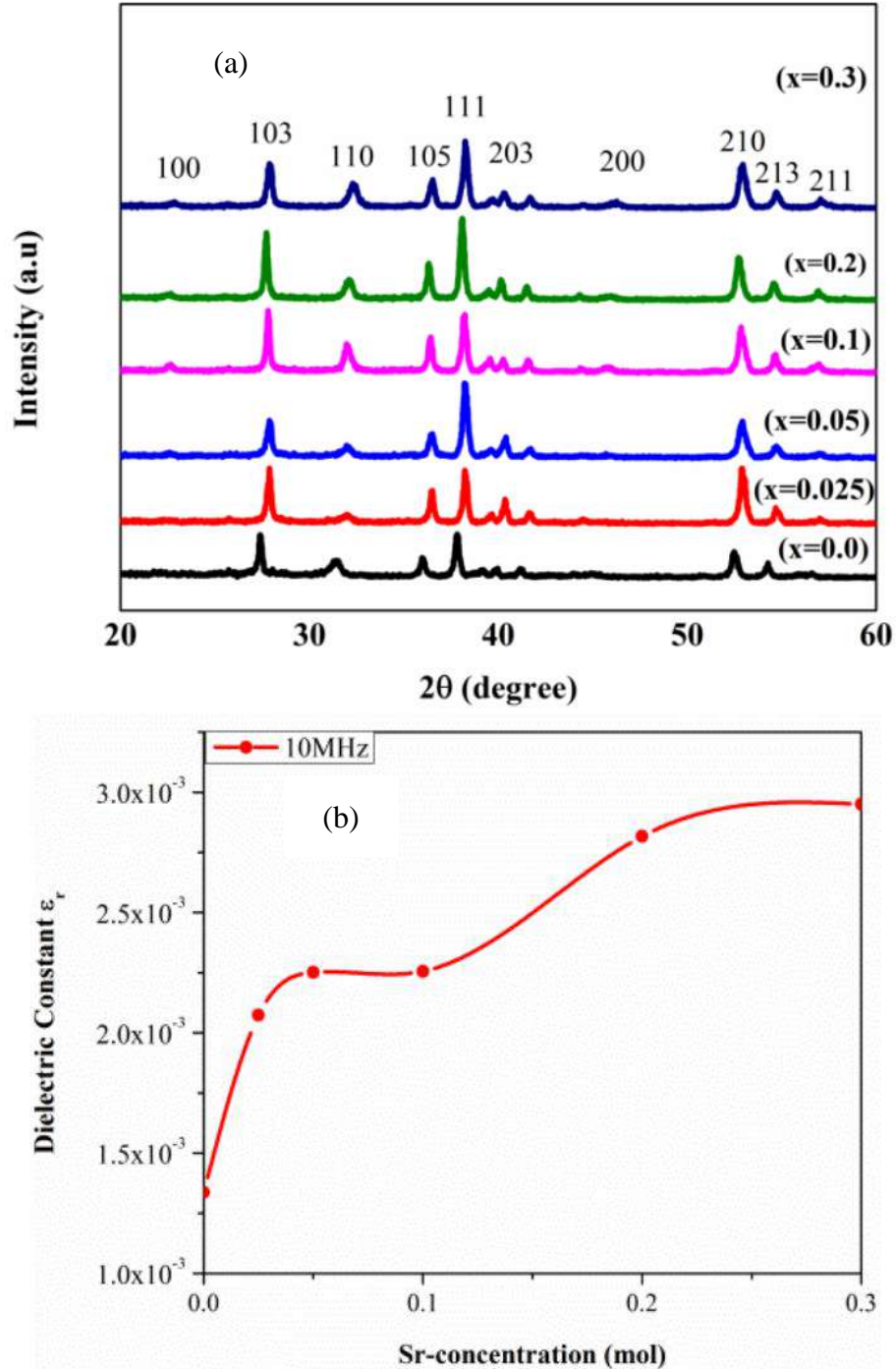
Cheng *et al.* [67] reported the structural and dielectric properties of  $Ba_xSr_{1-x}TiO_3$  ( $x = 1, 0.9, 0.8, 0.7$ ) ceramics prepared by a conventional solid-state reaction technique. They have studied the dielectric constant of  $Ba_xSr_{1-x}TiO_3$  as a function of temperature for various Sr concentrations. Fig. 2.4 (b) shows that the ferroelectric  $T_c$  decreases with the increase of the Sr content.



**Fig. 2.4** The variation of the dielectric constant of  $Ba_xSr_{1-x}TiO_3$  ( $x = 1, 0.9, 0.8, 0.7$ ) ceramics as a function of temperature for various Sr concentrations at 1, 10, and 100 kHz [67].

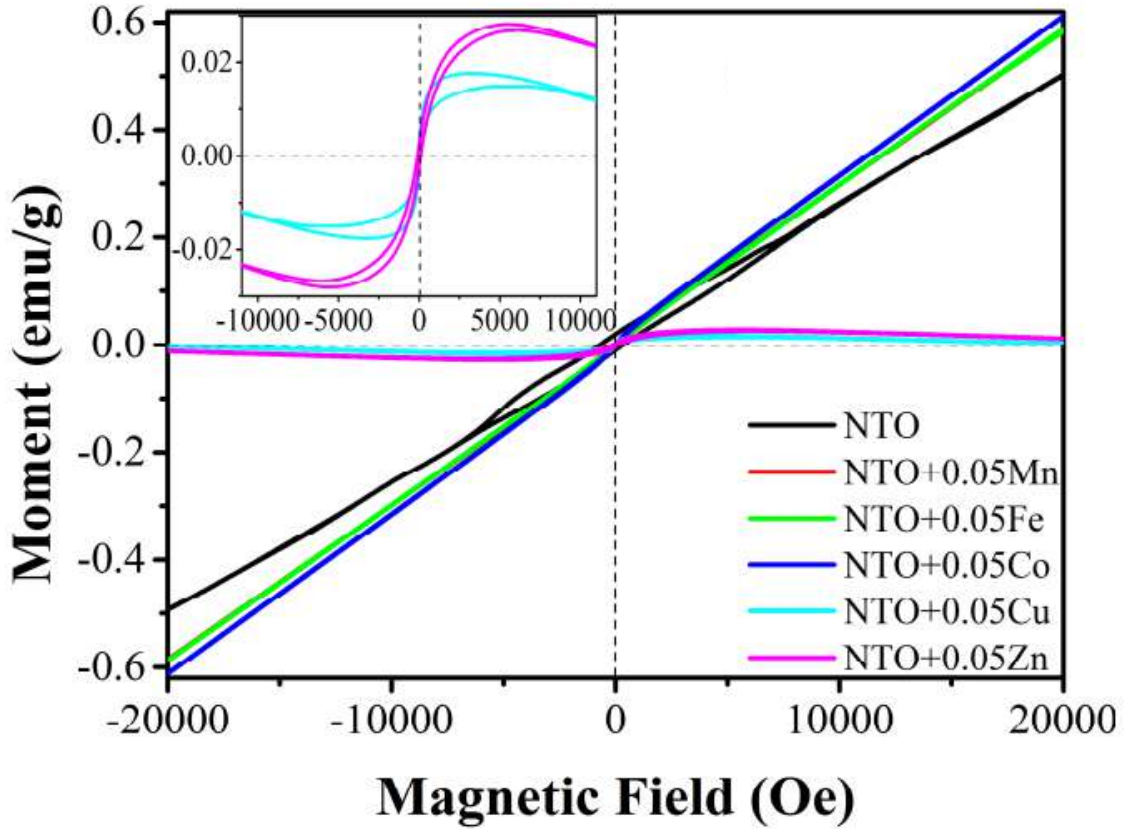


Shahid *et al.* [66] investigated *Sr*-doped  $BaTiO_3$  with compositional formula  $BaTiO_3 + xSr$  ( $x = 0.0, 0.025, 0.05, 0.1, 0.2,$  and  $0.3$ ). The crystallinity in films improved with the *Sr* content. The dielectric constant vs. frequency increased dielectric constant and decreased ferroelectric Curie temperature with *Sr* concentration.



**Fig. 2.5** Graphs of  $BaTiO_3 + xSr$  compositions (a) XRD spectra, and (b) Variation in dielectric constant with *Sr*-content [66].

Tursun *et al.* [78] have investigated the magnetic properties through the M-H hysteresis of  $NiTiO_3$ . They have stated that  $NiTiO_3$  is antiferromagnetic and amalgamation of  $Cu$  and  $Zn$  can develop ferromagnetism in  $NiTiO_3$ .



**Fig. 2.6** Room temperature magnetic M-H hysteresis loops of  $Ni_{1-x}A_xTiO_3$  ( $A = Mn, Fe, Co, Cu, Zn$ ;  $x = 0, 0.05, 0.1$ ) samples with  $x = 0$ , and  $0.05$  [78].

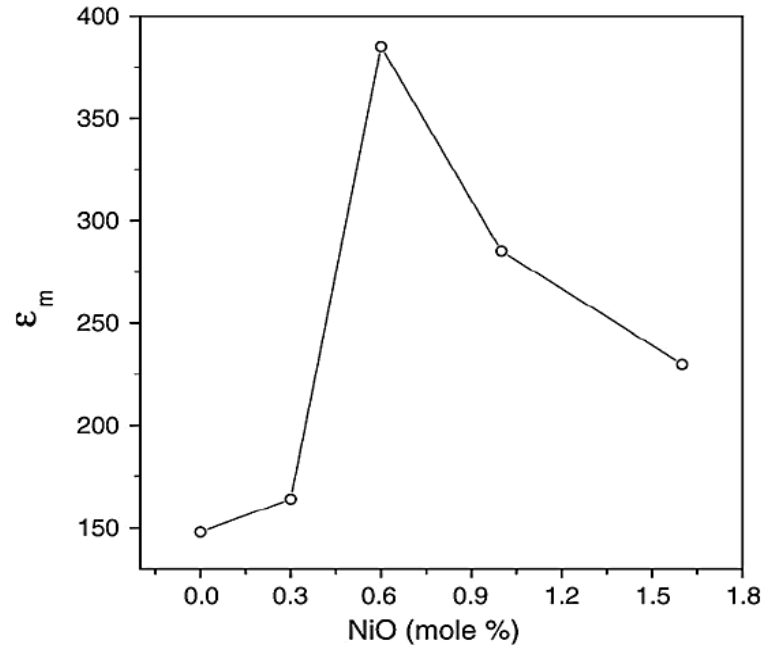
This study also showed that the value of a coercive magnetic field,  $H_c = 40.871$  Oe, saturation magnetization,  $M_s = 0.482$  emu/g, a remnant of magnetization,  $M_r = 12.57 \times 10^{-3}$  emu/g and  $M_r/M_s = 0.026$  for  $NiTiO_3$ .

Jana *et al.* [85] synthesized  $Ni$ -doped  $BaTiO_3$  with the formula  $Ba(Ti_{1-x}Ni_x)O_3$  ( $x = 0, 0.03, 0.06, 0.10, 0.16$ ) through a chemical route using polyvinyl alcohol (PVA) and analyzed the structure and dielectric properties of the compositions. According to their study, the particle sizes in the specimen range from 24 to 35 nm (Table 2.1). The dielectric permittivity of doped ceramics is higher than that of pristine  $BaTiO_3$  (Fig 2.7).

**Table 2.1** Composition, crystal structure, crystalline size (d), and  $T_c$  of the  $Ba(Ti_{1-x}Ni_x)O_3$  samples.

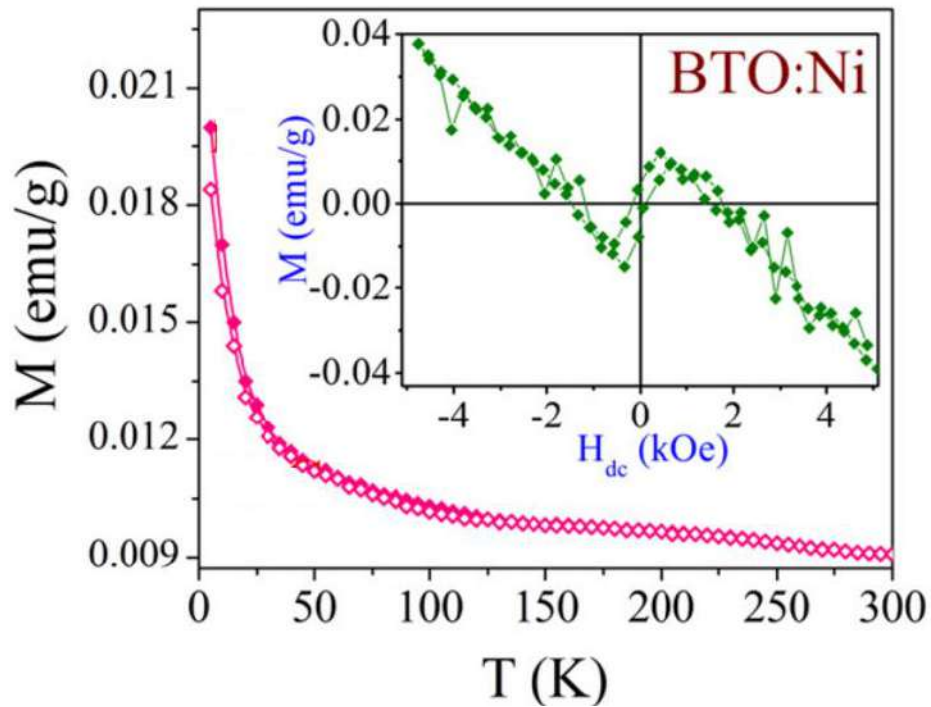
$x$	Crystal structure	Particle diameter (nm)	$T_c$ (°C)
0.0	Tetragonal	24	125
0.03	Tetragonal	25	120
0.06	Tetragonal	25	108
0.10	Tetragonal	33	120
0.16	Tetragonal	35	116

From Table 2.1, it is also observed that the ferroelectric  $T_c$  is reduced in  $Ni$ -doped  $BTO$  and lowest in  $Ba(Ti_{0.94}Ni_{0.06})O_3$ .



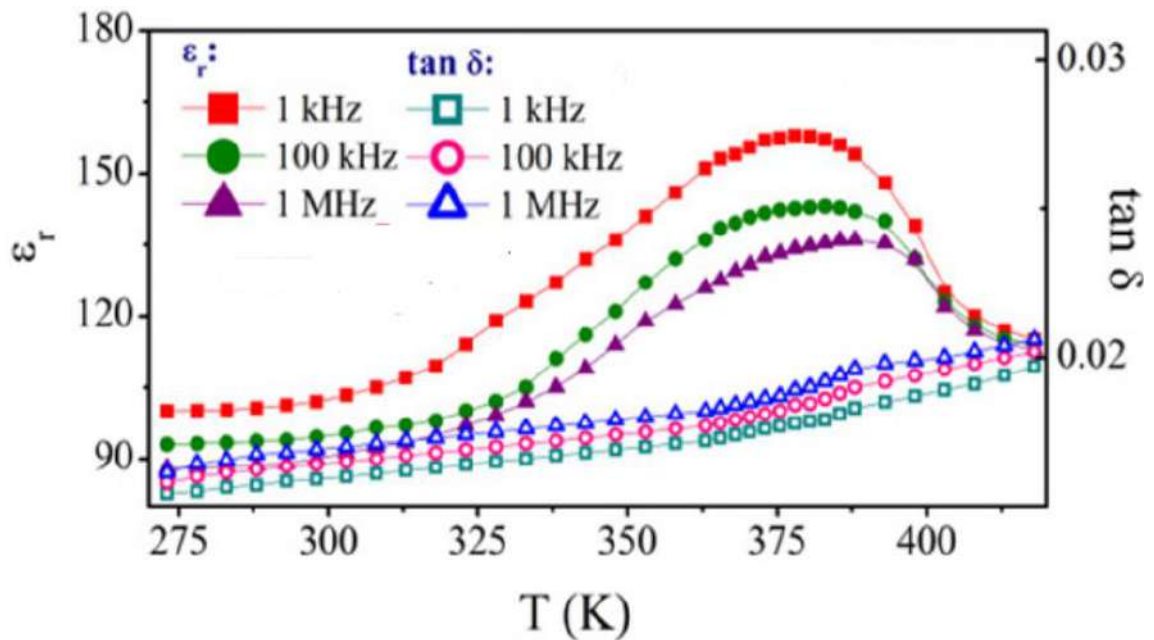
**Fig. 2.7** Variation of  $\epsilon_m$  with mole % of the dopant [85].

Verma *et al.* [86] investigated the effect of  $Ni$  doping with  $BaTiO_3$  with a composition of  $BaNi_{0.01}Ti_{0.99}O_3$  nanoparticles prepared by the sol-gel method. They reported that the saturation magnetization,  $M_s = 0.013 \text{ emu/g}$ , remanent magnetization,  $M_r = 0.004 \text{ emu/g}$ , and coercivity,  $H_c = 149 \text{ Oe}$  (Fig 2.8) at room temperature and revealed ferromagnetic. Long-range  $Ni^{2+}-Ni^{2+}$  ferromagnetic interaction arbitrated by low donor electrons could explain the ferromagnetic characteristics of  $Ni$ -substituted  $BaTiO_3$  nanoparticles [87-88].



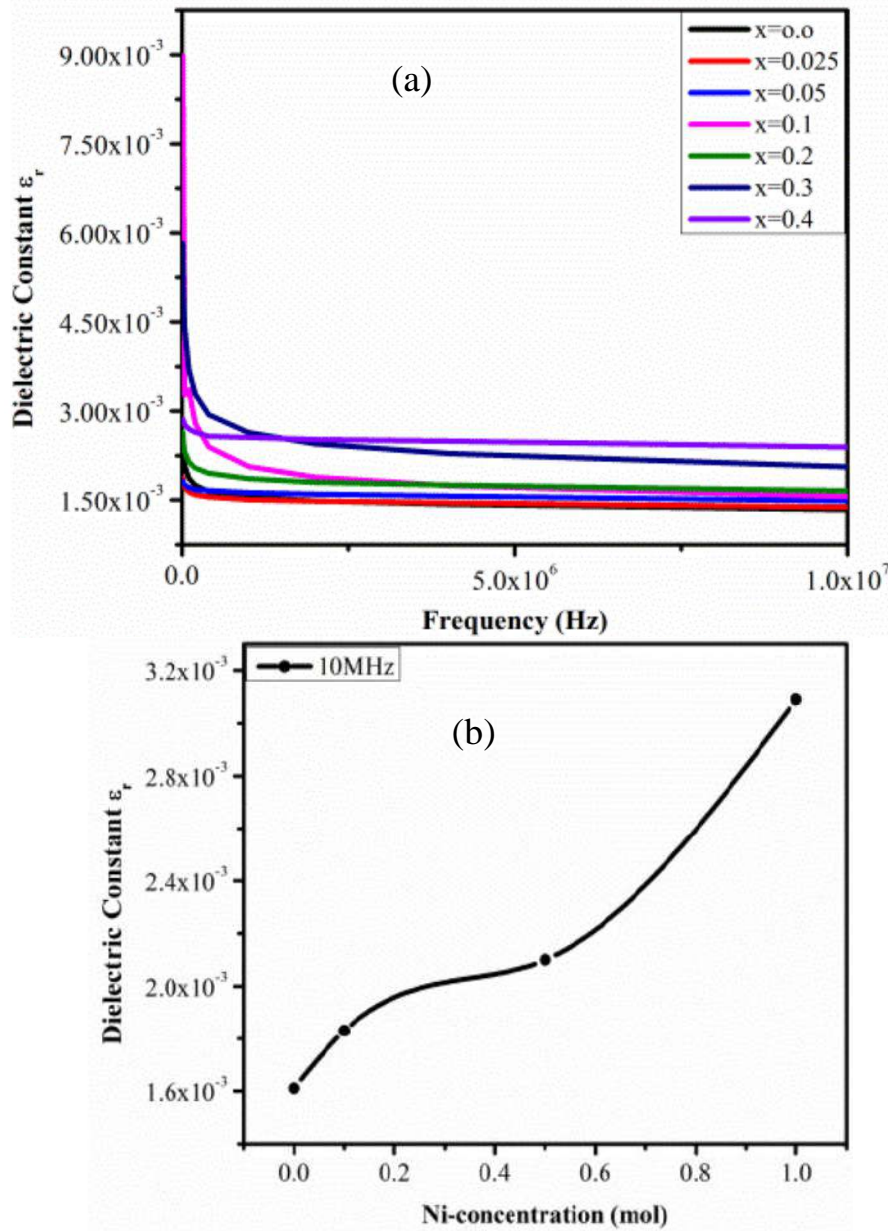
**Fig. 2.8** Magnetization ( $M$ ) as a function of temperature ( $T$ ) where the inset shows the magnetization ( $M$ ) versus magnetizing field ( $H_{dc}$ ) for  $BaNi_{0.01}Ti_{0.99}O_3$  [86].

They also studied the temperature-dependent  $\epsilon_r$  and  $\tan\delta$  for  $Ni$ -substituted  $BaTiO_3$  nanoparticles at frequencies 1 kHz, 100 kHz, and 1 MHz. At room temperature and 1 MHz measurement,  $\epsilon_r$  is 88 and  $\tan\delta$  is 0.0161 for this sample which are shown in Fig. 2.9.



**Fig. 2.9** Temperature dependent  $\epsilon_r$  and  $\tan\delta$  of  $BaNi_{0.01}Ti_{0.99}O_3$  [86].

Shahid *et al.* [89] have studied the thin films of *Ni*-substituted *BaTiO<sub>3</sub>* with the compositional formula *BaTiO<sub>3</sub>+xNi* ( $x = 0.0, 0.025, 0.05, 0.1, 0.2, 0.3, 0.4$ ). They reported that the dielectric constant increases with increasing *Ni*-dopant concentration as shown in Fig. 2.10.



**Fig. 2.10** (a) Dielectric constant as a function of frequency at room temperature of *BaTiO<sub>3</sub> + xNi* thin films and (b) Dielectric constant vs *Ni*-concentration (mol) of the samples [89].

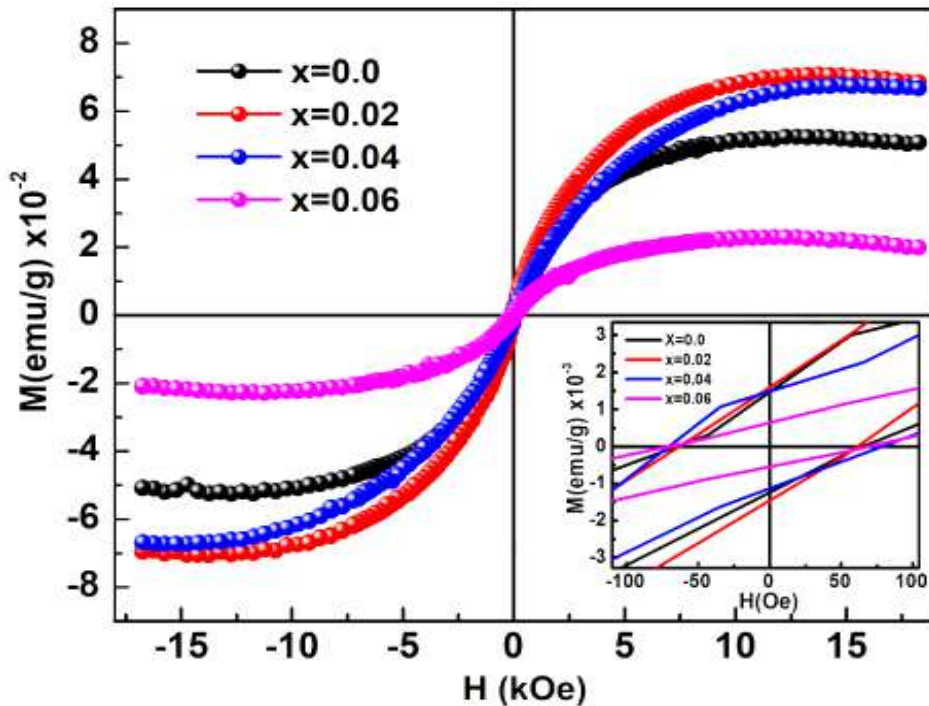


Arshad *et al.* [90] also synthesized  $Ba(Ti_{1-x}Ni_x)O_3$  ( $0 \leq x \leq 0.06$ ) through the sol-gel auto-combustion process. Their study of dielectric properties demonstrated that the dielectric loss ( $\tan\delta$ ) decreases and dielectric strength ( $\Delta\varepsilon'$ ) increases with the addition of  $Ni$  shown in Table 2.2.

**Table 2.2**  $\varepsilon'_r$ ,  $\tan\delta$  and  $\Delta\varepsilon'$  of different  $BaTi_{1-x}Ni_xO_3$ .

$Ni$ concentration ( $x$ )	$\varepsilon'_r$	$\tan\delta$	$\Delta\varepsilon'$
0.00	237	0.49	65
0.02	189	0.27	43
0.04	117	0.16	32
0.06	167	0.11	76

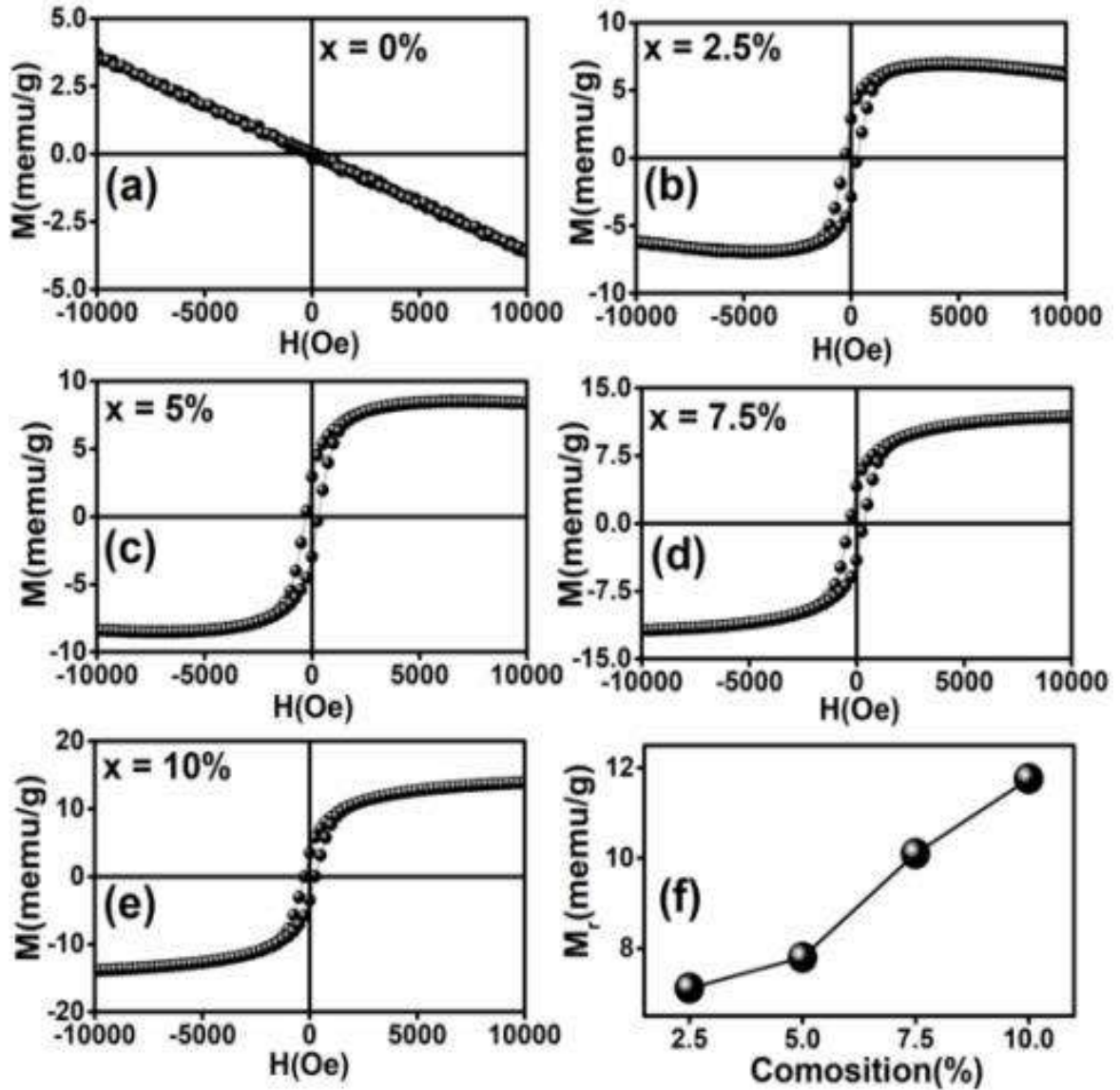
Magnetic studies at room temperature show that all of the samples are ferromagnetic, with a slight diamagnetic component at stronger fields (Fig. 2.11).



**Fig. 2.11** Magnetic hysteresis (M-H) loops of  $Ba(Ti_{1-x}Ni_x)O_3$  ( $0 \leq x \leq 0.06$ ) at room temperature [90].

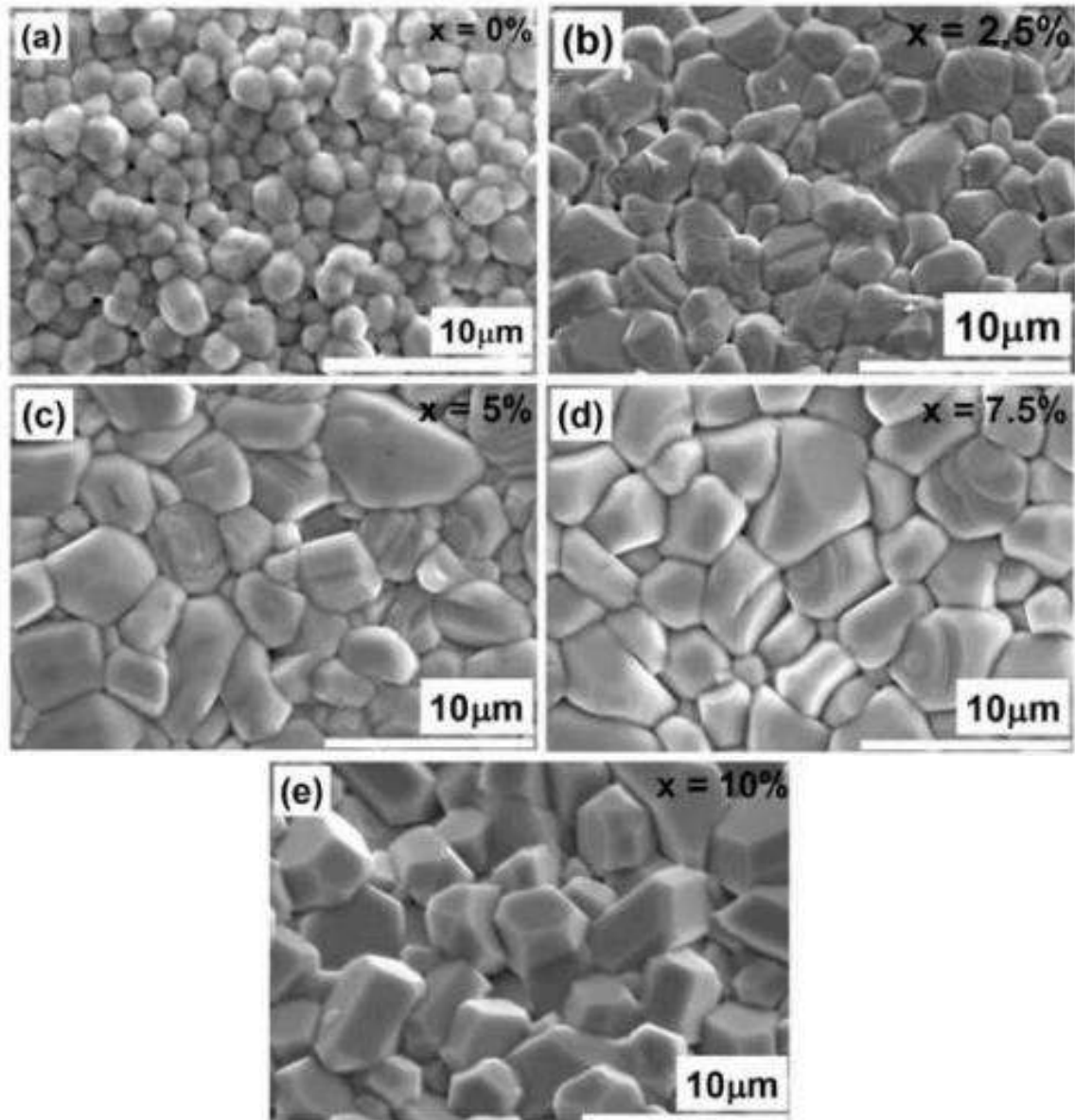
Another investigation was done by Rani *et al.* [91] structural, multiferroic, and magnetoelectric properties of tetragonal  $Ba(Ti_{1-x}Ni_x)O_3$  ( $0 \leq x \leq 10 \text{ mol}\%$ ) ceramics. Except for  $x = 2.5 \text{ mol}\%$  of  $Ni$  doping concentration, all  $BTNO$  samples had a ferromagnetic character with a saturated magnetic hysteresis (M-H) loop at room temperature (Fig. 2.12). At higher fields, a tiny quantity of diamagnetism is found

alongside ferromagnetism at  $x = 2.5 \text{ mol\%}$ . The F-center exchange interaction via oxygen vacancies is the source of ferromagnetism. For  $x = 10 \text{ mol\%}$ , the highest residual magnetization,  $M_r = 11.76 \text{ m emu/g}$ . Fig. 2.12 (f) shows that the  $M_r$  increases with doping concentration.



**Fig. 2.12** Magnetic hysteresis loops at room temperature for  $\text{Ba}(\text{Ti}_{1-x}\text{Ni}_x)\text{O}_3$ ; (a)  $x = 0\%$ , (b)  $x = 2.5\%$ , (c)  $x = 5\%$ , (d)  $x = 7.5\%$ , (e)  $x = 10\%$  ceramics and figure (f) shows the remnant magnetization behavior of *BTNO* samples as a function of composition.

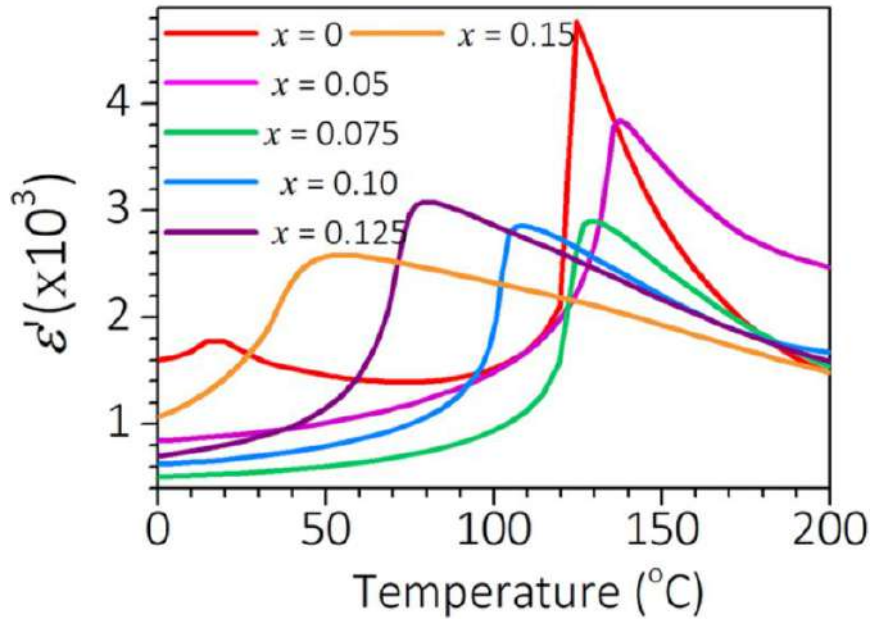
The micrograph of a pristine  $BaTiO_3$  sintered sample shows homogeneous grain size, as shown in Fig. 2.13 (a). In comparison to pure  $BaTiO_3$ , the sample exhibits plate-like inhomogeneous grain distribution at  $x = 2.5 \text{ mol\%}$  of  $Ni$  content (Fig. 2.13 (b)). Furthermore, the grain size increases slightly from  $x = 5$  to  $x = 10 \text{ mol\%}$ .



**Fig. 2.13** SEM micrographs of  $Ba(Ti_{1-x}Ni_x)O_3$  ceramics (a)  $x = 0\%$ , (b)  $x = 2.5\%$ , (c)  $x = 5\%$ , (d)  $x = 7.5\%$ , and (e)  $x = 10\%$  [91].

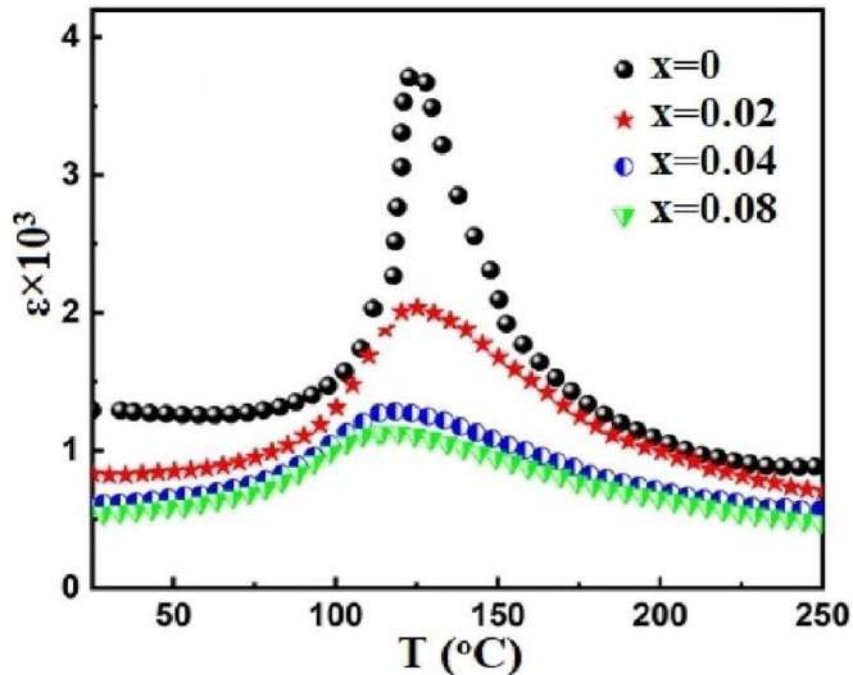


Pal *et al.* [80] have synthesized  $Ba_{1-x}(Bi_{0.5}Li_{0.5})_xTiO_3$  samples ( $x = 0.0, 0.05, 0.075, 0.1, 0.125, 0.15$ ) by the solid-state method. Fig. 2.14 shows ferroelectric  $T_c$  is  $124\text{ }^\circ\text{C}$  for undoped  $BaTiO_3$  and decreases to  $108, 79,$  and  $55\text{ }^\circ\text{C}$  for the doping concentration  $x = 0.10, 0.125,$  and  $0.15,$  respectively.



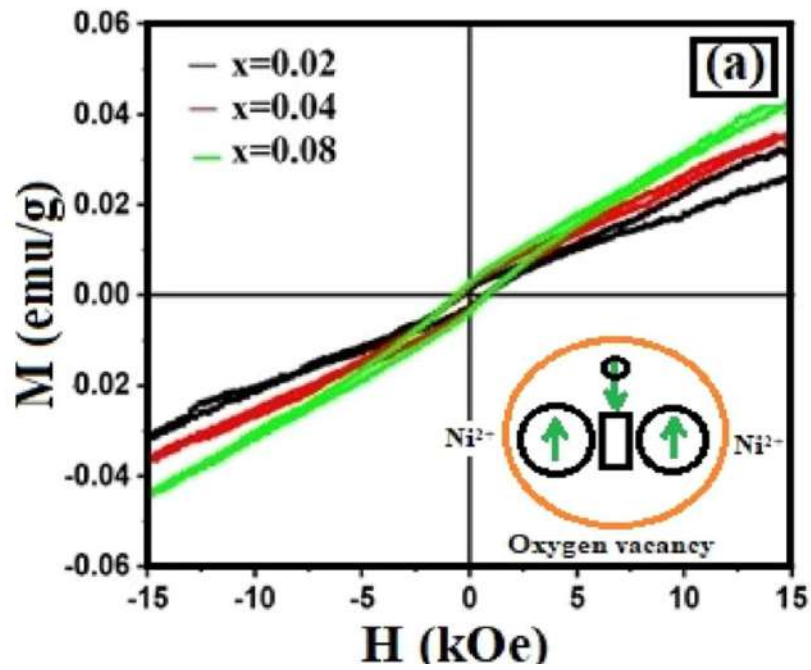
**Fig. 2.14** The  $\epsilon'$  versus temperature curves at  $1\text{ kHz}$  show the ferroelectric  $T_c$  transition [80].

Alkathy *et al.* [92] have investigated different properties of  $Ba_{1-x}(Ni_{x/2}Na_x)TiO_3$  ( $0 \leq x \leq 0.08$ ) ceramics. The temperature-dependent dielectric properties show the  $T_c$  decreases with the increase of  $x$  (Fig. 2.15).



**Fig. 2.15** Dielectric constant as a function of temperature [92].

At room temperature, the P-E and M-H hysteresis loops (Fig. 2.16) were also investigated by them, and the findings demonstrate that weak ferromagnetic and ferroelectric characteristics co-exist.



**Fig. 2.16** M–H hysteresis loops and the inset is a representation of F-center exchange interaction [92].

# CHAPTER 3

## THEORETICAL METHODOLOGY AND EXPERIMENTAL TECHNIQUES

### 3.1 Theoretical Methodology

For materials modeling, several computational approaches are available. First-principles calculations are a vital tool that is particularly helpful for phenomena that are governed by the atomic-scale characteristics of materials in the solid state [93]. These calculations are referred to as ab-initio or first-principles calculations because the numerical model does not use any experimental parameters. They are developed from the fundamental ideas of quantum mechanics. While approximations and reformulations can be employed to achieve a result that converges to the Schrödinger equation, solving the fundamental equations of quantum mechanics for the many-body system explicitly is practically impossible [94]. Using functionals of electron density, density functional theory (DFT) is a well-known first-principles approach for quantum mechanical modeling. A many-body system at the atomic level can be characterized using quantum mechanics by merely its atomic arrangement and electronic structure, without any empirical characteristics. A quick overview of essential quantum mechanics topics will be offered here to set the scenario for which equations must always be resolved to understand materials [93].

#### 3.1.1 The Schrödinger equation

The fundamental physics equation for describing quantum mechanical phenomena is the Schrödinger equation. A partial differential equation known as the Schrödinger wave equation describes how a physical system's wave function evolves over time. The formulation of the time-independent Schrödinger equation is the starting point for both density functional theory and wave function mechanics [94].

$$H\hat{\psi} = E\psi$$

where " $\psi$ " is the wave function that holds all of the data about the described system, " $H$ " represents the Hamiltonian operator that influences the wave function, and " $E$ " is the resultant it produces, which is the total energy of the system. Various additional operators

are accessible, such as spin, electric dipole moments, etc. From the wave function, these can be utilized to derive the expectation values of physical observables.

### **3.1.2 Born-Oppenheimer approximation**

The Born-Oppenheimer approximation is based on the notion that atomic nuclei and electron movements within a molecule can be distinguished [95]. It enables the division of a molecule's wave function into its electronic and nuclear (vibrational, rotational) components on a mathematical level. The approximation simplifies the calculation of a typical molecule's energy and wave function. The problems related to electronic as well as nuclear can be explained with different wave functions since the movement of both electrons and nuclei can be distinguished. Since the nuclei are thought to be immobile, the Coulomb interaction between them is constant. As a result, the final element in the Schrödinger equation can be ignored and afterward added as a constant to the total energy. Separating electronic and nuclear constraints is known as the Born-Oppenheimer approximation.

### **3.1.3 Hartree-Fock approximation**

The Hartree-Fock (HF) technique is an estimation approach for figuring out the energy and wave function of a stationary quantum many-body system [96]. When applied to fermions or bosons, the HF approach frequently undertakes that the actual  $N$ -body wave function of the arrangement can approximately be determined by a single Slater determinant or by a single permanent of  $N$  spin-orbitals. Using the variational technique, a set of  $N$ -coupled equations for the  $N$  spin orbitals can be obtained. These equations can be solved to provide the system's energy and Hartree-Fock wave function.

HF is also known as the self-consistent field approach (SCF). Hartree needed the final field to be self-consistent with the presumed initial field in order to derive what is now known as the Hartree equation, which is an approximation of the Schrödinger equation. As a result, the solution required self-consistency. The solution was kept because the solutions to the non-linear HF equations similarly behave as though each particle is subject to the mean field produced by all other particles. Although the fixed-point iteration procedure does not always converge, it is generally universally used to solve equations [96]. The HF approach does not always require this solution scheme, nor is it the only one that can be used. The central starting point for all methods that more

effectively describe the many-electron arrangement for both atoms and molecules is the HF solution.

### **3.1.4 Density Functional Theory**

A different form of the ab-initio approach is density functional theory (DFT). For the purpose of analyzing the electronic composition of many-body systems, such as atoms, molecules, and condensed phases, or the spatially dependent electron density, this method is a quantum mechanical theory that can be utilized in both physics and chemistry. [97]. DFT's primary notion represents an interacting system of fermions by its density rather than its many-body wave function. This indicates that the basic variable of the system only depends on the three spatial coordinates  $x$ ,  $y$ , and  $z$  rather than  $3N$  degrees of freedom for  $N$ -electrons in a solid, which follow the Pauli principle and repel one another via the Coulomb potential [97]. The two theorems that Hohenberg and Kohn proved in 1964 [98] and the computational scheme that Kohn and Sham (KS) proposed the following year [99] form the foundation of density functional (DF) techniques. They demonstrated that the overall energy and electron density relationship is valid. This means that the essential concept in density functional theory—electromagnetic density—can be understood without having to be familiar with the challenging many-electron wave function.

### **3.1.5 Generalized Gradient Approximation**

Density-functional theory (DFT) gives structures, bond energies, and reaction activation energies in several applications where the exchange-correlation functional's generalized gradient approximation (GGA) has led to the outstanding agreement with both the experiment and the most precise ab initio calculations [97]. More sophisticated approximations are currently used by many advanced theoretical algorithms based on density functional theory to increase accuracy for specific physical attributes. Using the GGA, the DFT calculations in this study were completed. The LDA (local-density approximation) is less effective than the GGA.

No matter how homogeneous the actual charge density is, the LDA uses exchange-correlation energy to create a homogenous electron gas across the system. When charge densities are not uniform, the exchange-correlation energy might deviate significantly from the uniform result. Higher spatial derivatives of the total charge density and the

gradient can be used to evaluate this divergence [97]. The gradient of the charge density is used by the GGA to correct this deviation. The GGA has been shown to be more effective than LDA in systems with slowly fluctuating charge densities [97]. It also applies to the inhomogeneous electron gas system [97]. As a result, it can produce more suitable outcomes. The goal of introducing GGA is to considerably increase the outcomes from LDA.

### **3.1.6 k-point sampling**

The closest region of the reciprocal space to the origin  $(0,0,0)$  is the initial Brillouin zone of the material, which is where k-points are sampling points (usually called the Gamma point). Electronic states are only allowed at a limited number of k-points defined by the bulk solid boundary constraints. There are infinitely many k-points, which can be used to explain the unlimited number of electrons in the periodic solid. If the k-points are chosen to properly sample the reciprocal space, it is possible to employ a finite number of them [97]. Electronic wave functions at very close k-points will be nearly indistinguishable. This demonstrates that the summation over k-points (or, equally, the integration over the Brillouin zone) contained in the DFT formulations can indeed be efficiently evaluated using a mathematical model that performs accumulation over a constrained collection of special Brillouin zone points. The complicated section of the Brillouin zone should only be taken into consideration, according to symmetry concerns. For creating these points and the accompanying weights to be employed in the summation, a number of guidelines exist [97]. By calculating the states of electrons at a relatively small magnitude of k-points, one can use these techniques to derive an estimation of the electronic potential and total energy of an insulator that is both exact and precise. A denser set of k-points is needed in computations for metallic systems to precisely calculate the Fermi level. Using a denser set of k-points will always result in a smaller inaccuracy in the total energy caused by the limited k-point sampling, much like how achieving convergence about the number of basis set functions is done. When comparing the energies of two systems with various symmetries, such as when examining the comparative stabilities of the structures of FCC and an HCP, it is critical to attaining high convergence concerning the k-point sample. As a result, both energies must be completely converged because there is no mistake cancellation in this situation. Monkhorst and Pack [100] presented among the most efficient techniques for generating

k-points. Along the three axes in reciprocal space, a uniform grid of k-points is produced by this method, which was later improved to incorporate hexagonal systems.

### **3.1.7 Cut-off energy**

Since there are theoretically an infinite number of electrons in a solid, a wave function must be constructed for each of the infinite numbers of electrons that stretch throughout the solid's whole space, and the basis set used to define the wave function must also be infinite. According to Bloch's theorem, the number of electrons in the crystal's unit cell may be determined from an infinite number of one-electron wave functions by using its periodicity [97].

The wave function of an infinite crystal can be expressed using this theory in terms of wave functions at reciprocal space vectors of a Bravais lattice. Bloch's Theorem has reduced the problem of an infinite number of electrons by requiring that only the number of electrons in the unit cell (or half that number, relying on whether the states are spin-degenerate or not) be taken into account at a constrained number of k-points chosen to sample the Brillouin Zone [93]. The electronic wavefunctions at each k-point can be enlarged in terms of a discrete plane-wave basis set, according to Bloch's theorem. In theory, such development requires an endless number of plane waves. As opposed to those with extremely high kinetic energy, plane waves with lower kinetic energy often play a more significant role [97]. Thus, the plane-wave basis set can be trimmed to incorporate only plane waves with kinetic energies less than certain cut-off energy. The estimated total energy and its derivatives will contain an error due to the truncation of the basis set at finite cutoff energy. It is feasible to lower the value of the inaccuracy systematical by increasing the magnitude of the cut-off energy. The cut-off energy should ideally be raised until the computed total energy converges within the necessary tolerance.

### **3.1.8 Pseudopotential**

In order for, the Schrödinger equation to have an improved efficient potential component rather than the Coulombic potential term for core electrons often present in the Schrödinger equation, the pseudopotential is able to be characterized as an idea to substitute the complex impacts of the movement of the atom's non-valence electrons and its nucleus with an efficient potential [93]. Even when all the electrons in a system are

explicitly allowed to perform a computation with the entirely Coulombic potential of the nuclei, the amount of processing time required is still prohibitive when using a plane-wave basis set. The orthogonality requirement between different states and the region's extremely powerful potential makes a very large cut-off energy necessary for the wavefunctions' rapid oscillations close to the nucleus, which is why a basis set was created [97]. A fascinating finding from physics and chemistry research is that while the core electrons of different atoms are largely independent of their surroundings, the valence electrons actively add to interactions between atoms. The core electrons' energy levels can be regarded as stable consequently, and each atom can have its own pseudopotential that takes into consideration the influences of the nucleus and core electrons. This enhanced potential's pseudo wavefunctions do not vary as quickly as the actual wavefunctions. As a result, it reduces the number of plane waves necessary for depiction. Once the valence electrons are explicitly taken into account, the computations can be performed with much less work [97]. Pseudopotentials are categorized into two classes- (a) Ultra-soft Pseudopotential and (b) Norm-conserving Pseudopotential.

Due to the norm-conserving pseudopotential, the estimation may expand linearly with the overall dimension of the basis set [93]. Vanderbilt [101] proposed a novel and innovative way of producing substantially softer pseudopotentials dubbed ultrasoft pseudopotentials in 1990. (USP). Within the core region, the pseudo-wave functions are permitted to be as soft as feasible in this technique, allowing the cutoff energy to be considerably reduced. As a result, they are commonly referred to as ultrasoft pseudopotentials (USP). The electron density is separated into two parts in this scheme: (a) a smooth portion that spreads throughout the unit cell, and (b) a hard component that is concentrated in the core areas. The increased component is only visible in the density, not in the wave functions.

### **3.1.9 Ground state energy**

The CASTEP code used for the Geometry Optimization job permits one to improve the geometry to obtain a stable structure of a 3D periodic system [97]. The cell dimensions and atom locations are modified iteratively to achieve the goal of minimizing the system's overall energy in the process. The system's ground state energy is represented by this minimized total energy [97]. Energy optimization or geometry optimization is energy reduction which is a method of identifying a spatial configuration of a collection



of elements [97]. A group of atoms could be an ion, a single molecule, a transition state, a condensed phase, or any mix of these. In this case, the mathematical model of chemical bonding may be based on quantum physics. The geometry of a collection of atoms can be expressed as a vector of particle locations [97]. This might be the atoms' Cartesian coordinates. These could be "internal coordinates," which are made up of a variety of bond lengths, bond angles, and dihedral angles [97] when referring to molecules.

### **3.1.10 CASTEP**

CASTEP code [93,97] is a quantum mechanical model based on the first-principles which is used for computing electronic structures. It is possible to simulate a wide range of materials within the density functional formalism, including molecules, crystalline solids, amorphous materials, and liquids. Any material's properties can be conceptualized as a calculable collection of nuclei and electrons. The use of computers, which have limited speed and capacity, is the only constraint. Given that the goal is to rely solely on quantum mechanics and avoid using any experimental (empirical) data, this simulation strategy is very ambitious.

### **3.1.11 Computation of different properties**

Density Functional Theory (DFT) based on a plane-wave pseudopotential method was used to carry out this study using a framework- Cambridge Serial Total Energy Package (CASTEP) code [102]. The exchange-correlation energy of electrons is evaluated under the generalized gradient approximation (GGA) with the method of Perdew–Burke–Ernzerhof (PBE) [103]. The k-point sampling of the Brillouin zone was constructed using the Monkhorst-Pack scheme [100]. The geometrical optimization of the crystal structures was performed in the Broyden-Fletcher-Goldfarb-Shanno (BFGS) relaxation method [104].

## 3.2 Sample Preparation and Experimental Techniques

Preparing polycrystalline compositions with the appropriate characteristics remains a complex and demanding undertaking. Controlling the chemical composition, uniformity, and microstructure is essential. Polycrystalline ceramics with optimal characteristics must be prepared with care. The following are some sample preparation techniques-

- (a) Standard solid-state reaction
- (b) Sol-gel method
- (c) Auto-combustion synthesis and
- (d) Co-precipitation technique

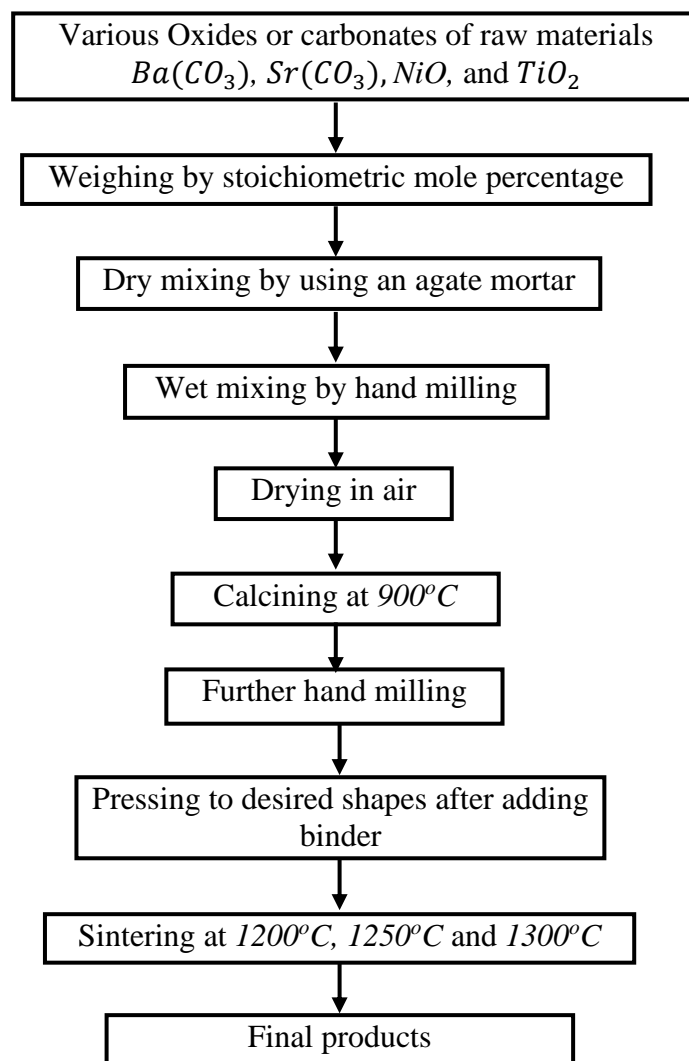
In this investigation, a standard solid-state reaction technique was used to synthesize all the samples. The procedure for sample preparation is succinctly explained here.

### 3.2.1 Standard solid-state reaction technique

A standard solid-state reaction technique is a high-temperature direct reaction between starting reagents (typically powders). A high temperature provides the energy required for the reaction to take place. Since a lot of bonds are broken during a solid-state reaction and the ions move through the solid, unlike in gas phase and solution reactions, solid-state reactions are often slow. Diffusion is frequently the limiting factor in solid-state reactions. Consequently, the diffusion of the cations through the product layer is the process that determines the rate of a solid-state reaction. As temperature rises, solid-state reactions happen considerably more quickly, but generally, they don't happen until the temperature of the reaction exceeds at least  $3/2$  of the melting point of one of the reactants.

In the solid-state reaction technique, the weights of the raw components are determined using the compound's stoichiometry while taking into account the impurity and moisture levels. After mechanically mixing the raw components, grinding operations are undertaken to control particle size and homogeneity of the mixture. To achieve this, a milling operation that can reduce the particle size to the  $1-10 \mu\text{m}$  range is carried out. A further reduction in particle size may have an impact on the material's homogeneity and purity. Since it is readily available with sufficient purity at reasonable prices and is non-flammable, distilled water or alcohol is utilized as a wetting medium. The next stage is a solid-state reaction between the elements of the starting materials at a sufficient

temperature. This is known as firing or calcination. Stoichiometry control during calcination is crucial, and volatile ingredients must be made up for. A homogenous body is produced during calcination as a result of the elements interacting through ion interdiffusion. Therefore, it is thought that calcination is a component of the combining or mixing process. Calcination additionally influences sintering-related shrinking. The "green body" is the result of compacting the powder after it has been calcined to produce the shape that is needed. Sintering is then used to make the green body denser. The following sections will provide an overview of calcination, shaping, pressing, and sintering.



**Fig. 3.1.** Flow chart for the solid-state reaction method of sample preparation.

## **3.2.2 Details of sample preparation: calcination, shaping and pressing, sintering, and etching**

### **3.2.2.1 Calcination**

The partial or final phase of the molecule is created by the chemical reaction process known as calcination. During the breakdown of the constituent compounds, it also aids in the removal of undesirable gases and byproducts. Additionally, calcination enhances material homogenization and lessens shrinkage of the final formed samples during the subsequent sintering process. A solid phase reaction, which entails the chemical process involving atomic diffusion across grains at temperatures lower than the melting points of the raw components, is used to synthesize the phase of a molecule [105]. The calcination temperature is often set sufficiently high to initiate a chemical reaction process while being kept as low as possible allowing for subsequent grinding. It is important to keep the calcination temperature low enough in materials with volatile contents to prevent the loss of those components.

To achieve great homogeneity, the calcining procedure might be conducted multiple times. The granules that have been calcined are crushed and ground into fine powders. The optimal properties of fine powders are [106]-

- (1) small particle size,
- (2) narrow distribution in particle size,
- (3) dispersed particles,
- (4) equiaxed shape of particles,
- (5) high purity and
- (6) homogeneous composition.

### **3.2.2.2 Shaping and pressing**

Calcined powders are re-hand milled to shape the power. The uniaxial pressing mechanism (Fig. 3.2) is then employed to produce compacts of calcined powder in tiny sizes and simplified shapes. It is done in a die with a moveable top. In the lower part, a cavity forms at the bottom. This chamber is stuffed with loosely dispersed powdery granules that are attached to the top to decompose. Before compaction, a binder is

normally added at a concentration of less than 5% wt [106]. Polymers or waxes serve as binders. In this case, polyvinyl alcohol is used as a binder. The binder enhances particle flow during compacting and increases particle bonding, presumably by establishing particle-binder-particle links. Binder breakdown and binder removed from the ceramics during sintering. Compacting pressures vary greatly but are often many tons per square inch. Powders are taken from the calcined powders to produce a 90 g pellet and a toroidal-80 g ring. A Hydraulic press is used to apply pressure in the range of 20-50 MPa utilizing the top punch.

### 3.2.2.3 Sintering

By heating the compressed powder for a set period of time, sintering generates a dense, durable body. Normally, the sintering temperature is well over the melting point of the constituents, but definitely below the temperature that would considerably increase diffusion. Sintering is propelled by a reduction in the powder's surface-free energy. Some of this energy is transformed into interfacial energy in the resulting polycrystalline body [106]. The period and temperature of sintering, and the furnace environment all have a significant impact on a material's electrical and magnetic characteristics. The sintering process serves the following functions:

- (1) to combine the particles so that the final product has enough strength,
- (2) to eliminate the pores in order to make the material denser and
- (3) to homogenize the substance by finishing the reactions that were left unfinished during the calcining process.

According to Coble and Burke's [108] investigation into the sintering of crystalline materials, the rate of grain growth exhibits the following empirical connection-

$$\bar{D} = kt^n$$

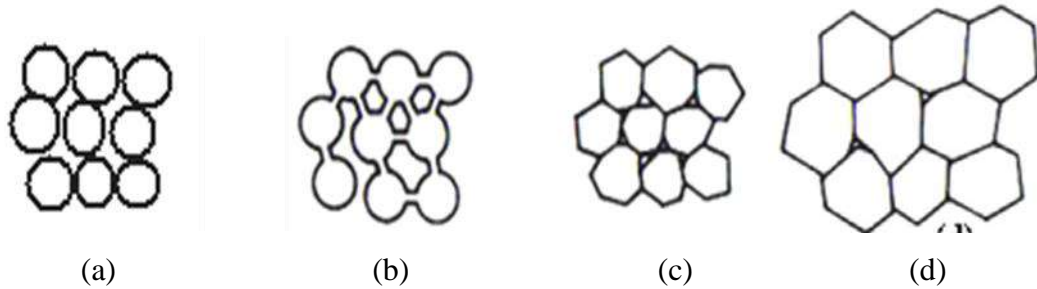
where  $\bar{D}$  is the average grain size,  $n$  is approximately one-third shaped,  $t$  is the sintering duration, and  $k$  is a temperature-dependent component.

As illustrated in Fig. 3.2, there are three stages of sintering [108].

Stage 1: The area of contact between particles expands.

Stage 2: Porosity transitions from open to close.

Stage 3: Pore volume declines, but grains increase in size.



**Fig. 3.2** Different stages of sintering: (a) green body (b) primary stage (c) intermediate stage, and (d) the finishing stage.

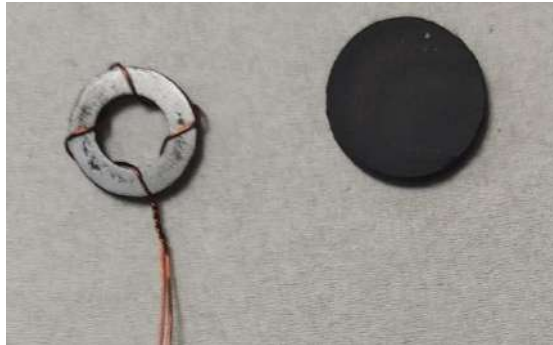
Surface diffusion in the early phases, as well as an evaporation-condensation mechanism at high temperatures, cause neighboring particles to form a neck. Grain formation begins during the middle sintering stage. Pore reduction rates decrease as grain boundaries serve as sources for vacancies as the spacing for both pores and grain boundaries increases, affecting the surface area of the grain boundaries themselves. In the last stage, grain development is substantially speeded up, and the isolation of remaining pores may be observed.

#### 3.2.2.4 Etching

Etching is a method for uncovering the sample's small characteristics. It is a method of making the material's microstructure visible. Etching methods include (a) thermal etching, (b) chemical etching, and (c) electrolytic etching. Thermal etching is employed in this work. The surface of a metallic sample needs to be polished to a thin mirror-like exterior to analyze the microstructural properties of a sample. In contrast, a sample's polished surface seems to be a blank white space when viewed under a microscope. Thus, the thermal etching approach is employed to highlight different components of the sample's microstructure. In this situation, the etching temperature is a few hundred degrees lower than the sample's sintering temperature.

### 3.2.3 Preparation of the samples

Standard solid-state techniques were used to produce nanocrystalline  $Ba_{1-x}(Sr_{0.5}Ni_{0.5})_xTiO_3$  ( $x = 0.00$  to  $0.60$ ). Powdered  $Ba(CO_3)$ ,  $Sr(CO_3)$ ,  $NiO$ , and  $TiO_2$  with analytical grade are used as raw materials and are weighed in accordance with stoichiometric amounts. For 6 hours, these fine powders were crushed and then ground by hand milling. The fine powders are then calcined in air for 5 hours at  $9000^\circ C$ . Then again, these calcined powders were thoroughly crushed and milled by hand milling method for an additional 4 hours. The granulated small particles are compressed into disk- and toroid-shaped samples (Fig. 3.3) using Poly Vinyl Alcohol (PVA) as a binder. At various temperatures, the samples are sintered in the air for 5 hours. The temperature gradients for sintering are  $5^\circ C/min$  for heating and  $10^\circ C/min$  for cooling.



**Fig. 3.3** Toroid- and disk-shaped samples.

### 3.2.4 Structural and morphological characterization

The structural investigation of the synthesized compositions using an XRD is covered in this section. The surface morphology of all materials is studied utilizing a Field Emission Electron Microscope (FESEM). These fundamental principles are explained in the next section.

#### 3.2.4.1 X-ray diffraction

When an atomic-scale crystal lattice plane spacing is hit with X-rays of a specific wavelength and at specific incident angles, rebounded X-rays are produced when the scattered X-ray wavelengths constructively interact; the differences in the travel path must be integer multiples of the wavelength. In the case of constructive interference, an X-ray diffracted beam exits the crystal at the same angle as the incident beam. Bragg's

Law states that the following general formula connects the incoming X-ray wavelength, incidence angle, and atom lattice plane spacing-

$$2d\sin\theta = n\lambda$$

where  $n$  is an integer that denotes the order of diffraction,  $\lambda$  signifies the wavelength of the incident X-rays,  $d$  is the crystal's interplanar spacing, and  $\theta$  is the incidence angle, as illustrated in Fig. 3.4. Diffraction is only conceivable when  $\lambda \leq 2d$  [109]. The crystal structure is significantly revealed by X-ray diffraction (XRD). An XRD was used to investigate the nominal composition of various  $Ba_{1-x}(Sr_{0.5}Ni_{0.5})_xTiO_3$ . Monochromatic  $Cu-K\alpha$  radiation was employed for this investigation.

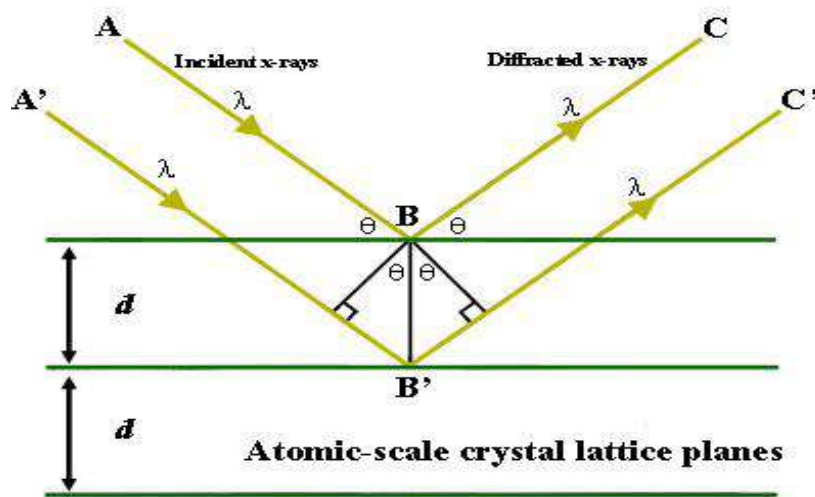


Fig. 3.4 Bragg law of X-ray diffraction.

### 3.2.4.2 Lattice constant, density, and porosity

#### Lattice constant

Utilizing the following relations, the samples' lattice parameters were determined by-

$$\frac{1}{d_{hkl}^2} = \frac{(h^2+k^2+l^2)}{a^2} \quad (\text{for cubic})$$

$$\frac{1}{d_{hkl}^2} = \frac{4(h^2+hk+k^2)}{3a^2} + \frac{l^2}{c^2} \quad (\text{for rhombohedral})$$

And 
$$\frac{1}{d_{hkl}^2} = \frac{h^2}{a^2} + \frac{k^2}{b^2} + \frac{l^2}{c^2} \quad (\text{for orthorhombic})$$

where  $h$ ,  $k$ , and  $l$  are the Miller indices of the crystal planes.



### *Bulk density*

The bulk density ( $\rho_B$ ) of each combination was calculated by using the following relation [110]-

$$\rho_B = \frac{m}{\pi r^2 d}$$

where  $r$ ,  $m$ , and  $d$  are radius, mass and sample thickness, respectively.

The theoretical or X-ray density ( $\rho_x$ ) was calculated by the following relation [110]-

$$\rho_x = \frac{nM_w}{N_A V}$$

where  $n$  signifies the number of atoms, the sample's molar mass is  $M_w$ , Avogadro's number is  $N_A$  and the unit cell volume is  $V$ .

### *Porosity*

The porosity of the combinations was determined using the relation [110]-

$$P(\%) = \frac{\rho_x - \rho_B}{\rho_x} \times 100$$

### **3.2.4.3 Microstructural and elemental analysis**

FESEM was used to examine the grain distribution on the surface of the ceramic samples (model JEOL JSM 7600F). *ImageJ* software was used to compute the  $\bar{D}$ . EDS is an empirical process used to characterize a material's molecular or elemental composition. The EDS system was used to perform compositional analysis in this paper.

### **3.2.5 Electrical properties**

#### **3.2.5.1 Dielectric properties**

An Impedance Analyzer was used to investigate the dielectric characteristics as a function of frequency (WAYNE KERR 6500B). To confirm satisfactory electrical connections, on both surfaces of the samples, silver paste was applied to test dielectric characteristics. At room temperature, the dielectric characteristics of disk-shaped samples were measured in the frequency range of 20 Hz-10 MHz.

The following relationships were used to determine the dielectric parameters [110]-

$$\varepsilon' = \frac{C}{C_o} = \frac{Cd}{\varepsilon_o A}$$

$$\varepsilon'' = \varepsilon' \tan \delta_E$$

where  $C$  refers to the capacitance of the materials and  $C_o = \frac{\varepsilon_o A}{d}$  was derived geometrically. And  $C_o$  is the capacitance of the capacitor without the materials,  $\varepsilon_o$  is the permittivity of free space and  $A$  is the electrode's cross-sectional area.

### 3.2.5.2 Complex impedance spectroscopy

The electrical properties of compositions and their interaction with microstructures are studied using complex impedance spectroscopy. It is applied to investigate the dynamics of mobile or bound charges in grain or grain border areas. AC measurements are frequently done with a Wheatstone bridge type of device, called an impedance analyzer. This device is used to evaluate impedance spectroscopy. While doing so, the sample's resistance  $R$  and capacitance  $C$  are measured and balanced against variable resistors and capacitors. For the supplied sample, the impedance  $|Z|$  ( $\sim Z^*$ ) and phase difference ( $\varphi$ ) between voltage and current are measured as a function of frequency. The data is then evaluated by graphing the  $Z' = |Z| \cos \varphi$  versus the  $Z'' = |Z| \sin \varphi$  on a complex plane known as the impedance plot. The analogous circuit given by the brick layer model [111] is compared to an impedance plot with a linear scale. The impedance curve of a pure resistor is a position on the real axis, whereas the impedance plot of a pure capacitor is a straight line parallel to the imaginary axis. A parallel RC combination's impedance is stated as follows [110]-

$$Z^* = Z' - jZ'' = \frac{R}{1 + (\omega RC)^2} - j \frac{\omega R^2 C}{1 + (\omega RC)^2}$$

After simplification, one gets,

$$\left(Z' - \frac{R}{2}\right)^2 + Z''^2 = \left(\frac{R}{2}\right)^2$$

This equation describes a circle with a radius of  $\frac{R}{2}$  and a center at  $\left(\frac{R}{2}, 0\right)$ . As a result, a plot of  $Z'$  versus  $Z''$  (as a parametric function of  $\omega$ ) yields a semicircle (Fig. 3.5) of radius  $\frac{R}{2}$ . This plot is commonly referred to as the Nyquist plot or the Cole-Cole plot.

### 3.3.5.3 The ac conductivity

To study the room temperature conduction mechanism, the ac conductivity ( $\sigma_{ac}$ ) of these samples was measured in the frequency range  $20\text{ Hz} - 10\text{ MHz}$ . The  $\sigma_{ac}$  can be calculated by [110]-

$$\sigma_{ac} = \omega \varepsilon' \varepsilon_0 \tan \delta_E$$

### 3.2.5.4 Electric modulus

The study of complex modulus is an alternate technique for studying the electrical characteristics and modifying any other effects that may have existed in the sample because of variable relaxation time constants. It is an important tool for figuring out electrical transport phenomena including conductivity relaxation time and carrier/ion hopping rate, and so many more.

The complex electrical modulus  $M^*$  can be expressed using the relation [112] -

$$M^*(\omega) = \frac{1}{\varepsilon^*} = \frac{1}{\varepsilon' - j\varepsilon''} = \frac{\varepsilon'}{\varepsilon'^2 + \varepsilon''^2} + j \frac{\varepsilon''}{\varepsilon'^2 + \varepsilon''^2} = M'(\omega) + M''(\omega)$$

Simplifying and substituting  $\varepsilon''$  by  $\varepsilon' \tan \delta_E$ , we get

$$M^*(\omega) = M'(\omega) + M''(\omega) = \frac{1}{\varepsilon'(1 + \tan^2 \delta_E)} + j \frac{\tan \delta_E}{\varepsilon'(1 + \tan^2 \delta_E)}$$

$M'$  is the energy given to the system, and the energy lost from it during transmission is represented by the symbol  $M''$ .

### 3.2.6 Magnetic properties

#### 3.2.6.1 Complex initial permeability

In studying magnetic characteristics, permeability is one of the most important properties of ferromagnetic materials. The complex initial permeability can be written as follows-

$$\mu_i^* = \mu_i' - \mu_i''$$

The energy that the system stores is described by the  $\mu_i'$  which also declares that the  $B$  and the  $H$  are in phase. The  $\mu_i''$  symbol represents energy dissipation, which explains why  $B$  is out of phase with  $H$ . Using an impedance analyzer, the frequency-dependent complex permeability spectra of the ceramics stated were examined (WAYNE KERR

6500B). At room temperature, complex permeability studies on toroid-shaped specimens were performed in the frequency range of  $10\text{ kHz} - 120\text{ MHz}$ . Utilizing the following relations, the  $\mu'_i$  and  $\mu''_i$  of the complex initial permeability were calculated:

$$\mu'_i = \frac{L_s}{L_o}$$

$$\mu''_i = \mu'_i \tan \delta_M$$

where,  $L_s$  denotes the self-inductance of the sample core and  $L_o = \frac{\mu_o N^2 S}{\pi \bar{d}}$  is derived using geometry.  $L_o$  represents the inductance of the winding coil without the sample core,  $N$  is the number of turns of the coil ( $N = 4$ ), and  $S$  is the area of the cross-section of the toroidal sample which can be given as [97]-

$$S = g \times h$$

where

$$g = \frac{d_2 - d_1}{2}$$

$d_1$  is inner diameter,  $d_2$  represents outer diameter,  $h$  is height and  $\bar{d}$  is the toroidal sample's mean diameter, as shown below [97]-

$$\bar{d} = \frac{d_1 + d_2}{2}$$

The relative quality factor ( $RQF$ ) was calculated using the ratio [97]-

$$RQF = \frac{\mu'_i}{\tan \delta_M}$$

### 3.2.6.2 M-H plot

A Vibrating Sample Magnetometer was used to measure the samples' M-H plot (VSM, model Micro Sense, EV9). The sample is magnetized inside a uniform magnetic field in this type of magnetometer. In this case, the pickup coil's magnetic moment causes an induced voltage that is proportional to the sample's magnetization. The materials' magnetic field-dependent magnetization hysteresis curve can therefore be calculated by measuring the generated voltage.

## CHAPTER 4

### RESULTS AND DISCUSSION

In the present research, structural and microstructural characterization, compositional analysis, and different electromagnetic properties of various *Sr*- and *Ni* co-substituted *BaTiO<sub>3</sub>* are thoroughly investigated both theoretically and experimentally.

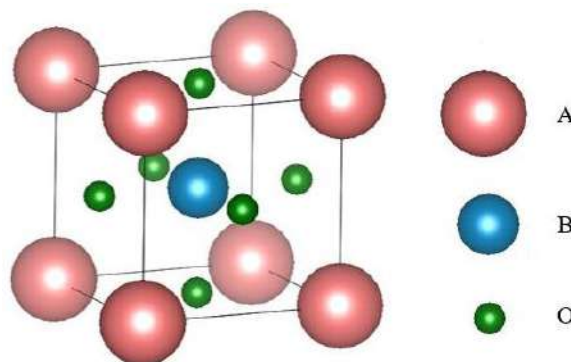
#### 4.1 Theoretical Investigation

##### 4.1.1 Different *ABO<sub>3</sub>* perovskites

This part of the research uses a computational method to investigate the structural, elastic, thermodynamic, electronic, and optical properties of different cubic *ABO<sub>3</sub>* [where *A* = *Ca*, *Ba*, *Sr*; *B* = *Ce*, *Ti*, *Zr*] perovskites and then compared with each other. The material with a low band gap was taken for further theoretical and then experimental study.

##### 4.1.1.1 Computational parameters

The converging cut off the energy *650 eV* of a plane-wave along with k-points  $5 \times 5 \times 5$  with convergence tolerances energy  $1.0 \times 10^{-5}$  *eV/atom*, maximum force on atoms  $0.03$  *eV/Å*, the maximum stress of  $0.05$  *GPa*, and the maximum atomic displacement  $1.0 \times 10^{-3}$  *Å* have been taken to optimize the structures while investigating the structural, electronic, and optical properties. For elastic properties, fine quality with energy  $2.0 \times 10^{-6}$  *eV/atom*, maximum force on atoms  $0.006$  *eV/Å*, and maximum displacement  $2.0 \times 10^{-4}$  *Å* were considered. For thermodynamic properties calculation, k-points were kept the same but the cut-off energy was taken at *830 eV* with Local-density Approximations (LDA) functional. The cubic configuration of the studied materials has been shown in Fig. 4.1.



**Fig. 4.1** Crystal structure of cubic *ABO<sub>3</sub>* [*A* = *Ba*, *Ca*, *Sr*; *B* = *Ce*, *Ti*, *Zr*] perovskites (3D view).

#### 4.1.1.2 Structural properties

In each case, the structure has been optimized geometrically. Cubic structures are considered in this study and then performed geometrical optimization. Structures remain cubic after being optimized geometrically. The computed lattice parameters and density in the ground state under the same computational parameters are listed in Table 4.1.

**Table 4.1** Calculated structural parameters of cubic  $ABO_3$  ( $A = Ba, Ca, Sr$ ;  $B = Ce, Ti, Zr$ ) materials.

<i>Materials</i>	<i>This study,</i> $a_0$ (Å)	<i>Other</i> <i>Theoretical</i> <i>studies,</i> $a_0$ (Å)	<i>Experimental</i> <i>studies,</i> $a_0$ (Å)	<i>Calculated</i> <i>density,</i> $\rho$ (g/cm <sup>3</sup> )
<i>BaCeO<sub>3</sub></i>	4.48	4.43 [114]	4.40 [114]	6.03
<i>CaCeO<sub>3</sub></i>	4.40	-	-	4.44
<i>SrCeO<sub>3</sub></i>	4.43	-	-	5.26
<i>BaTiO<sub>3</sub></i>	4.03	4.03 [113]	4.01 [114]	5.94
<i>CaTiO<sub>3</sub></i>	3.88	3.89 [114]	3.84 [114]	3.86
<i>SrTiO<sub>3</sub></i>	3.94	3.93 [114]	3.91 [114]	5.00
<i>BaZrO<sub>3</sub></i>	4.23	4.23 [113]	4.19 [114]	6.07
<i>CaZrO<sub>3</sub></i>	4.13	3.95 [114]	4.01 [114]	4.22
<i>SrZrO<sub>3</sub></i>	4.17	4.06 [114]	4.10 [114]	5.20

From Table 4.1, it is observed that the lattice parameter is the highest in *BaCeO<sub>3</sub>* and the lowest in *CaTiO<sub>3</sub>*. It is well known that the radius- $R_{Ba} > R_{Sr} > R_{Ca}$  and  $R_{Ce} > R_{Zr} > R_{Ti}$  [115] and a clear reflection in the structural properties is observed accordingly.

#### 4.1.1.3 Mechanical properties

The study of elastic moduli, ductility or brittleness, elastic anisotropy, mechanical stability, and stiffness of solid materials are very substantial properties for material engineering. These properties can be studied by using elastic constant which can be calculated from the linear finite strain-stress method using the CASTEP formulation [115-117].

A proportional elastic constant  $C_{ij}$  can be expressed as-

$$\sigma_i = \sum_{j=1}^6 C_{ij} \epsilon_j$$

where  $\sigma$  is stress and  $\epsilon$  is strain.

In a cubic crystal, the system has three elastic constants-  $C_{11}$ ,  $C_{12}$ , and  $C_{44}$  [118]. For a cubic system, The Born stability criteria [119] are  $C_{11} - C_{12} > 0$ ,  $C_{11} + 2C_{12} > 0$ ,  $C_{11} > 0$ , and  $C_{44} > 0$ .

The internal strain parameter, the Kleinman parameter ( $\zeta$ ) is very useful to describe the relative position of the cation and anion sublattices due to volume-conserving strain distortions. It is a parameter that determines the stability of a compound against the stretching and bending types of strains [120-122]. The  $\zeta$  of a compound is given by-

$$\zeta = \frac{C_{11} + 8C_{12}}{7C_{11} + 2C_{12}}$$

where  $0 \leq \zeta \leq 1$ . When  $\zeta$  is close to 1, under the application of pressure, the bond bending phenomenon is seen, while if it is close to 0, bond stretching is detected.

A material's Cauchy pressure ( $C''$ ) is defined as,  $C'' = C_{12} - C_{44}$ . This value is positive for ductile material and related to ionic bonding, whereas the negative value indicates brittleness and is related to covalent bonding [123-124]. The Poisson's ratio ( $\nu$ ) is also an index for distinguishing between the brittleness or ductility of materials. The material is brittle when  $\nu < 0.26$ , and ductile for  $\nu > 0.26$  [125]. The Pugh's ratio ( $B/G$ ) is another useful parameter to separate the ductility or brittleness nature of a material. If this value of a material is greater than 1.75 that is ductile, and if the value is less than 1.75 the material is brittle [126].

The Debye temperature ( $\theta_D$ ) is a characteristic temperature to evaluate material properties such as thermal expansion, thermal conductivity, lattice vibration, melting point, specific heat, etc. This temperature can be calculated using the formula-

$$\theta_D = \left( \frac{h}{k_B} \right) \left[ \frac{3n}{4\pi} \left( \frac{N_A \rho}{M} \right) \right]^{1/3} V_m$$

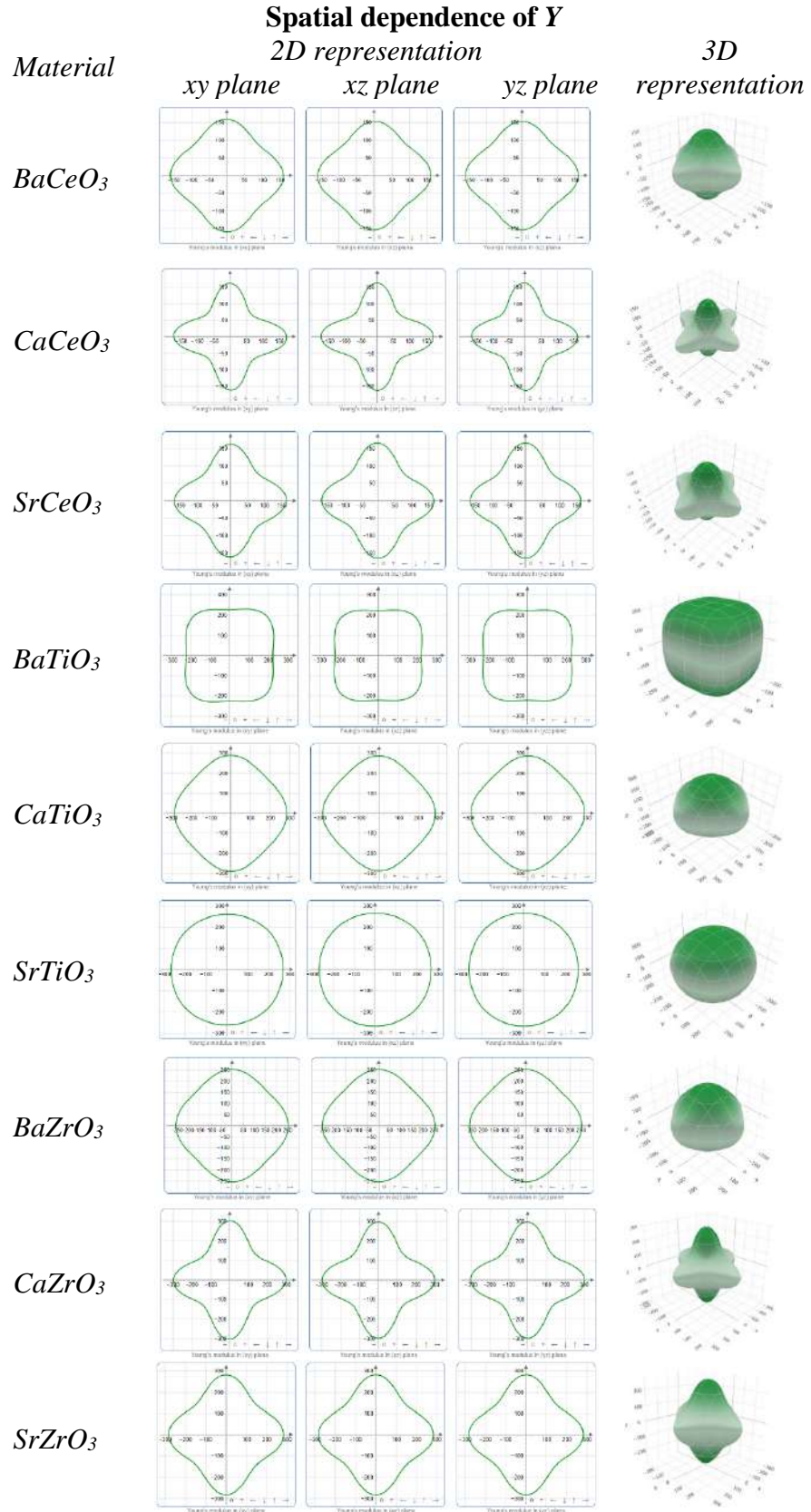
where  $V_m$  is the average sound velocity. The studied mechanical properties of the materials have been tabulated in Table 4.2.

**Table 4.2** The calculated elastic constants ( $C_{11}$ ,  $C_{12}$ ,  $C_{44}$ ),  $Y$ ,  $B$ ,  $G$ ,  $C''$ ,  $\nu$ ,  $B/G$  ratio, Compressibility ( $K$ ), Universal Anisotropic factor,  $\theta_D$  and  $V_m$  of various  $ABO_3$  perovskites.

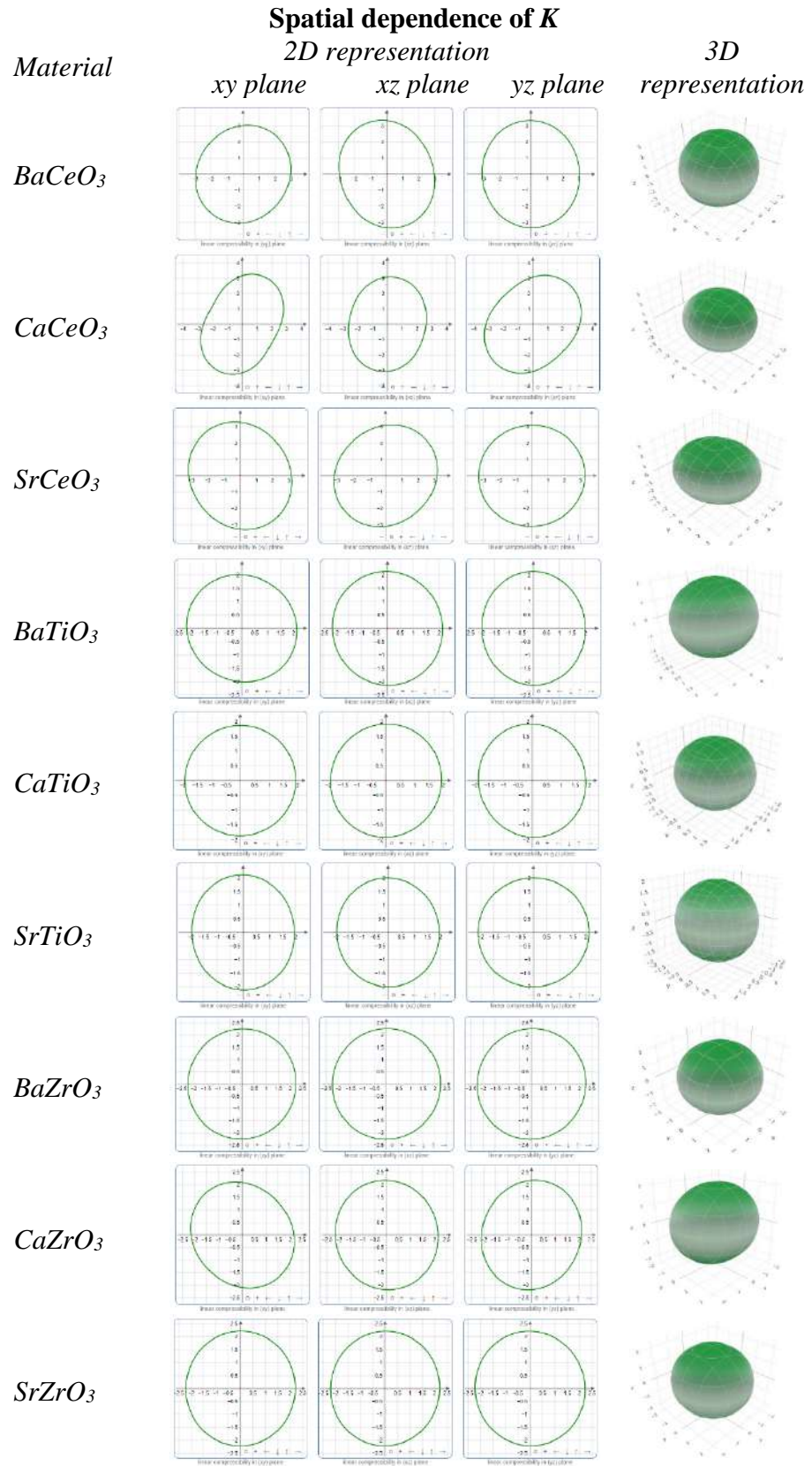
Material Parameter	$BaCeO_3$	$CaCeO_3$	$SrCeO_3$	$BaTiO_3$	$CaTiO_3$	$SrTiO_3$	$BaZrO_3$	$CaZrO_3$	$SrZrO_3$
$C_{11}$ (GPa)	194.96	212.21	193.34	275.23	328.67	312.99	288.02	323.91	309.66
$C_{12}$ (GPa)	68.70	71.25	59.82	101.71	97.49	92.26	78.78	72.54	71.77
$C_{44}$ (GPa)	44.39	30.67	37.40	121.02	96.47	109.99	84.85	62.86	73.12
$C_{11}-C_{12}$ (GPa)	126.27	140.96	133.52	173.52	231.18	220.74	209.24	251.36	237.89
$C_{11}+2C_{12}$ (GPa)	332.36	354.70	312.98	478.65	523.65	497.50	445.58	468.00	453.20
Kleinman Parameter, $\zeta$	0.496	0.480	0.456	0.511	0.444	0.442	0.422	0.375	0.382
Young's Modulus, $Y$ (Gpa)	133.65	118.74	126.88	264.36	261.72	267.94	230.09	232.2	228.03
Bulk Modulus, $B$ (GPa)	107.47	113.74	104.95	159.76	174.94	164.78	148.08	155.78	150.82
Shear Modulus, $G$ (Gpa)	51.69	44.78	48.85	107.97	104.63	109.01	92.7	88.49	91.36
Cauchy pressure, $C''$ (Gpa)	24.31	40.58	22.42	-19.31	1.02	-17.73	-6.07	9.69	-1.36
Poisson's Ratio, $\nu$	0.29	0.33	0.30	0.22	0.25	0.23	0.24	0.26	0.25
Pugh's ratio, $B/G$	2.08	2.54	2.15	1.48	1.67	1.51	1.60	1.76	1.65
Compressibility (1/GPa)	0.0093	0.0089	0.0095	0.0063	0.0057	0.0061	0.0068	0.0064	0.0066
Universal Anisotropic Index	0.1488	0.7594	0.4011	0.1202	0.0448	0.0016	0.0523	0.6209	0.2874
Debye temperature, $\theta_D$ (K)	368	393	381	592	756	669	520	603	558
Average sound velocity, $V_m$ (m/s)	3235	3399	3317	4683	5759	5168	4317	4897	4566

The anisotropic data are always useful for materials to understand the mechanical efficiency of material in practical use [127-128]. The ELATE code has been used to illustrate the 2D and 3D visualizations of the anisotropy of  $Y$ ,  $K$ ,  $G$ , and  $\nu$  in the  $xy$ ,  $yz$ , and  $xz$  planes of  $ABO_3$  perovskites which are illustrated in Fig. 4.2 [129].

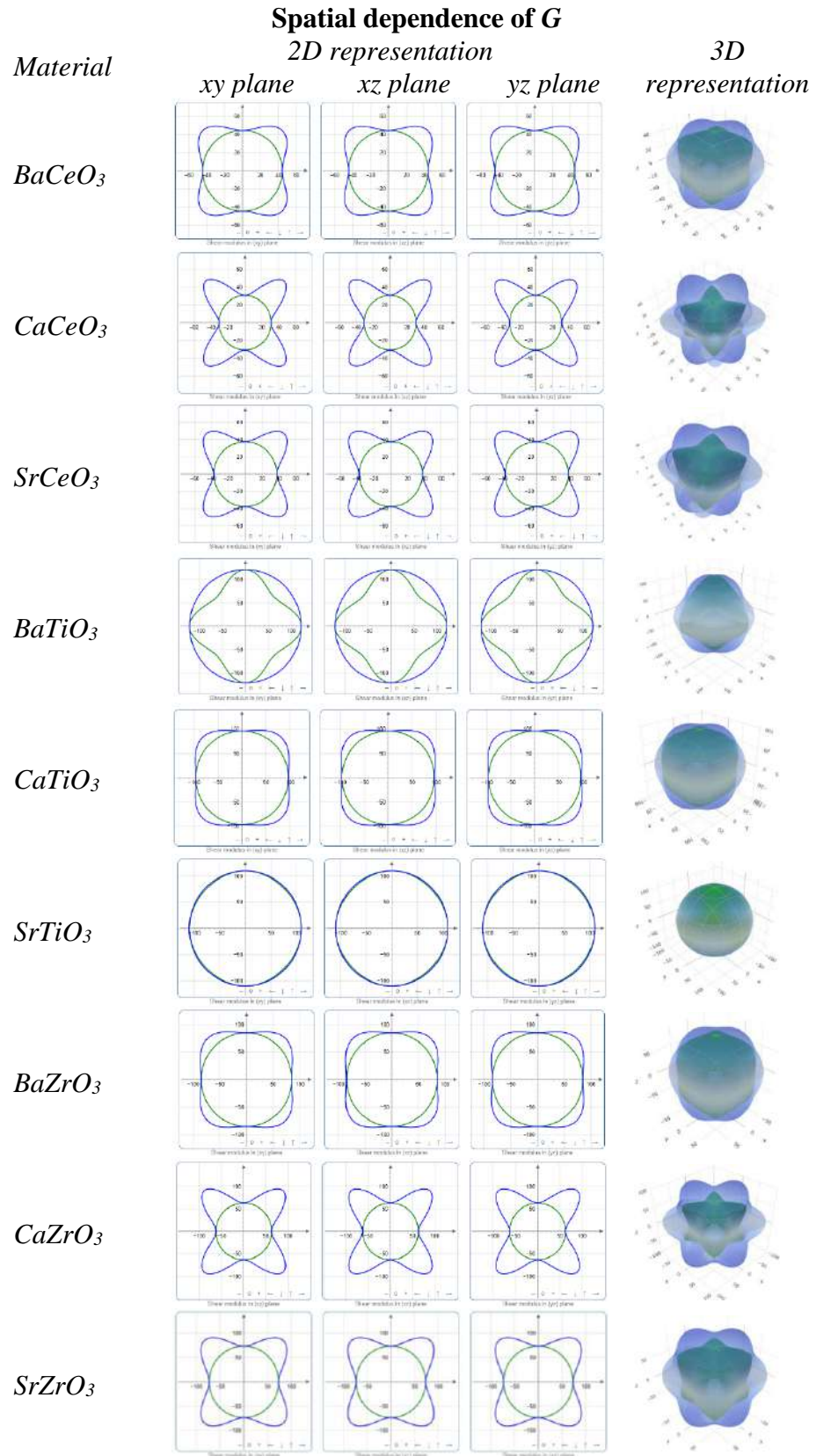




**Fig 4.2 (a)** The 2D and 3D plots of  $Y$  of  $ABO_3$  perovskites at  $0\text{ GPa}$ .

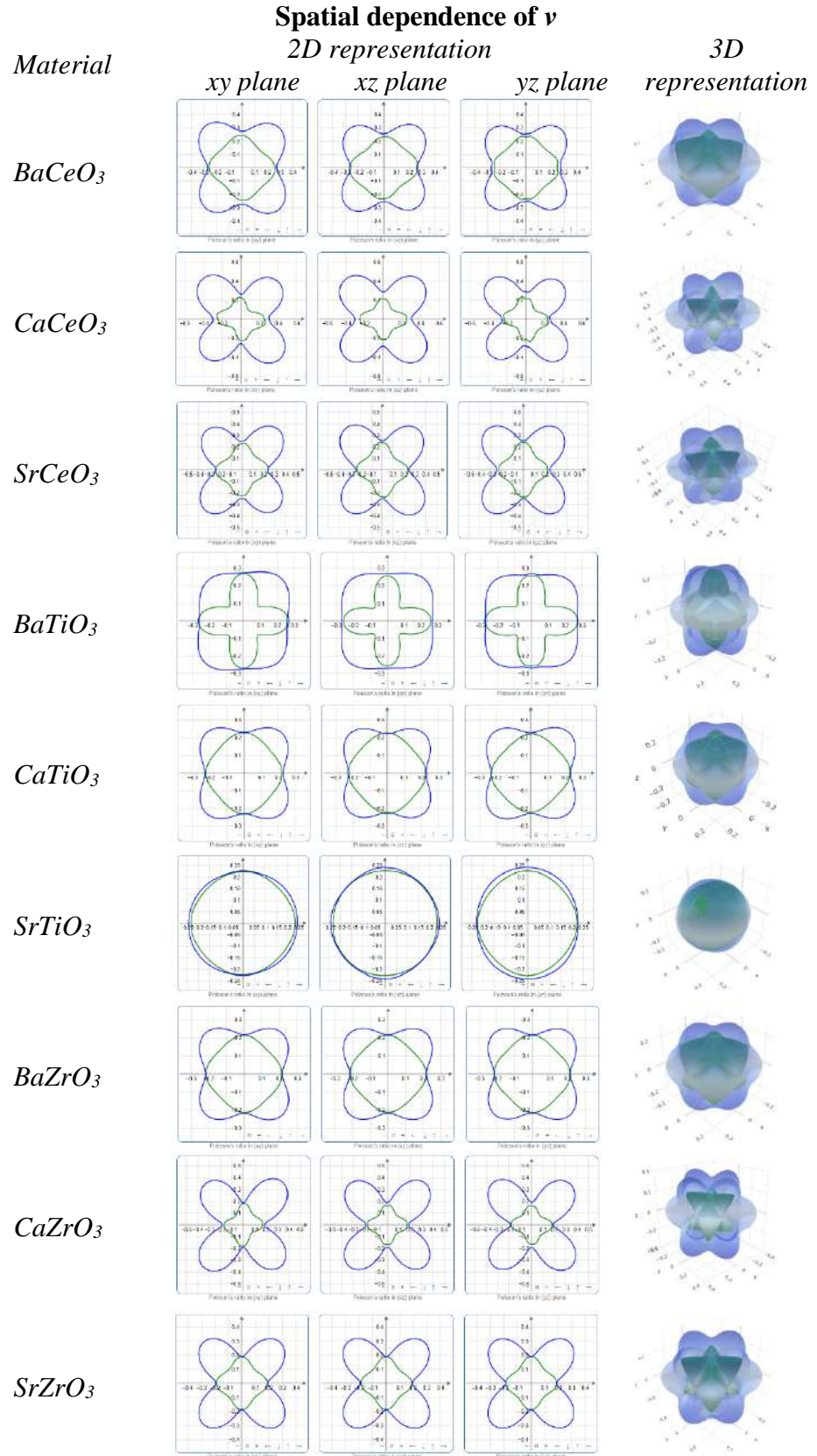


**Fig. 4.2 (b)** The 2D and 3D plots of  $K$  of  $ABO_3$  perovskites at  $0\text{ GPa}$ .



**Fig. 4.2 (c)** The 2D and 3D plots of  $G$  of  $ABO_3$  perovskites at  $0\text{ GPa}$ .





**Fig. 4.2 (d)** The 2D and 3D plots of  $v$   $ABO_3$  perovskites at  $0$  GPa.

According to the  $\zeta$ , the  $BaTiO_3$  is the bending type and the rest of them are the stretching type under pressure. The  $C''$ ,  $\nu$ , and  $B/G$  data reveal the ductile nature of the Cerate family and  $CaZrO_3$ , while  $BaTiO_3$ ,  $SrTiO_3$ ,  $BaZrO_3$ , and  $SrZrO_3$  are brittle. Exceptions are seen for the calculated values for the  $CaTiO_3$ . The Pugh's ratio and Poisson's Ratio data show it is brittle but the Cauchy pressure shows it is ductile. In the ground state condition, all three calculated values of  $CaTiO_3$  are very close to the boundary of the ductility and brittleness region.

#### 4.1.1.4 Thermodynamic properties

Thermodynamic properties are defined as system characteristics that can specify the system's state. [130]. The lattice dynamics as well as the dielectric properties, the phonon dispersion curves, and the phonon density of states are very significant. These properties can be calculated using density functional perturbation theory [131]. The vibrational properties can be calculated using a harmonic approximation [132-135]-

$$D_{\mu\nu}(\mathbf{R} - \mathbf{R}') = \left. \frac{\partial^2 E}{\partial u_\mu(\mathbf{R}) \partial u_\nu(\mathbf{R}')} \right|_{u=0}$$

where  $u$  is the displacement of a given atom and  $E$  is the total energy in the harmonic approximation.

In reciprocal space, this dynamical force constants matrix is-

$$D_{\mu\nu}(\mathbf{q}) = \frac{1}{N_R} \sum_{\mathbf{R}} D_{\mu\nu}(\mathbf{R}) e^{-i\mathbf{q}\mathbf{R}}$$

Here the plane waves are evaluated for each atomic displacement-

$$u(\mathbf{R}, t) = \varepsilon e^{i(\mathbf{q}\mathbf{R} - \omega(\mathbf{q})t)}$$

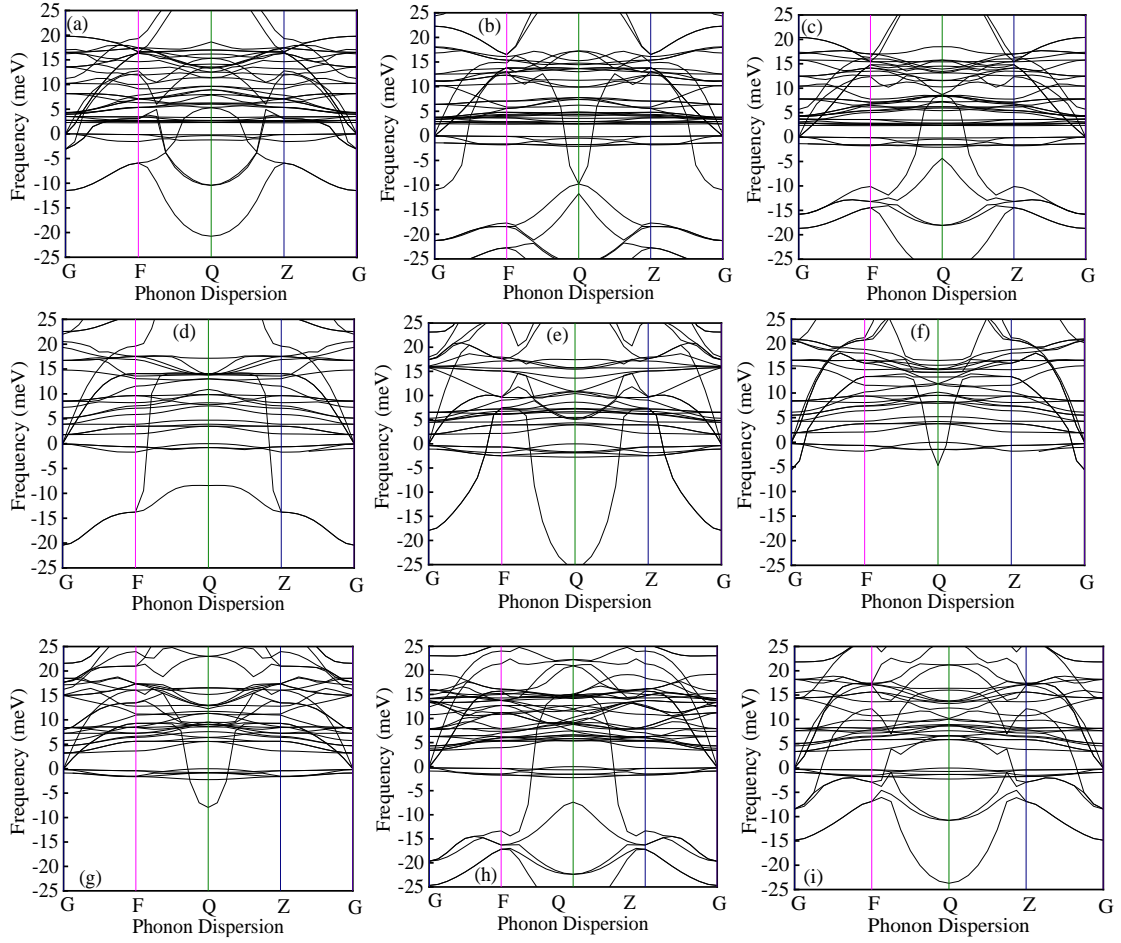
The polarization vector ( $\varepsilon$ ) of each mode is an eigenvector of  $3N$  dimensions of the eigenvalue problem:

$$M\omega(\mathbf{q})^2 \varepsilon = D(\mathbf{q})\varepsilon$$

The partial density of state contribution on atom from each phonon band is-

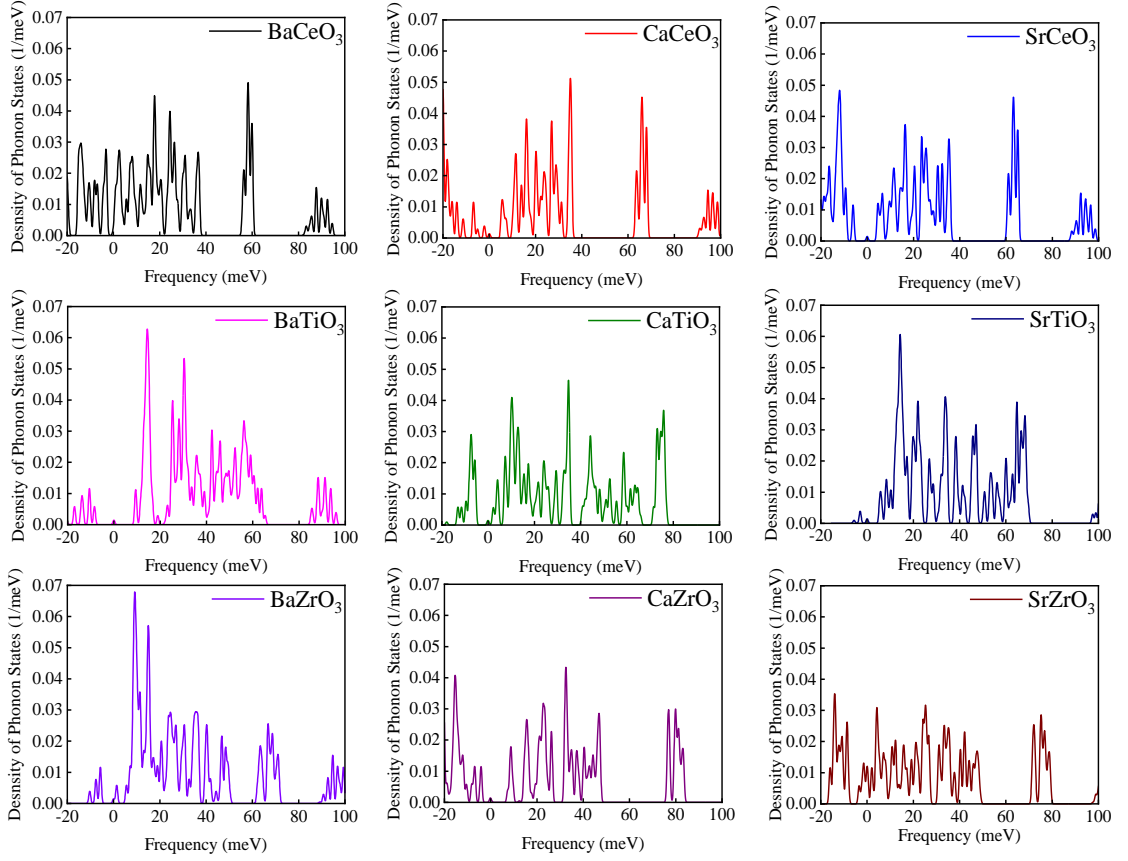
$$N_i(E) = \int \frac{d\mathbf{k}}{4\pi^3} |e_j(i)|^2 \delta(E - E_n(\mathbf{k}))$$

where  $e_j$  is the eigenvector related to the mode of the energy  $E_j$ .



**Fig. 4.3** The calculated phonon dispersion curves along the high-symmetry points (a)  $BaCeO_3$ , (b)  $CaCeO_3$ , (c)  $SrCeO_3$ , (d)  $BaTiO_3$ , (e)  $CaTiO_3$ , (f)  $SrTiO_3$ , (g)  $BaZrO_3$ , (h)  $CaZrO_3$ , (i)  $SrZrO_3$ .

In Fig. 4.3, the calculated phonon dispersion curves of various perovskites along the high-symmetry points in the Brillouin zone are shown. To get information about the dynamical stability of compounds, phonon dispersion curves are very important. The absence of negative frequencies covering the whole Brillouin zone indicates the dynamical stability against mechanical perturbation under normal pressure. There are two types of phonons - acoustic phonons and optical phonons. Acoustic phonons are related to the vibration of long-wavelength. In this case, in-phase vibrations are observed in the neighboring particles. Optical phonons are related to the vibrations of neighboring particles where the vibrations are nearly anti-phase. In the phonon dispersion curves, the acoustic modes are situated in the lower parts whereas the optical modes are in the upper parts [136]. In both phonon dispersion (Fig. 4.3) and phonon DOS curves (Fig. 4.4), there are some imaginary frequencies curves below zero frequencies which indicates the unstable modes. All the compounds have these unstable modes which are responsible for phase transition and ferroelectric responses of materials.



**Fig. 4.4** The calculated phonon Density of states of  $ABO_3$  perovskites.

At finite temperature, the thermodynamic properties like- enthalpy ( $H$ ), entropy ( $S$ ), and free energy ( $F$ ) can be calculated from the vibrational properties of the materials [137-138]-

$$H(T) = E_{tot} + \frac{1}{2} \int g(\omega) \hbar \omega d\omega + \int \frac{\hbar \omega}{e^{\frac{\hbar \omega}{k_B T}} - 1} g(\omega) d\omega$$

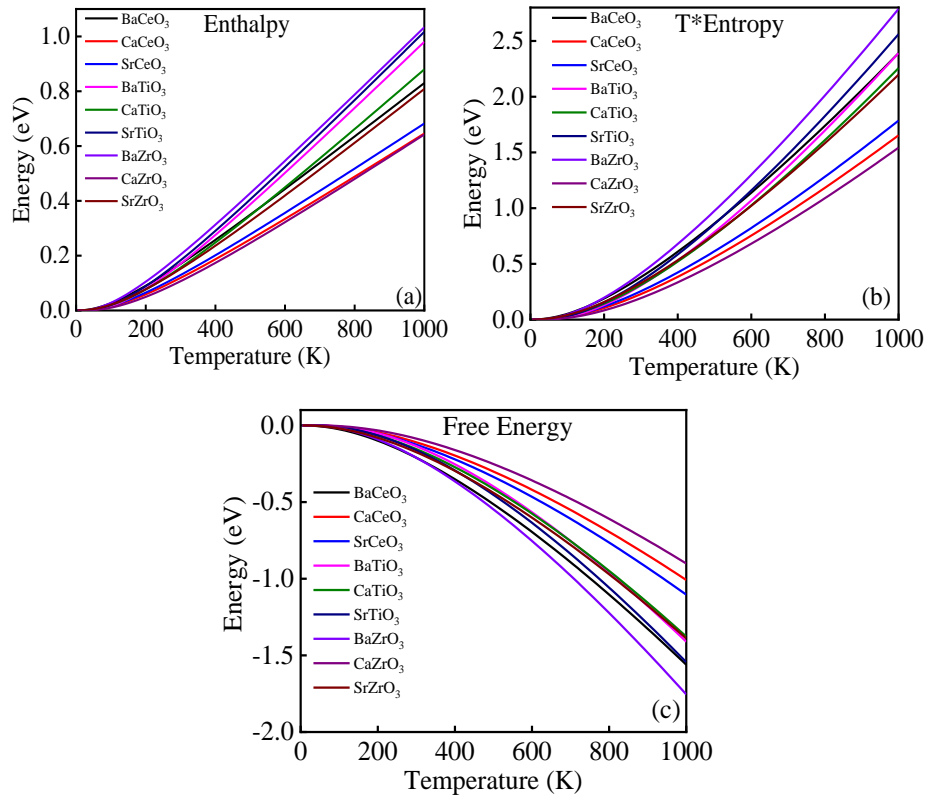
$$S(T) = k_B \left[ \int \frac{\frac{\hbar \omega}{k_B T}}{e^{\frac{\hbar \omega}{k_B T}} - 1} g(\omega) d\omega - \int g(\omega) \ln \left( 1 - e^{-\frac{\hbar \omega}{k_B T}} \right) d\omega \right]$$

$$F(T) = E_{tot} + \frac{1}{2} \int g(\omega) \hbar \omega d\omega + k_B T \int g(\omega) \ln \left( 1 - e^{-\frac{\hbar \omega}{k_B T}} \right) d\omega$$

where  $g(\omega)$  is the phonon density of states and  $k_B$  is the Boltzmann constant.

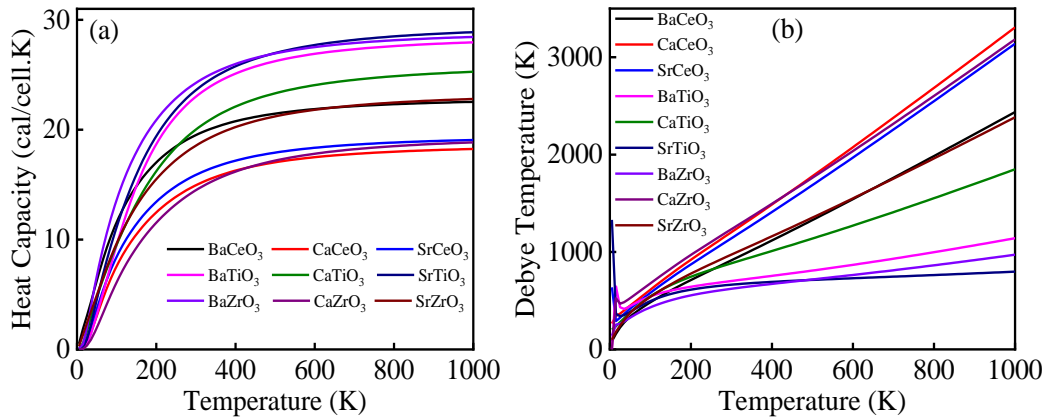
In Fig. 4.5, The calculated temperature-dependent enthalpy and temperature times entropy increase with the increase of temperature while free energy decreases in all the cases. The evaluated values for all the cases obeyed the third law of thermodynamics as

the values of all the terms for various  $ABO_3$  perovskites approach zero as the temperature approaches absolute zero.



**Fig. 4.5** The calculated (a) Enthalpy, (b)  $T^*$ Entropy, and (c) Free energy of  $ABO_3$  perovskites.

The temperature-dependent heat capacity and Debye temperature are calculated and the comparison between the perovskites is also illustrated in Fig. 4.6.



**Fig. 4.6** The calculated temperature-dependent (a) heat capacity and (b) Debye temperature of  $ABO_3$ .

The Zero-point energy is the lowest possible energy that a quantum mechanical system can have. The Zero-point energy of the studied materials is listed in Table 4.3.

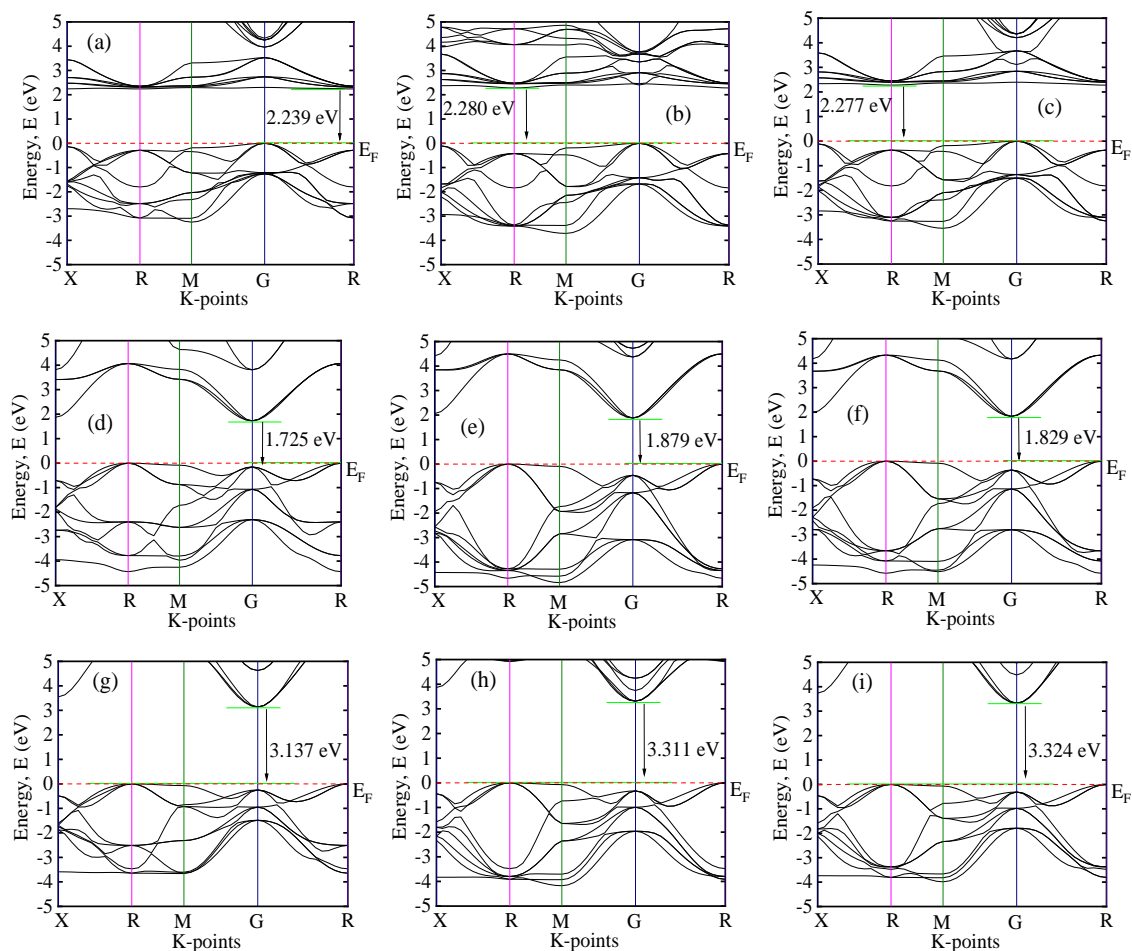
**Table 4.3** The calculated Zero-point energy.



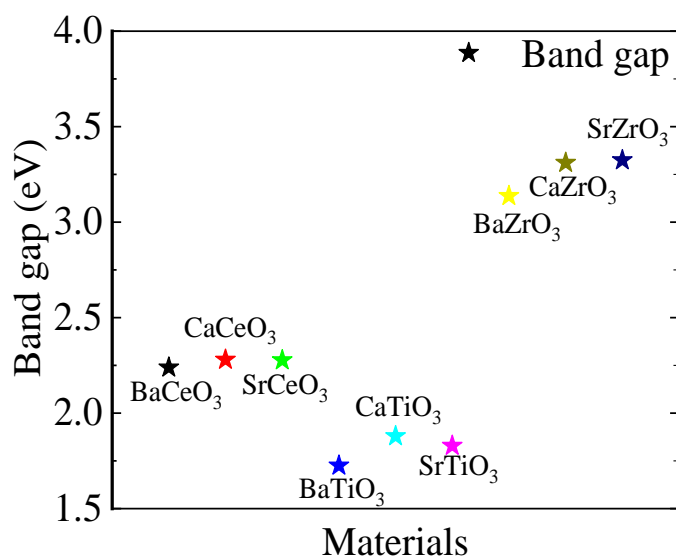
<i>Materials</i>	<i>Zero-Point Energy (eV)</i>
<i>BaCeO<sub>3</sub></i>	0.1828
<i>CaCeO<sub>3</sub></i>	0.1865
<i>SrCeO<sub>3</sub></i>	0.1832
<i>BaTiO<sub>3</sub></i>	0.2872
<i>CaTiO<sub>3</sub></i>	0.2837
<i>SrTiO<sub>3</sub></i>	0.2989
<i>BaZrO<sub>3</sub></i>	0.2500
<i>CaZrO<sub>3</sub></i>	0.2334
<i>SrZrO<sub>3</sub></i>	0.2347

#### 4.1.1.5 Electronic properties

The study of the electronic band structure of solids is one of the most significant ways of describing electronic properties such as conductivity, bonding properties, thermoelectric phenomenon, magnetic properties, etc. The electronic band structure ( $-5 eV$  to  $5 eV$ ) as a function of energy,  $E$  of different  $ABO_3$  [ $A = Ba, Ca, Co, Sr$ ;  $B = Ce, Ti, Zr$ ] perovskite structures at the ground state are shown in Fig 4.7. A comparative study on band gaps is illustrated in Fig. 4.8. While these computations at the ground state, the high-symmetry points ( $G-F-Q-Z-G$ ) in the first Brillouin zone have been considered. In each diagram, the red dotted horizontal dashed line represents the Fermi level ( $E_F$ ).



**Fig. 4.7** The calculated band diagrams along high-symmetry points (a)  $BaCeO_3$ , (b)  $CaCeO_3$ , (c)  $SrCeO_3$ , (d)  $BaTiO_3$ , (e)  $CaTiO_3$ , (f)  $SrTiO_3$ , (g)  $BaZrO_3$ , (h)  $CaZrO_3$ , (i)  $SrZrO_3$ .



**Fig. 4.8** Comparison of band gaps of different cubic  $ABO_3$  perovskites.

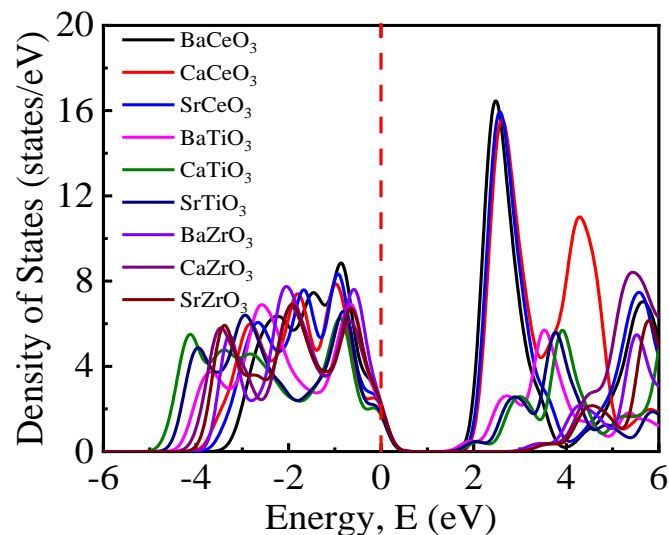
In Fig. 4.7, the valance bands are shown between  $0\text{ eV}$  to  $-5\text{ eV}$ , and the conduction bands are between  $0\text{ eV}$  to  $5\text{ eV}$ . There is no overlap between the valance and conduction bands

in all the cases. The bandgap for all the compounds is indirect. Fig. 4.8 shows the comparison based on the computed bandgap of these perovskites and the calculated sequence is-

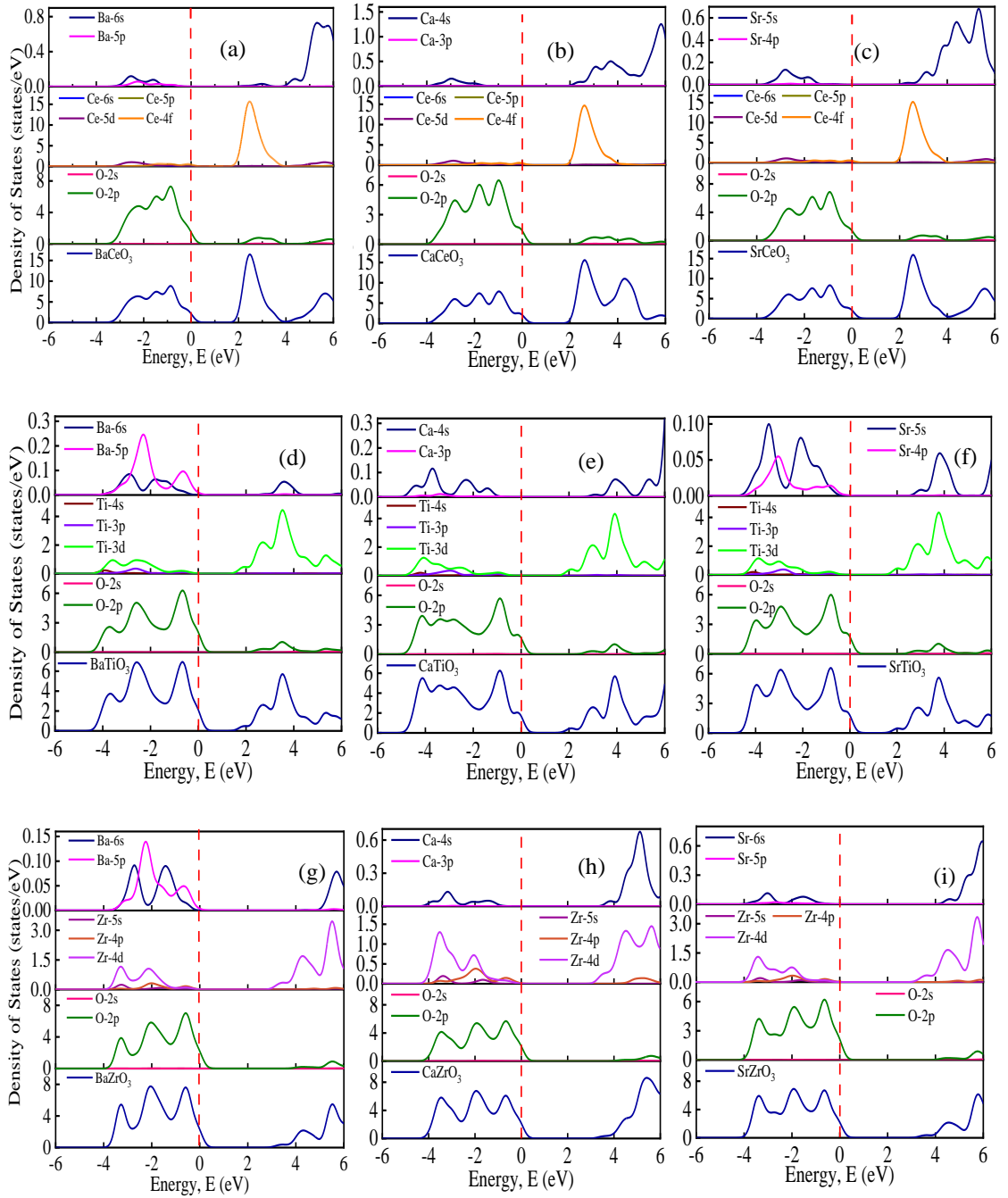


The  $BaTiO_3$  shows the lowest bandgap. Materials with a lower bandgap have a great impact on solar cells [139-141]. So,  $BaTiO_3$  has been considered for further study.

In the field of condensed matter physics, the number of electronic states available to be occupied per unit energy interval is the density of states (DOS) of that system. The density of states plays an important role in understanding the bonding nature, both thermal and electrical conductivity, magnetic and optoelectronic properties, determining the transition rates, and so on. The total density of states (TDOS) can be used to explain the performance of electronic devices [142]. The electronic and structural stability to some extent depends on the TDOS of the material and the position of the corresponding Fermi level [143-144]. Calculated TDOS and partial density of states (PDOS) from  $-6\text{ eV}$  to  $6\text{ eV}$  have been shown in Fig. 4.9 and 4.10. The dashed red line represents the Fermi level ( $E_F$ ). In the energy region  $0.5\text{ eV}$  to  $1.4\text{ eV}$ , the electrons for all the ceramics have negligible electronic contributions. It is clear that the Cerate, Titanate, and Zirconate families have almost the same patterns. However,  $CaCeO_3$  has an additional broad peak in the energy region from  $3.4\text{ eV}$  to  $5.1\text{ eV}$ .



**Fig. 4.9** Calculated electron density of states of various  $ABO_3$  perovskites.



**Fig. 4.10** The calculated partial density of states (PDOS) of (a)  $BaCeO_3$ , (b)  $CaCeO_3$ , (c)  $SrCeO_3$ , (d)  $BaTiO_3$ , (e)  $CaTiO_3$ , (f)  $SrTiO_3$ , (g)  $BaZrO_3$ , (h)  $CaZrO_3$ , (i)  $SrZrO_3$ .

The calculated partial density of states ( $-6\text{ eV}$  to  $6\text{ eV}$ ) has been illustrated in Fig. 4.10. The valence band in all cases lies between  $-6\text{ eV}$  to  $0\text{ eV}$ , and conduction bands are from  $0\text{ eV}$  to  $6\text{ eV}$ . In both the valence band and conduction band, most of the contribution comes from  $Ba-6s$ ,  $Ba-5p$ ,  $Ca-4s$ ,  $Ca-3p$ ,  $Sr-5s$ ,  $Sr-4p$ ,  $Ce-6s$ ,  $Ce-5p$ ,  $Ce-5d$ ,  $Ce-4f$ ,  $Ti-4s$ ,  $Ti-3p$ ,  $Ti-3d$ ,  $Zr-5s$ ,  $Zr-4p$ ,  $Zr-4d$ ,  $O-2s$ , and  $O-2p$  orbitals. In the Cerate family bonding mostly depends on  $Ba-6s$ ,  $Ba-5p$ ,  $Ca-4s$ ,  $Sr-5s$ ,  $Ce-4f$ ,  $O-2p$ , in Titanate family  $Ba-6s$ ,  $Ba-$

*5p, Ca-4s, Sr-5s, Sr-4p, Ti-3d, O-2p* have the most influence, and *Ba-6s, Ba-5p, Ca-4s, Sr-6s, Zr-4d, O-2p* in Zirconate family.

#### 4.1.1.6 Optical properties

When electromagnetic waves fall on the surface of a material, the photon interacts with the charge carriers of that material. This photon-charge carrier interaction influences the optical properties of a material. This type of photon-charge carrier interaction can be calculated by using some parameters which are a function of the frequency or the energy of the incident photon. While calculating the optical properties of all the structures, the considered frequency-dependent complex dielectric function is-

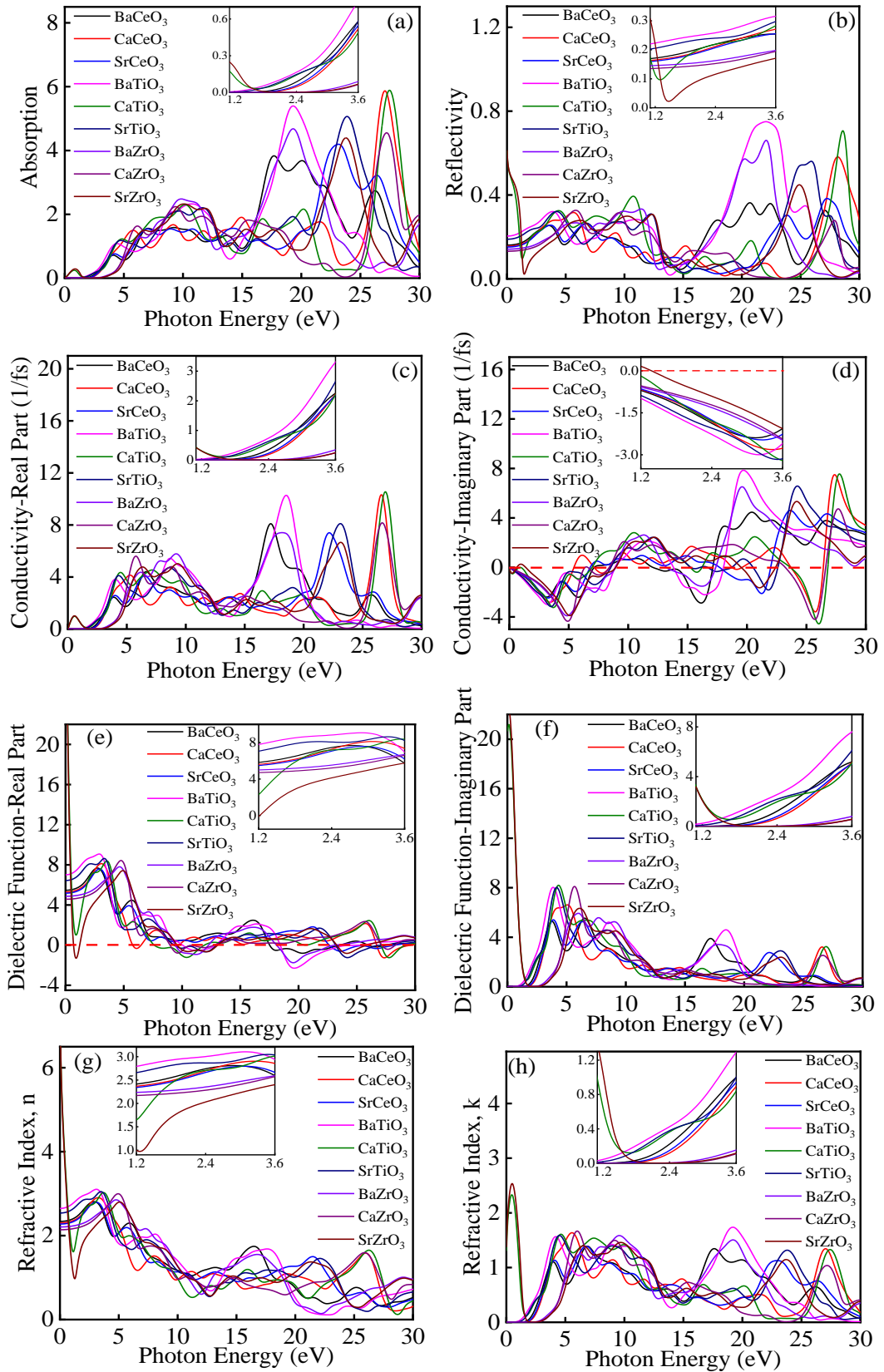
$$\mathcal{E}(\omega) = \mathcal{E}_1(\omega) + i\mathcal{E}_2(\omega)$$

here the real part of the dielectric function is  $\mathcal{E}_1(\omega)$  and according to Kramers-Kronig transformations, it depends on the imaginary part,  $\mathcal{E}_2(\omega)$ .

The imaginary part,  $\mathcal{E}_2(\omega)$  can be calculated using the matrix elements of optical transitions between occupied and unoccupied electronic orbitals which can be expressed with CASTEP formulation as-

$$\varepsilon_2(\omega) = \frac{2e^2\pi}{\Omega\varepsilon_0} \sum_{k,\nu,c} |\psi_k^c| \mathbf{u} \cdot \mathbf{r} |\psi_k^\nu|^2 \delta(E_k^c - E_k^\nu - E)$$

where,  $\omega$  is the frequency of the photon,  $e$  is the charge of the electron,  $\psi_k^c$  and  $\psi_k^\nu$  are the wave functions of the conduction band and valance band respectively and the polarization vector of the incident electric field is  $\mathbf{u}$ . Different optical parameters, like- absorptivity, reflectivity, refractive index, optical conductivity, and energy loss function can be determined by the dielectric function  $\varepsilon(\omega)$  [145-146].



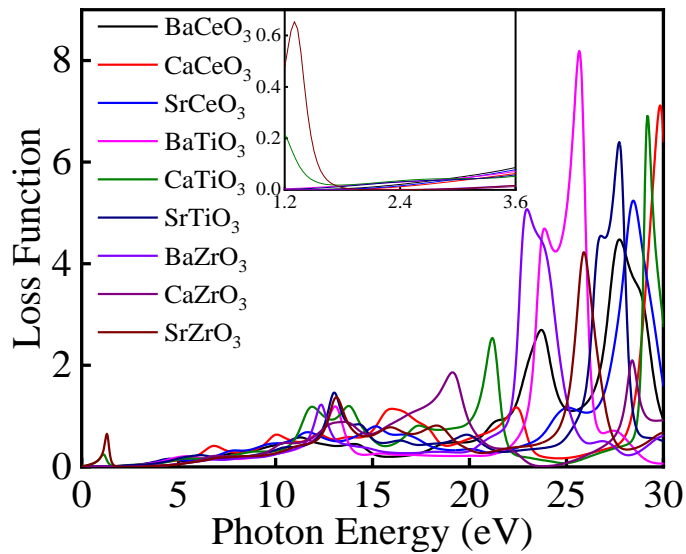
**Fig. 4.11** The calculated (a) absorption, (b) reflectivity, (c) real part of conductivity, (d) imaginary part of conductivity, (e) real part of the dielectric function, (f) imaginary part of the dielectric function, (g) refractive index ( $n$ ), (h) refractive index ( $k$ ) of various  $ABO_3$  perovskites.

From Fig. 4.11, it can be seen that in the region  $0-15\text{eV}$ , the behavior of all the materials is different from each other. In the energy region  $15-30\text{eV}$ , the Titanate and Zirconate families show a similar pattern in the case of absorption.

In the IR-UV ( $1.2-3.6\text{eV}$ ) region, linear progression is seen for absorption, reflectivity, and real part of refractive index ( $n$ ), while  $\text{CaTiO}_3$  has high and  $\text{SrZrO}_3$  has a higher value of absorption and is less reflective in the IR region. An exponential increase is seen in the real part of conductivity and imaginary part of refractive index ( $k$ ) for the Titanate and Cerate families are observed in the IR-UV region, but this rate is higher in the Titanate family.

In the IR region ( $\sim 1\text{eV}$ ),  $\text{CaTiO}_3$  and  $\text{SrZrO}_3$  has a higher value for absorption, the real part of conductivity, and the imaginary part of the dielectric function. The imaginary part of the conductivity is negative and decreasing in nature.

For all energy regions, the imaginary part of the conductivity and dielectric function, the real part of the refractive index ( $n$ ), and the imaginary part of the refractive index ( $k$ ) follow almost similar patterns for *Ba*, *Ca*, and *Sr* families.



**Fig. 4.12** The calculated Loss function of  $\text{ABO}_3$  perovskites.

The loss function is the loss of energy of the first electron passing through a material. It is associated with the collective oscillation frequency of the valance electron. The peaks of loss function are related to a characteristic frequency of a material, plasma frequency. In Fig. 4.12, minor peaks are observed in the IR region for the materials  $\text{CaTiO}_3$  and  $\text{SrZrO}_3$ . Several random peaks are observed for different perovskites after  $10\text{eV}$ .

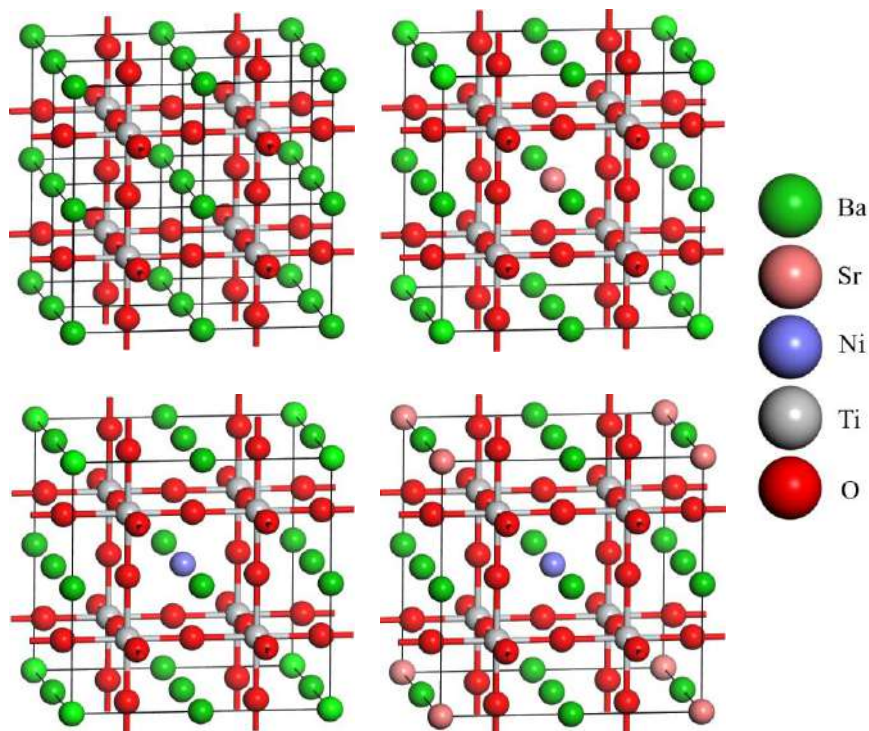


#### 4.1.2 Theoretical investigation of Sr- and Ni-doped $BaTiO_3$

In this section, we have used a computational method to investigate the electronic and optical properties of Sr, Ni-doped  $BaTiO_3$ . We have used four different structures where one is pristine  $BTO$ , one is 12.5% Sr atom doped  $BTO$  ( $BSTO$ ), another is 12.5% Ni atom doped  $BTO$  ( $BNTO$ ), and finally 25% (Sr, Ni) co-doped  $BTO$  ( $BSNTO$ ).

##### 4.1.2.1 Computational parameters

The valence electronic states were considered as  $5p^6 6s^2$  for Ba,  $4p^6 5s^2$  for Sr,  $3d^8 4s^2$  for Ni,  $3d^2 4s^2$  for Ti, and  $2s^2 2p^6$  for O. The k-point sampling of the Brillouin zone was constructed with  $4 \times 4 \times 4$  grids in primitive cells. The converging cut-off energy of a plane wave was set to 500 eV for all cases. The geometrical optimization of the crystals structures was by setting the convergence tolerances were set to  $1.0 \times 10^{-5}$  eV/atom for the energy, 0.03 eV/Å for the maximum force on atoms, 0.05 GPa for the maximum stress, and  $1.0 \times 10^{-3}$  Å for the maximum atomic displacement. To investigate the effect of Ni, Sr doping in pure  $BaTiO_3$  ceramic, a  $2 \times 2 \times 2$  supercell was built which are shown below in geometrically optimized form-



**Fig. 4.13** Geometrically optimized (a) pristine  $BaTiO_3$ , (b) 12.5% Sr atom doped  $BTO$ ,  $Ba_{0.875}Sr_{0.125}TiO_3$  ( $BSTO$ ) and (c) 12.5% Ni atom doped  $BTO$ ,  $Ba_{0.875}Ni_{0.125}TiO_3$  ( $BNTO$ ) and (d) 25% atom (Sr, Ni) co-doped  $BTO$ ,  $Ba_{0.75}(Sr_{0.5}Ni_{0.5})_{0.25}TiO_3$ ,  $BSNTO$ .

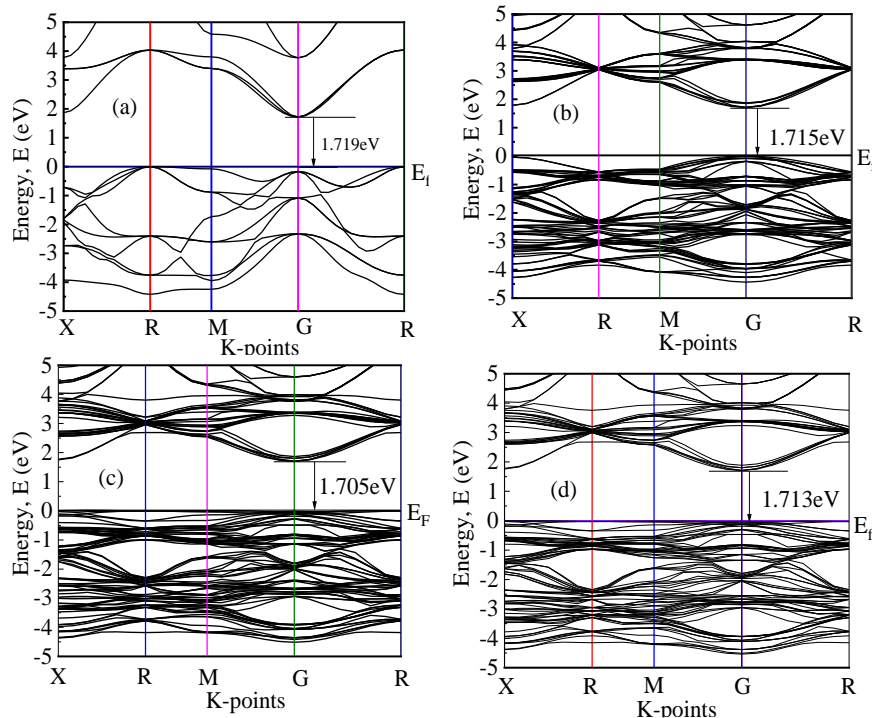


**Table 4.4** Calculated parameters of *Sr*, *Ni*-doped cubic *BaTiO<sub>3</sub>* perovskites.

<i>Materials</i>	<i>a</i> (Å)	<i>Volume</i> <i>V</i> (Å <sup>3</sup> )	<i>Calculated</i> <i>Density</i> , <i>ρ</i> (g/cm <sup>3</sup> )
Pristine BTO	4.03	65.67	5.90
BSTO	4.03	65.28	5.77
BNTO	4.02	64.84	5.72
BSNTO	4.01	64.29	5.56

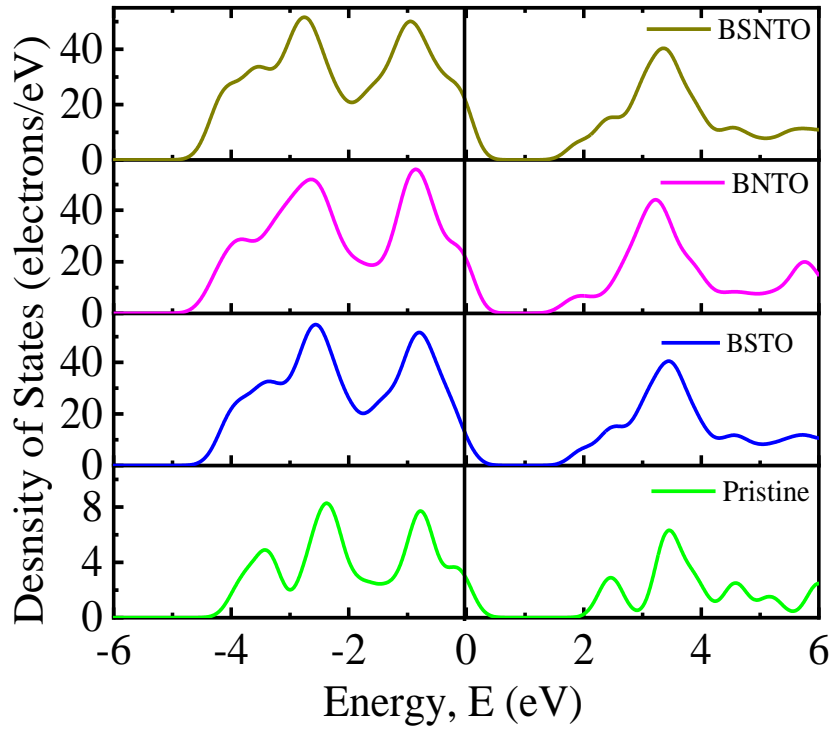
#### 4.1.2.2 Electronic properties

To investigate the nature of *BTO*, *BSTO*, *BNTO*, and *BSNTO*, the electronic band structure along the high symmetry direction in the Brillouin zones are shown above in Fig. 4.14. The band gap of *BTO* is found 1.719 eV, 1.715 eV for *BSTO*, *BNTO* is 1.705 eV and 1.713 eV for *BSNTO*. As the band gap of pure *BTO* shows good consistency with the previously calculated value (in single crystal 1.725 eV with cut-off energy 650 eV and k-point grid 5×5×5; Section 4.1.1.5) and, recommends the acceptability of the present calculation of this approach for other materials [124].



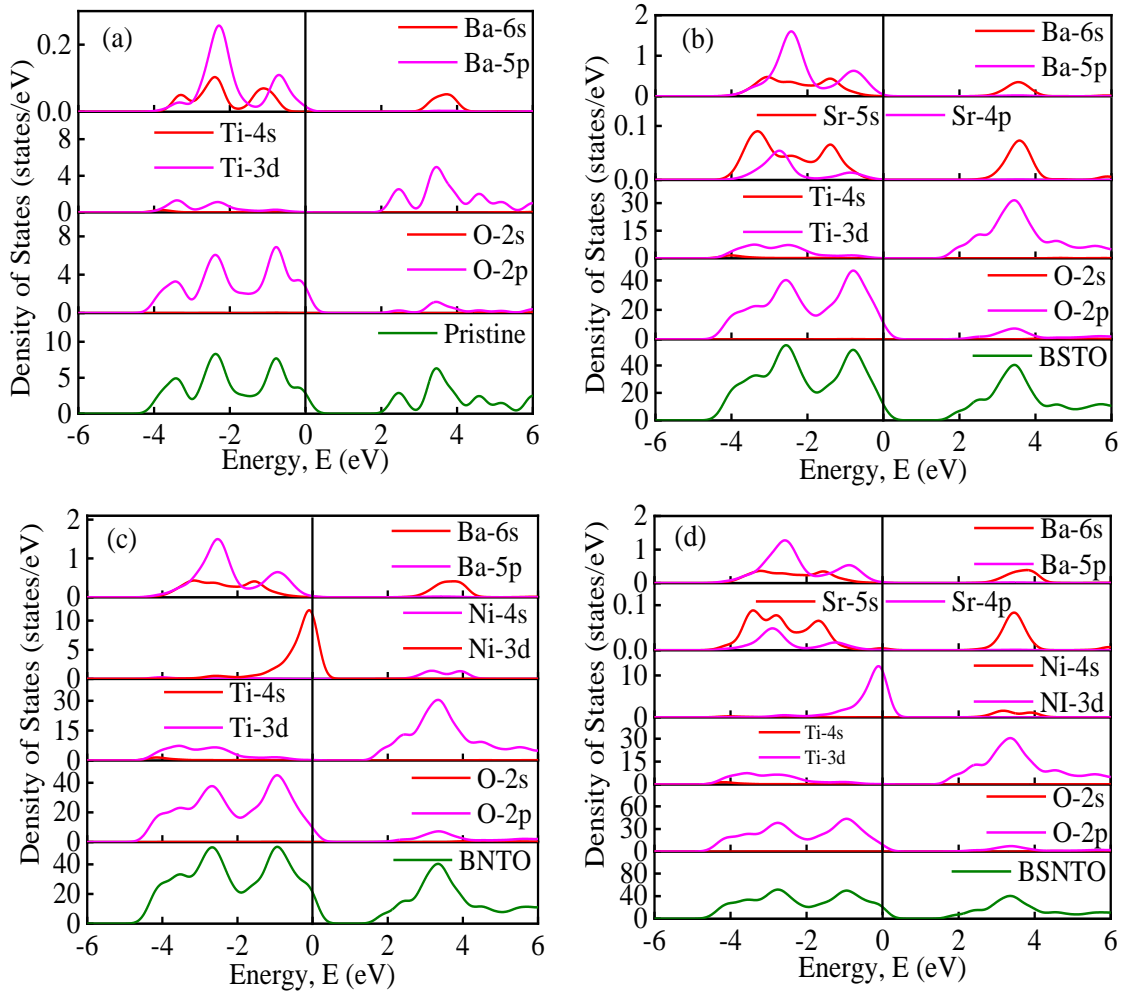
**Fig. 4.14** Electronic band structure of (a) pristine *BTO* (b) *BSTO* (c) *BNTO* and (d) *BSNTO*.

The band gap of (*Sr, Ni*) co-doped *BTO* is lower than the band gap of pristine *BTO* which means co-doping reduces the band gap slightly.



**Fig. 4.15** The density of states (DOS).

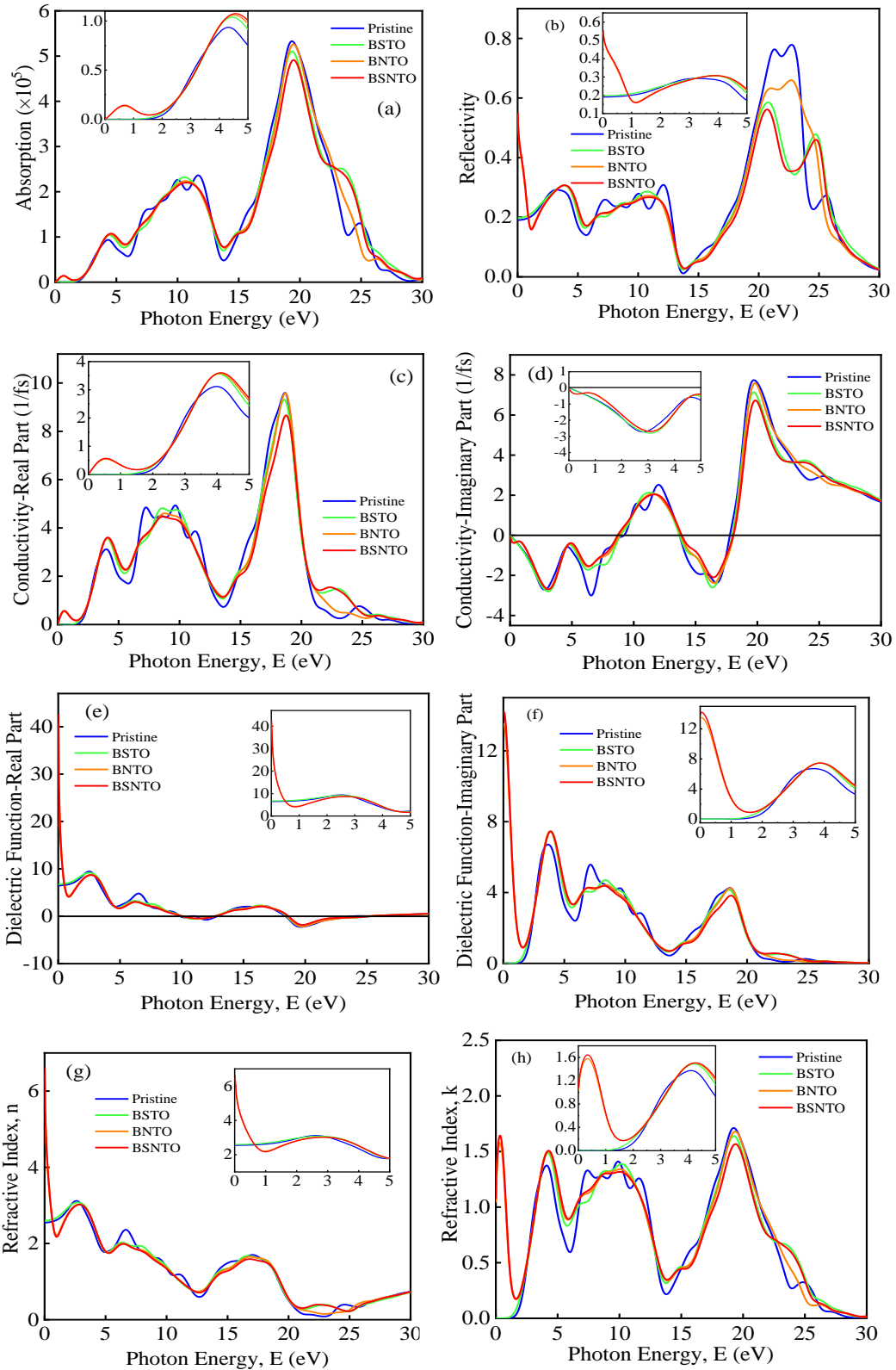
Fig. 4.15 & 4.16 show the total and partial density of states of our studied materials. From Fig. 4.14, 4.15 & 4.16, it can be shown that Oxygen (*O*) *2p* state dominates in all four compounds because of the highest valence band lies at the Fermi level ( $E_F$ ) at  $0\text{ eV}$ , which is the common characteristic of oxide materials. The valence band in all the cases lies between  $-6\text{ eV}$  to  $0\text{ eV}$  (Fermi level). In the valence band, most of the contribution comes from *Ba-6s*, *Ba-5p*, *Sr-5s*, *Sr-4p*, *Ni-4s*, *Ni-3d*, *Ti-4s*, *Ti-3d*, *O-2s*, and *O-2p* orbitals. In *BSNTO*, sharp peaks are observed in the valence and conduction band near the Fermi level. We also observe predominant hybridization for *Ti-3d* and *O-2s* states near the Fermi level. In the conduction band, a similar kind of domination of *Ti-3d* and *O-2s* states is noticed. In *BSNTO*, *Ni-4d* states also contribute to bonding with *O-2p* states. There is no overlapping of *Ti-4s* and *Ti-3d* with *O-2s* and *O-2p*, meaning the bonding is ionic in nature.



**Fig. 4.16** The total and partial density of states of (a) pristine *BTO*, (b) *BSTO*, (c) *BNTO*, and (d) *BSNTO*.

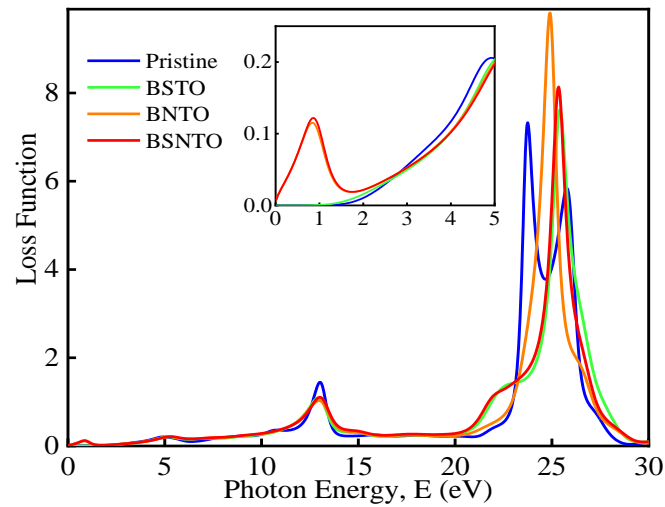
#### 4.1.2.3 Optical properties

In this work, optical properties are simulated by using polarized light with a smearing value of  $0.5 \text{ eV}$  in the direction  $[1 0 0]$ . Under that condition absorption, reflectivity, photoconductivity, real and imaginary parts of dielectric constant, refractive index, and loss function of these materials have been studied from the formalism developed in Cambridge Serial Total Energy Package (CASTEP).



**Fig. 4.17** The calculated photon energy dependent (a) absorption, (b) reflectivity, (c) real part of conductivity, (d) imaginary part of conductivity, (e) real part of the dielectric function, (f) imaginary part of the dielectric function, (g) refractive index,  $n$  and (h) refractive index,  $k$ .

In Fig. 4.17, *BSiTO* showed lower values in all the cases while the optical properties with a dielectric constant are slightly better in pure *BTO*. Almost similar patterns are noticed for all the materials in the 0-30 eV region. Yet some inconsistencies are observed in 5-15 eV and after 22 eV regions. Peaks are sharp in the case of reflectivity for *BSiTO* in the 15-30 eV region. An additional peak is also observed in *BSiTO* in the 20-30 eV region for the imaginary part of conductivity. Again, the optical constants ( $n$ ,  $k$ ) of these materials are consistent except for the energy regions 0-2 eV and 20-25 eV. But in the IR to UV regions things are diverse. *BSiTO* and *BNTiO* showed similar trends in all eight cases. Absorption (Fig. 4.17(a)) is high for *BSiTO* and *BNTiO* near the IR region and *BSiTO* is highest in the deep UV region. *BTO* & *BSiTO*. *BNTiO* & *BSiTO* showed similar patterns for reflectivity, conductivity, dielectric function, and refractive indexes in that region. In Fig. 4.18, the loss function shows similar patterns for all the materials except in the region 20-30 eV. The peak is large for *BNTiO*. Here also loss function is high in the IR zone for *BSiTO* and *BNTiO* and parallel trends are seen in the visible-to-UV region for all four materials.



**Fig. 4.18** Loss function as a function of photon energy.

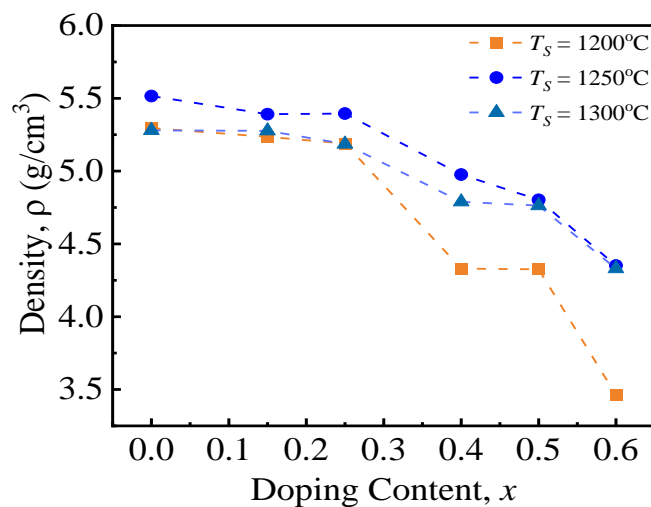
## 4.2 Experimental Investigation of Sr and Ni Co-doped BaTiO<sub>3</sub>

It is seen that the co-doping of Sr and Ni in the Ba site of BaTiO<sub>3</sub> enhanced its optoelectronic parameters. The effect of co-doping of these elements in BaTiO<sub>3</sub> is carried out experimentally with the formula Ba<sub>1-x</sub>(Sr<sub>0.5</sub>Ni<sub>0.5</sub>)<sub>x</sub>TiO<sub>3</sub>. The values of x are chosen as 0.00, 0.15, 0.25, 0.40, 0.50, and 0.60. The ionic radius of Ba, Sr, Ni, Ti, and O are considered as 1.61, 1.18, 0.69, 0.61, and 1.4 Å, respectively. The Rietveld analysis was done to further confirm these structures.

### 4.2.1 Structural properties

#### 4.2.1.1 Bulk density

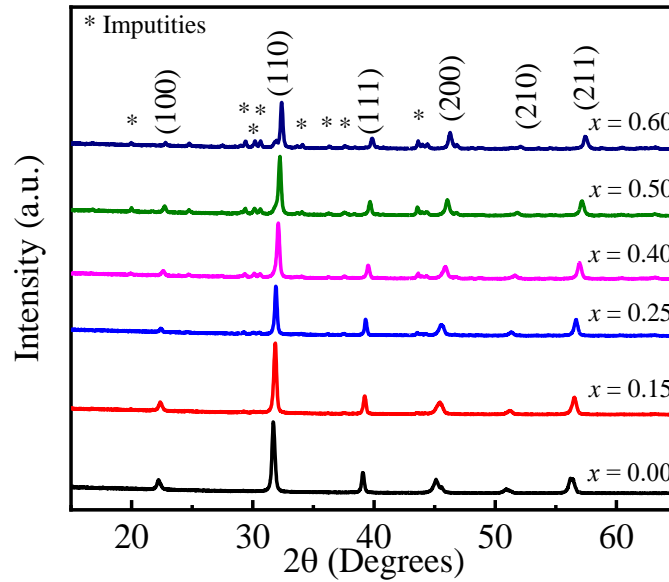
Density is important in influencing the properties of various materials. Fig. 4.19 depicts the variation in bulk density,  $\rho_B$ , with (Sr<sub>0.5</sub>Ni<sub>0.5</sub>)<sup>2+</sup> concentration for the sample sintered at various  $T_s$  (1200, 1250, and 1300°C). Fig. 4.19 shows that the  $\rho_B$  decreases with increasing the co-doping of Sr and Ni content. When  $T_s = 1250^\circ\text{C}$ , the  $\rho_B$  of the samples is the highest considering the other two sintering temperatures. Samples of  $T_s = 1250^\circ\text{C}$  are considered for further studies. At the  $T_s = 1250^\circ\text{C}$ , for  $x = 0.00$  to 0.25 the rate of decrease of  $\rho_B$  is very low. After that, the density decreases rapidly. The atomic mass of Ba is much higher than the mass of Sr and Ni. The substitution of Sr and Ni in the place of Ba, reduces the  $\rho_B$  of the samples. Moreover, the size of Ba is higher than the sizes of Sr and Ni that reduces the density. During the sintering process, thermal energy provides a force that pushes grain boundaries to move apart and create larger holes. This increases pore volume, which lowers material density.



**Fig. 4.19** Density as a function of sintering temperature for various Ba<sub>1-x</sub>(Sr<sub>0.5</sub>Ni<sub>0.5</sub>)<sub>x</sub>TiO<sub>3</sub>.

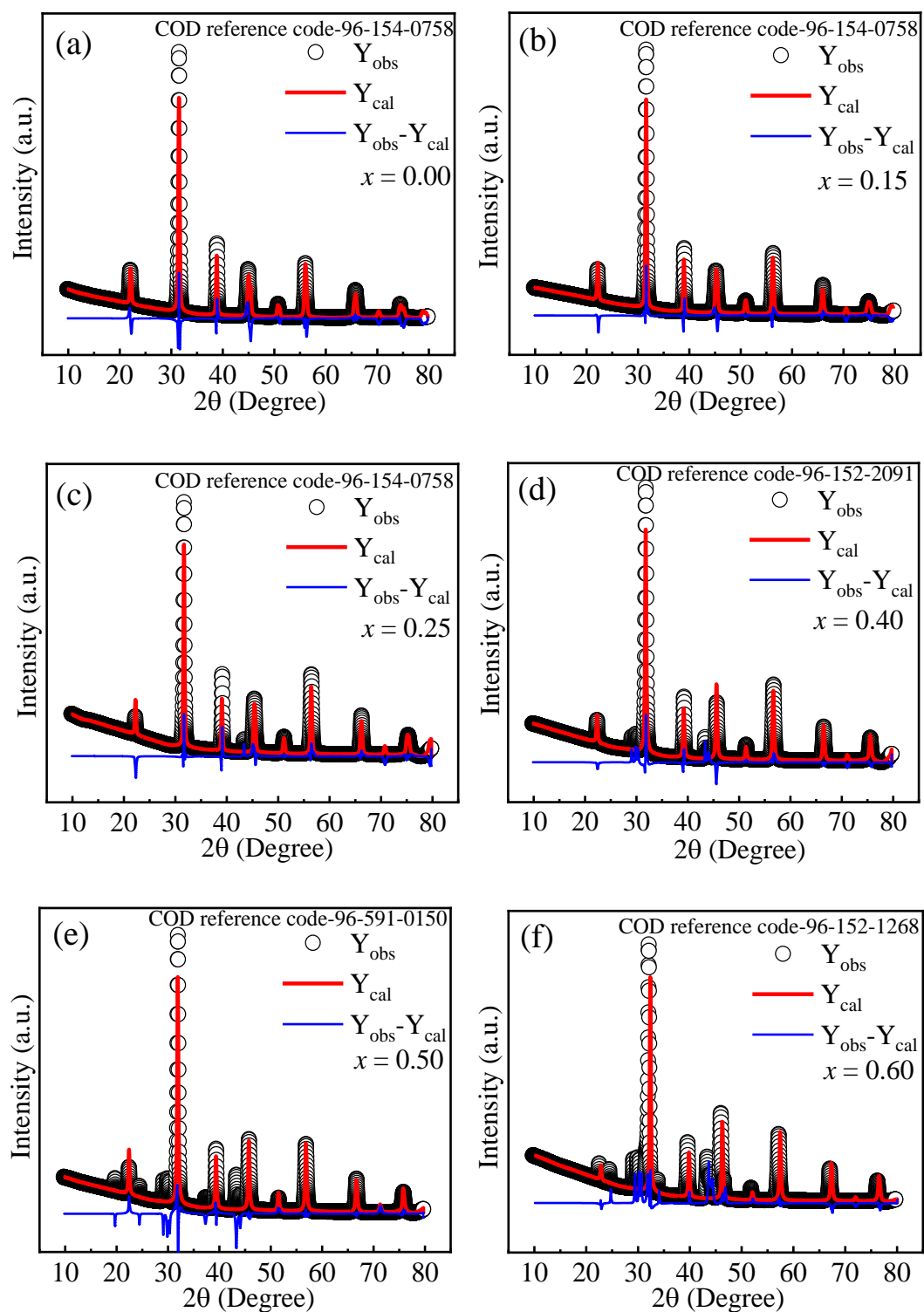
#### 4.2.1.2 X-ray diffraction analysis

As illustrated in Fig. 4.20, XRD data were collected at room temperature in the  $2\theta$  range of  $15^\circ$  to  $65^\circ$ . According to this illustration, the prominent identical peaks of the perovskite structure ( $100$ ), ( $110$ ), ( $111$ ), ( $200$ ), ( $210$ ), and ( $211$ ) confirm the formation of a clearly defined perovskite structure. The XRD patterns demonstrate typical perovskite reflections, with the most prominent ( $110$ ) peak.



**Fig. 4.20** XRD patterns for various  $Ba_{1-x}(Sr_{0.5}Ni_{0.5})_xTiO_3$ .

There are several peaks were found  $x \geq 0.25$  and peaks continue to be more intense up to  $x = 0.60$ . This suggests that the  $x = 0.00, 0.15, 0.25$  and  $x = 0.40, 0.50, 0.60$  are of different kinds. The size difference between  $Ba$  and the substitutes  $Sr$  and  $Ni$  leads to these variations. To eliminate the effects of impurities and to find the structural changes in details, the samples are studied further by the Rietveld refinement technique using both FullProf and Match 3.0 software, which are shown in Fig. 4.21.



**Fig. 4.21** Calculated Rietveld refinement of several  $Ba_{1-x}(Sr_{0.5}Ni_{0.5})_xTiO_3$ .

The observed and computed XRD patterns are in excellent agreement, as can be seen in these diagrams. Reproduction of an estimable model of refining needs that matched peak intensities and placements. From the Crystallography Open Database (COD), different initial parameters such as lattice constants, atomic position, and lattice space group were taken. The corresponding references from COD are also provided in each figure. While



doing these refinements, the pseudo-Voigt function was used as the peak profile, and the *12-Coefficients Fourier cosine series* was selected as the background mode. Since this function may be used to determine the size and strain contributions to peak expansion and is a linear combination of the Gaussian and Lorentzian functions, it was chosen for peak shapes. Following the initial refinement of the background coefficients, the peak positions were rectified using a series of subsequent refinements. The structural and microstructural parameters, including the position parameters, structure factor, occupancy, scale factor, and lattice parameters, were then improved.

For structure and background, peak form and position, and profile *R*-factors, the goodness of fit is evaluated (i.e., reliability factors like  $R_{wp}$  and  $R_p$ ). The lower values of  $R_{wp}$  and  $R_p$  are thought to be the beneficial refinement of the model. Table 4.5 summarizes the structural parameters obtained for several samples.

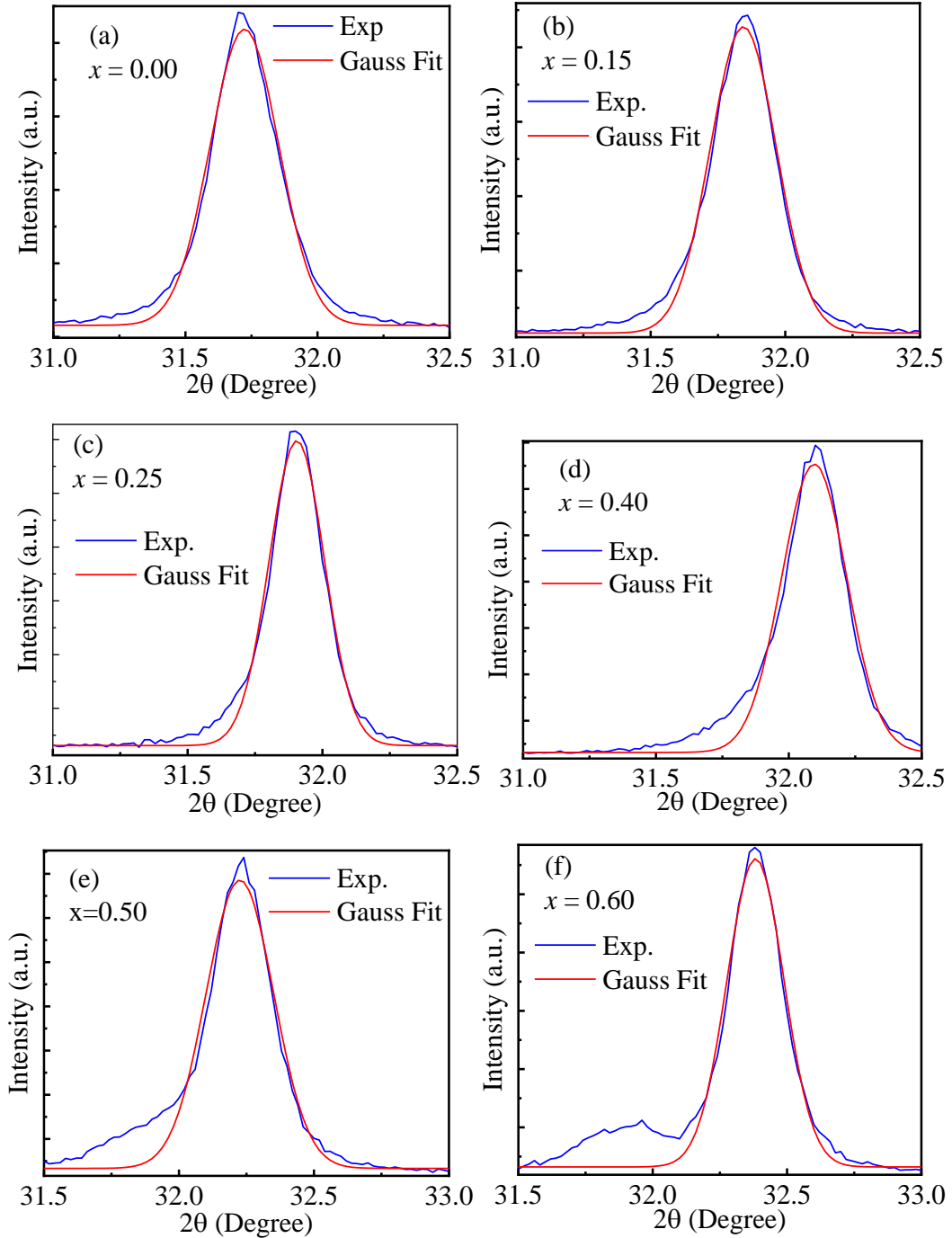
**Table 4.5** Calculated Rietveld refinement data from XRD data of different  $Ba_{1-x}(Sr_{0.5}Ni_{0.5})_xTiO_3$ .

<i>x</i>	<i>Phase name</i>	<i>Space group and Number</i>	<i>Lattice parameters (Å)</i>	<i>Volume (Å<sup>3</sup>)</i>	<i>COD reference code</i>
0.00	Orthorhombic	P2mm (25)	a = 3.9951 b = 4.0215 c = 4.0385	64.9	96-154-0758
0.15	Orthorhombic	P2mm (25)	a = 3.9905 b = 4.0063 c = 4.0213	64.3	96-154-0758
0.25	Orthorhombic	P2mm (25)	a = 3.9820 b = 3.9956 c = 4.0073	63.8	96-154-0758
0.40	Cubic	Pm-3m (221)	a = 3.9792	63.0	96-152-2091
0.50	Cubic	Pm-3m (221)	a = 3.9670	62.4	96-591-0150
0.60	Cubic	Pm-3m (221)	a = 3.9466	61.5	96-152-1268

The first three compositions show orthorhombic phases with close values of lattice parameters and volumes. The goodness of fit values is in acceptable ranges. The last three are showing cubic structures with space group *Pm-3m*.

### 4.2.1.3 Crystallite size using the Scherrer's method, theoretical density, and porosity

The most intense (*110*) peaks of various nanocrystalline  $Ba_{1-x}(Sr_{0.5}Ni_{0.5})_xTiO_3$  were taken to calculate the crystallite size using Scherrer's method which is depicted in Fig. 4.22.



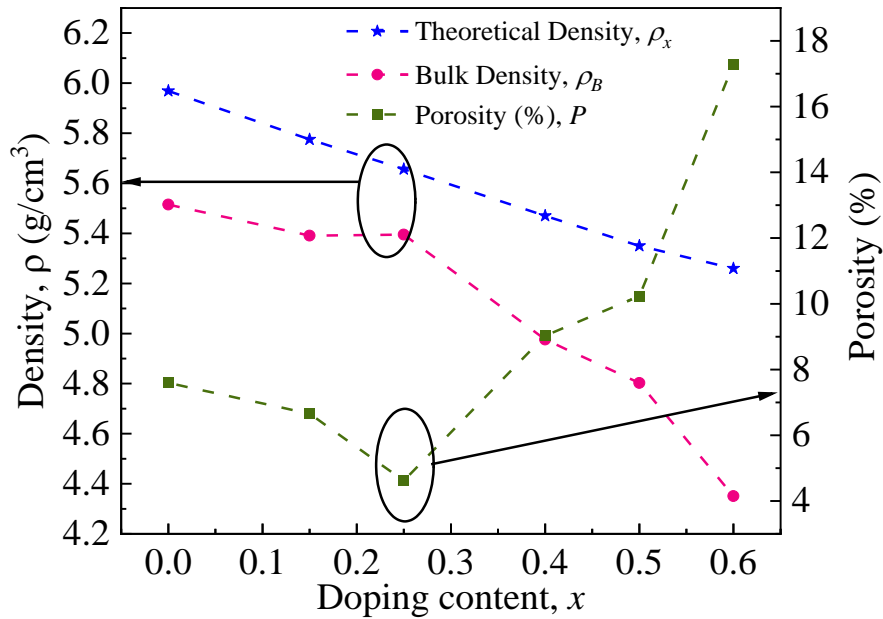
**Fig. 4.22** Determination of crystallite size from (*110*) peaks using the Gaussian fitting method of various  $Ba_{1-x}(Sr_{0.5}Ni_{0.5})_xTiO_3$ .

The crystallite size,  $d$ , and microstrain of the synthesized ceramics were estimated by using Scherrer's formula [97]-

$$d = \frac{0.9\lambda}{\beta \cos\theta}$$

where,  $\lambda$  represents the wavelength of the X-ray and  $\beta$  signifies the full width at half maximum (FWHM) of the reflection of (110) peak in radian, and  $\theta$  denotes the Bragg's angle in degree. If the particle size distribution is narrow and strain-induced effects are minimal, this equation gives the estimated crystallite size. The estimated dimension of the crystallites is between 28 to 36 nm. These results are presented in Table 4.6.

The variation of  $\rho_B$ ,  $\rho_x$ , and  $P(\%)$  with doping content are depicted in Fig. 4.23. The  $\rho_B$  is smaller than  $\rho_x$  for all the samples. This phenomenon is caused by the presence of pores in the specimens that were created and expanded during the sintering process [147]. Doping contents decrease both of the values of  $\rho_B$  and  $\rho_x$ . The value of  $P(\%)$  is lowest for  $x = 0.25$  and highest for  $x = 0.60$ . Density decreases linearly following the sum rule.



**Fig. 4.23** Plot of  $\rho_{th}$ ,  $\rho_B$ , and porosity (%) for various  $Ba_{1-x}(Sr_{0.5}Ni_{0.5})_xTiO_3$ .

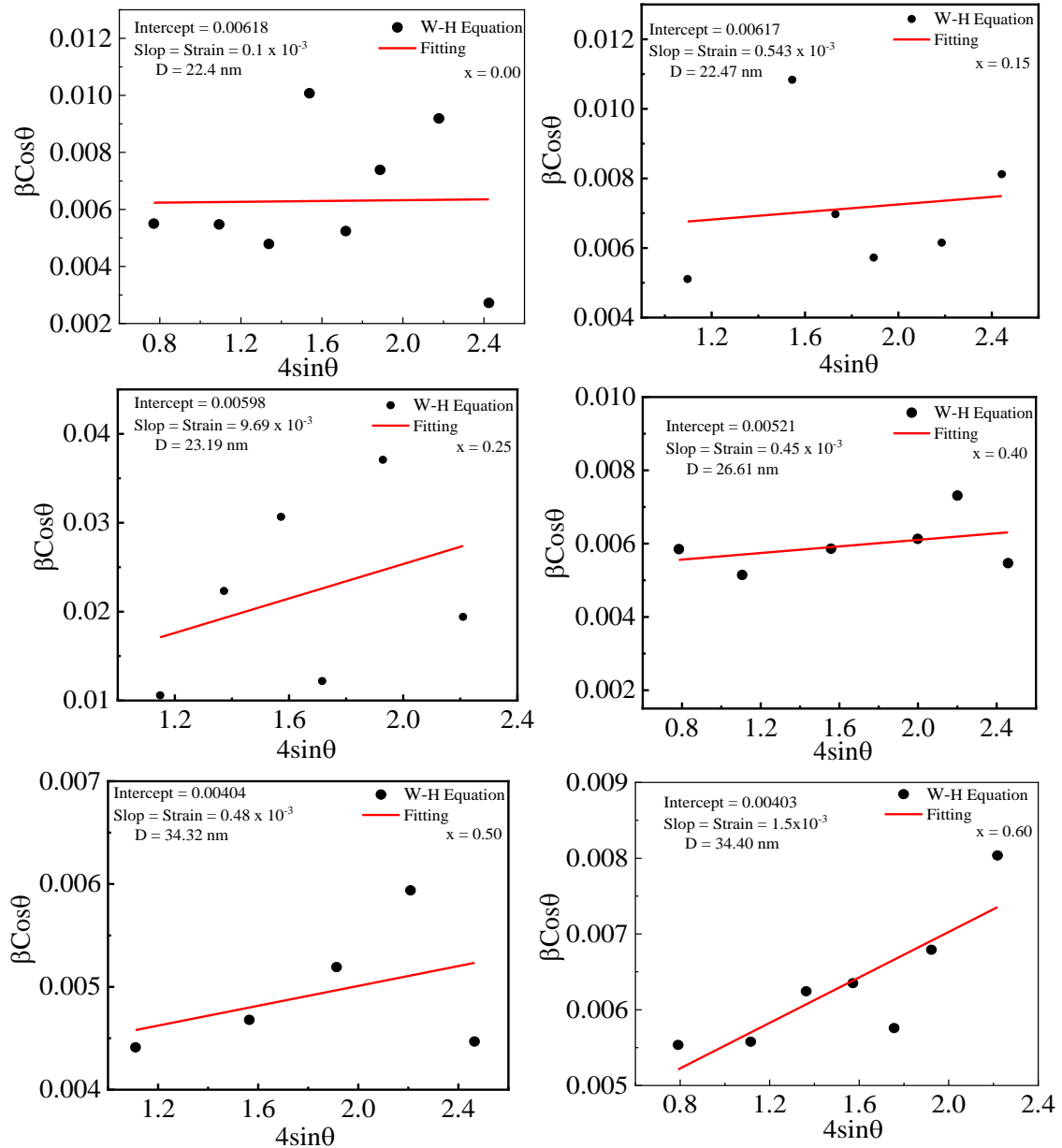
#### 4.2.1.4 Crystallite size and microstrain analysis using the Williamson-Hall method

By evaluating peak width as a function of  $2\theta$ , Williamson and Hall provided a method for calculating size and strain broadening. The strain component can be determined by

plotting the graph of the y-axis versus the x-axis, and the crystallite size component can be determined by the y-intercept using the formula below [148]-

$$\beta_{Total} \cos\theta = \varepsilon 4 \sin\theta + \frac{K\lambda}{D}$$

The method of calculation of crystallite size and microstrain is shown in Fig. 4.24 and tabulated in Table 4.6 to compare with the Scherrer methods.



**Fig. 4.24** Crystallite size and microstrain calculation from W-H method of various  $Ba_{1-x}(Sr_{0.5}Ni_{0.5})_xTiO_3$ .

The Scherrer equation calculates the crystallite size for a single peak. The Williamson-Hall plot approach's underlying equation becomes the Scherrer equation when the internal stress is zero. This means that when a phase has several peaks, it is always preferable to utilize the Williamson-Hall plot approach since peak broadening brought on by stress is

properly taken into account when determining the crystallite size. The compositions in the current investigation have several XRD peaks. Therefore, the crystallite sizes discovered by W-H techniques will be taken into consideration for further analysis.

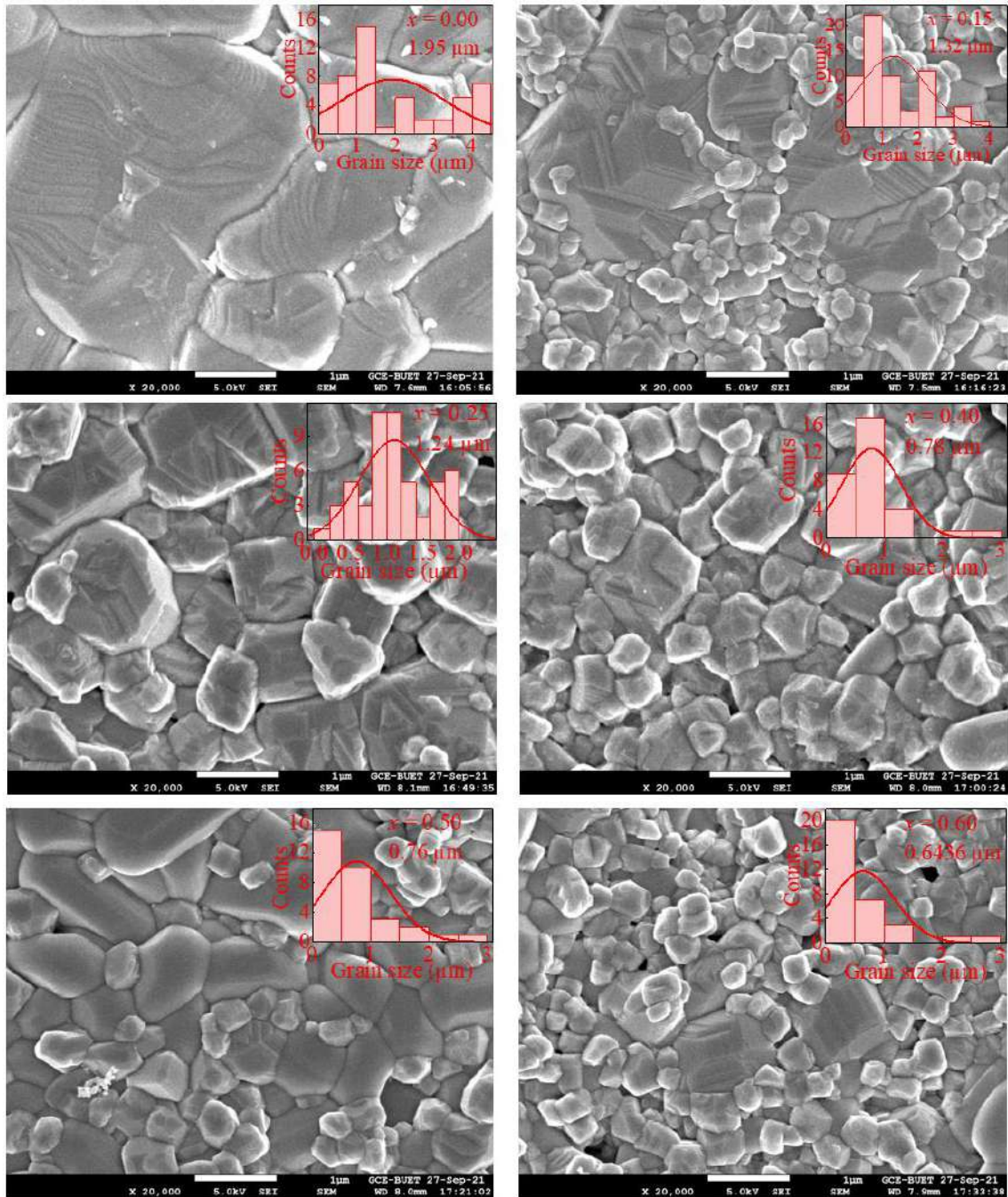
#### 4.2.1.5 Microstructural analysis

The electromagnetic characteristics are largely correlated to the microstructure of a compound. The average grain size,  $\bar{D}$ , has been determined from optical micrograph data. The FESEM image of different  $Ba_{1-x}(Sr_{0.5}Ni_{0.5})_xTiO_3$  ( $x = 0.00$  to  $0.60$ ) sintered at  $1250^\circ C$  are depicted in Fig. 4.25. The  $\bar{D}$  is found reliant on (Sr, Ni) doping. Insets of Fig. 4.25 also display the histogram of  $\bar{D}$ , determined from FESEM images of different  $Ba_{1-x}(Sr_{0.5}Ni_{0.5})_xTiO_3$  by linear intercept method.  $\bar{D}$  appears to decrease with doping content. In the orthorhombic structures ( $x = 0.00, 0.15, 0.25$ ), the crystallites are larger than in the cubic structures ( $x = 0.40, 0.50, 0.60$ ). The phase transformation after  $x = 0.25$  is also seen in this microstructural study. It is well known that  $\bar{D}$  signifies the existence of grain boundaries in the composition. The movement of pores at the grain boundary is hindered by irregular grain growth, which affects the domain wall's involvement in the magnetization process.

**Table 4.6** Calculation of crystallite size and microstrain from (110) peaks using Scherrer's equation, crystallite size and microstrain using W-H method  $\rho_{th}$ ,  $\rho_B$ , porosity (%) and grain size of various  $Ba_{1-x}(Sr_{0.5}Ni_{0.5})_xTiO_3$ .

Sample content, $x$	Scherrer method		W-H method		Theoretical density, $\rho_{th}$ ( $g/cm^3$ )	Bulk density, $\rho_B$ ( $g/cm^3$ )	Porosity, $P$ (%)	Grain size, $\bar{D}$ $\mu m$
	$D$ (nm)	$\epsilon$ ( $10^{-3}$ )	$D$ (nm)	$\epsilon$ ( $10^{-3}$ )				
0.00	28	4.72	22.4	0.07	5.97	5.52	7.60	1.95
0.15	30	4.40	22.47	0.54	5.78	5.39	6.65	1.32
0.25	36	3.69	23.19	9.69	5.66	5.40	4.62	1.24
0.40	30	4.27	26.61	0.45	5.47	4.98	9.03	0.78
0.50	29	4.46	34.32	0.43	5.35	4.80	10.24	0.76
0.60	35	3.75	34.40	1.50	5.26	4.35	17.28	0.64

The initial permeability strongly depends on the  $\bar{D}$ . Grain growth morphology also reflects the discrepancy between the propelling force causing grain boundary motion and the retarding forces produced by pores as well as other impurities.

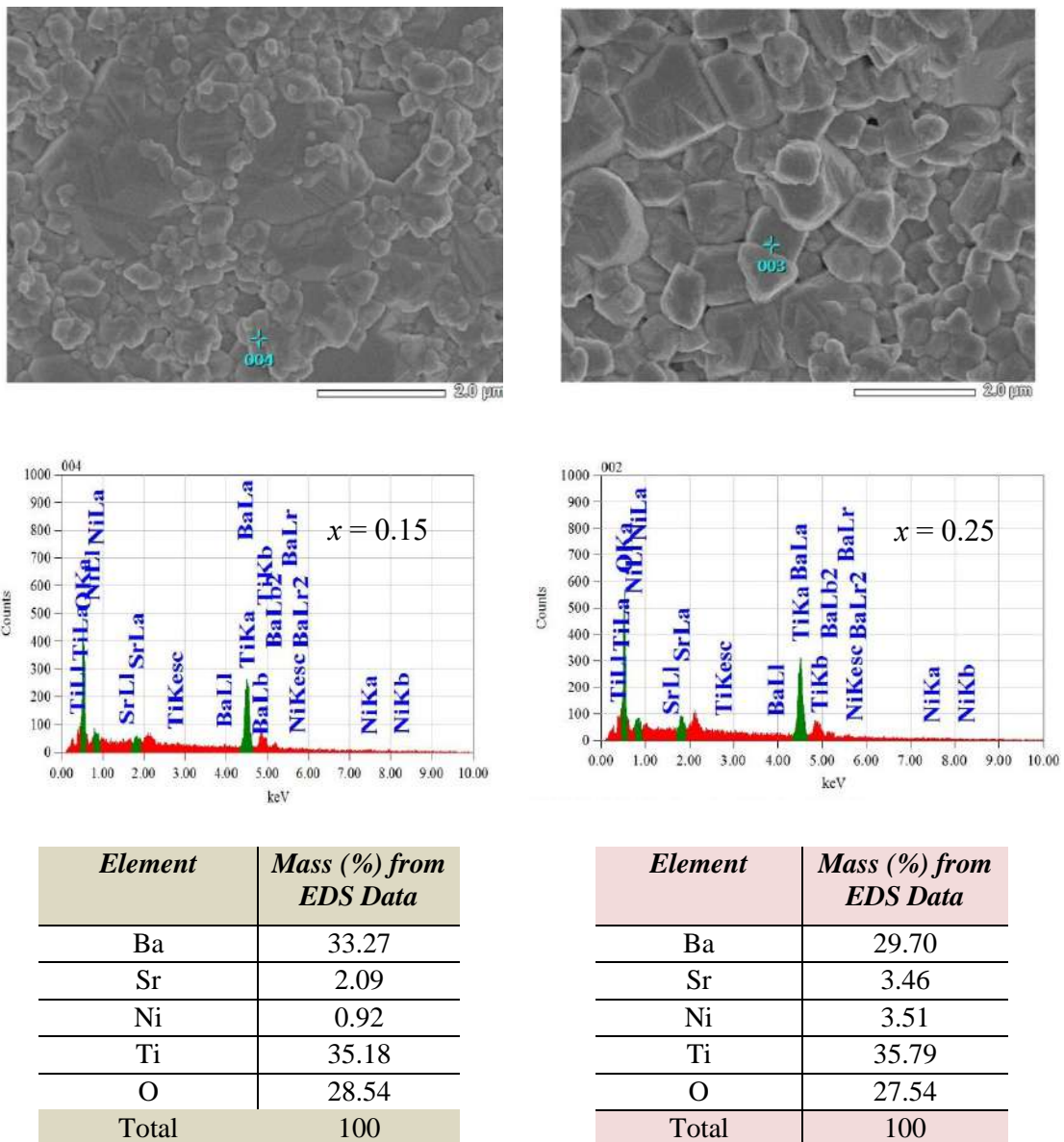


**Fig. 4.25** FESEM images of various  $Ba_{1-x}(Sr_{0.5}Ni_{0.5})_xTiO_3$  and the calculated average grain size using a histogram (in the inset of the corresponding image).



#### 4.2.1.6 Energy dispersive spectroscopy

Different samples of  $Ba_{1-x}(Sr_{0.5}Ni_{0.5})_xTiO_3$  had their surface elemental composition analyzed using EDS. Only the EDS of  $x = 0.15$  and  $0.25$  samples are shown below. EDS spectrums confirm the existence of *Ba*, *Sr*, *Ni*, *Ti*, and *O* elements. At several locations across the sample, EDS spectra were collected in order to produce the quantitative analysis. According to Fig. 4.26, there is a good match between the material stage's *mass %* of the individual amounts. In the accompanying EDS spectra, the percentages of elements contained in the compositions are also shown.



**Fig. 4.26** The EDS spectrum of  $Ba_{1-x}(Sr_{0.5}Ni_{0.5})_xTiO_3$  with (a)  $x = 0.15$ , and (b)  $x = 0.25$ .

## 4.2.2 Electric properties

### 4.2.2.1 Dielectric properties

The complex  $\varepsilon$  of a dielectric substance results from exposure to an alternating electric field. Since there is no energy loss during the transmission of an electric field in a lossless (pure) dielectric, some of the energy associated with a sinusoidal electric field that is propagating through a lossy dielectric medium is transformed to heat. In relation to complex impedance ( $Z^*$ ), the complex dielectric constant ( $\varepsilon^*$ ) is given by [110]-

$$\varepsilon^* = \varepsilon' - j\varepsilon'' = \frac{1}{j\omega C_0 Z^*}$$

Now, putting the value of  $C_0 \left( = \frac{\varepsilon_0 A}{d} \right)$  in the above equation, then the real and imaginary parts can be given by [110]-

$$\varepsilon' = \left[ \frac{tZ''}{A\omega\varepsilon_0(Z'^2 + Z''^2)} \right]$$

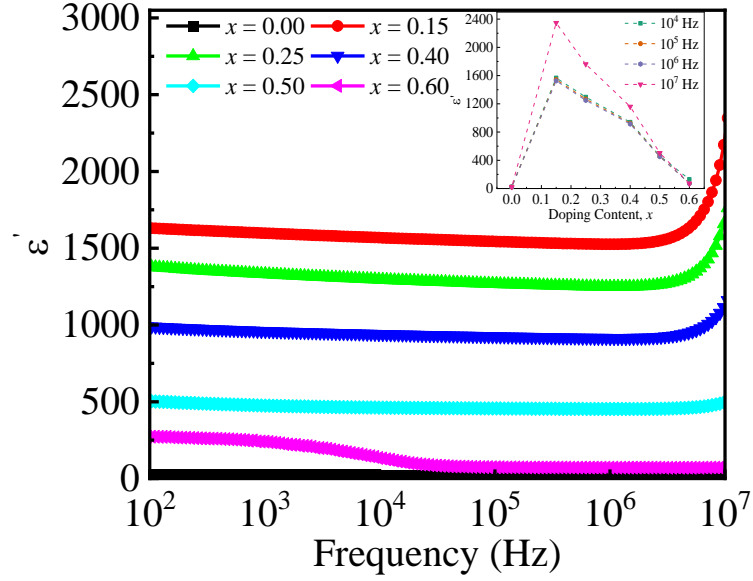
and

$$\varepsilon'' = \left[ \frac{tZ'}{A\omega\varepsilon_0(Z'^2 + Z''^2)} \right]$$

where  $\varepsilon'$  signifies the ability of the material to store the electric energy and  $\varepsilon''$  denotes the loss of the material.

The variation of the dielectric constant,  $\varepsilon'$  with frequency, is depicted in Fig. 4.27. In the frequency range of  $10^2$ - $10^6$  Hz,  $\varepsilon'$  is almost linear for all the samples except for  $x = 60$ .  $\varepsilon'$  of this sample decreases after  $10^4$  Hz. Inset shows the variations of  $\varepsilon'$  at  $10^4$ ,  $10^5$ ,  $10^6$ , and  $10^7$  Hz for different samples. In all the cases,  $x = 0.15$  has the highest  $\varepsilon'$ . After that  $\varepsilon'$  starts to decrease.





**Fig. 4.27** The variation of  $\varepsilon'$  with frequency for  $Ba_{1-x}(Sr_{0.5}Ni_{0.5})_xTiO_3$ .

According to Table 4.7, the dielectric constant increased initially as the doping contents increased before gradually falling. This pattern was similar to the tendency for variation in the relative densities brought on by lesser porosity. The porosity-corrected permittivity ( $\varepsilon'_{PC}$ ) was determined using the formula given below [148] in order to examine the impact of pores on the dielectric constant.

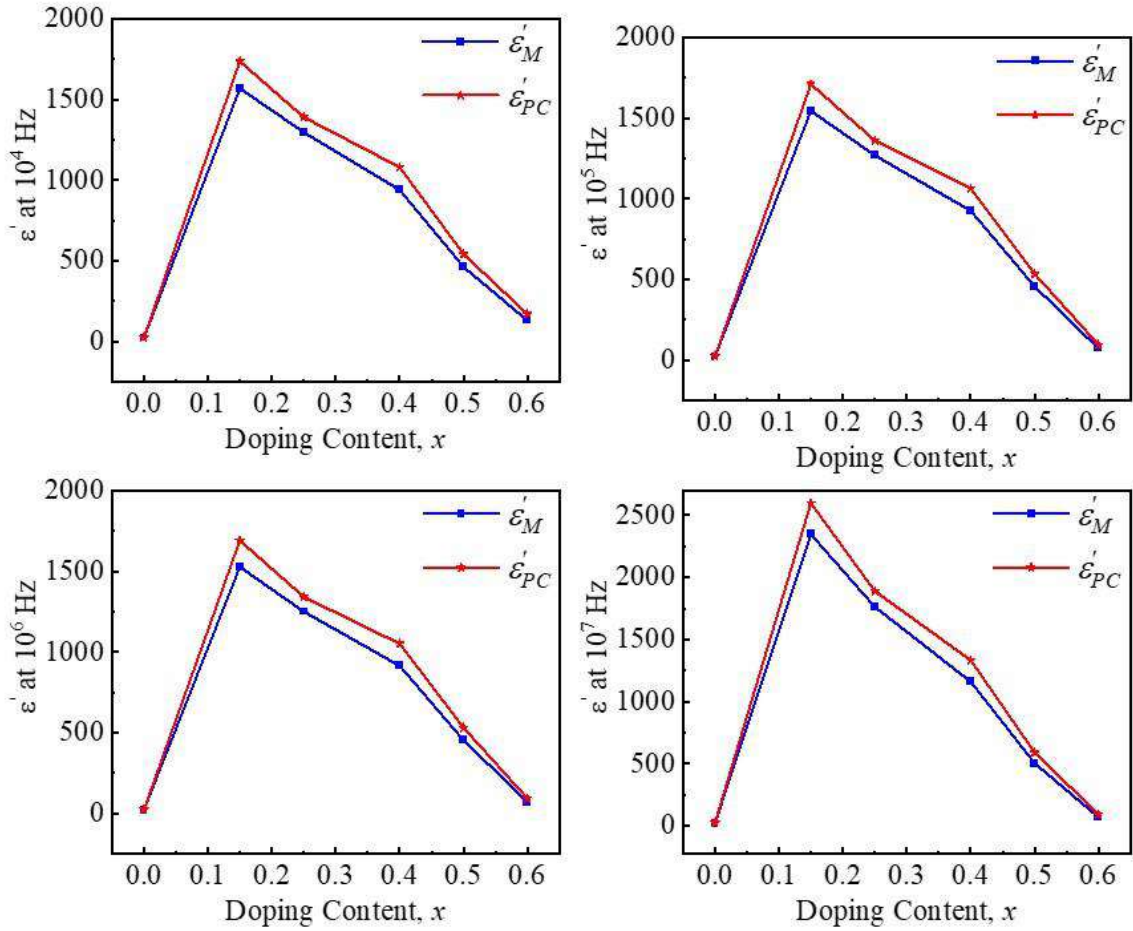
$$\varepsilon'_{PC} = \varepsilon'_M \times \frac{2 + P}{2(1 - P)}$$

where,  $\varepsilon'_M$  represents the estimated dielectric constant at different frequencies and  $P$  is the intragranular porosity of the composition.

**Table 4.7** The relative density (in %) of various  $Ba_{1-x}(Sr_{0.5}Ni_{0.5})_xTiO_3$  and  $\varepsilon'_{PC}$  and  $\varepsilon'_M$  at different frequencies.

$x$	Relative density (%)	$10^4$ Hz		$10^5$ Hz		$10^6$ Hz		$10^7$ Hz	
		$\varepsilon'_M$	$\varepsilon'_{PC}$	$\varepsilon'_M$	$\varepsilon'_{PC}$	$\varepsilon'_M$	$\varepsilon'_{PC}$	$\varepsilon'_M$	$\varepsilon'_{PC}$
0.00	92	24	27	23	26	23	25	23	25
0.15	93	1568	1735	1544	1709	1526	1689	2347	2598
0.25	95	1295	1390	1268	1361	1250	1341	1762	1890
0.40	91	940	1079	925	1063	914	1050	1161	1333
0.50	90	462	541	456	534	453	531	504	590
0.60	83	130	171	73	96	71	93	71	93

In Fig. 4.28, the computed values are presented. The magnitudes of  $\epsilon'_{PC}$  and  $\epsilon'_M$  at different frequencies and also with doping content can be observed from this figure.



**Fig. 4.28** The  $\epsilon'_{PC}$  and  $\epsilon'_M$  at different frequencies for various  $Ba_{1-x}(Sr_{0.5}Ni_{0.5})_xTiO_3$ .

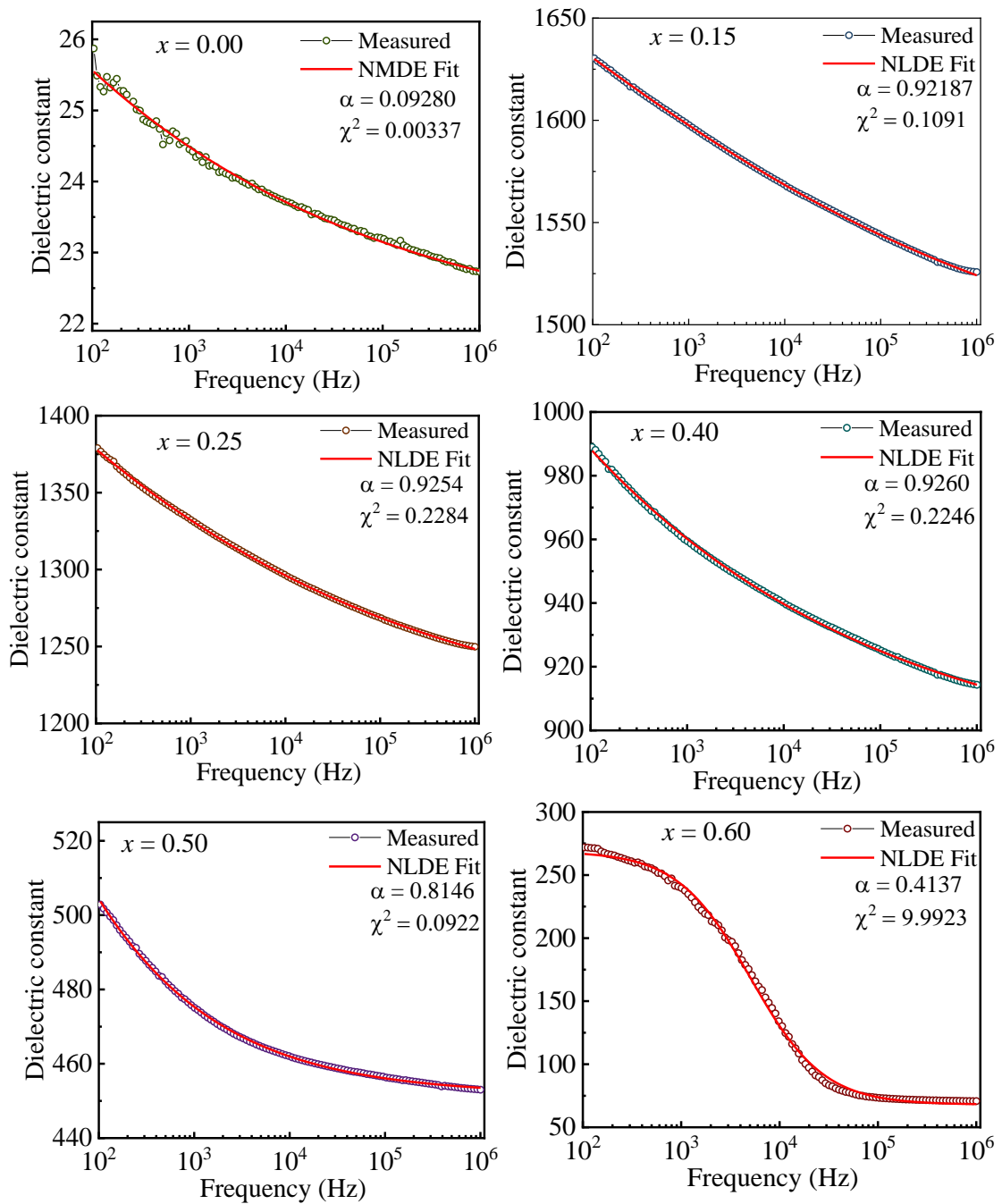
The  $\epsilon'_{PC}$  is dependent on the ionic polarizability [149]. The variation of  $\epsilon'_{PC}$  is quite correlated with the relative density. Additionally, Fig. 4.28 also shows that there are some influences of pores on the dielectric constant for the composition  $x = 0.15$  to  $0.50$ . As pores have less impact on these compositions, grain growth, and microwave dielectric characteristics may be enhanced.

A variety of charged ions of various sizes are present in every compound, and these ions participate in the conduction mechanism of electricity. Due to these, the frequency dispersion characteristic follows the modified Debye equation rather than the ideal Debye equation. The single-pole Debye equation, however, provides a poor representation of dielectric behavior for the majority of materials throughout a broad frequency range.

The single-pole Debye relaxation model was modified to include experimentally obtained Havriliak-Negami relaxation as a solution. Additionally, the equation contains two exponential parameters and is written as [150]-

$$\varepsilon' = \varepsilon_{\infty} + \frac{\varepsilon_0 - \varepsilon_{\infty}}{1 + (\omega\tau)^{2(1-\alpha)}}$$

where  $\varepsilon_0$  and  $\varepsilon_{\infty}$  represent the static permittivity and the infinite-frequency permittivity. In this study,  $\varepsilon_0 = 100\text{Hz}$  and  $\varepsilon_{\infty} = 1\text{MHz}$  are considered.  $\omega$ ,  $\tau$  and  $\alpha$  represent the angular frequency, relaxation time, and spreading parameter with  $0 \leq \alpha \leq 1$ , respectively.



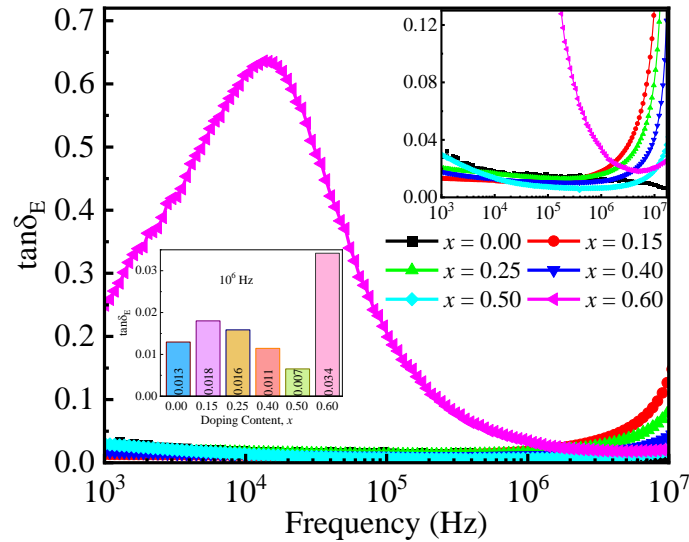
**Fig. 4.29** Frequency dispersion behavior of  $\varepsilon'$  for various  $Ba_{1-x}(Sr_{0.5}Ni_{0.5})_xTiO_3$  fit to the Nonlinear Debye's modified function.

All the fitted data using Non-Linear Modified Debye Equation (NMDE) show an acceptable value of goodness of fit ( $\chi^2$ ) except for  $x = 0.60$ . These data have been shown in Fig. 4.29. Low-frequency zones are home to a variety of phenomena, including space charge, ionic, electronic, and orientation polarization. Large frequency-dependent aids to the dielectric response, particularly at low frequencies, can be explained using Maxwell-Wagner-Sillars polarization which happens on a mesoscopic scale at the inner dielectric boundary layers, or on a macroscopic scale at the exterior electrode-sample contact. The  $\epsilon'$  decreases as frequency increases because all kinds of polarization do not have enough time to show their response at the higher frequency regions. However, electronic polarization induced by the polaron hopping mechanism can sometimes lead to low-frequency dispersion.

#### 4.2.2.2 Dielectric loss factor

The ratio of the  $\epsilon''$  and  $\epsilon'$  is the dielectric loss tangent, or  $\tan\delta_E$ , which is connected to the dielectric relaxation process. A dielectric media experiences two types of loss. Conduction loss is caused by the movement of charge through a substance. On the other hand, energy is lost in a dielectric loss due to the mobility of charges in an oscillating electromagnetic field as polarization alters. Heating results from an interaction between the applied field and the dielectric polarization as the polarization falls behind. Materials with greater dielectric constants frequently have larger  $\tan\delta_E$  values. The variation  $\tan\delta_E$  with the frequency of different  $Ba_{1-x}(Sr_{0.5}Ni_{0.5})_xTiO_3$  are shown in Fig. 4.30.

The  $\tan\delta_E$ , which results in heat generation and energy loss in the dielectric materials, is typically caused by impurities and flaws in the crystal lattice. However, it is sometimes thought to represent  $\epsilon''$ . Fig. 4.30 depicts that the  $\tan\delta_E$  increases up to  $x = 0.15$  then falls up to  $x = 0.50$ , then again rises for the sample  $x = 0.60$ . The attached inset diagram shows the value of  $\tan\delta_E$  at 1 MHz frequency. After 1 MHz frequency, the loss becomes higher for all the samples. For the frequency range,  $10^3$ - $10^6$  Hz, the samples become nearly frequency independent except for  $x = 0.60$ . Almost similar patterns are also seen for  $\epsilon'$  in this frequency range. This can be explained using the concepts of dielectric response and interfacial polarization. Due to the considerable resistance of grain boundaries, more energy is needed for electron exchange, which causes a significant energy loss. As frequency rises in the region, conductive grains become active and the energy required for electron exchange decreases, reducing dielectric loss.



**Fig. 4.30** Frequency dependence of  $\tan\delta_E$  for various  $Ba_{1-x}(Sr_{0.5}Ni_{0.5})_xTiO_3$ .

The loss is estimated to be rather large because, in a low-frequency region, the electron's hopping frequency follows the applied field frequency. The electron hopping frequency, however, is incapable to keep up with the frequency of the applied field as it rises. A wide relaxation peak arises at lower a frequency for the sample of  $x = 0.60$ , indicating the presence of Debye-like relaxation [151-152]. As a result, after a certain critical frequency ( $\omega\tau = 1$ ), the  $\tan\delta_E$  is greatly reduced for the sample  $x = 0.60$ . Electric dipoles tend to align with the electric field when subjected to an externally supplied field. However, the alignment does not occur instantly. It takes some time for the dipoles to align with the field.

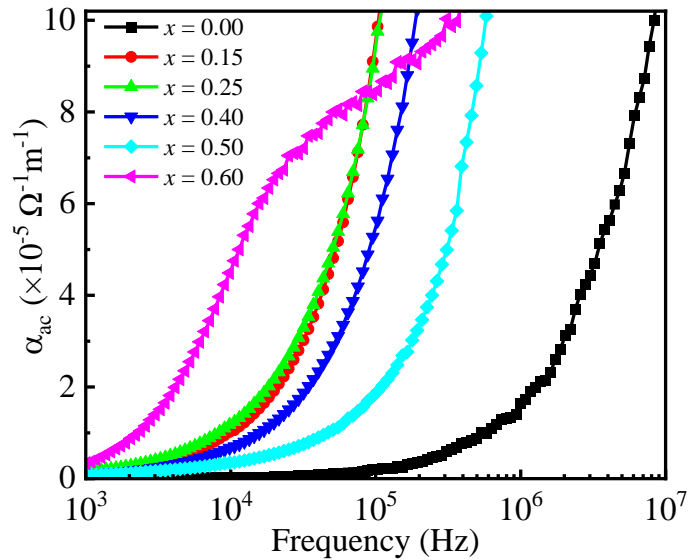
#### 4.2.2.3 The ac-conductivity

Understanding the conduction phenomena in various materials requires knowledge of the ac conductivity parameter  $\sigma_{ac}$ . Total conductivity can be described using Jonscher's power law [153] and can be written as

$$\sigma_{ac}(\omega) = \sigma_0 + A\omega^n$$

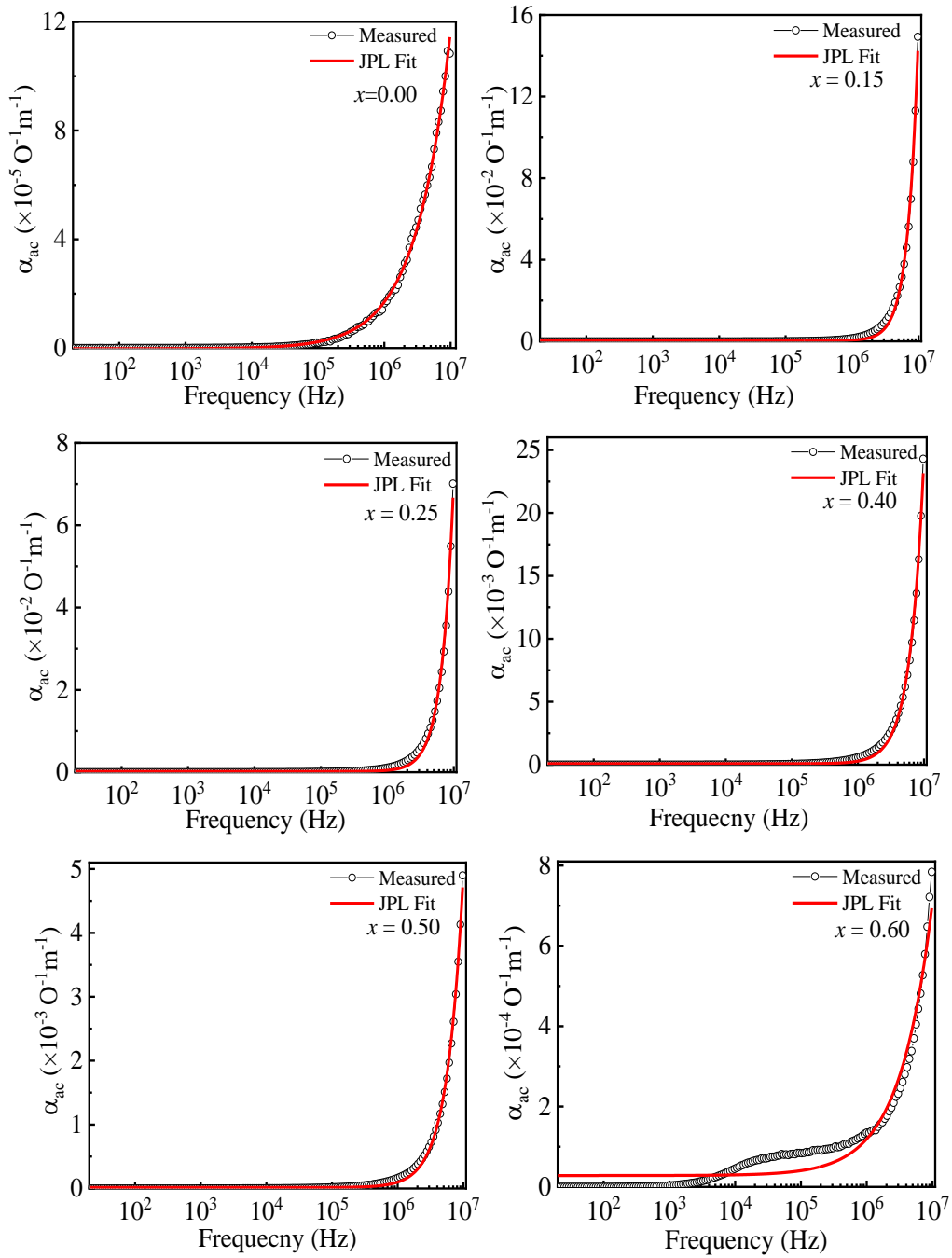
where,  $\sigma_0$  represents the frequency-independent or dc conductivity due to band conduction and is almost steady in the low-frequency region. Here,  $A = \pi N^2 e^2 / 6k_b T$  denotes a temperature-dependent factor, and  $n$  represents the strength of the lattice's interaction with mobile charge carriers, called power law exponent. The  $A\omega^n$  is the frequency-dependent ac conductivity resulting from the hopping concept that exists in the higher frequencies [154-155]. The frequency-dependent  $\sigma_{ac}$  for various  $Ba_{1-x}(Sr_{0.5}Ni_{0.5})_xTiO_3$  has been shown in Fig. 4.31. Up to  $10^3$  Hz, the  $\sigma_{ac}$  is almost

independent of frequency. The Maxwell-Wagner double-layer model [156] can capture the steady nature of  $\sigma_{ac}$  because resistive grain boundaries are more active at lower frequencies. The sample  $x = 0.60$  starts to conduct highly after  $10^3$  Hz. After  $10^5$  Hz, all the samples become very conductive. The hopping process, in which the growth of hopping carriers in the higher frequency zone i.e., hopping region is responsible for boosting conductivity, can thus be used to explain the mounting tendency of the  $\sigma_{ac}$  as the activeness of conductive grains develops at higher frequency regions. Austin and Mott's model also covers the frequency change of  $\sigma_{ac}$  [157]. According to this theory, the rising and falling tendency of ac conductivity is caused by short-range and long-range type polaron hopping [158].



**Fig. 4.31** Frequency dependence of  $\sigma_{ac}$  for various  $Ba_{1-x}(Sr_{0.5}Ni_{0.5})_xTiO_3$ .

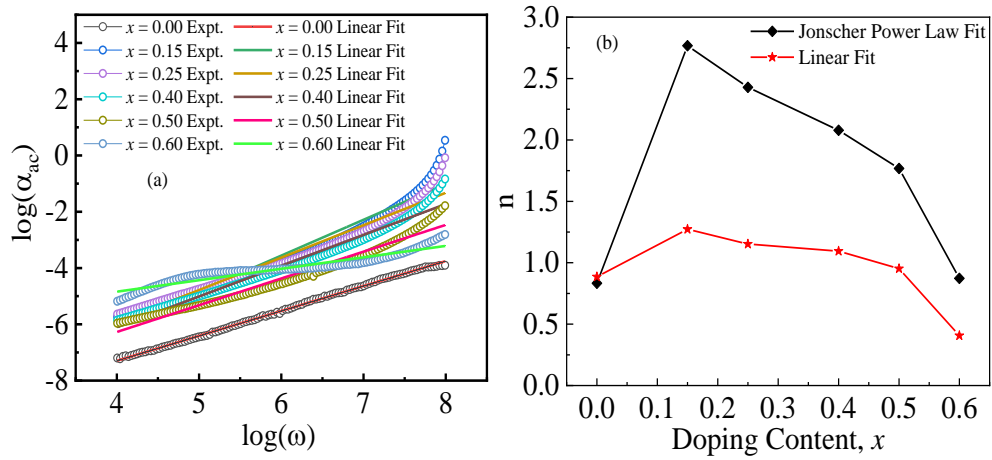
The Jonscher Power Law (JPL) fitted frequency-dependent  $\sigma_{ac}$  for different samples are also shown in Fig. 4.32. Except for the  $x = 0.60$  sample, all the other ones follow the JPL. According to Papathanassiou *et al.*, the frequency exponent is not constrained to values less than one [159].



**Fig. 4.32** Fitted data of frequency dependence of  $\sigma_{ac}$  for various  $Ba_{1-x}(Sr_{0.5}Ni_{0.5})_xTiO_3$  according to Jonscher's power law.

According to Jonscher's power law, the change of  $\log\sigma_{ac}$  with  $\log\omega$  is linear. In some cases, mixed polarons (small/large) conduction is accountable for a small plateau region in  $\sigma_{ac}$ . Variations of  $\log\sigma_{ac}$  with  $\log\omega$  data for these samples are shown in Fig. 4.33 (a). The  $n$  can be calculated from the  $\log\sigma_{ac}$  vs  $\log\omega$  plot which is displayed in Fig. 4.33 (b). The gradient of the slope is the value of  $n$ . According to JPL model, the growing and falling characteristics of  $\sigma_{ac}$  is due to the short-range and long-range type polaron

hopping, respectively [158]. The comparison of  $n$  calculated from JPL fit data and linear fitted data for  $\log\sigma_{ac}$  versus  $\log\omega$  plot are also illustrated in Fig. 4.33 (b).



**Fig. 4.33** (a) Variations of  $\log\sigma_{ac}$  with  $\log\omega$  (both experimental and linear fit) and (b) values of exponent  $n$  calculated from JPL fit and linear fit data for different  $Ba_{1-x}(Sr_{0.5}Ni_{0.5})_xTiO_3$ .

When the  $n < 1$ , the hopping motion combines translational motion with sudden hopping, while  $n > 1$  signifies limited hopping action without the species leaving the neighborhood. This might be explained by the movement of mobile charge carriers via quantum mechanical tunneling between asymmetric double-well potentials [160-161].

#### 4.2.2.4 Complex impedance spectroscopy analysis

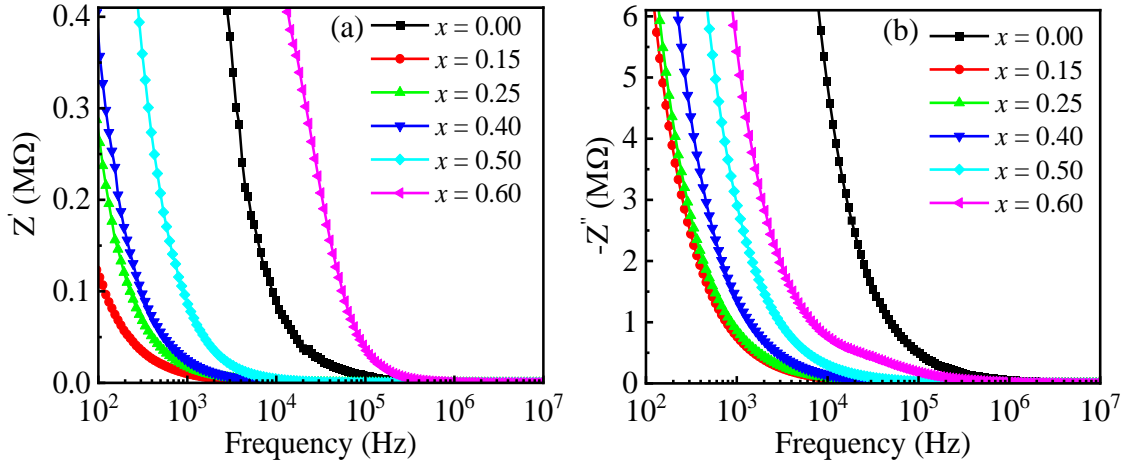
Complex impedance formalisms are used to investigate the characteristics of ceramic grain, grain boundary, and interface. These include measuring relaxation frequency, electronic conductivity, and capacitance at the bulk and grain boundaries. The grain and grain boundary properties of a polycrystalline material with varying time constants often form two sequential semicircles. A material's other important electrical properties can also be expressed in terms of complex impedance  $Z^*$  and electric modulus  $M^*$  [162]. Complex impedance,  $Z^*$ , can be expressed using the Debye model as [110]-

$$Z^* = Z' - jZ''$$

where,  $Z'$  and  $Z''$  signifies the real and imaginary component of impedance, respectively. Fig. 4.34 (a) depicts the values of  $Z'$  decrease gradually as frequency ( $>10^5$  Hz) increases and then it is nearly constant at high frequencies. This phenomenon suggests that the compositions under study become more electrically conductive as frequency rises. The  $x = 0.15$  sample start to conduct from around  $10^3$  Hz and the  $x = 0.60$  sample from around  $10^5$  Hz. As the total polarization appears to be high, then all kinds of polarization



exist at lower frequencies. Because of this, the  $Z'$  appears to be higher in the low-frequency region. The likelihood of a release of space charge and a corresponding decrease in the energy barrier properties increases with decreasing  $Z'$  values [163-165]. The  $Z''$  exhibits almost alike pattern as  $Z'$ . No relaxation peak is observed in Fig. 4.34 (b) that signifies the absence of immobile charges. Faster recombination is observed at a higher frequency as the space charge has less time to relax and thus impedance decreases.



**Fig. 4.34** Frequency dependence of (a)  $Z'$ , and (b)  $Z''$  for various  $Ba_{1-x}(Sr_{0.5}Ni_{0.5})_xTiO_3$ .

#### 4.2.2.5 Electric modulus study

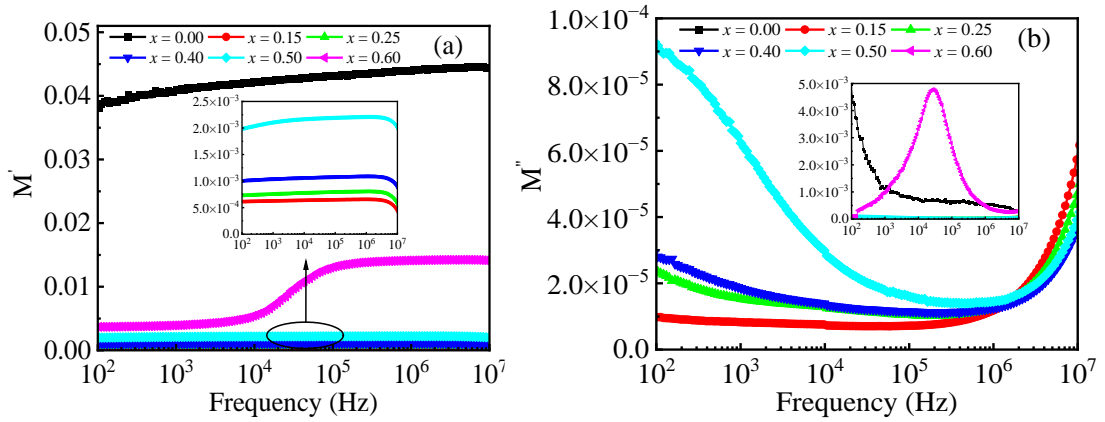
The frequency and temperature dependence of the conductivity of samples has been investigated using the complex electric modulus ( $M^*$ ) analysis [166]. Electric modulus typically refers to the relaxation of the electric field within the compound when the electric movement is persistent [167-169]. The  $M^*$  can be estimated by the following relation [110]-

$$M^*(\omega) = M' + jM''$$

here,  $M'$  ( $= \omega C_o Z''$ ) and  $M''$  ( $= \omega C_o Z'$ ) denote the real and imaginary parts, respectively.

The frequency-dependent  $M'$  spectrum for various  $Ba_{1-x}(Sr_{0.5}Ni_{0.5})_xTiO_3$  is shown in Fig. 4.35 (a). The  $M'$  is almost frequency independent and very low in all the frequency regions (in the inset of Fig. 4.35 (a)) for the samples  $x = 0.15, 0.25, 0.40,$  and  $0.50$ . For the samples,  $x = 0.00$  and  $0.60$ , with the frequency, the  $M'$  dispersion continues to develop. Due to charge carrier mobility over a large distance and the absence of electronic polarization, the lower value of  $M'$  in the low-frequency region causes a significant upsurge in capacitance for these two samples [170]. The inability to restore charge carrier

flow may result from an induced steady electric field. The conduction mechanism, however, can be seen in the way  $M'$  increases with frequency due to the short-range mobility of charge carriers.



**Fig. 4.35** Frequency dependence of (a)  $M'$ , and (b)  $M''$  for different  $Ba_{1-x}(Sr_{0.5}Ni_{0.5})_xTiO_3$ .

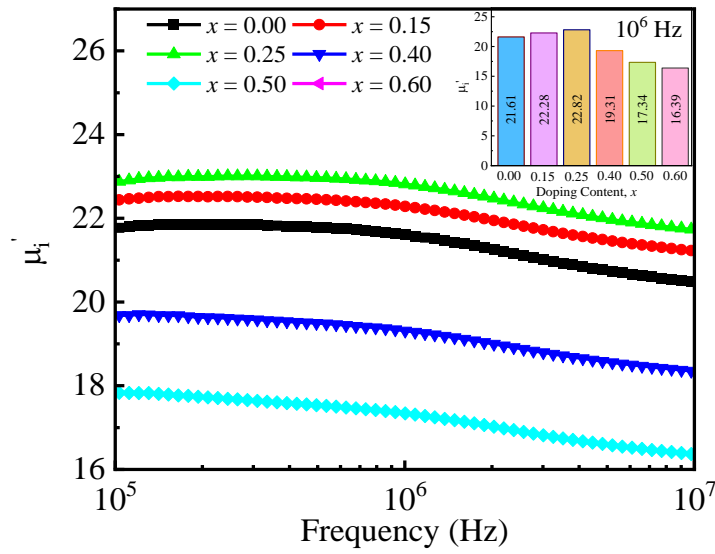
Fig. 4.35 (b) shows the variation of  $M''$  as a function of frequency for various  $Ba_{1-x}(Sr_{0.5}Ni_{0.5})_xTiO_3$ . The  $M''$  is higher in the region of the low-frequency region except for  $x = 0.60$ . This sample has a peak in the midst of this frequency region (in the inset of Fig. 4.35 (b)), called the relaxation peak. The longer relaxation times with various time constants seen in the asymmetric peak expansion support the non-Debye type relaxation. With the increase of frequency, it decreases for other values of  $x$  first, then it again increases except for the sample  $x = 0.00$ . The lack of carriers at potential wells is responsible for these decreases of  $M''$ . The  $x = 0.15$  samples show an almost steady nature up to  $10^6$  Hz.

### 4.2.3 Magnetic properties

#### 4.2.3.1 Initial permeability

The  $\mu_i'$  represents the magnetic energy contained in the system. It also represents the magnetic induction component  $B$  in phase with the alternating magnetic field  $H$ . Fig. 4.36 shows that for all samples,  $\mu_i'$  decreases slightly with the increase of frequency. Both lower and higher frequencies of the pinning points are present. At the surface of the samples, pinning points were produced by intragranular holes and contaminant-filled grains. The rapidly varying magnetic field causes the pinning points to restrict the motion of the domain wall more when the frequency is higher. The composition, stoichiometry,

impurity, average grain size, porosity, coercivity, and other factors influence the  $\mu_i'$  of the samples. This impedes spin motion as well as domain wall movement [171].



**Fig. 4.36** The variation of  $\mu_i'$  with respect to frequency for various  $Ba_{1-x}(Sr_{0.5}Ni_{0.5})_xTiO_3$ .

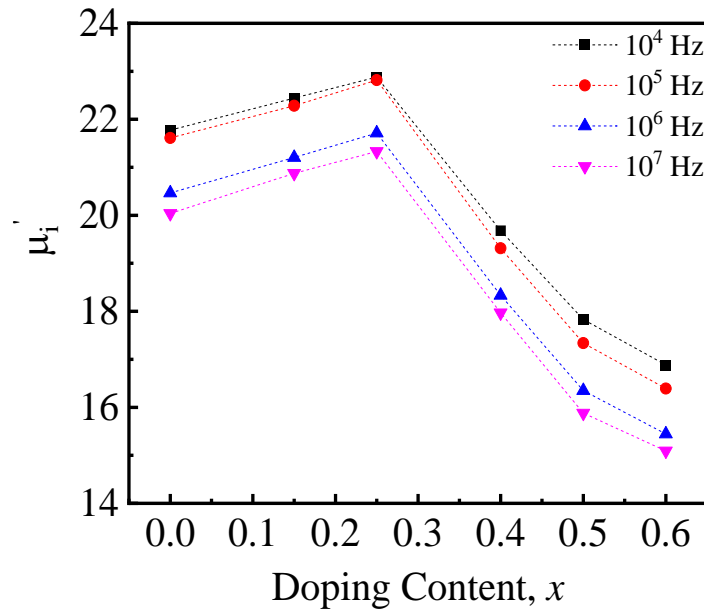
In comparison,  $\mu_i'$  increases from  $x = 0.00$  to  $x = 0.25$  then falls abruptly from  $x = 0.40$  to  $x = 0.60$ . The  $\mu_i'$  maximum value is found for the sample  $x = 0.25$ . In the inset of the Fig. 4.37, the values of  $\mu_i'$  for all the samples at the frequency of 1 MHz are shown. The  $\mu_i'$  is correlated with the average grain and crystallite size. Domain wall motion contributes more to magnetization. This is because domain wall movement requires less energy than domain rotation does. Moving walls contribute more to magnetization as grains become larger. In this case, the correlation of  $\mu_i'$  with the grain size is well observed. When  $(Sr_{0.5}Ni_{0.5})^{2+}$  are substituted,  $\mu_i'$  increases due to an increase in  $\bar{D}$ . The size of  $(Sr_{0.5}Ni_{0.5})^{2+}$  is less than the size of  $Ba^{2+}$  (1.61 Å), this may cause the porosity as well as the decrease of  $\mu_i'$  by accumulating grain boundaries and also preventing grain growth. Thus, it restricts grain boundary mobility. This makes domain rotation and wall motion more difficult, resulting in a drop in  $\mu_i'$

Snoek's law can be applied to these materials as there is an inversely proportional relationship between  $\mu_i'$  and  $f_r$  [172]. The relationship is given by-

$$\mu_i' \propto \frac{1}{f_r}$$

This relationship suggests that the value of  $f_r$  decreases as the value of  $\mu_i'$  increases. Impurities between grain and intra-granular pores operate as pinning sites at higher

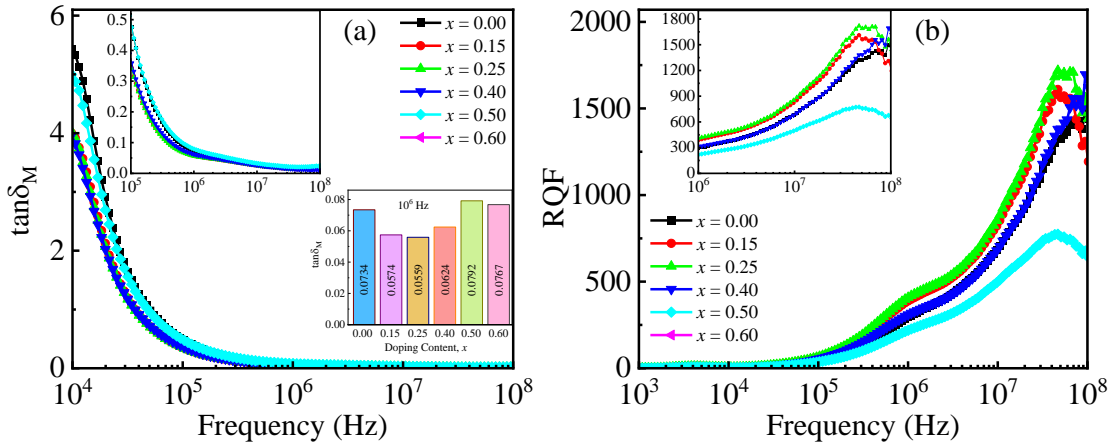
frequencies, thereby inhibiting spin motion and domain wall motion. Fig. 4.37 illustrates that the change of  $\mu_i'$  at four fixed frequencies  $10^5$ ,  $10^6$ ,  $10^7$ , and  $10^8$  Hz exhibits nearly identical variations.



**Fig. 4.37** The variation of  $\mu_i'$  at different frequencies with doping content for various  $Ba_{1-x}(Sr_{0.5}Ni_{0.5})_xTiO_3$ .

#### 4.2.3.2 Magnetic loss-function

The change of  $tand_M$  of the compositions as a function of frequency is depicted in Fig. 4.38 (a). From an application standpoint, it is very desired to maintain this value as low as possible as it serves as a gauge of the magnetic system's inefficiency. The  $tand_M$  is caused by a lag in domain wall motion with an increase in ac magnetic field frequency. It is attributed to a number of flaws, including domain wall nucleation and annihilation, localized flux density variation, non-uniform and irreversible domain wall motion, and domain wall bowing [173]. At lower frequencies, the value of  $tand_M$  is observed to be high, but at a certain frequency, it almost becomes constant for lowering the frequency-dependent domain wall motion. The movement of the domain wall becomes unpredictable and incapable of following the frequency in this frequency zone. The amount of  $(Sr_{0.5}Ni_{0.5})^{2+}$  in the current ceramics causes the  $tand_M$  to drop. The mobility of charge carriers and domain defects diminishes with a rise in  $(Sr_{0.5}Ni_{0.5})^{2+}$  concentration, which causes a reduction in  $tand_M$ . In the inset of Fig. 4.38 (a), the  $tand_M$  for all the compositions is shown. The variation agrees well with the sequence of  $\mu_i'$ .



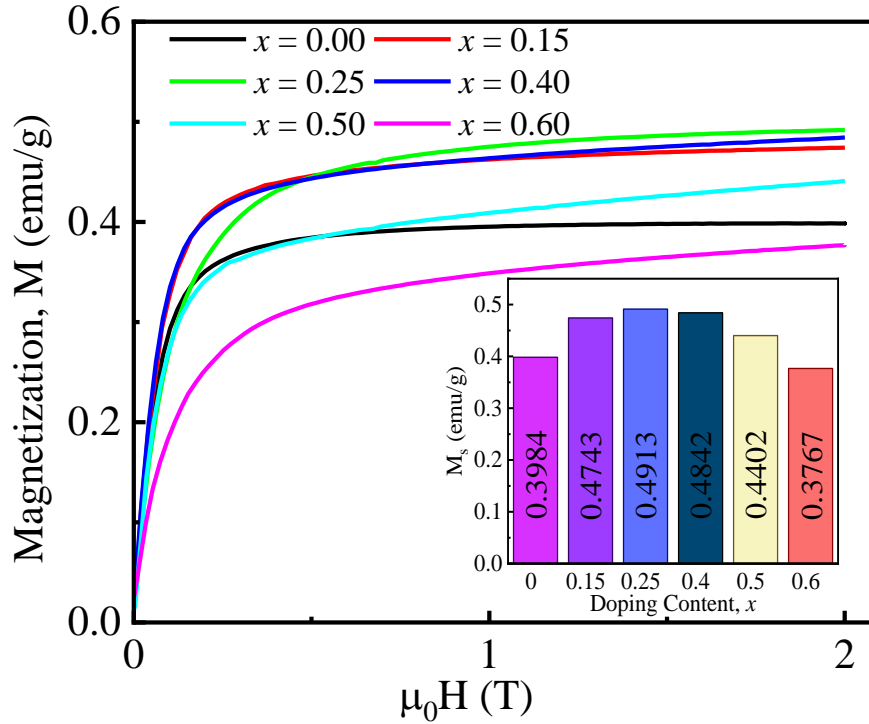
**Fig. 4.38** The variation of (a)  $\tan \delta_M$  and (b)  $RQF$  with frequency for different  $Ba_{1-x}(Sr_{0.5}Ni_{0.5})_xTiO_3$ .

#### 4.2.3.3 Relative Quality Factor

The Relative Quality Factor ( $RQF$ ) is often considered a parameter of material performance in practice. The variation of frequency-dependent  $RQF$  is shown in Fig. 4.38 (b). As the frequency rises, the  $RQF$  rises as well, reaching a peak value before decreasing as the frequency rises again. With increasing doping content, the peak shifts to the lower frequency band. The  $x = 0.25$  has the highest value of  $RQF$  at a higher frequency region. This is a result of the Snoek relationship.

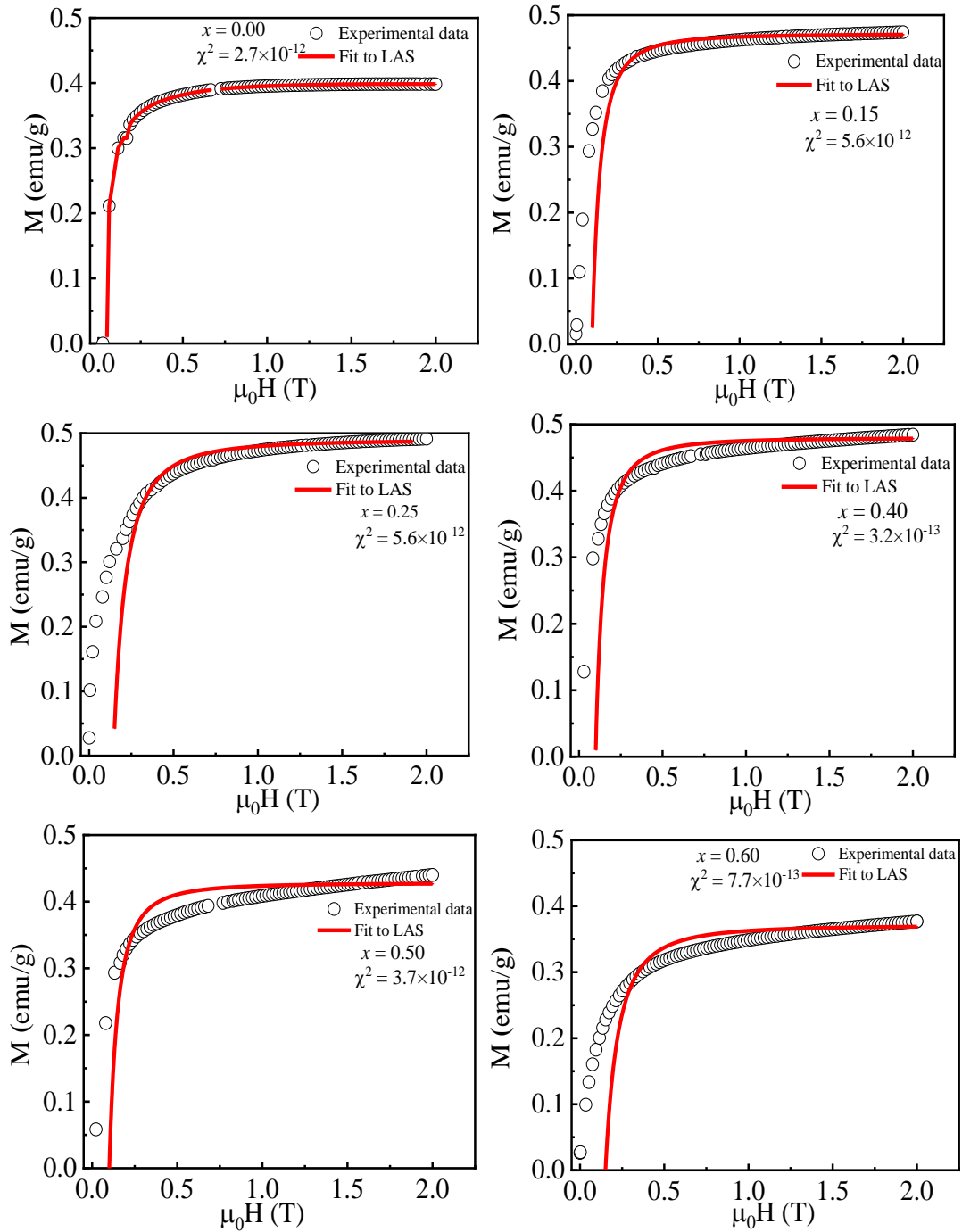
#### 4.2.3.4 Hysteresis plot analysis

An approach that is frequently used to identify the magnetic properties and potential uses of soft magnetic materials is the magnetic hysteresis loop study. Various  $Ba_{1-x}(Sr_{0.5}Ni_{0.5})_xTiO_3$ 's  $M-H$  hysteresis plots are displayed in Fig. 4.39. The magnetization is seen to rise rapidly with magnetic field strength,  $H$ , up to  $0.50 T$ . After that field, it approaches to saturation after  $1.5 T$ . With  $H$  above this field, magnetization nearly remains constant; saturation takes place. Because of this, it is obvious that the samples are in a ferrimagnetic condition at ambient temperature. Nonmagnetic  $Ba^{2+}$  is replaced by  $Ni^{2+}$  (magnetic moment =  $2.8 \mu_B$ ) at  $A$ -sites. As a result, the magnetic moment at  $A$ -sites increases. Net magnetization consequently rises as  $(Sr_{0.5}Ni_{0.5})^{2+}$  concentration is increased. The theoretical research suggested this prediction of  $Ni$ 's participation in  $BTO$ . Saturation Magnetization,  $M_s$  of all samples are also shown in the inset of Fig. 4.39 to visualize the effect of doping.



**Fig. 4.39** M-H hysteresis plot of various  $Ba_{1-x}(Sr_{0.5}Ni_{0.5})_xTiO_3$ .

Magnetization curves may be impacted by modifications to cation distribution, particle size, and chemical composition. The size of the particles is an important factor in the variation of magnetism. With an increase in doping contents starting at  $x = 0.40$ , it was discovered that  $M_s$  values fell. As doping contents continue to increase, the exchange interaction may become less significant. The lack of complete alignment of the spins in large applied fields, or the disordered surface layer, which is present throughout the particle's volume, can be an explanation for the decrease in  $M_s$  [174]. The surface spins are evoked to become disordered or out of alignment by the layer that is disorganized as a result of demagnetization. As a result of this process, the total magnetization of the particles is reduced [175].



**Fig. 4.40** Saturation magnetization as a function of doping content of various  $Ba_{1-x}(Sr_{0.5}Ni_{0.5})_xTiO_3$ .

The magnetocrystalline anisotropy of  $Ba_{1-x}(Sr_{0.5}Ni_{0.5})_xTiO_3$  can be estimated using the law-of-approach-to-saturation (LAS) technique using the following equation [176-177]-

$$M = M_s \left[ 1 - \frac{b}{H^2} \right]$$

where  $b$  represents the anisotropy term.

The anisotropy constant ( $K_1$ ) provides statistics concerning the magnitude of the magnetic anisotropy. Using the value of  $b$  in the above [176-177], the  $K_1$  may be calculated by-

$$b = \frac{8}{105} \frac{K_1^2}{\mu_0 M_s^2}$$

The LAS fit of all the samples is displayed in Fig. 4.44. The data is tabulated in Table 4. Values of  $K_1$  increase with the increases of the doping contents.

The values of  $H_a$  (anisotropy field) can be calculated using the following equation [178] based on  $K_1$  and  $M_s$ .

$$H_a = \frac{2K_1}{M_s}$$

**Table 4.8** Magnetic properties of various  $Ba_{1-x}(Sr_{0.5}Ni_{0.5})_xTiO_3$  compounds calculated from M-H hysteresis plots.

$x$	$M_s$ <i>Experimental data at 2T</i>	$M_s$ <i>Calculated from LAS</i>	$K_1$ <i>Calculated from LAS</i> <i>erg/cm<sup>3</sup></i>	$H_a$ <i>Calculated from LAS</i> <i>(Oe)</i>
0.00	0.398	0.399	1.33	6.67
0.15	0.474	0.472	1.66	7.03
0.25	0.491	0.490	2.55	10.41
0.40	0.484	0.493	4.90	19.88
0.50	0.440	0.448	5.13	22.90
0.60	0.377	0.387	4.94	25.53



## CHAPTER 5

### CONCLUSION

#### 5.1 Summary of the Present Investigation

The present research involves both theoretical and experimental study of structural, electronic, optical, dielectric, and magnetic properties of (*Sr*, *Ni*) co-doped *BaTiO<sub>3</sub>* ceramics. At first DFT based computational investigation has been carried out to analyze and compare nine different cubic perovskite structures having the formula *ABO<sub>3</sub>*, where *A* = *Ca*, *Ba*, *Sr* and *B* = *Ce*, *Ti*, *Zr*. This study involves structural, electronic, optical, mechanical, and thermodynamic properties. Then again theoretical investigations of the effect of *Sr* doping, *Ni* doping, and (*Sr*, *Ni*) co-doping on *BaTiO<sub>3</sub>* have been performed. From the above investigation, a clear influence of doping was observed and also enhanced some of the properties of *BaTiO<sub>3</sub>*. Based on these results experimental investigation of *Sr* and *Ni* co-doping on *BaTiO<sub>3</sub>* have been carried out. The disk- and toroid-shaped samples were made and then they are sintered at different temperatures. Various experiments are carried out, and the findings are meticulously examined, in order to analyze changes in the structural, dielectric, and magnetic characteristics of the studied samples. Following is a summary of the investigation's main findings-

- The first-principles method based on DFT within GGA-PBE exchange-co has been used to study the structural, mechanical, thermodynamic, electronic, and optical properties of *ABO<sub>3</sub>* [*A* = *Ba*, *Ca*, *Sr*; *B* = *Ce*, *Ti*, *Zr*] perovskites. Each material shows different behavior considering different parameters. Several mechanical properties of materials, such as 2D and 3D visualization of Young's modulus, shear modulus, compressibility, Poisson's ratio, phonon dispersion, phonon density of states, different thermodynamic properties, band structure, the electron density of states, the partial density of states, and different optical properties of all the perovskites have been calculated and compared.
- Among *ABO<sub>3</sub>* [*A* = *Ba*, *Ca*, *Sr*; *B* = *Ce*, *Ti*, *Zr*] perovskites, *BaTiO<sub>3</sub>* has the lowest bandgap of 1.725 eV. This material has been chosen for the next theoretical investigation.

- The structural, electronic, and optical properties of pristine  $BaTiO_3$ ,  $Sr$ -doped,  $Ni$ -doped, and  $(Sr, Ni)$  co-doped  $BaTiO_3$  via density functional theory have been studied. In this study, structural properties showed cubic nature for the four materials. Co-doping reduces the lattice constant ( $4.03$  to  $4.01 \text{ \AA}$ ) and structural volume ( $65.67$  to  $64.29 \text{ \AA}^3$ ) as the ionic radius of  $Sr$  and  $Ni$  are smaller than  $Ba$ . A decrease in material density ( $5.90$  to  $5.56 \text{ g/cm}^3$ ) is also observed in co-doped  $BaTiO_3$ . A slight reduction of the bandgap is seen ( $1.719$  to  $1.713 \text{ eV}$ ) in co-doping material than the pristine  $BaTiO_3$ . In the optical properties, the influence of  $Sr$  in co-doping is visible in the high-energy regions. However, in the visible region, the  $Ni$ -doped  $BaTiO_3$  and  $(Sr, Ni)$  co-doped  $BaTiO_3$  have better absorption properties, i.e., the influence of  $Ni$  is clearly visible to the co-doped material.
- Multifunctional  $Ba_{1-x}(Sr_{0.5}Ni_{0.5})_xTiO_3$  ( $x = 0.00, 0.15, 0.25, 0.40, 0.50,$  and  $0.6$ ) ceramics have been successfully synthesized by the standard solid-state reaction technique.
- Rietveld refinement data calculated from XRD patterns confirmed that all the produced samples were found to be crystallized and have perovskite structures. Sample with compositions  $x = 0.00, 0.15,$  and  $0.25$  are found orthorhombic with space group  $P2mm$ , and compositions  $x = 0.40, 0.50,$  and  $0.60$  are cubic in nature with space group  $Pm-3m$ .
- Doping contents decrease both of the values of  $\rho_B$  and  $\rho_x$ .  $P$  is lowest for  $x = 0.25$  and highest for  $x = 0.60$ . Density decreases linearly following the sum rule.
- The Williamson-Hall plot approach shows that the crystallite size increases with doping concentration.
- The values of  $\bar{D}$  decreases with doping content. In the orthorhombic structures ( $x = 0.00, 0.15, 0.25$ ), the grains are larger than in the cubic structures ( $x = 0.40, 0.50, 0.60$ ). The phase transformation after  $x = 0.25$  is also seen in this microstructural study.
- Surface morphology and energy dispersive X-ray spectroscopy studies of the present research confirms the uniform distribution of distinct materials.

- The variation of  $\varepsilon'$  in the frequency range  $10^2$ - $10^6$  Hz is consistent and almost linear for all the samples except for  $x = 0.60$ .  $\varepsilon'$  of this sample decreases after  $10^4$  Hz. At  $10^4$ ,  $10^5$ ,  $10^6$ , and  $10^7$  Hz frequencies,  $x = 0.15$  has the highest value of  $\varepsilon'$ . After that  $\varepsilon'$  starts to decrease. Porosity-corrected data are also found consistent with these values. There are some influences of pores on  $\varepsilon'$  for the composition  $x = 0.15$  to  $0.50$ . The  $\tan\delta_E$  increases up to  $x = 0.15$  then falls up to  $x = 0.50$ , then again upsurges for the sample  $x = 0.60$ .
- For  $\varepsilon'$ , all the fitted data using Non-Linear Modified Debye Equation (NMDE) show an acceptable value of goodness of fit ( $\chi^2$ ) except for the  $x = 0.60$  sample.
- Up to  $10^3$  Hz, the frequency-dependent  $\sigma_{ac}$  data show that all the samples are almost independent of frequency. The sample  $x = 0.60$  starts to conduct highly after that frequency. After  $10^5$  Hz, all the samples become very conductive.
- Except for  $x = 0.60$  sample, all the other ones follow the Jonscher Power Law (JPL) fitted frequency-dependent  $\sigma_{ac}$ . The electrical conductivity in the synthesized samples may indeed be attributed to small polaron hopping.
- The complex impedance spectroscopy analysis confirmed that the  $x = 0.15$  sample started to conduct from around  $10^3$  Hz and the  $x = 0.60$  sample from  $10^5$  Hz. These data also confirm that all types of polarization are present at lower frequencies.
- The  $M'$  is almost frequency independent and very low in all the frequency regions for the samples  $x = 0.15$ ,  $0.25$ ,  $0.40$ , and  $0.50$ . For the samples,  $x = 0.00$  and  $0.60$ , with the frequency, the  $M'$  dispersion continues to grow. Due to charge carrier mobility over a large distance and the absence of electronic polarization, the lower magnitude of  $M'$  in the low-frequency area causes a significant rise in capacitance for these two samples. The  $M''$  is higher in the region of the low-frequency region except for  $x = 0.60$ . This sample has a relaxation peak amid this frequency region. The  $x = 0.15$  samples show an almost steady nature up to  $10^6$  Hz.
- The  $\mu_i'$  rises from  $x = 0.00$  to  $x = 0.25$  then falls abruptly from  $x = 0.40$  to  $x = 0.60$ . The maximum value of  $\mu_i'$  is found for the sample  $x = 0.25$ . The values of  $\mu_i'$  for all the samples at the frequency of  $1$  MHz are correlated with the average grain and particle size relating to domain wall motion which contributes more to

magnetization.  $RQF$  was found to be enhanced in all the samples. On the other hand, the value of  $\tan\delta_M$  was found to be decreased gradually.

- The enhancement of  $M_S$  was found in all the doped samples except for  $x = 0.60$ . Both experimental and law-of-approach-to-saturation (LAS) techniques show that  $x = 0.25$  has the highest value of  $M_S$ . The results obtained between the experimental and the calculated values of  $M_S$  were very close.

## 5.2 Conclusion

Theoretical studies on different  $ABO_3$  perovskites showed that  $BaTiO_3$  has the lowest bandgap. Theoretical investigation also showed a slight reduction of bandgap in  $(Sr, Ni)$  co-doped  $BaTiO_3$ . It is also found that in the visible regions, absorption and refractive index increased in  $Ni$ -doped and  $(Sr, Ni)$  co-doped  $BaTiO_3$ . The synthesized ceramics  $Ba_{0.85}(Sr_{0.5}Ni_{0.5})_{0.15}TiO_3$  increases dielectric constants by 65 times, has higher conductivity after  $10^4$  Hz, and has lower impedance. On the other hand,  $Ba_{0.75}(Sr_{0.5}Ni_{0.5})_{0.25}TiO_3$  sample has the highest value of  $\mu_i'$  (22.82 at 1 MHz) at all frequency regions, the lowest value of  $\tan\delta_M$  and the highest value of  $M_S$  (0.491 emu/g). Thus,  $Ba_{0.85}(Sr_{0.5}Ni_{0.5})_{0.15}TiO_3$  and  $Ba_{0.75}(Sr_{0.5}Ni_{0.5})_{0.25}TiO_3$  samples show dielectric and magnetic responses very well. These types of multifunctional materials are good candidates for dielectric capacitor technology, electromagnetics sensor, spintronics, etc. Additionally, the low cost of the raw elements favors their widespread use with an enormous market potential.

## 5.3 Suggestions for Further Research

The followings are some more researches that could be conducted on various areas for prospective applications of the multifunctional materials under study:

- For a thorough understanding of the domains, transmission electron micrographs (TEM) may be used.
- By using Mössbauer spectroscopy, one can determine the magnetic characteristics and atoms' preferred sites in a constituent.

### **The Novelty of the Present Research**

Experimentally synthesized  $Ba_{0.85}(Sr_{0.5}Ni_{0.5})_{0.15}TiO_3$  and  $Ba_{0.75}(Sr_{0.5}Ni_{0.5})_{0.25}TiO_3$  exhibited good electromagnetic properties confirming their suitability for applications in multifunctional devices.

## References

- [1] Katz, E. A., “Perovskite: Name Puzzle and German-Russian Odyssey of Discovery,” *Helv. Chim. Acta*, vol. 103, e2000061, 2020.
- [2] Goldschmidt, V. M., “Die Gesetze der Krystallochemie,” *Naturwissenschaften*, vol. 14, pp. 477–485, 1926.
- [3] Peña, M. A., and Fierro, J. L. G., “Chemical structures and performance of perovskite oxides,” *Chem. Rev.*, vol. 101, pp. 1981–2017, 2001.
- [4] Filip, M. R., and Giustino, F., “The geometric blueprint of perovskites,” *Proc. Natl. Acad. Sci. U. S. A.*, vol. 115, pp. 5397–5402, 2018.
- [5] Watthage, S. C., Song, Z., Phillips, A. B., and Heben, M. J., “Chapter 3 - Evolution of Perovskite Solar Cells,” *Perovskite Photovoltaics Basic to Adv. Concepts Implement*, pp. 43–88, 2018.
- [6] Stracher, G. B., “Crystallochemical Behavior of Slag Minerals and the Occurrence of Potentially New Mineral Species From Lapanouse-de-Sévérac, France,” in *Coal and Peat Fires: A Global Perspective* (ed. Stracher, G. B.) pp. 243–300, Elsevier, 2019.
- [7] Ellis, C. L. C., Smith, E., Javaid, H., Berns, G., and Venkataraman, D., “Ion Migration in Hybrid Perovskites: Evolving Understanding of a Dynamic Phenomenon,” *Perovskite Photovoltaics Basic to Adv. Concepts Implement.*, Vol. 163–196, 2018.
- [8] Saburi, O., “Properties of Semiconductive Barium Titanates,” *J. Phys. Soc. Jpn.*, vol. 14, pp. 1159-1174, 1959.
- [9] Harman, G. G., “Electrical Properties of BaTiO<sub>3</sub> Containing Samarium,” *Phys. Rev.*, vol. 106, 1358, 1957.
- [10] Jona, F., and Shirane, G. (1993) *Ferroelectric Crystals*. Dover Pubns, Unabridged, Reprint edition, USA.

- [11] Kishi, H., Mizuno, Y., and Chazono, H., “Base-metal Electrode-multilayer Ceramic Capacitors: Past, Present and Future Perspectives,” *Japanese J. Appl. Physics*, vol. 42, no. 1R, pp. 1–5, 2003.
- [12] Huybrechts, B., Ishizaki, K., and Takata, M., “The Positive Temperature Coefficient of Resistivity in Barium Titanate,” *J. Mater. Sci.*, vol. 30, pp. 2463–2474, 1995.
- [13] Jaffe, B., Cook Jr, W. R., and Jaffe, H. (1971) *Piezoelectric Ceramics*. Academic Press, London and New York.
- [14] Wu, T., Qin, Z., Wang, Y. *et al.*, “The Main Progress of Perovskite Solar Cells in 2020–2021,” *Nano-Micro Lett.*, vol. 13, 152, 2021.
- [15] Qin, S., Wu, X., Seifert, F., and Becerro, A. I., “Micro-Raman Study of Perovskites in the  $\text{CaTiO}_3$ – $\text{SrTiO}_3$  System,” *J. Chem. Soc. Dalt. Trans.*, issue 19, pp. 3751–3755, 2002. doi:10.1039/B207228A.
- [16] Acosta, M., Novak, N., Rojas, V. *et al.*, “ $\text{BaTiO}_3$ -based Piezoelectrics: Fundamentals, Current Status, and Perspectives,” *Appl. Phys. Rev.*, vol. 4, 041305, 2017.
- [17] Souza, J. A., and Rino, J. P., “A Molecular Dynamics Study of Structural and Dynamical Correlations of  $\text{CaTiO}_3$ ,” *Acta Mater.*, vol. 59, pp. 1409–1423, 2011.
- [18] Gillet, P., Guyot, F., Price, G. D., Tournier, B., and Le Cleach, A., “Phase Changes and Thermodynamic Properties of  $\text{CaTiO}_3$ . Spectroscopic Data, Vibrational Modelling and Some Insights on The Properties of  $\text{MgSiO}_3$  Perovskite,” *Phys. Chem. Miner.*, vol. 20, pp. 159–170, 1993.
- [19] Redfern, S. A. T., “High-temperature structural phase transitions in perovskite,” *J. Phys. Condens. Matter*, vol. 8, 8267, 1996.
- [20] Li, Y., Niu, S., Wang, J., *et al.*, “Mesoporous  $\text{SrTiO}_3$  Perovskite as a Heterogeneous Catalyst for Biodiesel Production: Experimental and DFT Studies,” *Renew. Energy*, vol. 184, pp. 164–175, 2022.

- [21] Panda, P. K., “Review: Environmental Friendly Lead-Free Piezoelectric Materials,” *J. Mater. Sci.*, vol. 44, pp. 5049–5062, 2009.
- [22] Courtney, D., and Meekin, S. R., “Changes in Blood Lead Levels of Solderers Following the Introduction of the Control of Lead at Work Regulations,” *J. Soc. Occup. Med.*, vol. 35, pp. 128–130, 1985.
- [23] Baldwin, D. R., and Marshall, W. J., “Heavy metal poisoning and its laboratory investigation,” *Ann. Clin. Biochem*, vol. 36, pp. 267–300, 1999.
- [24] Schileo, G., and Grancini, G., “Lead or No Lead? Availability, Toxicity, Sustainability and Environmental Impact of Lead-Free Perovskite Solar Cells,” *J. Mater. Chem. C*, vol. 9, pp. 67–76, 2021.
- [25] Buscaglia, V., and Randall, C. A., “Size and Scaling Effects in Barium Titanate. An Overview,” *J. Eur. Ceram. Soc.*, vol. 40, pp. 3744–3758, 2020.
- [26] Haertling, G. H., “Ferroelectric Ceramics: History and Technology,” *J. Am. Ceram. Soc.*, vol. 82, pp. 797–818, 1999.
- [27] Damjanovic, D., “Ferroelectric, Dielectric and Piezoelectric Properties of Ferroelectric Thin Films and Ceramics,” *Reports Prog. Phys.*, vol. 61, 1267, 1998.
- [28] Yoon, D. H., and Lee, B. I., “Processing of Barium Titanate Tapes with Different Binders for MLCC Applications—Part I: Optimization Using Design of Experiments,” *J. Eur. Ceram. Soc.*, vol. 24, pp. 739–752, 2004.
- [29] Kwon, S. G., Park, B. H., Choi, K., *et al.*, “Solvothermally Synthesized Tetragonal Barium Titanate Powders Using H<sub>2</sub>O/EtOH Solvent,” *J. Eur. Ceram. Soc.*, vol. 26, pp. 1401–1404, 2006.
- [30] Buscaglia, V., Buscaglia, M. T. and Canu, G., “BaTiO<sub>3</sub>-Based Ceramics: Fundamentals, Properties and Applications,” *Encycl. Mater. Tech. Ceram. Glas.*, vol. 3, pp. 311–344, 2021.
- [31] Kay, H. F., “Preparation and Properties of Crystals of Barium Titanate, BaTiO<sub>3</sub>,” *Acta Crystallogr.*, vol. 1, pp. 229–237, 1948.



- [32] Merz, W. J., “The Electric and Optical Behavior of BaTiO<sub>3</sub> Single-Domain Crystals,” *Phys. Rev.*, vol. 76, pp. 1221–1225, 1949.
- [33] Liu, Y., Wei, J., Yan, X., *et al.*, “Barium Charge Transferred Doped Carbon Dots with Ultra-High Quantum Yield Photoluminescence of 99.6% and Applications,” *Chinese Chem. Lett.*, vol. 32, pp. 861–865, 2021.
- [34] Beitollahi, A., and Mortazavi, S. A., “Effect of the Level of Addition of Nb<sub>2</sub>O<sub>5</sub>/Co<sub>2</sub>O<sub>3</sub> and Ba(Nb<sub>2/3</sub>Co<sub>1/3</sub>)O<sub>3</sub> on The Structure, Microstructure, and Dielectric Properties of BaTiO<sub>3</sub>,” *J. Mater. Sci. Mater. Electron.*, vol. 14, pp. 129–134, 2003.
- [35] Jayanthi, S., and Kutty, T. R. N., “Extended Phase Homogeneity and Electrical Properties of Barium Calcium Titanate Prepared by the Wet Chemical Methods,” *Mater. Sci. Eng. B*, vol. 110, pp. 202–212, 2004.
- [36] Shvartsman, V. V., Kleemann, W., Dec, J., Xu, Z. K., and Lu, S. G., “Diffuse Phase Transition in BaTi<sub>1-x</sub>Sn<sub>x</sub>O<sub>3</sub> Ceramics: An Intermediate State Between Ferroelectric and Relaxor Behavior,” *J. Appl. Phys.*, vol. 99, 124111, 2006.
- [37] Cui, B., Yu, P., Tian, J., and Chang, Z., “Preparation and Characterization of Co-doped BaTiO<sub>3</sub> Nanosized Powders and Ceramics,” *Mater. Sci. Eng. B*, vol. 133, pp. 205–208, 2006.
- [38] Rout, S. K., Sinha, E., and Panigrahi, S., “Dielectric Properties and Diffuse Phase Transition in Ba<sub>1-x</sub>Mg<sub>x</sub>Ti<sub>0.6</sub>Zr<sub>0.4</sub>O<sub>3</sub> Solid Solutions,” *Mater. Chem. Phys.*, vol. 101, pp. 428–432, 2007.
- [39] Becker, J. A., Green, C. B., and Pearson, G. L., “Properties and Uses of Thermistors—Thermally Sensitive Resistors,” *Bell Syst. Tech. J.*, vol. 26, pp. 170–212, 1947.
- [40] Tomar, R., Pandey, R., Singh, N. B., Gupta, M. K., and Gupta, P. “Electrical Properties of Barium Titanate in Presence of Sn<sup>2+</sup> dopant,” *SN Appl. Sci.*, vol. 2, 226, 2020.

- [41] Mrooz, O., Kovalski, A., Pogorzelska, *et al.*, “Thermoelectrical Degradation Processes in NTC Thermistors for In-rush Current Protection of Electronic Circuits,” *Microelectron. Reliab.*, vol. 41, pp. 773–777, 2001.
- [42] Fritsch, S., Sarrias, J., Brieu, M., *et al.*, “Correlation Between the Structure, the Microstructure and the Electrical Properties of Nickel Manganite Negative Temperature Coefficient (NTC) Thermistors,” *Solid State Ion.*, vol. 109, pp. 229–237, 1998.
- [43] Makovec, D., Samardžija, Z., and Drogenik, M., “Solid Solubility of Holmium, Yttrium, and Dysprosium in BaTiO<sub>3</sub>,” *J. Am. Ceram. Soc.*, vol. 87, pp. 1324–1329, 2004.
- [44] Bouwma, J., de Vries, K. J., and Burggraaf, A. J., “Non-stoichiometry, Defect Structure, and Dielectric Relaxation in Lanthana-Substituted SrTiO<sub>3</sub>,” *Phys. status solidi*, vol. 35, pp. 281–290, 1976.
- [45] Kumar, P. M., and Rao, K. S., “Influence of Alkali-Rare Earth Ions on The Synthesis Dielectric and Ferroelectric Properties of BaTiO<sub>3</sub> Ceramics,” *Ferroelectr.*, vol. 94, pp. 299–303, 2011.
- [46] Maier, J., Schwitzgebel, G. and Hagemann, H. J., “Electrochemical Investigations of Conductivity and Chemical Diffusion in Pure and Doped Cubic SrTiO<sub>3</sub> and BaTiO<sub>3</sub>,” *J. Solid State Chem.*, vol. 58, pp. 1–13, 1985.
- [47] Uematsu, K., Sakurai, O., Mizutani, N., and Kato, M., “Electrical Properties of La-doped SrTiO<sub>3</sub> (La: 0.1 to 2.0 at %) Single Crystals Grown by Xenon-arc Image Floating Zone Method,” *J. Mater. Sci.*, vol. 19, pp. 3671–3679, 1984.
- [48] Johnson, D. W., Cross, L. E., and Hummel, F. A. “Dielectric Relaxation in Strontium Titanates Containing Rare-Earth Ions,” *J. Appl. Phys.*, vol. 41, 2828, 2003.
- [49] Zheng, R. K., Wang, J., Wang, X. G., *et al.*, “Effects of Ca Doping on the Curie Temperature, Structural, Dielectric, and Elastic Properties of Ba<sub>0.4</sub>Sr<sub>0.6-x</sub>Ca<sub>x</sub>TiO<sub>3</sub> (0 ≤ x ≤ 0.3) Perovskites,” *J. Appl. Phys.*, vol. 98, 084108, 2005.

- [50] Qi, J. Q., Chen, W. P., Wang, Y., Chan, H. L. W., and Li, L. T., “Dielectric Properties of Barium Titanate Ceramics Doped by B<sub>2</sub>O<sub>3</sub> Vapor,” *J. Appl. Phys.*, vol. 96, 6937, 2004.
- [51] Tian, H. Y., Wang, Y., Miao, J., Chan, H. L. W., and Choy, C. L. “Preparation and Characterization of Hafnium Doped Barium Titanate Ceramics,” *J. Alloys Compd.*, vol. 431, pp. 197–202, 2007.
- [52] Wegmann, M., Brönnimann, R., Clemens, F., and Graule, T., “Barium Titanate-based PTCR Thermistor Fibers: Processing and Properties,” *Sensors Actuators A Phys.*, vol. 135, pp. 394–404, 2007.
- [53] Murakami, T., Miyashita, T., Nakahara, M., and Sekine, E. “Effect of Rare-Earth Ions on Electrical Conductivity of BaTiO<sub>3</sub> Ceramics,” *J. Am. Ceram. Soc.*, vol. 56, pp. 294–297, 1973.
- [54] Wernicke, R., “The Influence of Kinetic Processes on the Electrical Conductivity of Donor-Doped BaTiO<sub>3</sub> Ceramics,” *Phys. status solidi*, vol. 47, pp. 139–144, 1978.
- [55] Saburi, O., “Semiconducting Bodies in the Family of Barium Titanates,” *J. Am. Ceram. Soc.*, vol. 44, pp. 54–63, 1961.
- [56] Kim, J. G., Cho, W. S. and Park, K., “PTCR Characteristics in Porous (Ba,Sr)TiO<sub>3</sub> Ceramics Produced by Adding Partially Oxidized Ti Powders,” *Mater. Sci. Eng. B*, vol. 77, pp. 255–260, 2000.
- [57] Nasrallah, M. M., Anderson, H. U., Agarwal, A. K., and Flandermeyer, B. F. “Oxygen Activity Dependence of the Defect Structure of La-Doped BaTiO<sub>3</sub>,” *J. Mater. Sci.* vol. 19, pp. 3159–3165, 1984.
- [58] Katiyar, R. K. Sharma, Y., Misra P., *et al.*, “Studies of the Switchable Photovoltaic Effect in Co-Substituted BiFeO<sub>3</sub> Thin Films,” *Appl. Phys. Lett.*, vol. 105, 172904, 2014.

- [59] Kumari, S., Ortega, N., Kumar, A., Scott, J. F., and Katiyar, R. S., “Ferroelectric and Photovoltaic Properties of Transition Metal Doped  $\text{Pb}(\text{Zr}_{0.14}\text{Ti}_{0.56}\text{Ni}_{0.30})\text{O}_{3-\delta}$  Thin Films,” *AIP Adv.*, vol. 4, 037101, 2014.
- [60] Phuyal, D., Mukherjee, S., Jana, S., *et al.*, “Ferroelectric Properties of  $\text{BaTiO}_3$  Thin Films Co-doped with Mn and Nb,” *AIP Adv.*, vol. 9, 095207, 2019.
- [61] Khushbu, Kumar, P., and Kumar, V., “Effect of Co-substitution of  $\text{Sm}^{3+}$  and  $\text{Fe}^{3+}$  Ions on Structural and Dielectric Properties of  $\text{BaTiO}_3$  Ceramics,” *J. Alloys Compd.*, vol. 731, pp. 760–765, 2018.
- [62] Buscaglia, M. T., Viviani, M., Buscaglia, V., Bottino, C., and Nanni, P., “Incorporation of  $\text{Er}^{3+}$  Into  $\text{BaTiO}_3$ ,” *J. Am. Ceram. Soc.*, vol. 85, pp. 1569–1575, 2002.
- [63] Drdlik, D., Marak, V., Maca, K., and Drdlikova, K. “Modification of Barium Titanate Sintering Via Rare Earth Oxides Addition: Dilatometric and Microstructural Study,” *Ceram. Int.*, vol. 48, pp. 24599–24608, 2022.
- [64] Bobade, S. M., Gopalan, P., and Choi, D. K., “Dielectric Properties of  $\text{La}^{3+}$  at A Site and  $\text{Al}^{3+}$  and  $\text{Ga}^{3+}$  Doped at B Site in  $\text{BaTiO}_3$ ,” *Jpn. J. Appl. Phys.*, vol. 48, 041402, 2009.
- [65] Ioachim, A., Toacsan, M. I., Banciu, M. G., *et al.*, “Barium Strontium Titanate-Based Perovskite Materials for Microwave Applications,” *Prog. Solid State Chem.*, vol. 35, pp. 513–520, 2007.
- [66] Shahid, M., Anwar, A., Malik, F., *et al.*, “Effect of Sr-Doping on Ferroelectric and Dielectric Properties of Sol-Gel Synthesized  $\text{BaTiO}_3$  Thin Films,” *Dig. J. Nanomater. Biostructures*, vol. 12, No. 3, pp. 669-677, 2017.
- [67] Cheng, X., and Shen, M., “Enhanced Spontaneous Polarization in Sr and Ca Co-Doped  $\text{BaTiO}_3$  Ceramics,” *Solid State Commun.*, vol. 141, pp. 587–590, 2007.
- [68] Coey, J. M. D., Venkatesan, M., and Fitzgerald, C. B., “Donor Impurity Band Exchange in Dilute Ferromagnetic Oxides,” *Nat. Mater.*, vol. 4, pp. 173–179, 2005.

- [69] Xin, C., Wang, Y., Sui, Y., *et al.*, “Electronic, Magnetic and Multiferroic Properties of Magnetoelectric NiTiO<sub>3</sub>,” *J. Alloys Compd.*, vol. 613, pp. 401–406, 2014.
- [70] Kumar, B. S., Shanmugaraj, A. M., Kalpathy, S. K., and Anandhan, S. “Some New Observations on The Structural and Phase Evolution of Nickel Titanate Nanofibers,” *Ceram. Int.*, vol. 43, pp. 6845–6857, 2017.
- [71] Li, M. W., Yuan, J. P., Gao, X. M., Liang, E. Q., and Wang, C. Y., “Structure and Optical Absorption Properties of NiTiO<sub>3</sub> nanocrystallites,” *Appl. Phys. A Mater. Sci. Process.*, vol. 122, pp. 1–7, 2016.
- [72] Vijayalakshmi, R., and Rajendran, V., “Effect of Reaction Temperature on Size and Optical Properties of NiTiO<sub>3</sub> Nanoparticles,” *J. Chem.*, vol. 9, 607289, 2012.
- [73] Lakshmi, M., Roy, A. S. Khasim, S. *et al.*, “Dielectric Property of NiTiO<sub>3</sub> Doped Substituted Ortho-chloropolyaniline Composites,” *AIP Adv.*, vol. 3, 112113, 2013.
- [74] Li, T., Wang, C. C., Lei, C. M., *et al.*, “Conductivity Relaxation in NiTiO<sub>3</sub> at High Temperatures,” *Curr. Appl. Phys.*, vol. 13, pp. 1728–1731, 2013.
- [75] Qu, Y. Zhou, W., Ren, Z., *et al.*, “Facile Preparation of Porous NiTiO<sub>3</sub> Nanorods with Enhanced Visible-Light-Driven Photocatalytic Performance,” *J. Mater. Chem.*, vol. 22, pp. 16471–16476, 2012.
- [76] Zhao, G. Y., Zhang, Y., Jiang, L., and Zhang, H. M., “NiTiO<sub>3</sub>/Ag<sub>3</sub>PO<sub>4</sub> Composites with Improved Photocatalytic Activity Under Visible-Light Irradiation,” *Ceram. Int.*, vol. 43, pp. 3314–3318, 2017.
- [77] Hosseini, S. A., “Investigation of The Structural, Photocatalytic and Magnetic Properties of MgAl<sub>2</sub>O<sub>4</sub>/NiTiO<sub>3</sub> Nanocomposite Synthesized Via Sol–Gel Method,” *J. Mater. Sci. Mater. Electron.*, vol. 28, pp. 10765–10771, 2017.
- [78] Tursun, R., Su, Y. C., Yu, Q. S., *et al.*, “Effect of Doping on The Structural, Magnetic, and Ferroelectric Properties of Ni<sub>1-x</sub>A<sub>x</sub>TiO<sub>3</sub> (A = Mn, Fe, Co, Cu, Zn; x = 0, 0.05, and 0.1),” *J. Alloys Compd.*, vol. 773, pp. 288–298, 2019.

- [79] Langhammer, H. T., Muller, T., Walther, T. *et al.*, “Ferromagnetic Properties of Barium Titanate Ceramics Doped with Cobalt, Iron, And Nickel,” *J. Mater. Sci.*, vol. 51, pp. 10429–10441, 2016.
- [80] Pal, S., Swain, A. B., Biswas, P. P. *et al.*, “Giant Photovoltaic Response in Band Engineered Ferroelectric Perovskite,” *Sci. Rep.*, vol. 81, 8005, 2018.
- [81] Rawat, M. and Yadav, K. L., “Compositional Effects on Structural, Dielectric, Ferroelectric and Transport Properties of  $\text{Ba}_{1-x}(\text{Bi}_{0.5}\text{Li}_{0.5})_x\text{TiO}_3$  Ceramics,” *Mater. Chem. Phys.*, vol. 148, pp. 655–663, 2014.
- [82] Shirane, G., Danner, H. R., and Pepinsky, R., “Neutron Diffraction Study of Orthorhombic  $\text{BaTiO}_3$ ,” *Phys. Rev.*, vol. 105, 856, 1957.
- [83] Zeng, L., and Jiang, Y., “X-Ray Diffraction Study of Orthorhombic Barium Titanate,” *J. Beijing Univ. Technol.*, vol. 17, 1991.
- [84] Ram, S., Jana, A., and Kundu, T. K., “Ferroelectric  $\text{BaTiO}_3$  Phase of Orthorhombic Crystal Structure Contained in Nanoparticles,” *J. Appl. Phys.*, vol. 102, 054107, 2007.
- [85] Jana, A., and Kundu, T. K., “Microstructure and Dielectric Characteristics of Ni Ion Doped  $\text{BaTiO}_3$  Nanoparticles,” *Mater. Lett.*, vol. 61, pp. 1544–1548, 2007.
- [86] Verma, K. C., and Kotnala, R. K., “Multiferroic Approach for Cr, Mn, Fe, Co, Ni, Cu Substituted  $\text{BaTiO}_3$  Nanoparticles,” *Mater. Res. Express*, vol. 3, 055006, 2016.
- [87] Huang, G. J., Wang, J. B., Zhong, X. L., Zhou, G. C., and Yan, H. L., “Synthesis, Structure, and Room-Temperature Ferromagnetism of Ni-Doped  $\text{ZnO}$  Nanoparticles,” *J. Mater. Sci.*, vol. 42, pp. 6464–6468, 2007.
- [88] Oyarzabal, I., Ruiz, J., Mota, A. J., *et al.*, “An Experimental and Theoretical Magneto-Structural Study of Polynuclear  $\text{Ni}^{\text{II}}$  Complexes Assembled From A Versatile Bis(Salicylaldehyde)Diamine Polytopic Ligand,” *Dalt. Trans.*, vol. 44, pp. 6825–6838, 2015.

- [89] Shahid, M. Y., Asghar, M., Malik, F., and Warsi, M. F., “Ferroelectric and Dielectric Properties of Nickel Doped BaTiO<sub>3</sub> Thin Films Developed by Sol-Gel Spin-Coating Process,” *J. Ovonic Res.*, vol. 13, pp. 143–153, 2017.
- [90] Arshad, M., Khan, W., Abushad, M., *et al.*, “Correlation Between Structure, Dielectric and Multiferroic Properties of Lead Free Ni Modified BaTiO<sub>3</sub> Solid Solution,” *Ceram. Int.*, vol. 46, pp. 27336–27351, 2020.
- [91] Rani, A., Kolte, J., and Gopalan, P., “Investigation on The Structural, Multiferroic and Magnetoelectric Properties of BaTi<sub>1-x</sub>Ni<sub>x</sub>O<sub>3</sub> Ceramics,” *Ceram. Int.*, vol. 45, pp. 5312–5320, 2019.
- [92] Alkathy, M. S., Eiras, J. A., Zabotto, F. L., and Raju, K. C. J. “Structural, Optical, Dielectric, and Multiferroic Properties of Sodium and Nickel Co-Substituted Barium Titanate Ceramics,” *J. Mater. Sci. Mater. Electron.*, vol. 32, pp. 12828–12840, 2021.
- [93] Suwa, Y., Okamoto, M., and Hamada, T. “First-principles Materials-simulation Technology,” *Hitachi Rev.*, vol. 63, pp. 65–74, 2014.
- [94] Schrödinger, E., “Quantisierung als Eigenwertproblem,” *Ann. Phys.*, vol. 384, pp. 361–376, 1926.
- [95] Combes, J. M., “The Born-Oppenheimer Approximation,” in Thirring, W., Urban, P. (eds) *The Schrödinger Equation. Acta Physica Austriaca*, vol 17, 1977. Springer, Vienna.
- [96] Mayer, I., “The Hartree-Fock Method,” in: Simple Theorems, Proofs, and Derivations in Quantum Chemistry. *Mathematical and Computational Chemistry*, 2003, Springer, Boston, MA.
- [97] Rahaman, M. Z., *Experimental and Theoretical Investigations of Multifunctional (Li, Nd) Co-Doped ZnO Ceramics for the Application in Microelectronics*, M.Sc. Thesis, Department of Physics, Bangladesh University of Engineering and Technology, 2019.

- [98] Hohenberg, P., and Kohn, W., “Inhomogeneous Electron Gas,” *Phys. Rev.*, vol. 136, pp. B864-B871, 1964.
- [99] Kohn, W., and Sham, L. J., “Self-Consistent Equations Including Exchange and Correlation Effects,” *Phys. Rev.*, vol. 140, A1133, 1965.
- [100] Monkhorst, H. J., and Pack, J. D., “Special Points for Brillouin-Zone Integrations,” *Phys. Rev. B*, vol. 13, 5188, 1976.
- [101] Vanderbilt, D., “Soft Self-Consistent Pseudopotentials in A Generalized Eigenvalue Formalism,” *Phys. Rev. B*, vol. 41, 7892, 1990.
- [102] Segall, M. D., Lindan, P. J. D., Probert, M. J., *et al.*, “First-Principles Simulation: Ideas, Illustrations and The CATEP Code,” *J. Phys. Condens. Matter*, vol. 14, 2717, 2002.
- [103] Perdew, J. P., Burke, K., and Ernzerhof, M., “Generalized Gradient Approximation Made Simple,” *Phys. Rev. Lett.*, vol. 77, 3865, 1996.
- [104] Fischer, T. H., and Almlöf, J., “General Methods for Geometry and Wave Function Optimization,” *J. Phys. Chem.*, vol. 96, pp. 9768–9774, 1992.
- [105] Xu, Y. (1991) *Ferroelectric Materials and Their Applications*. Elsevier Science Pub. Co., New York, USA.
- [106] Valenzuela, R. (1994) *Magnetic Ceramics*. Cambridge University Press.
- [107] Coble, R. L., and Burke, J. E., *4<sup>th</sup> Int. Symp. On the Reactivity of Solids*, Amsterdam, pp. 38-51. 1960.
- [108] Kittel, C. (1996) *Introduction to Solid State Physics*. John Wiley & Sons Inc.
- [109] Bragg, W. H. S., “The Structure of Magnetite and the Spinel,” *Nature*, vol. 95, 561, 1915.
- [110] Momin, A. A., Parvin, R., Islam, M. F., Hossain, A. K. M. A., “Structural, magnetic and electrical properties of multiferroic  $x\text{Li}_{0.1}\text{Ni}_{0.2}\text{Mn}_{0.6}\text{Fe}_{2.1}\text{O}_4 - (1-x)\text{Bi}_{0.8}\text{Y}_{0.2}\text{FeO}_3$  composites,” *J. Magn. Magn. Mater.*, vol. 526, 167708, 2021.



- [111] Ding, J., McCormick, P. G., and Street, R., “Formation of Spinel Mn-Ferrite During Mechanical Alloying,” *J. Magn. Magn. Mater.*, vol. 171, pp. 309–314, 1997.
- [112] Soares, B. G., Leyva, M. E., Barra, G. M. O., and Khastgir, D., “Dielectric Behavior Of Polyaniline Synthesized By Different Techniques,” *Eur. Polym. J.*, vol. 42, pp. 676–686, 2006.
- [113] Liu, S. Y., Zhang, E, Liu, S., *et al.*, “Composition- and Pressure-Induced Relaxor Ferroelectrics: First-Principles Calculations and Landau-Devonshire Theory,” *J. Am. Ceram. Soc.*, vol. 99, pp. 3336–3342, 2016.
- [114] Verma, A. S., and Jindal, V. K., “Lattice Constant of Cubic Perovskites,” *J. Alloys Compd.*, vol. 485, pp. 514–518, 2009.
- [115] Moreira, R. L., and Dias, A., “Comment on “Prediction of lattice constant in cubic perovskites”,” *J. Phys. Chem. Solids*, vol. 68, pp. 1617–1622, 2007.
- [116] Jiang, L. Q., Guo, J. K., Liu, H. B., *et al.*, “Prediction of Lattice Constant in Cubic Perovskites,” *J. Phys. Chem. Solids*, vol. 67, pp. 1531–1536, 2006.
- [117] Murnaghan, F. D., “Finite Deformations of an Elastic Solid,” *Am. J. Math.*, vol. 59, 235, 1937.
- [118] Rabiei, M., Palevicius, A., Dashti, A., *et al.* “Measurement Modulus of Elasticity Related to the Atomic Density of Planes in Unit Cell of Crystal Lattices,” *Mater.*, vol. 13, 4380, 2020.
- [119] Liu, S. Y., Zhang, S., Liu, S., *et al.* “Phase Stability, Mechanical Properties and Melting Points of High-Entropy Quaternary Metal Carbides from First-Principles,” *J. Eur. Ceram. Soc.*, vol. 41, pp. 6267–6274, 2021.
- [120] Han, Y., Wu, Y., Li, T., *et al.* “Electronic, Magnetic, Half-Metallic, and Mechanical Properties of a New Equiatomic Quaternary Heusler Compound YRhTiGe: A First-Principles Study,” *Mater.*, vol. 11, 797, 2018.
- [121] Kleinman, L., “Deformation Potentials in Silicon. I. Uniaxial Strain,” *Phys. Rev.*, vol. 128, 2614, 1962.

- [122] Harrison, W. A. (1989) *Electronic Structure and the Properties of Solids: The Physics of the Chemical Bond*. Dover Publications.
- [123] Feng, W., and Cui, S., “Mechanical and Electronic Properties of  $Ti_2AlN$  and  $Ti_4AlN_3$ : A First-Principles Study,” *Can. J. Phys.*, vol. 92, pp. 1652–1657, 2014.
- [124] Pettifor, D. G., “Theoretical Predictions of Structure and Related Properties of Intermetallics,” *Mater. Sci. Technol.*, vol. 8, pp. 345–349, 2013.
- [125] Butt, M. K., Yaseen, M., Bhatti, I. A., *et al.* “A DFT Study of Structural, Magnetic, Elastic and Optoelectronic Properties of Lanthanide Based  $XAlO_3$  ( $X=Nd, Gd$ ) Compounds,” *J. Mater. Res. Technol.*, vol. 9, pp. 16488–16496, 2020.
- [126] Pugh, S. F., “XCII. Relations Between the Elastic Moduli and the Plastic Properties of Polycrystalline Pure Metals,” *Lond. Edinb. Dublin Philos. Mag. J. Sci.*, vol. 45, pp. 823–843, 1954.
- [127] Ledbetter, H., and Migliori, A., “A General Elastic-Anisotropy Measure,” *J. Appl. Phys.*, vol. 100, 063516, 2006.
- [128] Ranganathan, S. I., and Ostoja-Starzewski, M., “Universal Elastic Anisotropy Index,” *Phys. Rev. Lett.*, vol. 101, 055504, 2008.
- [129] Gaillac, R., Pullumbi, P., and Coudert, F. X., “ELATE: An Open-Source Online Application for Analysis and Visualization of Elastic Tensors,” *J. Phys. Condens. Matter*, vol. 28, 275201, 2016.
- [130] Liu, S. Y., Zhang, S., Liu, S., *et al.* “Stability and Mechanical Properties of Single-Phase Quinary High-Entropy Metal Carbides: First-Principles Theory and Thermodynamics,” *J. Eur. Ceram. Soc.*, vol. 42, pp. 3089–3098, 2022.
- [131] Refson, K., Tulip, P. R., and Clark, S. J., “Variational Density-Functional Perturbation Theory for Dielectrics and Lattice Dynamics,” *Phys. Rev. B*, vol. 73, 155114, 2006.

- [132] Tkatchenko, A., and Scheffler, M., “Accurate Molecular van Der Waals Interactions from Ground-State Electron Density and Free-Atom Reference Data”. *Phys. Rev. Lett.*, vol. 102, 073005, 2009.
- [133] Moreira, E., Barboza, C. A., Albuquerque, E. L., *et al.* “Vibrational and Thermodynamic Properties of Orthorhombic  $\text{CaSnO}_3$  from DFT and DFPT Calculations,” *J. Phys. Chem. Solids*, vol. 77, pp. 85–91, 2015.
- [134] Maris, H. J., and Elbaum, C., “Validity of the Born-Huang Relations in Lattice Dynamics,” *Phys. Lett. A*, vol. 25, pp. 96–97, 1967.
- [135] Ashcroft, N. W., and Mermin, N. D. (1976) *Solid State Physics*. Saunders College, Philadelphia, USA.
- [136] Akhtar, S., Alay-e-Abbas, S. M., Batool, J., *et al.* “Investigation of Structural, Electronic and Optical Properties of (V+P)-Doped  $\text{BaZrO}_3$  for Photocatalytic Applications using Density Functional Theory,” *J. Phys. Chem. Solids*, vol. 147, 109662, 2020.
- [137] Baroni, S., De Gironcoli, S., Dal Corso, A., and Giannozzi, P., “Phonons and Related Crystal Properties from Density-Functional Perturbation Theory,” *Rev. Mod. Phys.*, vol. 73, 515, 2001.
- [138] Luo, B., Wang, X., Tian, E., Li, G., and Li, L., “Electronic Structure, Optical and Dielectric Properties of  $\text{BaTiO}_3/\text{CaTiO}_3/\text{SrTiO}_3$  Ferroelectric Superlattices from First-Principles Calculations,” *J. Mater. Chem. C*, vol. 3, pp. 8625–8633, 2015.
- [139] Pearton, S. J., Norton, D. P., Ip, K., Heo, Y. W., Steiner, T., “Recent Progress in Processing and Properties of  $\text{ZnO}$ ,” *Superlattices Microstruct.*, vol. 34, pp. 3–32, 2003.
- [140] Granqvist, C. G., “Transparent Conductors as Solar Energy Materials: A Panoramic Review,” *Sol. Energy Mater. Sol. Cells*, vol. 91, pp. 1529–1598, 2007.

- [141] Hosono, H., “Recent Progress in Transparent Oxide Semiconductors: Materials and Device Application,” *Thin Solid Films*, vol. 515, pp. 6000–6014, 2007.
- [142] Haus, J. W., “Nanophotonic Devices,” in *Fundamentals and Applications of Nanophotonics*, Chap. 11, pp. 341–395, Woodhead Publishing, 2016.
- [143] Xu, J. H., Oguchi, T., and Freeman, A. J., “Solid-Solution Strengthening: Substitution of V in Ni<sub>3</sub>Al and Structural Stability of Ni<sub>3</sub>(Al,V),” *Phys. Rev. B*, vol. 36, 4186, 1987.
- [144] Hong, T., Watson-Yang, T. J., Freeman, A. J., Oguchi, T., et al. “Crystal Structure, Phase Stability, and Electronic Structure of Ti-Al Intermetallics: TiAl<sub>3</sub>,” *Phys. Rev. B*, vol. 41, 12462, 1990.
- [145] Hasan, M., and Hossain, A. K. M. A., “First-Principles Calculations to Investigate the Structural, Electronic, Optical Anisotropy, And Bonding Properties of a Newly Synthesized ThRhGe Equiatomic Ternary Intermetallic Superconductor,” *Results Phys.*, vol. 42, 106004, 2022.
- [146] Dresselhaus, M. S. (1999) *Solid State Physics Part II Optical Properties of Solids*.
- [147] Yang, Y., Liu, X., and Jin, D., “Influence of Heat Treatment Temperatures on Structural and Magnetic Properties of Sr<sub>0.50</sub>Ca<sub>0.20</sub>La<sub>0.30</sub>Fe<sub>11.15</sub>Co<sub>0.25</sub>O<sub>19</sub> Hexagonal Ferrites,” *J. Magn. Magn. Mater.*, vol. 364, pp. 11–17, 2014.
- [148] Boudad, L., Taibi, M., Belayachi, A., and Abd-lefdil, M., “Structural, Morphological, Dielectric and Optical Properties of Double Perovskites RBaFeTiO<sub>6</sub> (R = La, Eu),” *RSC Adv.*, vol. 11, pp. 40205-40215, 2021.
- [149] Manu, K. M., Karthik, C., Ubig, R., and Sebastian, M. T., “Effect of Ca<sup>2+</sup> Substitution on the Structure, Microstructure, and Microwave Dielectric Properties of Sr<sub>2</sub>Al<sub>2</sub>SiO<sub>7</sub> Ceramic,” *J. Am. Ceram. Soc.*, vol. 96, pp. 3842–3848 2013.

- [150] Havriliak, S., and Negami, S., "A Complex Plane Representation of Dielectric and Mechanical Relaxation Processes in Some Polymers," *Polymer*, vol. 8, pp. 161–210, 1967.
- [151] Tang, R., Jiang, C., Qian, W., *et al.* "Dielectric Relaxation, Resonance and Scaling Behaviors in  $\text{Sr}_3\text{Co}_2\text{Fe}_{24}\text{O}_{41}$  Hexaferrite," *Sci. Rep.*, vol. 5, 13645, 2015.
- [152] Lunkenheimer, P., Bobnar, V., Pronin, A. V., *et al.* "Origin of Apparent Colossal Dielectric Constants," *Phys. Rev. B*, vol. 66, 052105, 2002.
- [153] Jonscher, A. K., "The 'Universal' Dielectric Response," *Nat.*, vol. 267, pp. 673–679, 1977.
- [154] Atif, M., Asghar, M. W., Nadeem, M., *et al.* "Synthesis and Investigation of Structural, Magnetic and Dielectric Properties of Zinc Substituted Cobalt Ferrites," *J. Phys. Chem. Solids*, vol. 123, pp. 36–42, 2018.
- [155] Upadhyay, S., Sahu, A. K., Kumar, D., and Parkash, O., "Probing Electrical Conduction Behavior of  $\text{BaSnO}_3$ ," *J. Appl. Phys.*, vol. 84, 828, 1998.
- [156] Patil, A. N., Patil, M. G., Patankar, K. K., *et al.* "Dielectric Behaviour and A.C. Conductivity in  $\text{Cu}_x\text{Fe}_{3-x}\text{O}_4$  Ferrite," *Bull. Mater. Sci.*, vol. 23, pp. 447–452, 2000.
- [157] Austin, I. G., and Mott, N. F., "Polarons in Crystalline and Non-Crystalline Materials," *Adv. Phys.*, vol. 18, pp. 41–102, 1969.
- [158] Verma, A., Thakur, O. P., Prakash, C., Goel, T. C., and Mendiratta, R. G., "Temperature Dependence of Electrical Properties of Nickel–Zinc Ferrites Processed by the Citrate Precursor Technique," *Mater. Sci. Eng. B*, vol. 116, pp. 1–6, 2005.
- [159] Papathanassiou, A. N., Sakellis, I., and Grammatikakis, J., "Universal Frequency-Dependent Ac Conductivity of Conducting Polymer Networks," *Appl. Phys. Lett.*, vol. 91, 122911, 2007.

- [160] Mechi, N., Mallah, A., Hcini, S., *et al.* “Effects of Sintering Temperature on Microstructural, Magnetic, and Impedance Spectroscopic Properties of  $\text{Ni}_{0.4}\text{Cd}_{0.3}\text{Zn}_{0.3}\text{Fe}_2\text{O}_4$  Ferrites,” *J. Supercond. Nov. Magn.*, vol. 33, pp. 1547–1557, 2020.
- [161] Dhahri, A., Dhahri, E., and Hlil, E. K., “Electrical Conductivity and Dielectric Behaviour of Nanocrystalline  $\text{La}_{0.6}\text{Gd}_{0.1}\text{Sr}_{0.3}\text{Mn}_{0.75}\text{Si}_{0.25}\text{O}_3$ ,” *RSC Adv.*, vol. 8, pp. 9103–9111, 2018.
- [162] Macdonald, R.J. and Johnson, W.B., “Fundamental of Impedance Spectroscopy,” in E. Barsoukov, and R. J. Macdonald, Eds., *Impedance Spectroscopy: Theory, Experiment, and Applications*, 2<sup>nd</sup> Edition, John Wiley & Sons, Inc., New Jersey, 2005.
- [163] Kumar, A., Singh, B. P., Choudhary, R. N. P., and Thakur, A. K., “Characterization of Electrical Properties of Pb-Modified  $\text{BaSnO}_3$  using Impedance Spectroscopy,” *Mater. Chem. Phys.*, vol. 99, pp. 150–159, 2006.
- [164] Behera, B., Nayak, P., and Choudhary, R. N. P., “Impedance Spectroscopy Study of  $\text{NaBa}_2\text{V}_5\text{O}_{15}$  Ceramic,” *J. Alloys Compd.*, vol. 436, pp. 226–232, 2007.
- [165] Płcharski, J., and Weiczorek, W., “PEO Based Composite Solid Electrolyte Containing Nasicon,” *Solid State Ion.*, vol. 28–30, pp. 979–982, 1988.
- [166] Roling, B., “Scaling Properties of The Conductivity Spectra of Glasses and Supercooled Melts,” *Solid State Ion.*, vol. 105, pp.185–193, 1998.
- [167] Liu, J., Duan, C. G., Yin, W. G., *et al.* “Dielectric Permittivity and Electric Modulus in  $\text{Bi}_2\text{Ti}_4\text{O}_{11}$ ,” *J. Chem. Phys.*, vol. 119, 2812, 2003.
- [168] León, C., Lucía, M., and Santamaría, J., “Correlated Ion Hopping in Single-Crystal Ytria-Stabilized Zirconia,” *Phys. Rev. B*, vol. 55, 882, 1997.
- [169] Richert, R., and Wagner, H., “The Dielectric Modulus: Relaxation Versus Retardation,” *Solid State Ion.*, vol. 105, pp. 167–173, 1998.

- [170] Chowdari, B. V. R., Gopalakrishnan, R., “AC Conductivity Analysis of Glassy Silver Iodomolybdate System,” *Solid State Ion.*, vol. 23, pp. 225–233, 1987.
- [171] Globus, A., Duplex, P., “Separation of Susceptibility Mechanisms for Ferrites of Low Anisotropy,” *IEEE Trans. Magn.*, vol. 2, pp. 441–445, 1966.
- [172] Snoek, J. L., “Dispersion and Absorption in Magnetic Ferrites at Frequencies Above One Mc/s,” *Physica*, vol. 14, pp. 207–217, 1948.
- [173] Haque, M. M., Huq, M., Hakim, M. A., “Influence of CuO and Sintering Temperature on the Microstructure and Magnetic Properties of Mg–Cu–Zn Ferrites,” *J. Magn. Magn. Mater.*, vol. 320, pp. 2792–2799, 2008.
- [174] Islam, M. A., Hasan, M., and Hossain, A. K. M. A. Enhancement of Initial Permeability and Reduction of Loss Factor in Zn Substituted Nanocrystalline  $\text{Li}_{0.35-0.5x}\text{Ni}_{0.3}\text{Zn}_x\text{Fe}_{2.35-0.5x}\text{O}_4$ ,” *J. Magn. Magn. Mater.*, vol. 424, pp. 108–114, 2017.
- [175] Caizer, C., and Stefanescu, M., “Magnetic Characterization of Nanocrystalline Ni–Zn Ferrite Powder Prepared by the Glyoxylate Precursor Method,” *J. Phys. D. Appl. Phys.*, vol. 35, 3035, 2002.
- [176] Grössinger, R., “A Critical Examination of The Law of Approach to Saturation. I. Fit Procedure,” *Phys. status solidi*, vol. 66, pp. 665–674, 1981.
- [177] Kumar, L., Kumar, P., and Kar, M., “Cation Distribution by Rietveld Technique and Magnetocrystalline Anisotropy of Zn Substituted Nanocrystalline Cobalt Ferrite,” *J. Alloys Compd.*, vol. 551, pp. 72–81, 2013.
- [178] Tanwar, K., Gyan, D. S., Gupta, P., *et al.* “Investigation of Crystal Structure, Microstructure and Low Temperature Magnetic Behavior of  $\text{Ce}^{4+}$  and  $\text{Zn}^{2+}$  Co-Doped Barium Hexaferrites ( $\text{BaFe}_{12}\text{O}_{19}$ ),” *RSC Adv.*, vol. 8, pp. 19600–19609, 2018.

## List of Peer-Reviewed Journal Articles from This Research

[1] **Hasan, M.**, Nasrin, S., Islam, M. N., and Hossain, A. K. M. A., "First-Principles Insights into the Electronic, Optical, Mechanical and Thermodynamic Properties of Lead-Free Cubic  $ABO_3$  [A=Ba, Ca, Sr; B=Ce, Ti, Zr] Perovskites" *AIP Advances*, vol. 12, no. 08, 085327, 2022.

[2] **Hasan, M.**, and Hossain, A. K. M. A., "Structural, electronic and optical properties of strontium and nickel Co-doped  $BaTiO_3$ : A DFT based study", *Comput. Condens. Matter*, 28, e00578, 2021.



## List of Conference Abstracts / Presentations

- [1] **M. Hasan**, and A. K. M. A. Hossain, “Strontium and nickel co-doped barium titanate: Theoretical and experimental approach”, *1<sup>st</sup> International Conference on Frontier in Sciences (ICFS-2022)*, Bangladesh University of Engineering and Technology (BUET), Dhaka, Bangladesh, November 11-12, 2022.
- [2] **M. Hasan**, and A. K. M. A. Hossain, “First-Principles Insights into the Lattice Parameter, Electronic, Optical, Mechanical and Thermodynamic Properties of  $ABO_3$  [A=Ba, Ca, Sr; B=Ce, Ti, Zr] Perovskites”, *International Conference on Physics-2022*, Atomic Energy Centre Dhaka, May 19-21, 2022.
- [3] **M. Hasan**, M. N. I. Khan, and A. K. M. A. Hossain, “Investigation of Structural, Dielectric and Magnetic Properties Barium-Strontium-Nickel Titanate”, *International Conference on Electronics and Informatics 2021 (ICEI 2021)*, Atomic Energy Centre, Dhaka, November 27-28, 2021.
- [4] **M Hasan**, and A. K. M. A. Hossain, “Study of structural and initial permeability of strontium and nickel co-doped barium titanate sintered at  $1250^\circ\text{C}$ ”, *National Conference on Physics–2021*, Organized by Bangladesh Physical Society, Virtual Conference, August 06-07, 2021.
- [5] **M. Hasan**, and A. K. M. A. Hossain, “Computational Investigations of Strontium and Nickel Doped Barium Titanate”, *The 6<sup>th</sup> Conference of BCA, Organized by Bangladesh Crystallographic Association*, Virtual Conference, January 14 – 16, 2021.
- [6] **M. Hasan**, M. K. Das, and A. K. M. A. Hossain, "Study of Electromagnetic Properties of Sr and Ni Substituted  $BaTiO_3$  Ceramics", *International Conference on Physics-2020*, Organized by Bangladesh Physical Society, Atomic Energy Centre, Dhaka, Bangladesh, March 05-07, 2020.
- [7] **M. Hasan**, M. K. Das, and A. K. M. A. Hossain, "Influence of double doping of Strontium and Nickel on magnetic and dielectric properties of Barium Titanate", *National Conference on Physics-2019*, Organized by Bangladesh Physical Society, Department of Physics, University of Dhaka, Dhaka, February 07-09, 2019.

# First-principles insights into the electronic, optical, mechanical, and thermodynamic properties of lead-free cubic $ABO_3$ [A = Ba, Ca, Sr; B = Ce, Ti, Zr] perovskites

Cite as: AIP Advances 12, 085327 (2022); <https://doi.org/10.1063/5.0104191>

Submitted: 18 June 2022 • Accepted: 21 July 2022 • Published Online: 30 August 2022

 Mehedi Hasan, Sharifa Nasrin,  M. Nazrul Islam, et al.

## COLLECTIONS

 This paper was selected as an Editor's Pick



View Online



Export Citation



CrossMark

## ARTICLES YOU MAY BE INTERESTED IN

[Comparison of Poynting's vector and the power flow used in electrical engineering](#)

AIP Advances 12, 085219 (2022); <https://doi.org/10.1063/5.0101339>

[Geometric and doping effects on radiative recombination in thin-film near-field energy converters](#)

AIP Advances 12, 095006 (2022); <https://doi.org/10.1063/5.0103358>

[Terahertz beam array generated by focusing two-color-laser pulses into air with a microlens array](#)

AIP Advances 12, 095113 (2022); <https://doi.org/10.1063/5.0098771>



# First-principles insights into the electronic, optical, mechanical, and thermodynamic properties of lead-free cubic $ABO_3$ [A = Ba, Ca, Sr; B = Ce, Ti, Zr] perovskites

Cite as: AIP Advances 12, 085327 (2022); doi: 10.1063/5.0104191

Submitted: 18 June 2022 • Accepted: 21 July 2022 •

Published Online: 30 August 2022



View Online



Export Citation



CrossMark

Mehedi Hasan,<sup>1,2,a)</sup>  Sharifa Nasrin,<sup>3,4</sup> M. Nazrul Islam,<sup>2,5</sup>  and A. K. M. Akther Hossain<sup>2</sup>

## AFFILIATIONS

<sup>1</sup>General Education Department, City University, Dhaka, Bangladesh

<sup>2</sup>Department of Physics, Bangladesh University of Engineering and Technology, Dhaka, Bangladesh

<sup>3</sup>Directorate of Secondary and Higher Education, Ministry of Education, Government of the People's Republic of Bangladesh, Dhaka, Bangladesh

<sup>4</sup>Department of Physics, University of Dhaka, Dhaka, Bangladesh

<sup>5</sup>Department of Science and Humanities, Bangladesh Army International University of Science and Technology (BAIUST), Cumilla, Bangladesh

<sup>a)</sup>Author to whom correspondence should be addressed: [mehedi.physics@gmail.com](mailto:mehedi.physics@gmail.com)

## ABSTRACT

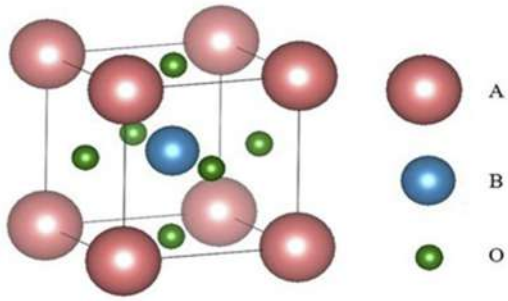
A comparative study on mechanical, thermodynamic, electronic, and optical properties has been performed on various compounds having an  $ABO_3$ , where A = Ba, Ca, Sr and B = Ce, Ti, Zr, perovskite structure using first-principles calculations. These materials' properties have been thoroughly investigated for their ground states under the same computational parameters. The computed lattice parameters in the ground state agreed with other theoretical studies. Elastic moduli, ductility or brittleness, elastic anisotropy, mechanical stability, and stiffness of solid materials are studied. Enthalpy (H), entropy (S), and free energy (F) were reported from the vibrational properties of the materials. The temperature-dependent heat capacity and Debye temperature are investigated. The electronic band structure as a function of energy, of different perovskite structures at the ground state, is also studied. From this study, the  $ABO_3$  perovskite has emerged as the most promising material for applications in optoelectronics, photonics, and mechanical and thermoelectric devices.

© 2022 Author(s). All article content, except where otherwise noted, is licensed under a Creative Commons Attribution (CC BY) license (<http://creativecommons.org/licenses/by/4.0/>). <https://doi.org/10.1063/5.0104191>

## I. INTRODUCTION

The mineral  $CaTiO_3$  was discovered in the Ural Mountains of Russia by Gustav Rose in 1839 and named “perovskite,” in honor of the Russian mineralogist Count Lev Alekseyevich von Perovski.<sup>1</sup> In the later years, a broad family of crystals is found to have the same structures of  $CaTiO_3$ .<sup>2,3</sup> Materials with the same type of crystal structure as that of  $CaTiO_3$  were known as perovskite materials.<sup>4</sup> The perovskite-type oxides have the general formula  $ABO_3$ , where “A” and “B” are cations and “O” is an anion. Usually, cation “A” is

larger than cation “B”. The oxide-type perovskites have always been a great consideration in the device industry and solar cell fabrication because of their decent dielectric, ferroelectric, piezoelectric, and electro-optical properties, thermal conductivity, insulator-to-metallic transitions, half-metallic behavior, exhibition of fluorescence with laser action, etc. Both experimental and theoretical studies are still a matter of interest for material scientists to fabricate multifunctional materials based on perovskites. These types of materials are used as the base materials for many important ceramic components and devices, such as multi-layer ceramic capacitors



**FIG. 1.** Crystal structure of  $ABO_3$  [A = Ba, Ca, Sr; B = Ce, Ti, Zr] perovskites (3D view).

(MLCCs), electrodes for fuel cells, and piezoelectric ceramic transducers and in the spintronics industry.<sup>5–10</sup>  $BaTiO_3$ ,  $CaTiO_3$ , and  $SrTiO_3$  are common perovskite-type materials used for the above purposes. Although lead titanate, lead zirconate titanate, and lead lanthanum zirconate titanate show good ferroelectric and piezoelectric behavior, however, lead compounds are unstable under ambient conditions and, therefore, decompose into toxic substances. This might have disastrous consequences for the ecosystem. They are also harmful for human health.<sup>11</sup> As a result, lead-free perovskite structures with different multifunctional properties are a great matter of interest for scientists and engineers.<sup>12,13</sup> In this research, a computational method has been used to investigate the structural, elastic, thermodynamic, electrical, and optical properties of different  $ABO_3$  (where A = Ca, Ba, Sr; B = Ce, Ti, Zr) perovskites and compare their properties for the first time altogether.

## II. COMPUTATIONAL METHOD

To investigate the ground state's physical, elastic, thermodynamic, electronic, and optical properties, the Density Functional Theory (DFT) based calculations have been performed using the

CASTEP (CAMbridge Serial Total Energy Package) formulation.<sup>14</sup> A generalized gradient approximation (GGA) functional developed by Perdew, Burke, and Ernzerhof (PBE) is used in this investigation as the exchange-correlation functional.<sup>15</sup> The Vanderbilt model<sup>16</sup> OTFG ultrasoft pseudopotential has been used to describe the electron-ion interaction. The Broyden–Fletcher–Goldfarb–Shanno (BFGS) method<sup>17</sup> has been used to optimize the structure of the materials. The converging cut-off energy of a plane-wave of 650 eV along with k-points  $5 \times 5 \times 5$  with a convergence tolerance energy of  $1.0 \times 10^{-5}$  eV/atom, a maximum force on atoms of 0.03 eV/Å, a maximum stress of 0.05 GPa, and a maximum atomic displacement of  $1.0 \times 10^{-3}$  Å has been taken to optimize the structures while investigating the structural, electronic, and optical properties. To calculate the elastic properties, fine quality with an energy of  $2.0 \times 10^{-6}$  eV/atom, a maximum force on atoms of 0.006 eV/Å, and a maximum displacement of  $2.0 \times 10^{-4}$  Å were considered. For the calculation of thermodynamic properties, k-points were kept the same, but the cut-off energy was taken at 830 eV with the Local-Density Approximation (LDA) functional. While sampling the k-points within the Brillouin zone in all the cases, Monkhorst–Pack schemes were used.<sup>18</sup> The cubic configuration of the studied materials has been shown in Fig. 1.

## III. STRUCTURAL PROPERTIES

In each case, the structure has been optimized geometrically. All the structures are found cubic in nature after geometrical optimization. The computed lattice parameters and density in the ground state under the same computational parameters are listed in Table I.

From Table I, it is observed that the lattice parameter is the highest in  $BaCeO_3$  and the lowest in  $CaTiO_3$ . It is well known that the radius  $R_{Ba} > R_{Sr} > R_{Ca}$  and  $R_{Ce} > R_{Zr} > R_{Ti}$ ,<sup>22</sup> and a clear reflection in the structural properties is observed accordingly. The calculated lattice parameter of  $BaTiO_3$  agrees with the previously calculated value,<sup>19–21</sup> which makes all the calculations reliable. The slight deviations of experimental values can be observed with the calculated values, which is also a good indication of the dependability

**TABLE I.** Calculated structural parameters of  $ABO_3$  (A = Ba, Ca, Sr; B = Ce, Ti, Zr) materials.

Materials	This study $a_0$ (Å)	Other		Error percentage	Calculated density $\rho$ (g/cm <sup>3</sup> )
		theoretical studies $a_0$ (Å)	Experimental studies $a_0$ (Å)		
$BaCeO_3$	4.48	4.43 <sup>20</sup>	4.40 <sup>20</sup>	1.8	6.03
$CaCeO_3$	4.40	...	...	...	4.44
$SrCeO_3$	4.43	...	...	...	5.26
$BaTiO_3$	4.03	4.03 <sup>19,21</sup>	4.01 <sup>20</sup>	0.5	5.94
$CaTiO_3$	3.88	3.89 <sup>20</sup>	3.84 <sup>20</sup>	1.0	3.86
$SrTiO_3$	3.94	3.93 <sup>20</sup>	3.91 <sup>20</sup>	0.8	5.00
$BaZrO_3$	4.23	4.23 <sup>19</sup>	4.19 <sup>20</sup>	0.9	6.07
$CaZrO_3$	4.13	3.95 <sup>20</sup>	4.01 <sup>20</sup>	3.0	4.22
$SrZrO_3$	4.17	4.06 <sup>20</sup>	4.10 <sup>20</sup>	1.7	5.20

of our present study. It is observed that the density of CaTiO<sub>3</sub> is the lowest and BaZrO<sub>3</sub> has the highest density.

#### IV. MECHANICAL PROPERTIES

Elastic moduli, ductility or brittleness, elastic anisotropy, mechanical stability, and stiffness of solid materials are very substantial properties for material engineering. These properties can be studied by using an elastic constant that can be calculated from the linear finite strain–stress method using the CASTEP formulation.<sup>22–24</sup> A proportional elastic constant  $C_{ij}$  can be expressed as

$$\sigma_i = \sum_{j=1}^6 C_{ij} \epsilon_j,$$

where  $\sigma$  is the stress and  $\epsilon$  is the strain.

A cubic crystal system has three elastic constants:  $C_{11}$ ,  $C_{12}$ , and  $C_{44}$ .<sup>25</sup> For a cubic system, the Born stability criteria<sup>26</sup> are  $C_{11} - C_{12} > 0$ ,  $C_{11} + 2C_{12} > 0$ ,  $C_{11} > 0$ , and  $C_{44} > 0$ .

The internal strain parameter, the Kleinman parameter ( $\zeta$ ), is very useful to describe the relative position of the cation and anion sublattices due to volume conserving strain distortions. It is a parameter that determines the stability of a compound against the stretching and bending types of strains.<sup>27–29</sup> The  $\zeta$  of a compound is given by

$$\zeta = \frac{C_{11} + 8C_{12}}{7C_{11} + 2C_{12}},$$

where  $0 \leq \zeta \leq 1$ . When  $\zeta$  is close to 1, under the application of pressure, the bond bending phenomenon is seen, while if it is close to 0, bond stretching is detected.

The Cauchy pressure ( $C''$ ) of a material is defined as  $C'' = C_{12} - C_{44}$ . This value is positive for ductile materials and related to ionic bonding, whereas the negative value indicates brittleness and is related to covalent bonding.<sup>30,31</sup> Poisson's ratio ( $\nu$ ) is also an index for distinguishing between the brittleness or ductility of materials. The material is brittle when  $\nu < 0.26$  and ductile when  $\nu > 0.26$ .<sup>32</sup> Pugh's ratio (B/G) is another useful parameter to separate the ductility or brittleness nature of a material. If this value of a material is greater than 1.75, the material is ductile, and if the value is less than 1.75, the material is brittle.<sup>33</sup>

The Debye temperature ( $\theta_D$ ) is a characteristic temperature to evaluate material properties, such as thermal expansion, thermal conductivity, lattice vibration, melting point, and specific heat. This temperature can be calculated using the formula

$$\theta_D = \left( \frac{h}{k_B} \right) \left[ \frac{3n}{4\pi} \left( \frac{N_A \rho}{M} \right) \right]^{1/3} V_m,$$

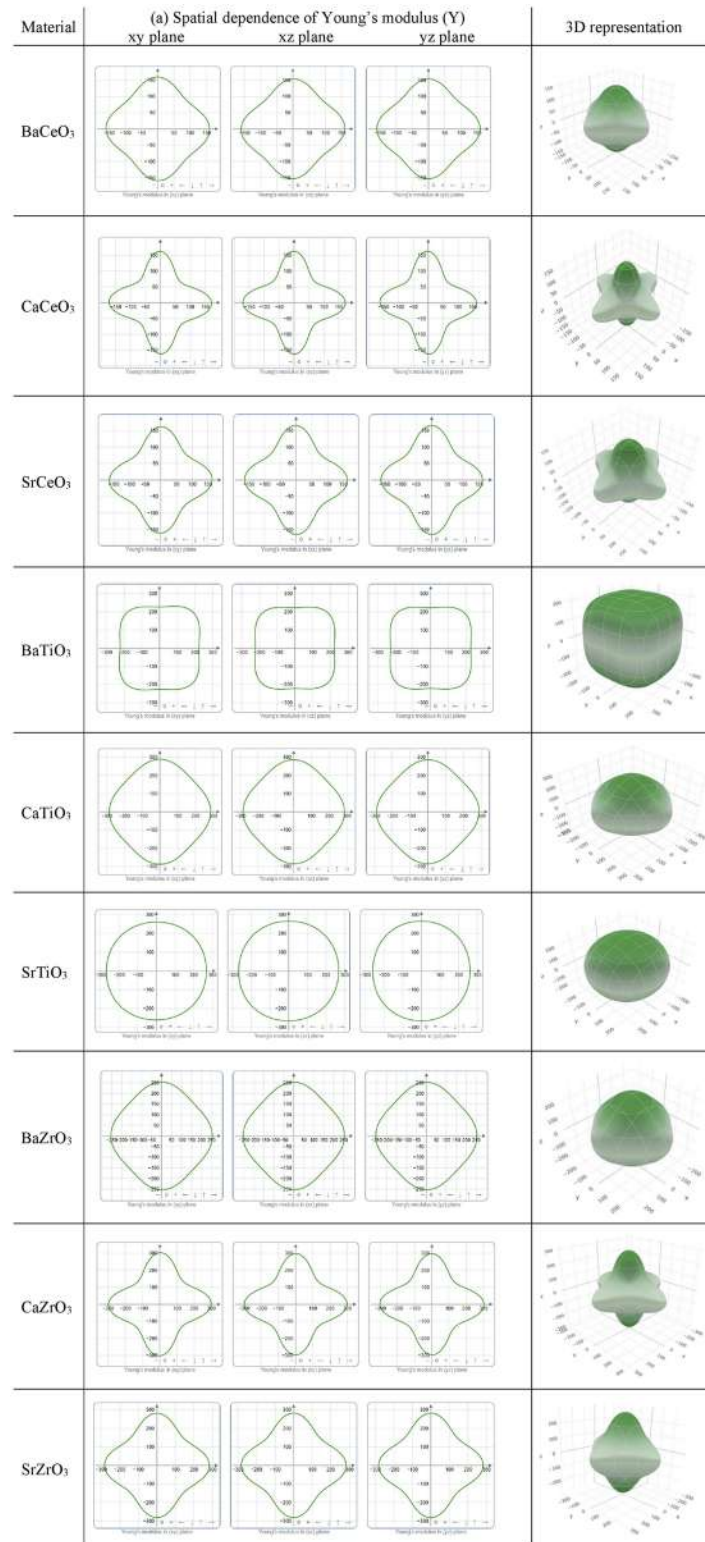
where  $V_m$  is the average sound velocity. The studied mechanical properties of the materials have been tabulated in Table II.

According to  $\zeta$ , BaTiO<sub>3</sub> is bending type and the rest of them are stretching type under pressure. The  $C''$ ,  $\nu$ , and B/G data reveal the ductile nature of the cerate family and CaZrO<sub>3</sub>, while BaTiO<sub>3</sub>, SrTiO<sub>3</sub>, BaZrO<sub>3</sub>, and SrZrO<sub>3</sub> are brittle. Exceptions are seen for the calculated values for CaTiO<sub>3</sub>. Pugh's ratio and Poisson's Ratio data show it is brittle, but the Cauchy pressure shows it is ductile. In the ground state condition, all the three calculated values of CaTiO<sub>3</sub> are very close to the boundary of the ductility and brittleness region.

The anisotropic data are always a useful tool for materials to understand the mechanical efficiency of materials in practical use.<sup>34,35</sup> The ELATE code has been used to illustrate the 2D and 3D visualizations of the anisotropy of Young's modulus (Y),

**TABLE II.** The calculated elastic constants ( $C_{11}$ ,  $C_{12}$ ,  $C_{44}$ ), Young's modulus (Y), bulk modulus (B), shear modulus (G), Cauchy pressure ( $C''$ ), Poisson's ratio ( $\nu$ ), Pugh's ratio (B/G), compressibility (K), universal anisotropic factor, Debye temperature ( $\theta_D$ ), and sound velocity ( $V_m$ ) of various ABO<sub>3</sub> perovskites.

Material	BaCeO <sub>3</sub>	CaCeO <sub>3</sub>	SrCeO <sub>3</sub>	BaTiO <sub>3</sub>	CaTiO <sub>3</sub>	SrTiO <sub>3</sub>	BaZrO <sub>3</sub>	CaZrO <sub>3</sub>	SrZrO <sub>3</sub>
Parameter									
$C_{11}$ (GPa)	194.96	212.21	193.34	275.23	328.67	312.99	288.02	323.91	309.66
$C_{12}$ (GPa)	68.70	71.25	59.82	101.71	97.49	92.26	78.78	72.54	71.77
$C_{44}$ (GPa)	44.39	30.67	37.40	121.02	96.47	109.99	84.85	62.86	73.12
$C_{11} - C_{12}$ (GPa)	126.27	140.96	133.52	173.52	231.18	220.74	209.24	251.36	237.89
$C_{11} + 2C_{12}$ (GPa)	332.36	354.70	312.98	478.65	523.65	497.50	445.58	468.00	453.20
Kleinman parameter, $\zeta$	0.496	0.480	0.456	0.511	0.444	0.442	0.422	0.375	0.382
Young's modulus, Y (Gpa)	133.65	118.74	126.88	264.36	261.72	267.94	230.09	232.2	228.03
Bulk modulus, B (GPa)	107.47	113.74	104.95	159.76	174.94	164.78	148.08	155.78	150.82
Shear modulus, G (Gpa)	51.69	44.78	48.85	107.97	104.63	109.01	92.7	88.49	91.36
Cauchy pressure, $C''$ (Gpa)	24.31	40.58	22.42	-19.31	1.02	-17.73	-6.07	9.69	-1.36
Poisson's ratio, $\nu$	0.29	0.33	0.30	0.22	0.25	0.23	0.24	0.26	0.25
Pugh's ratio, B/G	2.08	2.54	2.15	1.48	1.67	1.51	1.60	1.76	1.65
Compressibility (1/GPa)	0.0093	0.0089	0.0095	0.0063	0.0057	0.0061	0.0068	0.0064	0.0066
Universal anisotropic index	0.1488	0.7594	0.4011	0.1202	0.0448	0.0016	0.0523	0.6209	0.2874
Debye temperature (K)	368	393	381	592	756	669	520	603	558
Average sound velocity (m/s)	3235	3399	3317	4683	5759	5168	4317	4897	4566



**FIG. 2.** The 2D and 3D plots of (a) Y, (b) K, (c) G, and (d)  $\nu$  of ABO<sub>3</sub> perovskites at 0 GPa. (a) Spatial dependence of Young's modulus (Y). (b) Spatial dependence of linear compressibility (K). (c) Spatial dependence of shear modulus (G). (d) Spatial dependence of Poisson's ratio ( $\nu$ ).



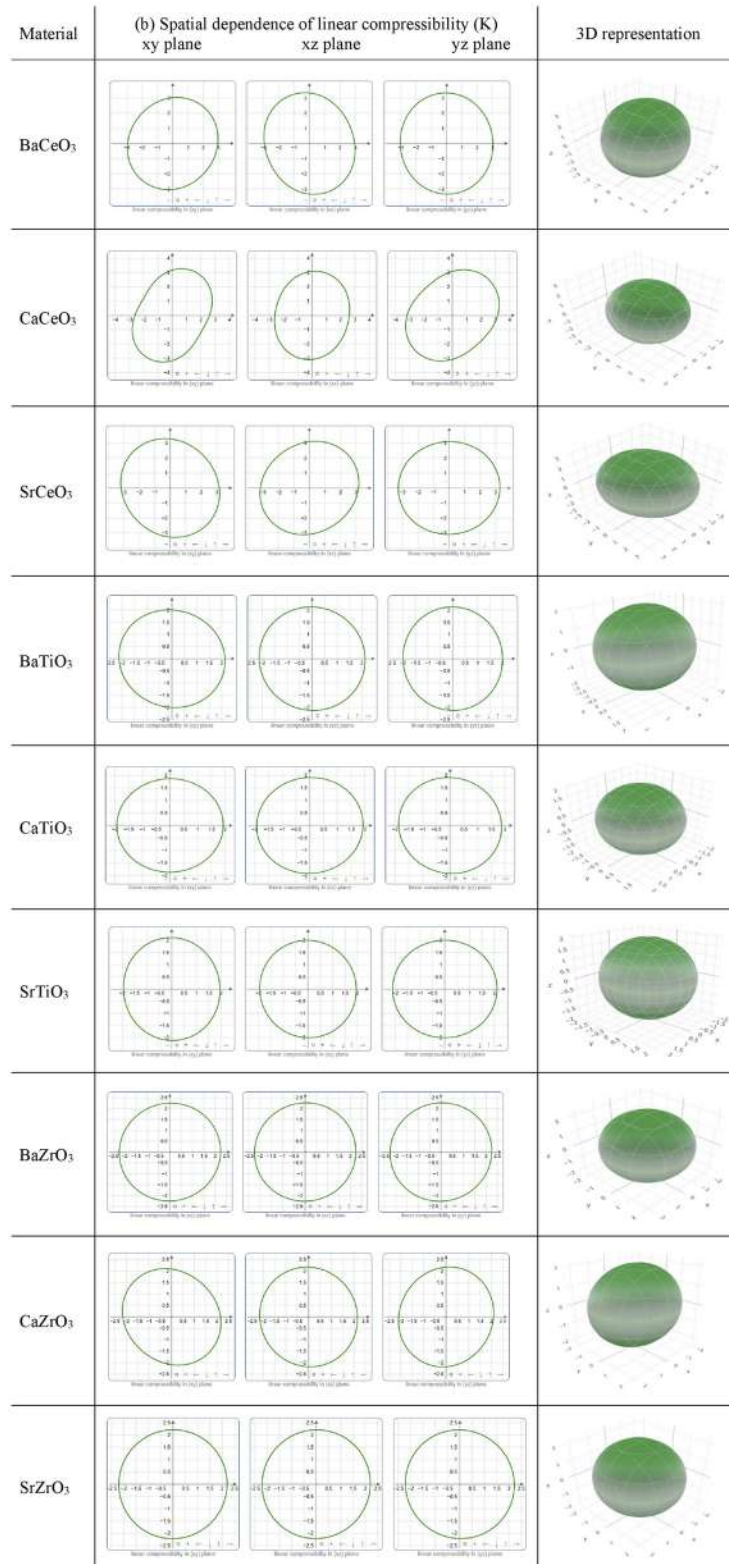


FIG. 2. (Continued.)

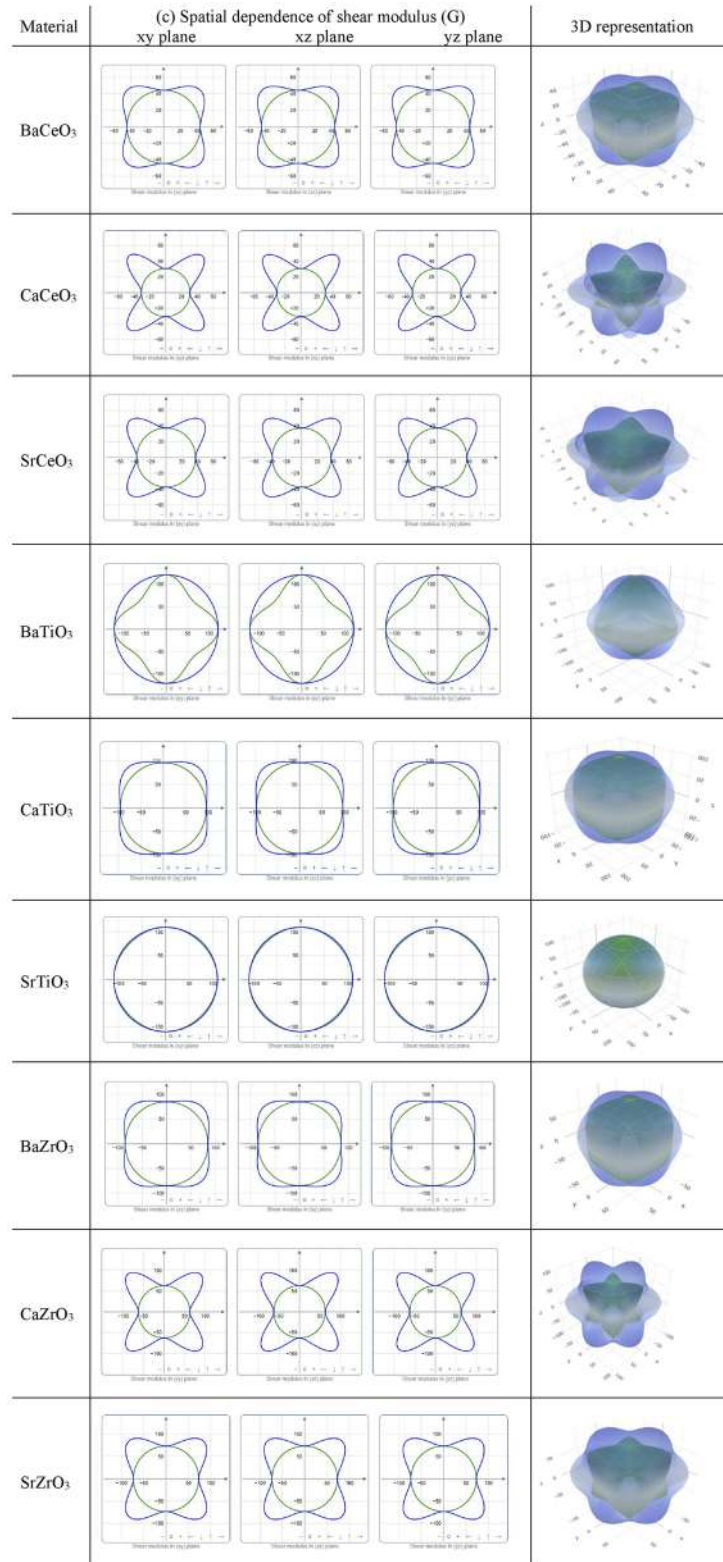


FIG. 2. (Continued.)



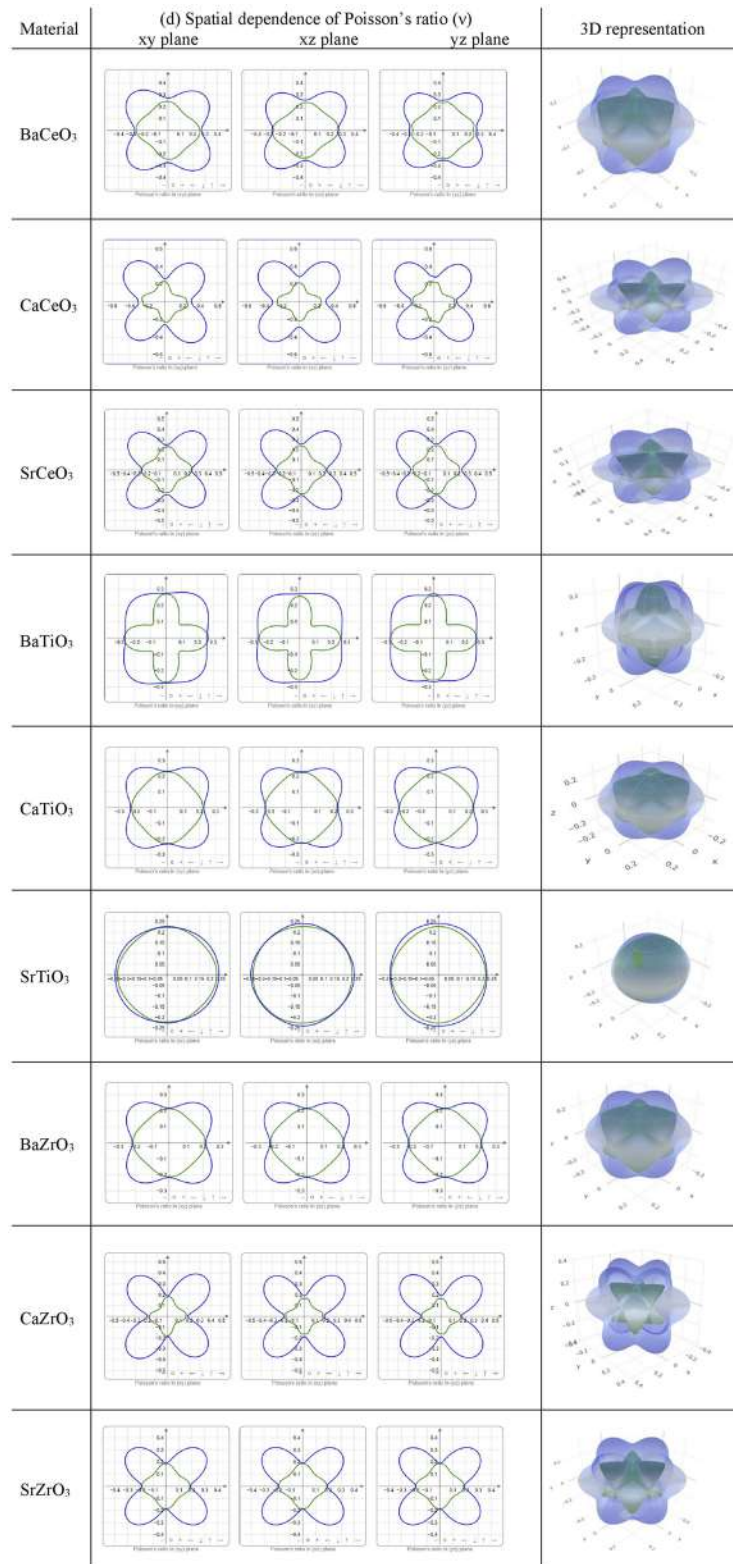


FIG. 2. (Continued.)

compressibility ( $K$ ), shear modulus ( $G$ ), and Poisson's ratio ( $\nu$ ) in the  $xy$ ,  $yz$ , and  $xz$  planes of  $ABO_3$  perovskites, which are illustrated in Fig. 2.<sup>36</sup>

## V. THERMODYNAMIC PROPERTIES

Thermodynamic properties are defined as system characteristics that can specify the system's state.<sup>37</sup> The lattice dynamics as well as the dielectric properties, the phonon dispersion curves, and the phonon density of states are very significant. These properties can be calculated using density functional perturbation theory.<sup>38</sup> The vibrational properties can be calculated using a harmonic approximation,<sup>39–42</sup>

$$D_{\mu\nu}(\mathbf{R} - \mathbf{R}') = \left. \frac{\partial^2 E}{\partial u_\mu(\mathbf{R}) \partial u_\nu(\mathbf{R}')} \right|_{u=0},$$

where  $u$  is the displacement of a given atom and  $E$  is the total energy in the harmonic approximation.

In reciprocal space, this dynamical force constant matrix is

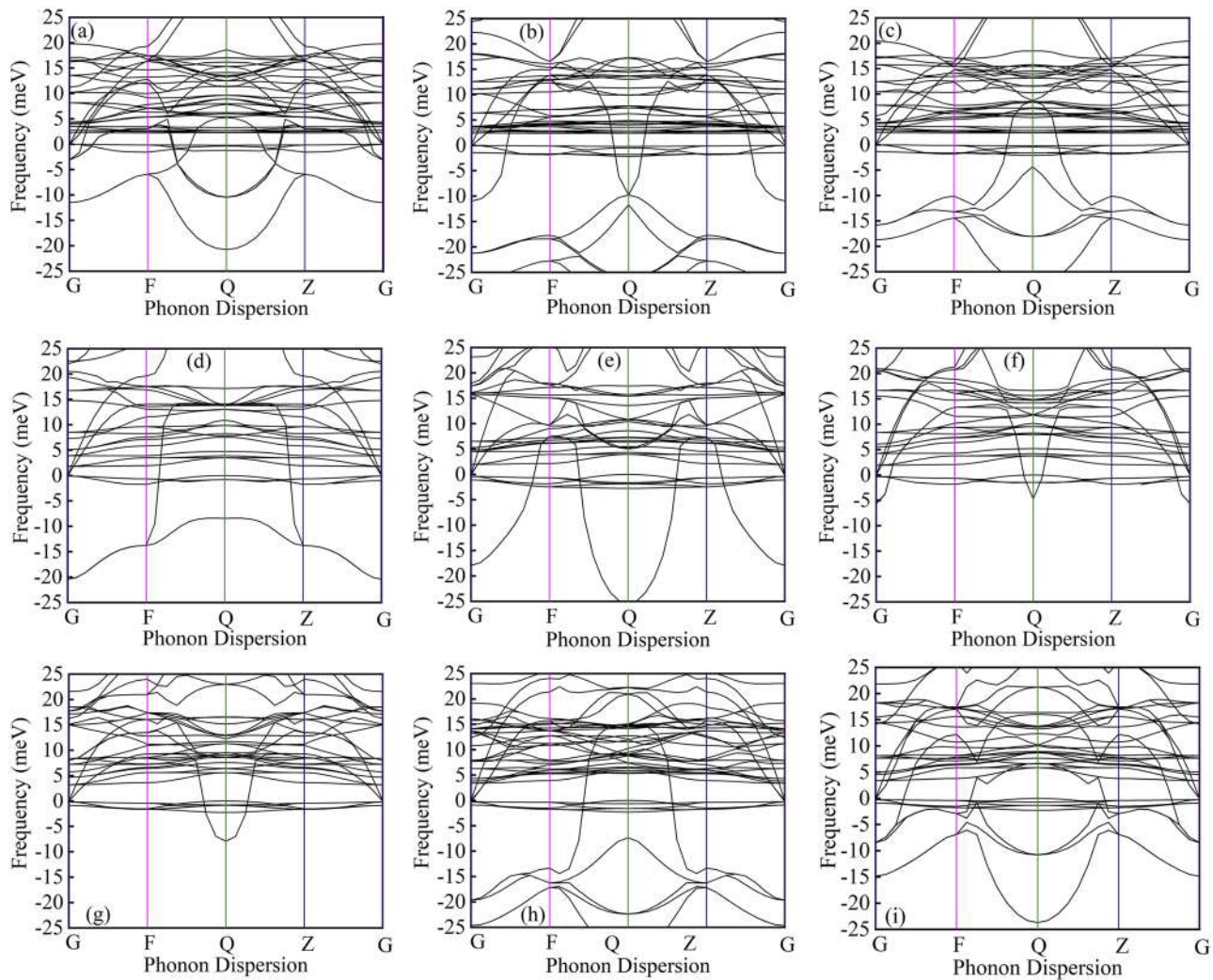
$$D_{\mu\nu}(\mathbf{q}) = \frac{1}{N_R} \sum_{\mathbf{R}} D_{\mu\nu}(\mathbf{R}) e^{-i\mathbf{q}\mathbf{R}}.$$

Here, the plane waves are evaluated for each atomic displacement,

$$u(\mathbf{R}, t) = \varepsilon e^{i(\mathbf{q}\mathbf{R} - \omega(\mathbf{q})t)}.$$

The polarization vector ( $\varepsilon$ ) of each mode is an eigenvector of 3N dimensions of the eigenvalue problem,

$$M\omega(\mathbf{q})^2 \varepsilon = D(\mathbf{q})\varepsilon.$$



**FIG. 3.** The calculated phonon dispersion curves along the high-symmetry points: (a) BaCeO<sub>3</sub>, (b) CaCeO<sub>3</sub>, (c) SrCeO<sub>3</sub>, (d) BaTiO<sub>3</sub>, (e) CaTiO<sub>3</sub>, (f) SrTiO<sub>3</sub>, (g) BaZrO<sub>3</sub>, (h) CaZrO<sub>3</sub>, and (i) SrZrO<sub>3</sub>.

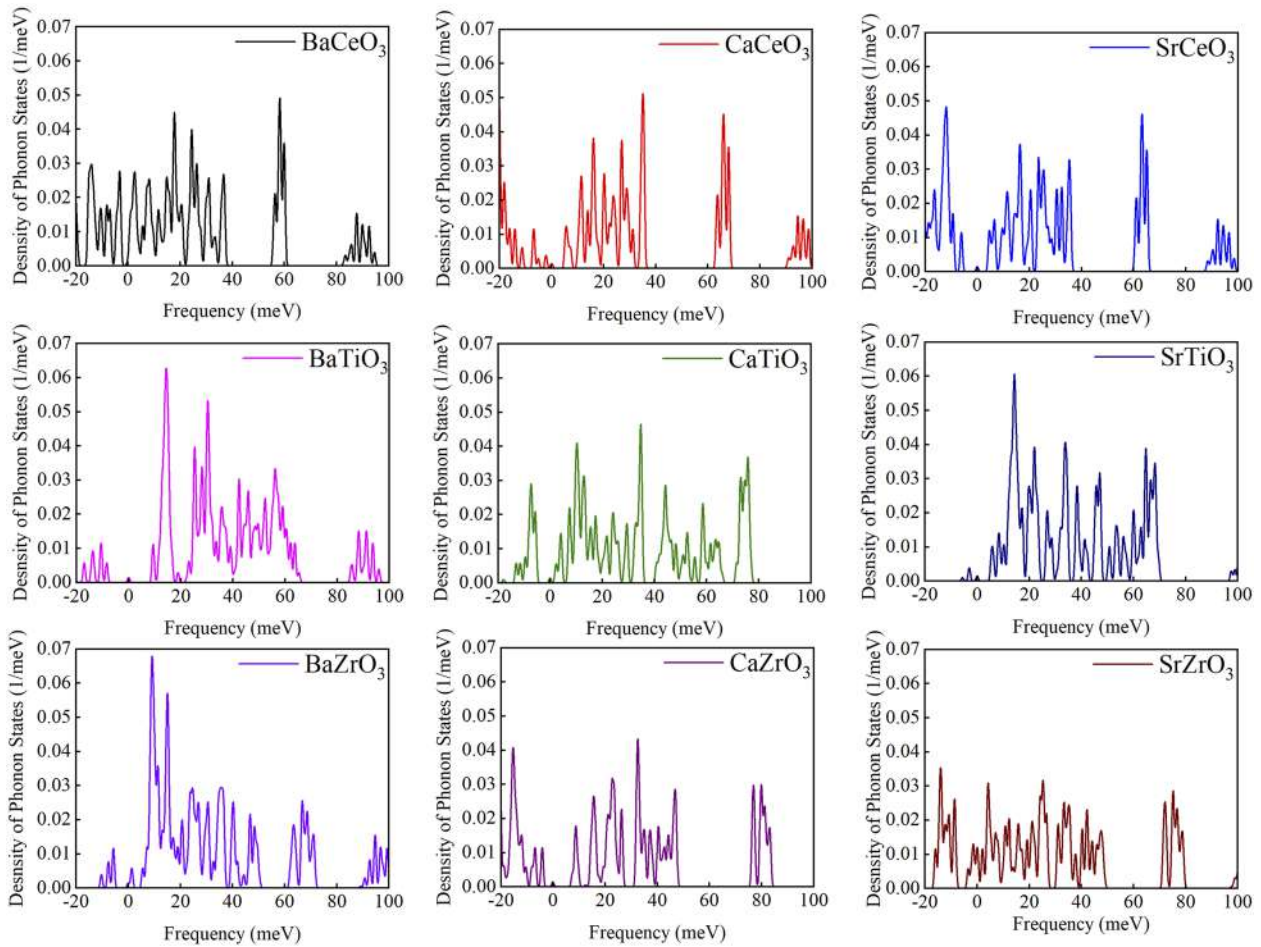


FIG. 4. The calculated phonon density of states of ABO<sub>3</sub> perovskites.

The partial density of state contribution on atom from each phonon band is

$$N_i(E) = \int \frac{d\mathbf{k}}{4\pi^3} |e_j(i)|^2 \delta(E - E_n(\mathbf{k})),$$

where  $e_j$  is the eigenvector related to the mode of the energy  $E_j$ .

In Fig. 3, the calculated phonon dispersion curves of various perovskites along the high-symmetry points in the Brillouin zone are shown. To get information about the dynamical stability of compounds, phonon dispersion curves are very important. The

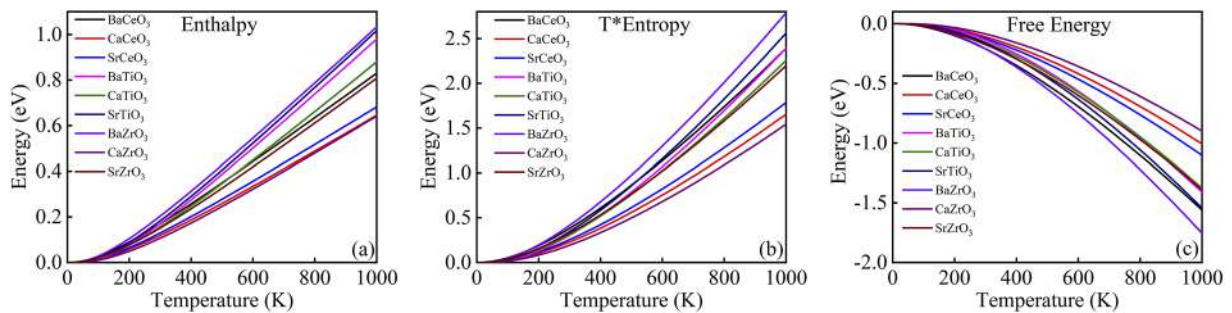


FIG. 5. The calculated (a) enthalpy, (b) T\*entropy, and (c) free energy of ABO<sub>3</sub> perovskites.



absence of negative frequencies covering the whole Brillouin zone indicates the dynamical stability against mechanical perturbation under normal pressure. There are two types of phonons—acoustic phonons and optical phonons. Acoustic phonons are related to the vibration of long-wavelength. In this case, in-phase vibrations are observed in the neighboring particles. Optical phonons are related to the vibrations of neighboring particles where the vibrations are nearly anti-phase. In the phonon dispersion curves, the acoustic modes are situated in the lower parts, whereas the optical modes are in the upper parts.<sup>43</sup> In both phonon dispersion (Fig. 3) and phonon DOS curves (Fig. 4), there are some imaginary frequencies curves below zero frequencies, which indicates the unstable modes. All the compounds have these unstable modes that are responsible for phase transition and ferroelectric responses of materials.

At finite temperature, the thermodynamic properties, such as enthalpy (H), entropy (S), and free energy (F), can be calculated from the vibrational properties of the materials,<sup>44,45</sup>

$$H(T) = E_{tot} + \frac{1}{2} \int g(\omega) \hbar \omega d\omega + \int \frac{\hbar \omega}{e^{\frac{\hbar \omega}{k_B T}} - 1} g(\omega) d\omega,$$

$$S(T) = k_B \left[ \int \frac{\frac{\hbar \omega}{k_B T}}{e^{\frac{\hbar \omega}{k_B T}} - 1} g(\omega) d\omega - \int g(\omega) \ln \left( 1 - e^{-\frac{\hbar \omega}{k_B T}} \right) d\omega \right],$$

$$F(T) = E_{tot} + \frac{1}{2} \int g(\omega) \hbar \omega d\omega + k_B T \int g(\omega) \ln \left( 1 - e^{-\frac{\hbar \omega}{k_B T}} \right) d\omega,$$

where  $g(\omega)$  is the phonon density of states and  $k_B$  is the Boltzmann constant.

In Fig. 5, the calculated temperature-dependent enthalpy and temperature times entropy increase with the increase in temperature, while the free energy decreases in all the cases. The evaluated values for all the cases obeyed the third law of thermodynamics as

TABLE III. The calculated zero point energy.

Materials	Zero-point energy (eV)
BaCeO <sub>3</sub>	0.1828
CaCeO <sub>3</sub>	0.1865
SrCeO <sub>3</sub>	0.1832
BaTiO <sub>3</sub>	0.2872
CaTiO <sub>3</sub>	0.2837
SrTiO <sub>3</sub>	0.2989
BaZrO <sub>3</sub>	0.2500
CaZrO <sub>3</sub>	0.2334
SrZrO <sub>3</sub>	0.2347

the values of all the terms for various ABO<sub>3</sub> perovskites approach zero as the temperature approaches absolute zero.

The temperature-dependent heat capacity and Debye temperature are calculated, and the comparison between the perovskites is also illustrated in Fig. 6.

The zero-point energy is the lowest possible energy that a quantum mechanical system can have. The zero-point energy of the studied materials is listed in Table III.

## VI. ELECTRONIC PROPERTIES

The study of the electronic band structure of solids is one of the most significant ways of describing electronic properties, such as conductivity, bonding properties, thermoelectric phenomenon, and magnetic properties. The electronic band structure (−5 eV to 5 eV) as a function of energy, E, of different ABO<sub>3</sub> [A = Ba, Ca, Co, Sr; B = Ce, Ti, Zr] perovskite structures at the ground state is shown in Fig. 7. A comparative study on bandgaps is illustrated in Fig. 8. While these computations at the ground state, the high-symmetry points (G-F-Q-Z-G) in the first Brillouin zone have been considered. In each diagram, the red horizontal dashed line represents the Fermi level ( $E_F$ ).

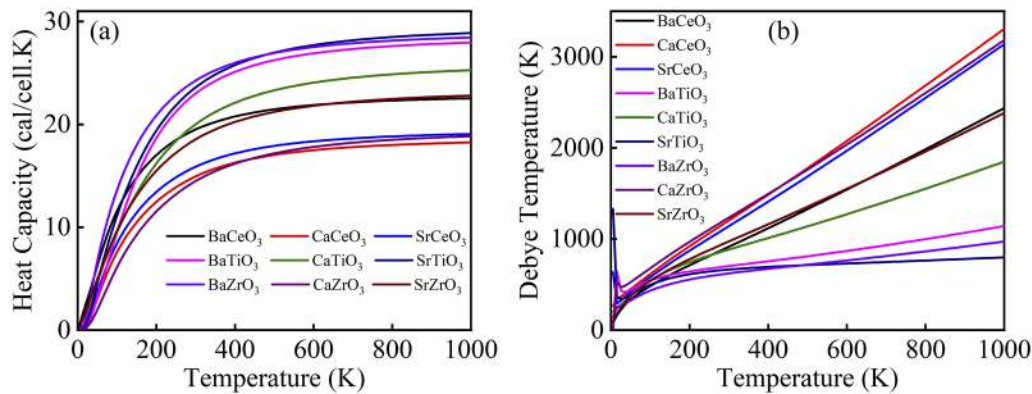
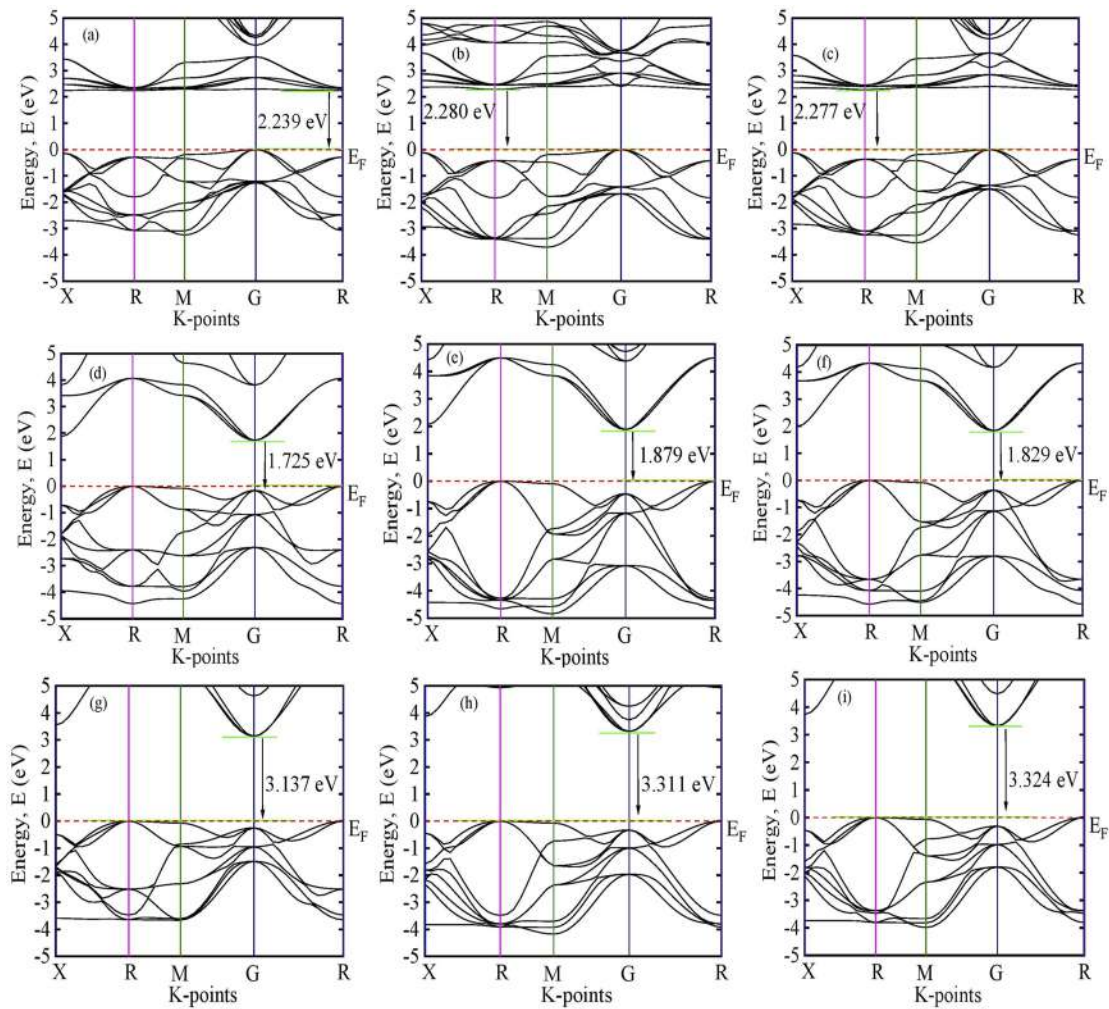


FIG. 6. The calculated temperature-dependent (a) heat capacity and (b) Debye temperature of ABO<sub>3</sub>.



**FIG. 7.** The calculated band diagrams along high-symmetry points: (a) BaCeO<sub>3</sub>, (b) CaCeO<sub>3</sub>, (c) SrCeO<sub>3</sub>, (d) BaTiO<sub>3</sub>, (e) CaTiO<sub>3</sub>, (f) SrTiO<sub>3</sub>, (g) BaZrO<sub>3</sub>, (h) CaZrO<sub>3</sub>, and (i) SrZrO<sub>3</sub>.

In Fig. 7, the valence bands are shown between 0 and  $-5$  eV and the conduction bands are between 0 and 5 eV. There is no overlap between the valance and conduction bands in all the cases. The bandgap for all the compounds is indirect. Figure 8 shows the comparison based on the computed bandgap of these perovskites, and the calculated sequence is

$$\begin{aligned} \text{SrZrO}_3 > \text{CaZrO}_3 > \text{BaZrO}_3 > \text{CaCeO}_3 > \text{SrCeO}_3 \\ > \text{BaCeO}_3 > \text{CaTiO}_3 > \text{SrTiO}_3 > \text{BaTiO}_3. \end{aligned}$$

The titanate family shows the lower bandgaps and the zirconate family has the higher bandgaps. The barium based ceramics show lower bandgaps in cerate, titanate, and zirconate families in this study. The bandgaps of cerates and zirconates lie in between conventional semiconductors and insulators with wide bandgaps.

Materials with wide bandgaps always have a scientific and technological interest because of their use in high-performance electronic and optoelectronic devices, such as blue LEDs and lasers. Higher bandgaps allow electronic devices to operate at higher temperatures. However, semiconductors with a lower bandgap have a great impact on solar cells.<sup>46–48</sup>

In the field of condensed matter physics, the number of electronic states available to be occupied per unit energy interval is the density of states (DOS) of that system. The density of states plays an important role in understanding the bonding nature, both thermal and electrical conductivity, and magnetic and optoelectronic properties; determining the transition rates; and so on. The total density of states (TDOS) can be used to explain the performance of electronic devices.<sup>49</sup> The electronic and structural stability to some extent depends on the TDOS of the material and the position of the corresponding Fermi level.<sup>50,51</sup> Calculated TDOS and partial

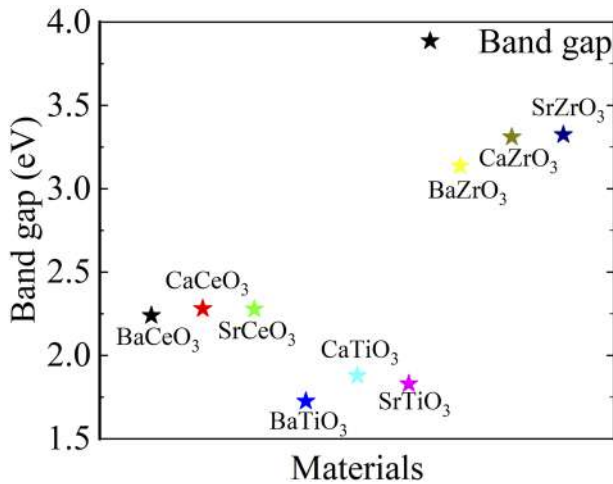


FIG. 8. Comparison of band gaps of ABO<sub>3</sub> perovskites.

density of states (PDOS) from  $-6$  to  $6$  eV have been shown in Figs. 9 and 10. The dashed red line represents the Fermi level ( $E_F$ ). In the energy region  $0.5$ – $1.4$  eV, the electrons for all the ceramics have negligible electronic contributions. It is clear that the cerate, titanate, and zirconate families have almost the same patterns. However, CaCeO<sub>3</sub> has an additional broad peak in the energy region from  $3.4$  to  $5.1$  eV.

The calculated partial density of states ( $-6$  to  $6$  eV) has been illustrated in Fig. 10. The valance band in all cases lies between  $-6$  and  $0$  eV, and conduction bands are from  $0$  to  $6$  eV. In the both valance band and conduction band, most of the contribution comes from Ba-6s, Ba-5p, Ca-4s, Ca-3p, Sr-5s, Sr-4p, Ce-6s, Ce-5p, Ce-5d, Ce-4f, Ti-4s, Ti-3p, Ti-3d, Zr-5s, Zr-4p, Zr-4d, O-2s, and O-2p orbitals. In the cerate family, bonding mostly depends on Ba-6s,

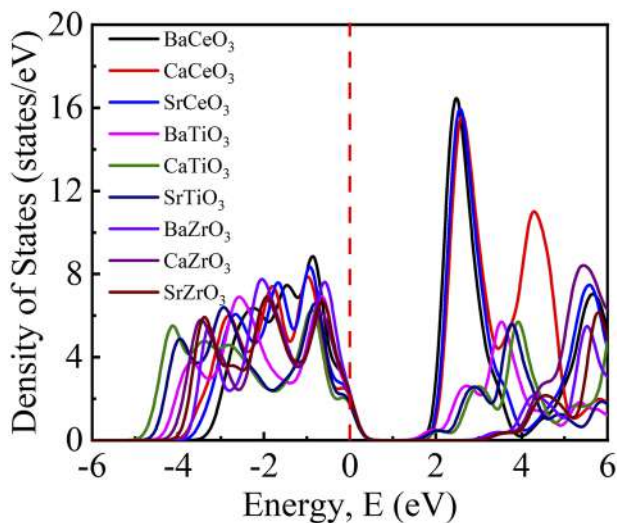


FIG. 9. Calculated electron density of states of various ABO<sub>3</sub> perovskites.

Ba-5p, Ca-4s, Sr-5s, Ce-4f, and O-2p; in the titanate family, Ba-6s, Ba-5p, Ca-4s, Sr-5s, Sr-4p, Ti-3d, and O-2p have the most influence; and in the Zirconate family, Ba-6s, Ba-5p, Ca-4s, Sr-6s, Zr-4d, and O-2p have the most influence.

## VII. OPTICAL PROPERTIES

When the electromagnetic waves fall on the surface of a material, the photon interacts with the charge carriers of that material. This photon-charge carrier interaction influences the optical properties of a material. This type of photon-charge carrier interaction can be calculated by using some parameters, which are a function of the frequency or the energy of the incident photon. While calculating the optical properties of all the structures, the considered frequency-dependent complex dielectric function is

$$\epsilon(\omega) = \epsilon_1(\omega) + i\epsilon_2(\omega).$$

Here, the real part of the dielectric function is  $\epsilon_1(\omega)$ , and according to Kramers–Kronig transformations, it depends on the imaginary part,  $\epsilon_2(\omega)$ .

The imaginary part,  $\epsilon_2(\omega)$ , can be calculated using the matrix elements of optical transitions between occupied and unoccupied electronic orbitals, which can be expressed with CASTEP formulation as

$$\epsilon_2(\omega) = \frac{2e^2\pi}{\Omega\epsilon_0} \sum_{k,v,c} |\psi_k^c| \mathbf{u} \cdot \mathbf{r} |\psi_k^v|^2 \delta(E_k^c - E_k^v - E),$$

where  $\omega$  is the frequency of the photon,  $e$  is the charge of the electron,  $\psi_k^c$  and  $\psi_k^v$  are the wave functions of the conduction band and valance band, respectively, and  $\mathbf{u}$  is the polarization vector of the incident electric field. Different optical parameters, such as absorptivity, reflectivity, refractive index, optical conductivity, and energy loss function, can be determined by the dielectric function  $\epsilon(\omega)$ .<sup>52,53</sup>

From Fig. 11, it can be seen that in the region  $0$ – $15$  eV, the behavior of all the materials is different from each other. In the energy region  $15$ – $30$  eV, the titanate and zirconate families show a similar pattern in the case of absorption.

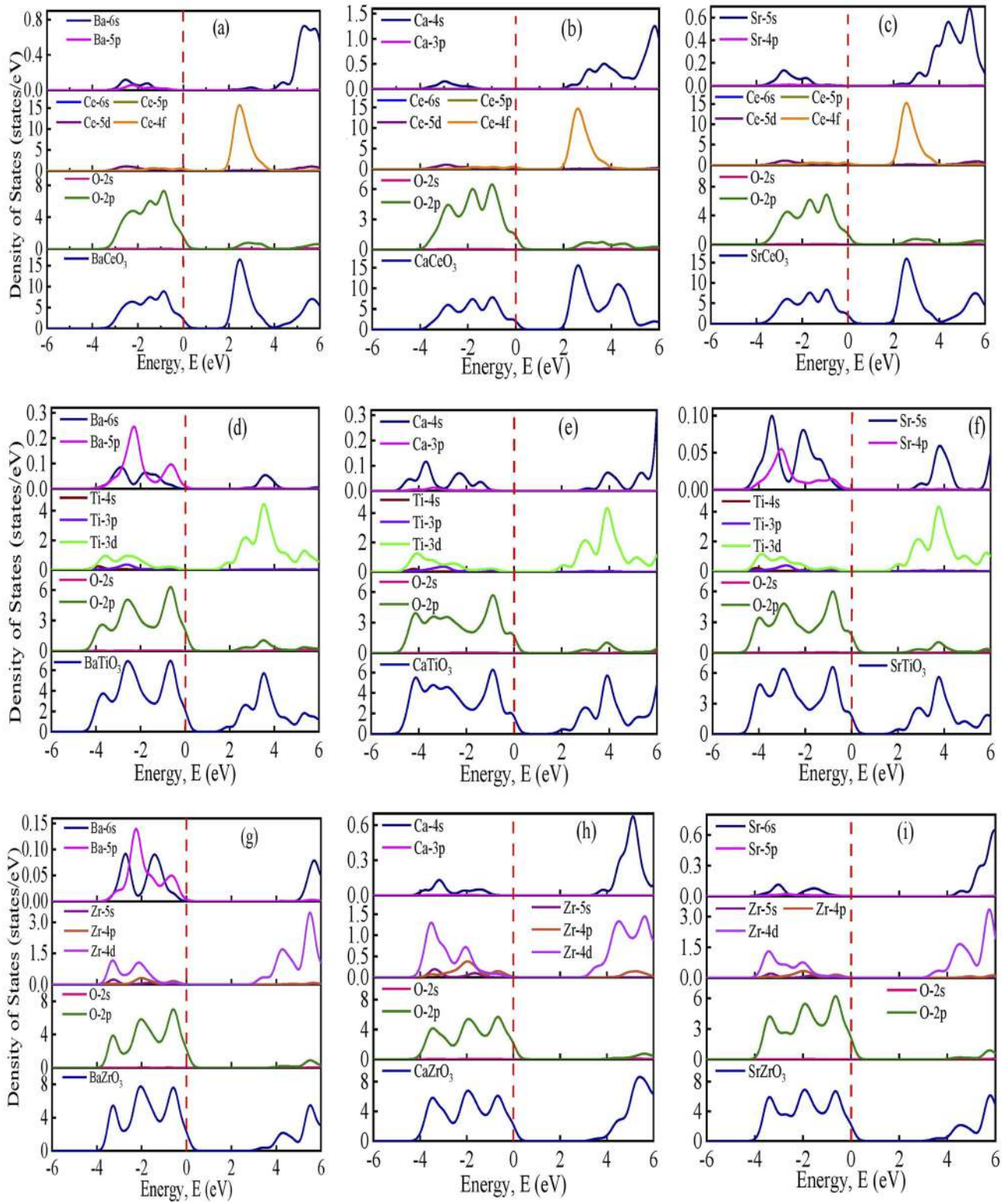
In the IR–UV ( $1.2$ – $3.6$  eV) region, linear progression is seen for absorption, reflectivity, and real part of the refractive index ( $n$ ), while CaTiO<sub>3</sub> and SrZrO<sub>3</sub> have higher values of absorption and they are less reflective in the IR region. An exponential increase in the real part of conductivity and the imaginary part of the refractive index ( $k$ ) for the titanate and cerate families is observed in the IR–UV region, but this rate is higher in the titanate family. The imaginary part of the conductivity is negative (except for SrZrO<sub>3</sub>) and decreasing in nature in all the materials.

In the IR region ( $\sim 1$  eV), CaTiO<sub>3</sub> and SrZrO<sub>3</sub> have higher values for absorption, the real part of conductivity, and the imaginary part of the dielectric function.

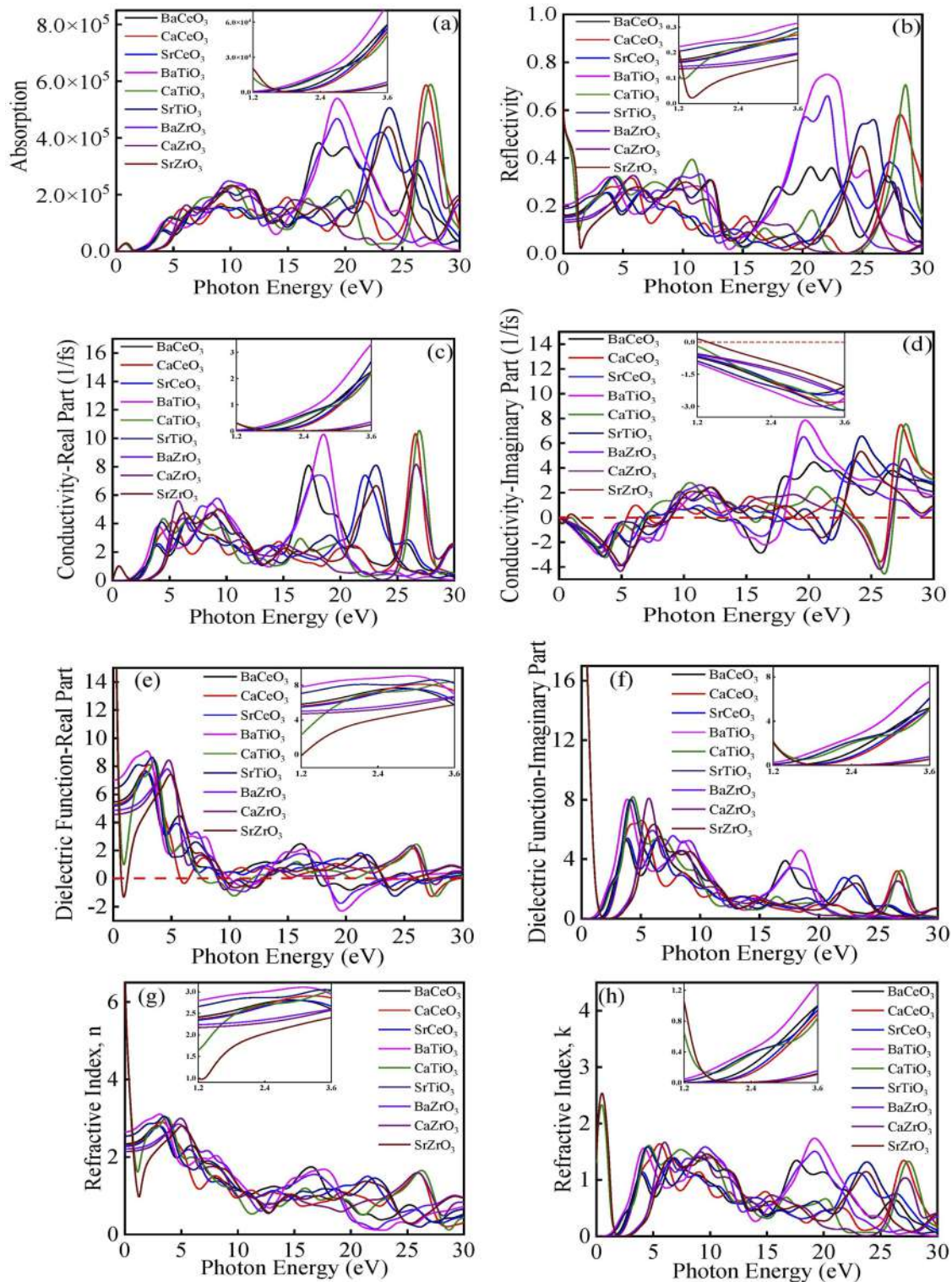
For all energy regions, the imaginary part of the conductivity and dielectric function, the real part of the refractive index ( $n$ ), and the imaginary part of the refractive index ( $k$ ) follow almost similar patterns for Ba, Ca, and Sr families.

The loss function is the loss of energy of the first electron passing through a material. It is associated with the collective oscillation frequency of the valance electron. The peaks of the loss function are





**FIG. 10.** The calculated partial density of states (PDOS) of (a) BaCeO<sub>3</sub>, (b) CaCeO<sub>3</sub>, (c) SrCeO<sub>3</sub>, (d) BaTiO<sub>3</sub>, (e) CaTiO<sub>3</sub>, (f) SrTiO<sub>3</sub>, (g) BaZrO<sub>3</sub>, (h) CaZrO<sub>3</sub>, and (i) SrZrO<sub>3</sub>.



**FIG. 11.** The calculated (a) absorption, (b) reflectivity, (c) real part of conductivity, (d) imaginary part of conductivity, (e) real part of the dielectric function, (f) imaginary part of the dielectric function, (g) refractive index ( $n$ ), and (h) refractive index ( $k$ ) of various  $ABO_3$  perovskites.



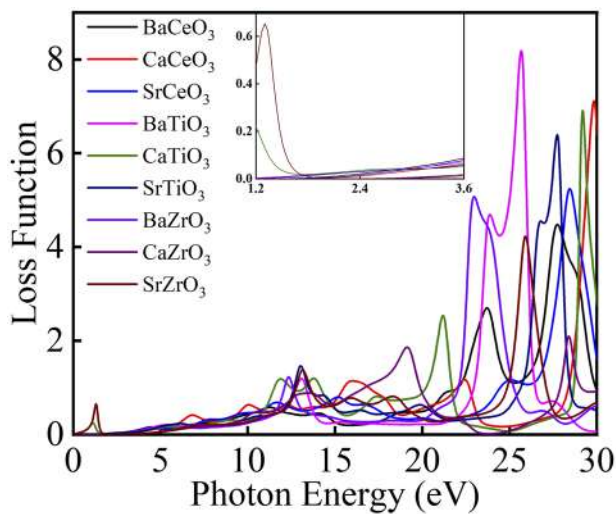


FIG. 12. The calculated loss function of ABO<sub>3</sub> perovskites.

related to a characteristic frequency of a material, plasma frequency. In Fig. 12, minor peaks are observed in the IR region for the materials CaTiO<sub>3</sub> and SrZrO<sub>3</sub>. Several but random peaks are observed for different perovskites after 10 eV.

## VIII. CONCLUSIONS

The first-principles method based on DFT within GGA-PBE exchange–correlation has been used to study the structural, mechanical, thermodynamic, electronic, and optical properties of ABO<sub>3</sub> [A = Ba, Ca, Sr; B = Ce, Ti, Zr] perovskites. Each material shows different behavior considering different parameters. Several mechanical properties of materials, such as 2D and 3D visualization of Young’s modulus, shear modulus, compressibility, Poisson’s ratio, phonon dispersion, phonon density of states, different thermodynamic properties, band structure, the electron density of states, the partial density of states, and different optical properties of all the perovskites have been calculated and compared. All the figures and tables provided in this paper give the statistics of a specific parameter to the researchers. This paper provides information about these commonly used materials, which will be useful in tailoring new materials based on these compounds.

## ACKNOWLEDGMENTS

The authors gratefully acknowledge ICT of Bangladesh University of Engineering and Technology for the server facility and thank Sunjida Haque, Assistant Professor, City University, and Dr. Roksana Parvin, Solid State Physics laboratory, BUET, for their support.

## AUTHOR DECLARATIONS

### Conflict of Interest

The authors have no conflicts to disclose.

## Author Contributions

**Mehedi Hasan:** Conceptualization (lead); Data curation (lead); Formal analysis (lead); Investigation (lead); Methodology (lead); Software (lead); Visualization (lead). **Sharifa Nasrin:** Formal analysis (supporting); Investigation (supporting). **M. Nazrul Islam:** Formal analysis (supporting); Investigation (supporting). **A. K. M. Akther Hossain:** Supervision (lead).

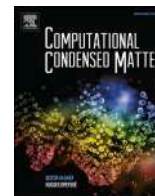
## DATA AVAILABILITY

The data that support the findings of this study are available from the corresponding author upon reasonable request.

## REFERENCES

- E. A. Katz, “Perovskite: Name puzzle and German–Russian odyssey of discovery,” *Helv. Chim. Acta* **103**(06), 1–12 (2020).
- V. M. Goldschmidt, “Die Gesetze der Krystallochemie,” *Naturwissenschaften* **14**, 477–485 (1926).
- M. A. Peña and J. L. G. Fierro, “Chemical structures and performance of perovskite oxides,” *Chem. Rev.* **101**(07), 1981–2018 (2001).
- M. R. Filip and F. Giustino, “The geometric blueprint of perovskites,” *Proc. Natl. Acad. Sci. U. S. A.* **115**(21), 5397–5402 (2018).
- O. Saburi, “Properties of semiconductive barium titanate,” *J. Phys. Soc. Jpn.* **14**(09), 1159–1174 (1959).
- G. G. Harman, “Electrical properties of BaTiO<sub>3</sub> containing samarium,” *Phys. Rev.* **106**, 1358–1359 (1957).
- F. Jona and G. Shirane, *Ferroelectric Crystals* (Elsevier, Amsterdam, 1963).
- H. Kishi, Y. Mizuno, and H. Chazono, “Base-metal electrode-multilayer ceramic capacitors: Past, present and future perspectives,” *Jpn. J. Appl. Phys.* **42**, 1–15 (2003).
- B. Huybrechts, K. Ishizaki, and M. Takata, “The positive temperature coefficient of resistivity in barium titanate,” *J. Mater. Sci.* **30**(10), 2463–2474 (1995).
- B. Jaffe, W. R. Cook, and H. Jaffe, *Piezoelectric Ceramics* (Academic Press, London, 1971), Vol. 3, p. 120.
- P. K. Panda, “Review: Environmental friendly lead-free piezoelectric materials,” *J. Mater. Sci.* **44**, 5049–5062 (2009).
- S.-Y. Liu, M. Sun, S. Zhang, S. Liu, D.-J. Li, Z. Niu, Y. Li, and S. Wang, “First-principles study of thermodynamic miscibility, structures, and optical properties of Cs<sub>2</sub>Sn(X<sub>1-x</sub>Y<sub>x</sub>)<sub>6</sub> (X, Y = I, Br, Cl) lead-free perovskite solar cells,” *Appl. Phys. Lett.* **118**, 141903 (2021).
- S.-Y. Liu, Y. Meng, S. Liu, D.-J. Li, Y. Li, Y. Liu, Y. Shen, and S. Wang, “Compositional phase diagram and microscopic mechanism of Ba<sub>1-x</sub>Ca<sub>x</sub>Zr<sub>y</sub>Ti<sub>1-y</sub>O<sub>3</sub> relaxor ferroelectrics,” *Phys. Chem. Chem. Phys.* **19**(33), 22190–22196 (2017).
- S. J. Clark, M. D. Segall, C. J. Pickard, P. J. Hasnip, M. I. J. Probert, K. Refson, and M. C. Payne, “First principles methods using CASTEP,” *Z. Kristallogr.* **220**, 567–570 (2005).
- J. P. Perdew, K. Burke, and M. Ernzerhof, “Generalized gradient approximation made simple,” *Phys. Rev. Lett.* **77**(18), 3865–3868 (1996).
- D. Vanderbilt, “Soft self-consistent pseudopotentials in a generalized eigenvalue formalism,” *Phys. Rev. B* **41**(11), 7892–7895 (1990).
- T. H. Fischer and J. Almlof, “General methods for geometry and wave function optimization,” *J. Phys. Chem.* **96**(24), 9768–9774 (1992).
- H. J. Monkhorst and J. D. Pack, “Special points for Brillouin-zone integrations,” *Phys. Rev. B* **13**(12), 5188–5192 (1976).
- S.-Y. Liu, E. Zhang, S. Liu, D.-J. Li, Y. Li, Y. Liu, Y. Shen, and S. Wang, “Composition- and pressure-induced relaxor ferroelectrics: First-principles calculations and Landau–Devonshire theory,” *J. Am. Ceram. Soc.* **99**(10), 3336–3342 (2016).

- <sup>20</sup>A. S. Verma and V. K. Jindal, "Lattice constant of cubic perovskites," *J. Alloys Compd.* **485**(1-2), 514–518 (2009).
- <sup>21</sup>M. Hasan and A. K. M. Akther Hossain, "Structural, electronic and optical properties of strontium and nickel co-doped BaTiO<sub>3</sub>: A DFT based study," *Comput. Condens. Matter* **28**, e00578 (2021).
- <sup>22</sup>R. L. Moreira and A. Dias, "Comment on 'Prediction of lattice constant in cubic perovskites,'" *J. Phys. Chem. Solids* **68**, 1617–1622 (2007).
- <sup>23</sup>L. Q. Jiang, J. K. Guo, H. B. Liu, M. Zhu, X. Zhou, P. Wu, and C. H. Li, "Prediction of lattice constant in cubic perovskites," *J. Phys. Chem. Solids* **67**(07), 1531–1536 (2006).
- <sup>24</sup>F. D. Murnaghan, *Finite Deformation of an Elastic Solid* (Wiley, New York, 1951).
- <sup>25</sup>M. Rabiei, A. Palevicius, A. Dashti, S. Nasiri, A. Monshi, A. Vilkauskas, and G. Janusas, "Measurement modulus of elasticity related to the atomic density of planes in unit cell of crystal lattices," *Materials* **13**(19), 4380 (2020).
- <sup>26</sup>S.-Y. Liu, S. Zhang, S. Liu, D.-J. Li, Y. Li, and S. Wang, "Phase stability, mechanical properties and melting points of high-entropy quaternary metal carbides from first-principles," *J. Eur. Ceram. Soc.* **41**(13), 6267–6274 (2021).
- <sup>27</sup>Y. Han, Y. Wu, T. Li, R. Khenata, T. Yang, and X. Wang, "Electronic, magnetic, half-metallic, and mechanical properties of a new equiatomic quaternary Heusler compound YRhTiGe: A first-principles study," *Materials* **11**(05), 797 (2018).
- <sup>28</sup>L. Kleinman, "Deformation potentials in silicon. I. Uniaxial strain," *Phys. Rev.* **128**(06), 2614–2621 (1962).
- <sup>29</sup>W. A. Harrison, *Electronic Structure and the Properties of Solids* (Freeman, San Francisco, 1980).
- <sup>30</sup>W. Feng and S. Cui, "Mechanical and electronic properties of Ti<sub>2</sub>AlN and Ti<sub>4</sub>AlN<sub>3</sub>: A first principles study," *Can. J. Phys.* **92**(12), 1652–1657 (2014).
- <sup>31</sup>D. G. Pettifor, "Theoretical predictions of structure and related properties of intermetallics," *Mater. Sci. Technol.* **8**(04), 345–349 (1992).
- <sup>32</sup>M. K. Butt, M. Yaseen, I. A. Bhatti, J. Iqbal, Misbah, A. Murtaza, M. Iqbal, M. M. AL-Anazy, M. H. Alhossainy, and A. Laref, "A DFT study of structural, magnetic, elastic and optoelectronic properties of lanthanide based XAlO<sub>3</sub> (X = Nd, Gd) compounds," *J. Mater. Res. Technol.* **9**(6), 16488–16496 (2020).
- <sup>33</sup>S. F. Pugh, "Relations between the elastic moduli and the plastic properties of polycrystalline pure metals," *London, Edinburgh Dublin Philos. Mag. J. Sci.* **45**(367), 823–843 (1954).
- <sup>34</sup>H. Ledbetter and A. Migliori, "A general elastic-anisotropy measure," *J. Appl. Phys.* **100**(06), 063516 (2006).
- <sup>35</sup>S. I. Ranganathan and M. Ostojic-Starzewski, "Universal elastic anisotropy index," *Phys. Rev. Lett.* **101**(05), 055504 (2008).
- <sup>36</sup>R. Gaillac, P. Pullumbi, and F.-X. Coudert, "ELATE: An open-source online application for analysis and visualization of elastic tensors," *J. Phys.: Condens. Matter* **28**, 275201 (2016).
- <sup>37</sup>S.-Y. Liu, S. Zhang, S. Liu, D.-J. Li, Z. Niu, Y. Li, and S. Wang, "Stability and mechanical properties of single-phase quinary high-entropy metal carbides: First-principles theory and thermodynamics," *J. Eur. Ceram. Soc.* **42**(7), 3089–3098 (2022).
- <sup>38</sup>K. Refson, P. R. Tulip, and S. J. Clark, "Variational density-functional perturbation theory for dielectrics and lattice dynamics," *Phys. Rev. B* **73**(15), 155114 (2006).
- <sup>39</sup>A. Tkatchenko and M. Scheffler, "Accurate molecular van der Waals interactions from ground-state electron density and free-atom reference data," *Phys. Rev. Lett.* **102**(07), 073005-1-073005-4 (2009).
- <sup>40</sup>E. Moreira, C. A. Barboza, E. L. Albuquerque, U. L. Fulco, J. M. Henriques, and A. I. Araújo, "Vibrational and thermodynamic properties of orthorhombic CaSnO<sub>3</sub> from DFT and DFPT calculations," *J. Phys. Chem. Solids* **77**, 85–91 (2015).
- <sup>41</sup>M. Born and K. Huang, *Dynamical Theory of Crystal Lattices* (Oxford University Press, 1966).
- <sup>42</sup>N. W. Ashcroft and N. D. Mermin, *Solid State Physics* (Saunders College, Philadelphia, 1976), p. 2010.
- <sup>43</sup>S. Akhtar, S. M. Alay-e-Abbas, J. Batool, W. Zulfiqar, A. Laref, G. Abbas, and N. Amin, "Investigation of structural, electronic and optical properties of (V+P)-doped BaZrO<sub>3</sub> for photocatalytic applications using density functional theory," *J. Phys. Chem. Solids* **147**, 109662 (2020).
- <sup>44</sup>S. Baroni, S. de Gironcoli, A. Dal Corso, and P. Giannozzi, "Phonons and related crystal properties from density-functional perturbation theory," *Rev. Mod. Phys.* **73**(02), 515–562 (2001).
- <sup>45</sup>B. Luo, X. wang, E. Tian, G. Li, and L. Li, "Electronic structure, optical and dielectric properties of BaTiO<sub>3</sub>/CaTiO<sub>3</sub>/SrTiO<sub>3</sub> ferroelectric superlattices from first-principles calculations," *J. Mater. Chem. C* **3**, 8625–8633 (2015).
- <sup>46</sup>S. J. Pearton, D. P. Norton, K. Ip, Y. W. Heo, and T. Steiner, "Recent progress in processing and properties of ZnO," *Superlattices Microstruct.* **34**(1-2), 3–32 (2003).
- <sup>47</sup>C. G. Granqvist, "Transparent conductors as solar energy materials: A panoramic review," *Sol. Energy Mater. Sol. Cells* **91**(17), 1529–1598 (2007).
- <sup>48</sup>H. Hosono, "Recent progress in transparent oxide semiconductors: Materials and device application," *Thin Solid Films* **515**(15), 6000–6014 (2007).
- <sup>49</sup>J. W. Haus, "Nanophotonic devices," *Fundamentals and Applications of Nanophotonics* (Woodhead Publishing, 2016), Vol. 341–395.
- <sup>50</sup>J. H. Xu, T. Oguchi, and A. J. Freeman, "Solid-solution strengthening: Substitution of V in Ni<sub>3</sub>Al and structural stability of Ni<sub>3</sub>(Al, V)," *Phys. Rev. B* **36**(08), 4186–4189 (1987).
- <sup>51</sup>T. Hong, T. J. Watson-Yang, A. J. Freeman, T. Oguchi, and J.-h. Xu, "Crystal structure, phase stability, and electronic structure of Ti-Al intermetallics: TiAl<sub>3</sub>," *Phys. Rev. B* **41**(18), 12462–12467 (1990).
- <sup>52</sup>S. M. Alay-e-Abbas, F. Javed, G. Abbas, N. Amin, and A. Laref, "Density functional theory evaluation of ceramics suitable for hybrid advanced oxidation processes: A case study for Ce<sup>4+</sup>-doped BaZrO<sub>3</sub>," *J. Phys. Chem. C* **123**(10), 6044–6053 (2019).
- <sup>53</sup>M. S. Dresselhaus, *Solid State Physics Part II Optical Properties of Solids* (1999).



# Structural, electronic and optical properties of strontium and nickel co-doped BaTiO<sub>3</sub>: A DFT based study

Mehedi Hasan<sup>a,b,\*</sup>, A.K.M. Akther Hossain<sup>b</sup>

<sup>a</sup> General Education Department, City University, Bangladesh

<sup>b</sup> Department of Physics, Bangladesh University of Engineering and Technology, Dhaka, Bangladesh

## ARTICLE INFO

### Keywords:

DFT  
Perovskites  
Barium titanate  
Ni-doped  
Sr-doped

## ABSTRACT

Density functional theory-based investigation of the structural, electronic, and optical properties of pristine and strontium, nickel doped barium titanate has been carried out by the plane-wave pseudopotential technique with generalized gradient approximation. The lattice constants of optimized structure, the electronic band structures, total and partial density of states and the optical properties such as absorption, reflectivity, dielectric function, photoconductivity, refractive index and the loss function of the pristine and doped materials have been calculated and thoroughly explained. In this study, we have found (Sr, Ni) co-doping in BTO reduces the lattice constant and structural volume. The band gap of co-doped material found less than the pristine BTO. The simulated optical spectroscopic analysis reveals that the (Sr, Ni) co-doped materials are good dielectric and photoconductive materials.

## 1. Introduction

BaTiO<sub>3</sub> (BTO) is an important ferroelectric material with perovskite structure which shows good dielectric, ferroelectric, piezoelectric, and electro-optical properties hence it is widely used in electronic industries [1–3]. It is also used as a base material for many important ceramic components and devices, such as Multi-Layer Ceramic Capacitors (MLCC), piezoelectric ceramic transducers [4–6]. However, barium titanate shows a low Curie temperature,  $T_c = 120$  °C which can cause temperature stabilization problems and redundant aging [7,8]. To resolve this problem, some other materials were used to form a solid solution with barium titanate [9–11] have a great technological importance for device applications. Considerable work has been done for modifying the device parameter of these systems with a wide variety of substitution at the A-and/or B-site of the BTO system. In order to improve dielectric properties and to control grain-size for the electronic device applications, doping and co-doping on A-site has been done to BaTiO<sub>3</sub> based ceramics [12–18]. (see Table 1)

Doping with Bi<sup>3+</sup> and Li<sup>+</sup> on A-site of BaTiO<sub>3</sub>, enhanced the ferroelectric property, showed giant photovoltaic response [19] and low dielectric loss characteristics [20]. In Ba<sub>1-x</sub>Sr<sub>x</sub>TiO<sub>3</sub>, the temperature dependence of permittivity and of dielectric loss tangent at low frequency (1 kHz) showed a decrease of Curie temperature with the

increase of Sr content [21]. Polycrystalline Sr-doped BaTiO<sub>3</sub> showed a slight shift in diffraction peaks to the higher 2θ diffraction angle with the addition of Sr-content showing the improvement in crystallinity of the films, dielectric constant increases with Sr-dopant concentration [22]. The dielectric and ferroelectric properties of (Ba<sub>x</sub>Sr<sub>1-x</sub>)<sub>0.77</sub>Ca<sub>0.23</sub>TiO<sub>3</sub> ceramics showed that Sr doping of the Ba<sub>0.77</sub>Ca<sub>0.23</sub>TiO<sub>3</sub> ceramics causes a drastic decrease in the  $T_c$ , just like Sr doping of pristine BaTiO<sub>3</sub> ceramics, demonstrating a cell volume effect [23]. The fabrication of Ba<sub>1-x</sub>Ni<sub>x</sub>TiO<sub>3</sub> showed a decrease in crystallite size, lattice strain,  $c/a$  ratio and grain size with Ni doping, shifted in transition temperature, increasing diffuse phase transition and decreasing dielectric constant and  $T_c$  and maximum dielectric constant increase with increasing magnetic poling strength along with decreasing the nature of diffusivity thus showing multiferroic nature [24,25]. In this paper, we have used a computational method to investigate the structural, electronic and optical properties of Ni, Sr doped on A-site of BaTiO<sub>3</sub>. We have used four different structures where one is pristine BTO, BaTiO<sub>3</sub>, one is 12.5% Sr atom doped BTO, Ba<sub>0.875</sub>Sr<sub>0.125</sub>TiO<sub>3</sub> (BSTO), another is 12.5% Ni atom doped BTO, Ba<sub>0.875</sub>Ni<sub>0.125</sub>TiO<sub>3</sub> (BNTO) and finally 25% (Sr, Ni) co-doped BTO, Ba<sub>0.75</sub>(Sr<sub>0.5</sub>Ni<sub>0.5</sub>)<sub>0.25</sub>TiO<sub>3</sub> (BSNTO).

\* Corresponding author. General Education Department, City University, Bangladesh.  
E-mail address: [mehedi.physics@gmail.com](mailto:mehedi.physics@gmail.com) (M. Hasan).

<https://doi.org/10.1016/j.cocom.2021.e00578>

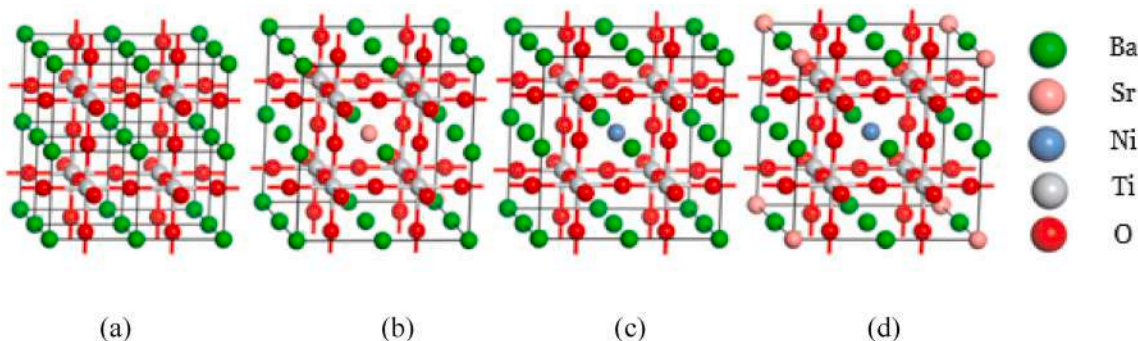
Received 20 May 2021; Received in revised form 5 June 2021; Accepted 6 July 2021

Available online 7 July 2021

2352-2143/© 2021 Elsevier B.V. All rights reserved.

**Table 1**  
Calculated parameters of pristine and Ni, Sr doped BaTiO<sub>3</sub> perovskites.

Material	Structure	a = b = c Å	Volume Å <sup>3</sup>	Density g/cm <sup>3</sup>
Pristine BTO (BaTiO <sub>3</sub> )	Cubic	This work: 4.03 Experimental Study: 4.00 [29] Other Theoretical Study: 4.01 [30]	65.67	5.90
BSTO (Ba <sub>0.875</sub> Sr <sub>0.125</sub> TiO <sub>3</sub> )	Cubic	4.03	65.28	5.77
BNT0 (Ba <sub>0.875</sub> Ni <sub>0.125</sub> TiO <sub>3</sub> )	Cubic	4.02	64.84	5.72
BSNTO (Ba <sub>0.75</sub> (Sr <sub>0.5</sub> Ni <sub>0.5</sub> ) <sub>0.25</sub> TiO <sub>3</sub> )	Cubic	4.01	64.29	5.56



**Fig. 1.** Geometrically optimized (a) Pristine BaTiO<sub>3</sub>, (b) 12.5% Sr atom doped BTO, (BSTO) and (c) 12.5% Ni atom doped BTO, (BNT0) and (d) 25% atom (Sr, Ni) co-doped BTO, BSNT0.

## 2. Computational methodology

Density Functional Theory (DFT) based a plane-wave pseudopotential method was used to carry out this study using a framework- Cambridge Serial Total Energy Package (CASTEP) code. The exchange-correlation energy of electrons is evaluated under the generalized gradient approximation (GGA) with the method of Perdew–Burke–Ernzerhof (PBE) [26]. The valence electronic states were considered as 5p<sup>6</sup> 6s<sup>2</sup> for Ba, 4p<sup>6</sup> 5s<sup>2</sup> for Sr, 3d<sup>8</sup> 4s<sup>2</sup> for Ni, 3d<sup>2</sup> 4s<sup>2</sup> for Ti and 2s<sup>2</sup> 2p<sup>6</sup> for O. The k-point sampling of the Brillouin zone was constructed using the Monkhorst-Pack scheme [27] with 4 × 4 × 4 grids in primitive cells. The converging cut off energy of a plane-wave was set to 500 eV for all cases. The geometrical optimization of the crystals structures were performed in the Broyden-Fletcher-Goldfarb-Shanno (BFGS) relaxation method [28] by setting the convergence tolerances 1.0 × 10<sup>-5</sup> eV/atom for the energy, 0.03 eV/Å for the maximum force on atoms, 0.05 GPa for the maximum stress and 1.0 × 10<sup>-3</sup> Å for the maximum atomic displacement. To investigate the effect of Sr, Ni doping in pristine BaTiO<sub>3</sub> ceramic, 2 × 2 × 2 supercell were built which are shown in geometrically optimized form (Fig. 1).

## 3. Electronic properties

Electronic properties like the band structure, the density of states (DOS), electron density, etc. provide important information about the material's physical properties with the bonding nature. The specific study of bonding characteristics of BSTO and BNT0 are so important. We used GGA for calculating their electronic properties. To achieve a good understanding of the bonding nature of these compounds, the total density of states (TDOS), and the partial density of states (PDOS) have been calculated. For those, k-points have been utilized. The Monkhorst–Pack technique was used for sampling the k-points over the first Brillouin zone (see Fig. 1).

To investigate the nature of BTO, BSTO, BNT0, and BSNT0, the electronic band structure along the high symmetry direction in the Brillouin zones are shown above in Fig. 2. The direct bandgap is seen in all the four cases, i.e., an electron in each case can move easily from the highest-energy state of the valence band to the lowest-energy state of the

conduction band without changing the crystal momentum. The band gap of pristine BTO is found 1.719 eV, 1.715 eV for BSTO, BNT0 is 1.705 eV and 1.713 eV for BSNT0 revealed semiconducting nature. As the band gap of pristine BTO shows good consistency with the previously calculated value, recommends the acceptability of the present calculation of this approach for other materials [31]. The band gap of (Sr, Ni) co-doped BTO is lower than the band gap of pristine BTO which means co-doping reduces the band gap slightly.

Figs. 3 and 4 show the total and partial density of states of our studied materials. From Figs. 2–4, it can be shown that Oxygen (O) 2p state dominate in all the four compounds because of the highest valence band lies at the Fermi level (E<sub>F</sub>) at 0 eV, which are the common characteristics of oxide semiconducting materials. The valence band in all the cases lie between -59.0 eV and 0 eV (E<sub>F</sub>). In the valence band, most of the contribution comes from Ba-6s, Ba-5p, Sr-5s, Sr-4p, Ni-4s, Ni-3d, Ti-4s, Ti-3d, O-2s and O-2p orbitals. In BSNT0, sharp peaks are observed in the valence and conduction band near the E<sub>F</sub>. We also observed predominant hybridization for Ti-3d and O-2s states near the E<sub>F</sub>. In the conduction band the similar kind of domination of Ti-3d and O-2s states are noticed. In BSNT0, Ni-4d states also contribute to bonding with O-2p states. There is no overlapping of Ti-4s and Ti-3d with O-2s and O-2p, mean the bonding may be ionic in nature.

## 4. Optical properties

Optical spectroscopy analysis is a substantial tool to study the metal oxide family to use those in optoelectronic devices such as solar cells [32–36]. In this paper, optical properties are simulated by using polarized light with smearing value 0.5 eV in the direction [100]. Under that condition absorption, reflectivity, photoconductivity, real and imaginary part of dielectric constant, refractive index and loss function of these materials have been studied from the formalism developed in CASTEP.

The optical properties of all the four cases are calculated by the frequency dependent complex dielectric function,  $\epsilon(\omega) = \epsilon_1(\omega) + i\epsilon_2(\omega)$ . The imaginary part of dielectric function  $\epsilon_2(\omega)$  is closely correlated with the band structure of a material and can be obtained from the momentum matrix elements between the occupied and the unoccupied



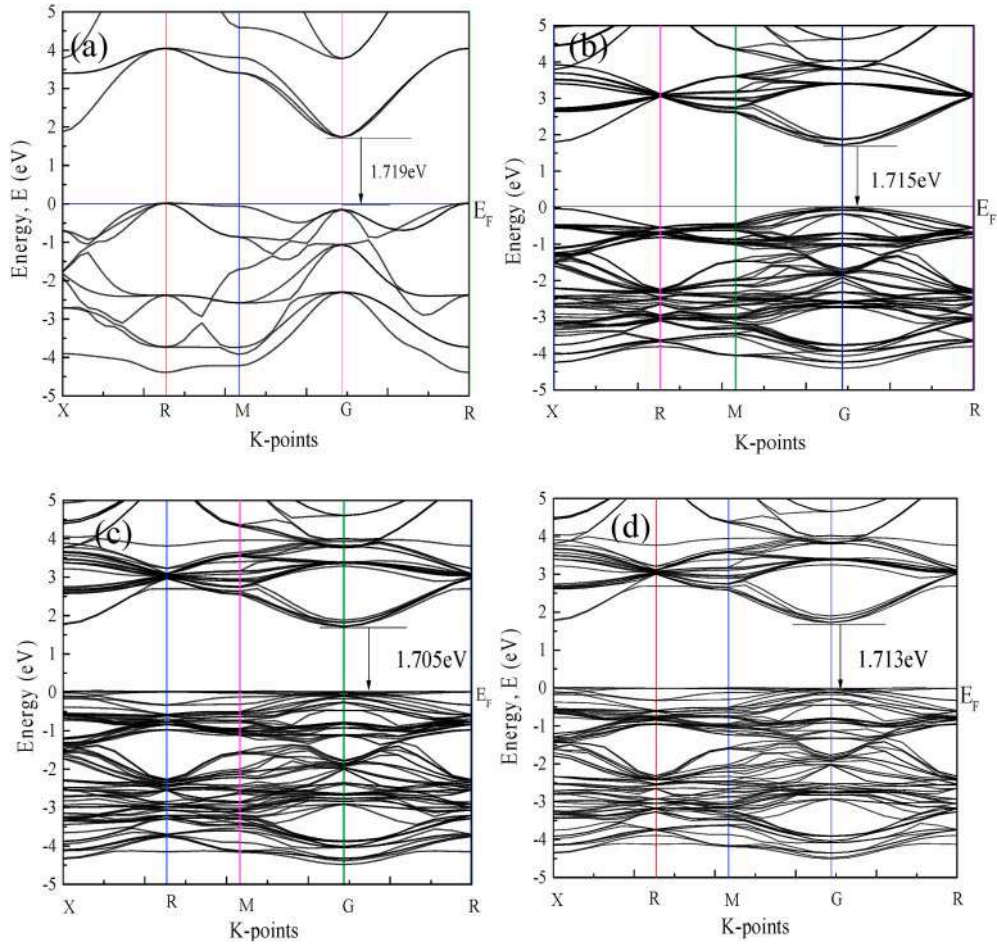


Fig. 2. Electronic band structure of (a) Pristine BTO (b) BSTO (c) BNTO and (d) BSNTO.

electronic state using the following equation-

$$\varepsilon_2(\omega) = \frac{2e^2\pi}{\Omega\epsilon_0} \sum_{k,\nu,c} |\psi_k^c| \mathbf{u} \cdot \mathbf{r} |\psi_k^\nu|^2 \delta(E_k^c - E_k^\nu - E)$$

where,  $\omega$  is the light frequency,  $e$  is the electron charge,  $\psi_k^c$  and  $\psi_k^\nu$  are the wave functions of conduction band and valance band respectively,  $\mathbf{u}$  is the polarization vector of the incident electric field. The real part of the dielectric function,  $\varepsilon_1(\omega)$ , can be obtained from the imaginary part,  $\varepsilon_2(\omega)$ , using the Kramers-Kronig transformation. The other optical properties, absorption, reflectivity, conductivity and refractive index can also be obtained from the frequency dependent complex dielectric function,  $\varepsilon(\omega)$  [37].

In Fig. 5, BSTO showed lower values in all the cases while the optical properties with a dielectric constant are slightly better in pristine BTO. Almost similar patterns are noticed for all the materials in the 0–50 eV region. Yet some inconsistencies are observed in 5–15 eV and 22–32.5 eV regions. Peaks are sharp in the case of reflectivity for BSTO in the 15–30 eV region. An additional peak is also observed in BSTO in the 20–30 eV region for the imaginary part of conductivity. In the real part of the dielectric function, we noticed the better values for BSNTO in the high energy region (>30 eV). A peak is also observed in the case of the imaginary part of dielectric constant at ~36 eV. Again, the optical constants of these materials are consistent except for the energy regions 0–2 eV and 20–25 eV. But in the IR to medium UV regions things are diverse. BSNTO and BNTO showed similar trends in all the eight cases. Absorption (Fig. 5(a)) is high for BSNTO and BNTO near IR region and BSNTO is highest in the medium UV region. BTO and BSTO showed similar pattern for reflectivity, conductivity, dielectric function and

refractive indexes while BSNTO follows the trend of BNTO in those cases. In the Fig. 6, the loss function shows similar patterns for all the materials except in the region 20–30 eV. The peak is large for BNTO. Here also loss function is high in the IR zone for BSNTO and BNTO and parallel trends are seen in the visible to UV region for all the four materials.

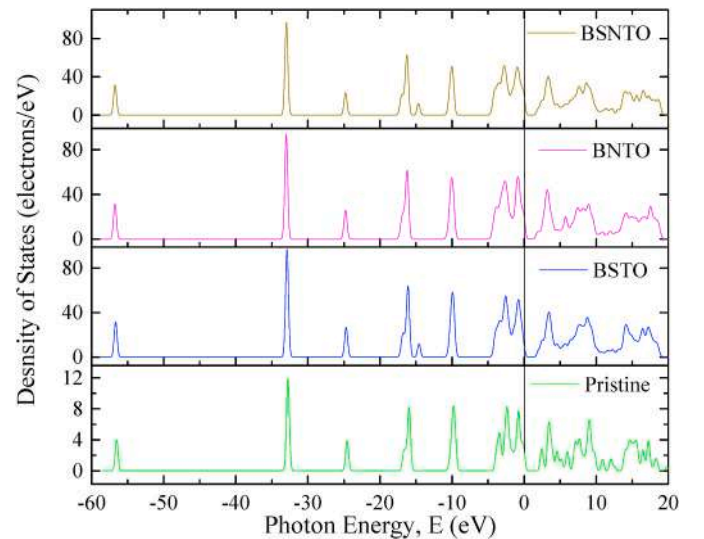


Fig. 3. Density of states (DOS) of Pristine BTO, BSTO, BNTO and BSNTO.

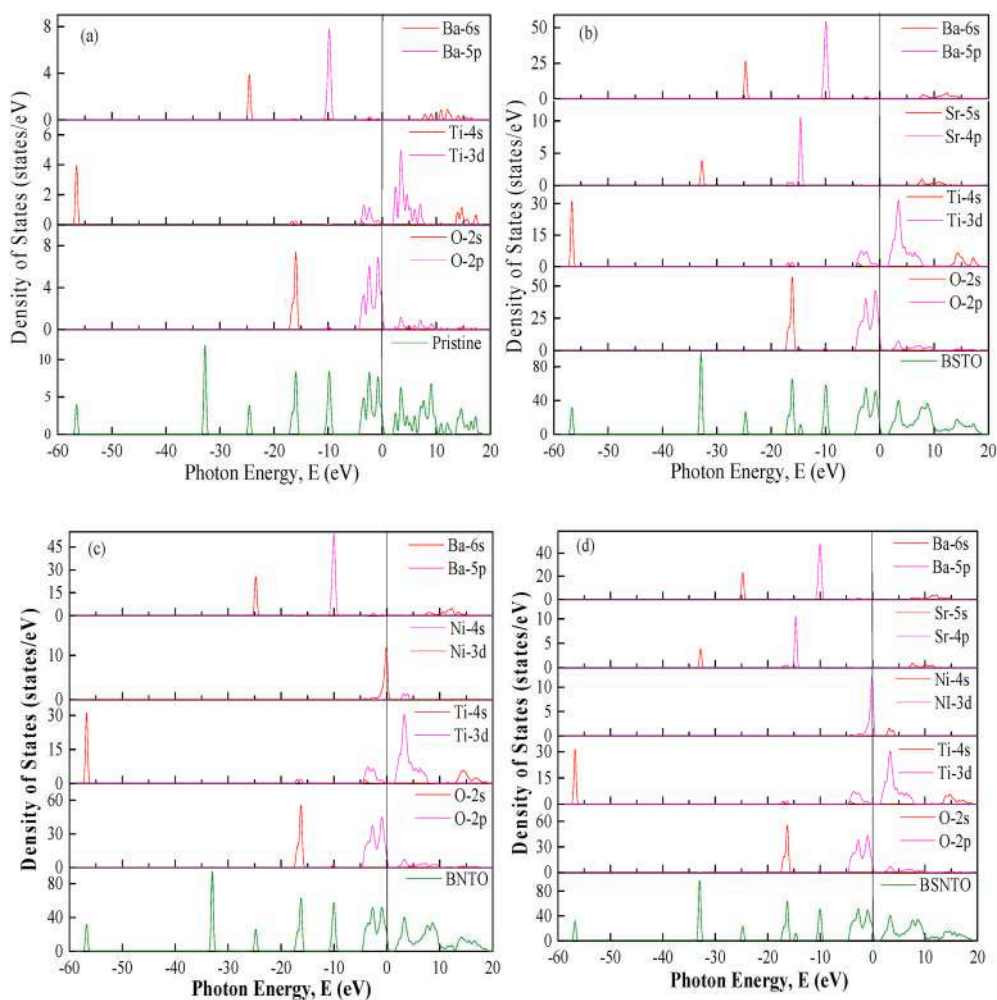


Fig. 4. The total and partial density of states of (a) Pristine BTO, (b) BSTO, (c) BNTO and (d) BSNTO.

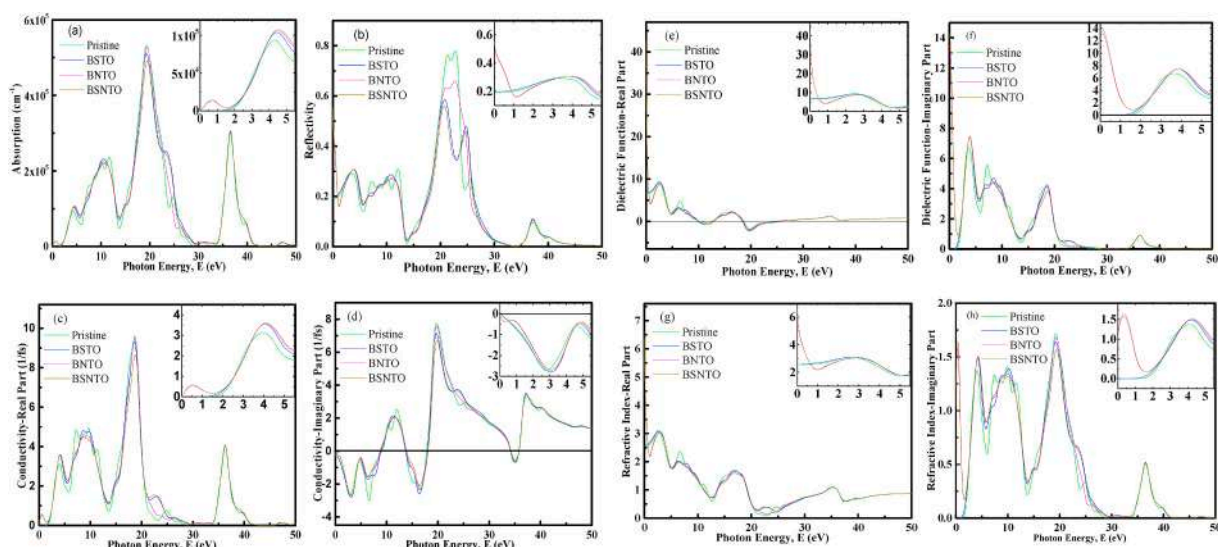


Fig. 5. The calculated photon energy dependent (a) absorption, (b) reflectivity, (c) real part of conductivity, (d) imaginary part of conductivity, (e) real part of dielectric function, (f) imaginary part of dielectric function, (g) refractive index-Real Part and (h) refractive index-Imaginary Part. In the inset of every diagram, the variations are illustrated for the IR to Medium UV regions.

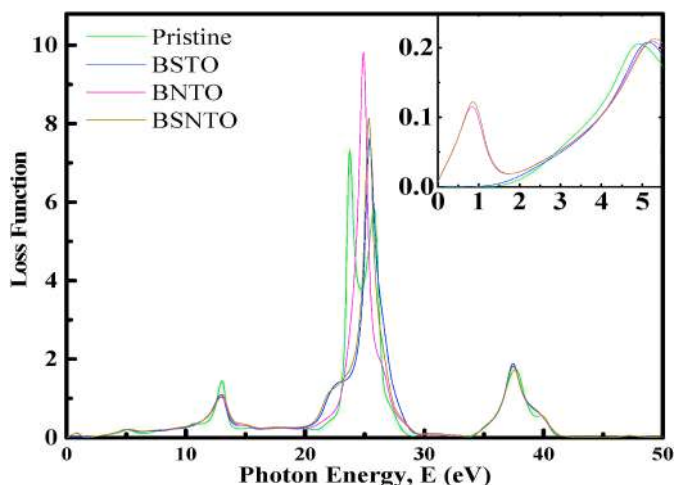


Fig. 6. Loss function as a function of photon energy of Pristine BTO, BSTO, BNTO and BSNTO.

## 5. Conclusions

The structural, electronic and optical properties of pristine BTO, Sr doped, Ni doped and (Sr, Ni) co-doped BTO via density functional theory have been studied. In this study, structural properties showed cubic nature for all the four materials. Co-doping reduces the lattice constant (4.03 to 4.01 Å) and structural volume (65.67 to 64.29 Å<sup>3</sup>) as the ionic radius of Sr and Ni are smaller than Ba. A decrease of material density (5.90 to 5.56 g/cm<sup>3</sup>) is also observed in co-doped BTO. A slight reduction of bandgap is seen (1.719 to 1.713 eV) in co-doping material than the pristine BTO. In the optical properties, the influence of Sr in co-doping is visible in the high energy regions. But in the IR to Medium UV region, the similar optical properties are observed in both Ni doped BTO and (Sr, Ni) co-doped BTO, i.e., the influence of Ni is clearly visible to the co-doped material. Similarly, Ni may also influence the magnetic properties in co-doping. From the above analysis, we can conclude that the (Sr, Ni) co-doped BTO showed a promising material for both electronic and optoelectrical devices. This type of material is expected to show a multiferroic nature.

## Funding

This study received no specific grant from any funding agency.

## Declaration of competing interest

The authors declare that they have no known competing financial interests or personal relationships that could have appeared to influence the work reported in this paper.

## References

- [1] O. Saburi, Properties of semiconductive barium titanate, *J. Phys. Soc. Jpn.* 14 (1959) 1159–1174.
- [2] G.G. Harman, Electrical properties of BaTiO<sub>3</sub> containing samarium, *Phys. Rev.* 106 (1957) 1358–1359.
- [3] F. Jona, G. Shirane, *Ferroelectric Crystals*, Elsevier, Amsterdam, 1963.
- [4] H. Kishi, Y. Mizuno, H. Chazono, Base metal electrode-multilayer ceramic capacitors: past, present and future perspectives, *Jpn. J. Appl. Phys.* 42 (2003) 1–15.
- [5] B. Huybrechts, K. Ishizaki, M. Takata, The positive temperature coefficient of resistivity in barium titanate, *J. Mater. Sci.* 30 (1995) 2463–2474.
- [6] B. Jaffe, W.R. Cook, H. Jaffe, *Piezoelectric Ceramics*, vol. 3, Academic Press, London, 1971, p. 120.
- [7] H.F. Kay, Preparation and properties of crystals of barium titanate BaTiO<sub>3</sub>, *Acta Crystallogr.* 1 (1948) 229–237.
- [8] W.J. Merz, The electric and optical behavior of BaTiO<sub>3</sub> single-domain crystals, *Phys. Rev.* 76 (1949) 1221–1225.
- [9] W.P. Mason, Use of temperature and time-stabilized barium titanate ceramics in transducers, mechanical wave transmission systems and force measurements, *Acustica* 4 (1954) 200–202.
- [10] A. Beitollahi, S.A. Mortazavi, Effect of the level of addition of Nb<sub>2</sub>O<sub>5</sub>/Co<sub>2</sub>O<sub>3</sub> and Ba(Nb<sub>2/3</sub>Co<sub>1/3</sub>)O<sub>3</sub> on the structure, microstructure and dielectric properties of BaTiO<sub>3</sub>, *J. Mater. Sci. Mater. Electron.* 14 (2003) 129–134.
- [11] S. Jayanthi, T.R.N. Kutty, Extended phase homogeneity and electrical properties of barium calcium titanate prepared by the wet chemical methods, *Mater. Sci. Eng. B* 110 (2004) 202–212.
- [12] V.V. Shvartsman, W. Kleemann, J. Dec, Z.K. Xu, S.G. Lu, Diffuse phase transition in BaTi<sub>1-x</sub>Sn<sub>x</sub>O<sub>3</sub> ceramics: an intermediate state between ferroelectric and relaxor behaviour, *J. Appl. Phys.* 99 (2006) 124111–124118.
- [13] B. Cui, P.F. Yu, J. Tian, Z.G. Chang, Preparation and characterization of Codoped BaTiO<sub>3</sub> nanosized powders and ceramics, *Mater. Sci. Eng. B* 133 (2006) 205–208.
- [14] S.K. Rout, E. Sinha, S. Panigrahi, Dielectric properties and diffuse phase transition in Ba<sub>1-x</sub>Mg<sub>x</sub>Ti<sub>0.6</sub>Zr<sub>0.4</sub>O<sub>3</sub> solid solutions, *Mater. Chem. Phys.* 101 (2007) 428–432.
- [15] J.A. Becker, C.B. Green, G.L. Pearson, Properties and uses of thermistors thermally sensitive resistors, *Trans. AIEE* 65 (1946) 711–725.
- [16] G. Lavenuta, Negative temperature coefficient thermistors, *Sensors* 14 (1997) 46–55.
- [17] O. Mrooz, A. Kovalski, J. Pogorzelska, O. Spotyuk, M. Vakiv, B. Butkiewicz, J. Maciak, Thermoelectrical degradation processes in NTC thermistors for inrush current protection of electronic circuits, *Microelectron. Reliab.* 41 (2001) 773–777.
- [18] J.G. Fagan, V.R.W. Amarkoon, Reliability and reproducibility of ceramic sensors: part I NTC thermistor, *Am. Ceram. Soc. Bull.* 72 (1993) 70–78.
- [19] S. Pal, A.B. Swain, P.P. Biswas, D. Murali, A. Pal, B.R.K. Nanda, P. Murugavel, Giant photovoltaic response in band engineered ferroelectric perovskite, *Sci. Rep.* 8 (2018).
- [20] Meera Rawat, K.L. Yadav, Compositional effects on structural, dielectric, ferroelectric and transport properties of Ba<sub>1-x</sub>(Bi<sub>0.5</sub>Li<sub>0.5</sub>)<sub>x</sub>TiO<sub>3</sub> ceramics, *Mater. Chem. Phys.* 148 (3) (2014) 655–663.
- [21] A. Ioachim, M.I. Toacsan, M.G. Banciu, L. Nedelcu, F. Vasiliu, H.V. Alexandru, C. Berbecaru, G. Stoica, Barium strontium titanate-based perovskite materials for microwave applications, *Pro. Solid State Chem* 35 (2007) 513–520.
- [22] M.Y. Shahid, A. Anwar, F. Malik, M. Asghar, M.F. Warsi, S.Z. Ilyas, Effect of Sr-doping on ferroelectric and dielectric properties of sol-gel synthesized BaTiO<sub>3</sub> thin films, *Dig. J. Nano. and Bio.* 12 (3) (2017) 669–677.
- [23] X. Cheng, M. Shen, Enhanced spontaneous polarization in Sr and Ca Co-doped BaTiO<sub>3</sub> ceramics, *Solid State Commun.* 141 (2007) 587–590.
- [24] S.R. Singamaneni, S. Punugupati, J.T. Prater, J. Narayan, Diamagnetism to ferromagnetism in Sr-substituted epitaxial BaTiO<sub>3</sub> thin films, *Appl. Phys. Lett.* 108 (2016) 142407.
- [25] Yogeswar Kumara, Md Ahamad Mohiddona, Alok Srivastavab, K.L. Yadava, Effect of Ni doping on structural and dielectric properties of BaTiO<sub>3</sub>, *Indian J. Eng. Mater. Sci.* 16 (2009) 390–394.
- [26] J.P. Perdew, K. Burke, M. Ernzerhof, Generalized gradient approximation made simple, *Phys. Rev. Lett.* 77 (1996) 3865.
- [27] H.J. Monkhorst, J.D. Pack, Special points for Brillouin-zone integrations, *Phys. Rev. B* 13 (1976) 5188.
- [28] B.G. Pfrommer, M. Côté, S.G. Louie, M.L. Cohen, Relaxation of crystals with the Quasi-Newton method, *J. Comput. Phys.* 131 (1997) 233–240.
- [29] K.H. Hellwege, A.M. Hellwege, *Ferroelectrics and Related Substances*, Landolt-Bornstein, vol. 3, Springer-Verlag, Berlin, 1969.
- [30] Y. Ma, H. Chen, F. Pan, Z. Chen, Z. Ma, X. Lin, F. Zheng, X. Ma, Electronic structures and optical properties of Fe/Co-doped cubic BaTiO<sub>3</sub> ceramics, *Ceram. Int.* 45 (5) (2019) 6303–6311.
- [31] Ph Ghose, J.-P. Michenaud, X. Gonze, Dynamical atomic charges: the case of ABO<sub>3</sub> compounds, *Phys. Rev. B* 58 (1998) 6224.
- [32] B. Amin, R. Khenata, A. Bouhemadou, I. Ahmad, M. Maqbool, Opto-electronic response of spinels MgAl<sub>2</sub>O<sub>4</sub> and MgGa<sub>2</sub>O<sub>4</sub> through modified Becke-Johnson exchange potential, *Physica B* 407 (2012) 2588–2592.
- [33] M. Maqbool, B. Amin, I. Ahmad, Bandgap investigations and the effect of the in and Al concentration on the optical properties of In<sub>x</sub>Al<sub>1-x</sub>N, *J. Opt. Soc. Am. B* 26 (2009) 2181–2184.
- [34] S.H. Shaha, W. Khan, A. Laref, G. Murtaza, Effects of anion replacement on the physical properties of CaCd<sub>2</sub>X<sub>2</sub> (X = P, As, Sb, Bi), *J. Phys. Chem. Solid.* 127 (2019) 81–87.
- [35] K.M. Wong, W. Khan, M. Shoaib, U. Shah, S.H. Khan, G. Murtaza, *Ab initio* investigation of the structural, electronic and optical properties of the Li<sub>2</sub>In<sub>2</sub>XY<sub>6</sub> (X = Si, Ge; Y = S, Se) compounds, *J. Electron. Mater.* 47 (1) (2018) 566–576.
- [36] K.M. Wong, M. Irfan, A. Mahmood, G. Murtaza, First principles study of the structural and optoelectronic properties of the A<sub>2</sub>InSbO<sub>6</sub> (A = Ca, Sr, Ba) compounds, *Optik* 130 (2017) 517–524.
- [37] S.M.A. Abbas, F. Javed, G. Abbas, N. Amin, A. Laref, Density functional theory evaluation of ceramics suitable for hybrid advanced oxidation processes: a case study for Ce<sup>4+</sup>-doped BaZrO<sub>3</sub>, *J. Phys. Chem. C* 123 (10) (2019) 6044–6053.